STUDY OF MECHANICAL PROPERTIES OF JOINTED ROCK MASS USING LATTICE-SPRING-BASED SYNTHETIC ROCK MASS (LS-SRM) MODELING APPROACH

by

Subash Bastola

A thesis submitted in partial fulfillment of the requirements for
the degree of Doctor of Philosophy (PhD) in Natural Resources Engineering

The Faculty of Graduate Studies
Laurentian University
Sudbury, Ontario, Canada

THESIS DEFENCE COMMITTEE/COMITÉ DE SOUTENANCE DE THÈSE
Laurentian Université/Université Laurentienne
Faculty of Graduate Studies/Faculté des études supérieures

Title of Thesis Titre de la thèse	STUDY OF MECHANICAL PROPERTIES OF JOINTED ROCK MASS USING LATTICE SPRING BASED SYNTHETIC ROCK MASS (LS-SRM) MODELING APPROACH
Name of Candidate Nom du candidat	Bastola, Subash
Degree Diplôme	Doctor of Philosophy
Department/Program Département/Programme	Natural Resources Engineering
Date of Defence Date de la soutenance	December 16, 2019

APPROVED/APPROUVÉ

Thesis Examiners/Examinateurs de thèse:

Dr. Ming Cai
(Supervisor/Directeur de thèse)

Dr. Shailendra Sharan
(Committee member/Membre du comité)

Dr. Eugene Ben-Awah
(Committee member/Membre du comité)

Dr. Mounir Naili
(Committee member/Membre du comité)

Dr. Steve Zou
(External Examiner/Examinateur externe)

Prof. Ross Sherlock
(Internal Examiner/Examinateur interne)

Approved for the Faculty of Graduate Studies
Approuvé pour la Faculté des études supérieures
Dr. David Lesbarrères
Monsieur David Lesbarrères
Dean, Faculty of Graduate Studies
Doyen, Faculté des études supérieures

ACCESSIBILITY CLAUSE AND PERMISSION TO USE

Abstract

With the recent development of high-end computation technology, it is feasible to use complex numerical modeling technique such as synthetic rock mass (SRM) modeling for the characterization of mechanical properties of rock mass. However, the SRM modeling approaches that have been used to date such as the ones based on bonded particle and bonded blocks cannot properly incorporate realistic discontinuity surface geometry (waviness and roughness) into the numerical model and discontinuities are often simplified as having planar surfaces. Models with simplified planar discontinuity surfaces do not represent the true geometry and physics of the natural discontinuities which raises the question on the reliability of the geotechnical parameters resulting from these models. It is widely known that the inherent surface roughness significantly influences the shear strength and stiffness of a non-planar discontinuity. The goal of this thesis is to develop numerical models that can incorporate these natural undulating discontinuities for the determination of reliable estimates of strength and deformation properties of jointed rock masses.

Three-dimensional lattice-spring-based synthetic rock mass (LS-SRM) models are generated by incorporating both planar and non-planar discontinuities to simulate the mechanical behaviors of both laboratory-scale jointed rock and mine-scale jointed rock masses. A calibration methodology is established by means of extensive sensitivity analysis of lattice model parameters. Studies are also conducted to understand the crack evolution mechanism (initiation and propagation) in pre-cracked marbles with both planar and non-planar cracks. Influences of joint properties (orientation, intensity, persistence, and roughness) on the strength and deformability of jointed rock under compression are also investigated. Influence of rock mass scale on the strength and deformation modulus is investigated to determine the representative elementary volume (REV) of the rock mass. Using the REV sized rock mass, the influence of discontinuity intensity and confining

pressure on the mechanical properties (strength & deformability) of jointed rock masses are also investigated. In addition, the influence of the pre-existing natural discontinuity of different configurations (waviness, intensity, size) and *in-situ* stress on slope stability and deformability of an open pit mine are investigated.

Complex crack propagation mechanism is observed in the laboratory-scale pre-cracked rocks with non-planar cracks under compression. There is an increase in the strength and deformation modulus for the laboratory-scale jointed rock models with non-planar discontinuities, lower discontinuity intensity, and lower discontinuity persistence. Peak strength and deformation modulus of the rock mass decreases with the increase of discontinuity intensity. Peak strength of the rock mass increases with the increase of confining pressure. Slopes excavated in the rock mass with non-planar discontinuities are found to be more stable than the slopes excavated in the rock mass with planar discontinuities. Similarly, slopes excavated in the rock mass with larger discontinuity size and higher discontinuity intensity are less stable than the ones excavated in the rock mass with smaller discontinuity size and lower discontinuity intensity. It is also found that the slopes exhibited localized instabilities under the influence of high *in-situ* stress.

The findings of this research aid in better characterization of the mechanical behavior of jointed rock mass and provide more reliable estimates of geotechnical design parameters.

Keywords

Jointed rock mass, lattice-spring-based synthetic rock mass (LS-SRM), discrete fracture network (DFN), non-planar discontinuities, discontinuity orientation, discontinuity roughness, discontinuity persistence, discontinuity intensity, crack propagation, slope stability.

Original contributions

Major contributions of this thesis are summarized below.

a) Developed calibration approaches for laboratory-scale intact rock (Chapter 3), laboratory-scale jointed rock (Chapter 4), and field-scale rock mass (Chapter 6) based on the extensive parametric study of lattice model parameters to investigate the mechanical behaviors of rock mass.

b) Enhanced the understanding of the cracking mechanism in non-planar and non-persistent cracks in laboratory-scale pre-cracked rocks under unconfined and confined compressions (Chapter 4).

c) Improved the knowledge on the influence of discontinuity orientation and persistence on the mechanical response of laboratory-scale jointed rock under triaxial loading condition (Chapter 5).

d) Enriched the understanding of the influence of joint waviness on the mechanical response of laboratory-scale jointed rock under both triaxial and true-triaxial loading conditions (Chapter 5).

e) New insights are developed on the influence of the natural discontinuity intensity and waviness on the mechanical responses of both the laboratory-scale jointed rock (Chapter 5) and large-scale rock mass (Chapter 7) under triaxial loading condition.

f) Elevated the understanding of the scale effect on the strength and deformability of rock mass under unconfined compression (Chapter 7).

g) Proposed empirical relations for the estimation of strength and deformation modulus of laboratory-scale jointed rock (Chapter 5) and large-scale jointed rock mass (Chapter 7).

h) Investigated the influence of different discontinuity configurations (waviness, size, intensity), and *in-situ* stress on slope deformation and stability (Chapter 6).

Acknowledgments

This research was supported by Ontario Trillium Scholarship at Laurentian University, Natural Sciences and Engineering Research Council (NSERC CRD 470490 - 14) of Canada, Nuclear Waste Management organization (NWMO), Rio Tinto, and Itasca Consulting Group through its Itasca Education Partnership (IEP) program, and MIRARCO Mining Innovation.

I would like to thank my thesis supervisor Dr. Ming Cai for his valuable guidance, support, and his patience during the research. I would like to acknowledge my committee members, Dr. Shailendra Sharan, Dr. Eugene Ben-Awah, Dr. Mounir Naili; internal examiner, Dr. Ross Sherlock; and external examiner, Dr. Steve Zou for reviewing the dissertation and providing valuable technical advice. I would also like to thank my Itasca Education Partnership (IEP) mentor Dr. Branko Damjanac from Itasca Consulting Group, Inc. for his support and technical advice in the use of SRMTools software and feedbacks during the manuscript preparation. Special thanks are also extended to Dr. Varun Varun and Maurilio Torres from Itasca Consulting Group, Inc. for their valuable guidance on the use of the software.

I would like to thank Dr. Lorrie Fava for inviting me to work at MIRARCO Mining innovation and pursue a PhD program at Laurentian University. I would also like to thank my friends, staffs, and colleagues at MIRARCO., especially to Qin Liang for her ensuring the availability of multiple high-end PCs, Mr. Darren Janeczek and Mr. Scott McGarvey for ensuring the timely bug fixes in MoFrac software, and Mingzheng Wang and Dr. Xin Wang for valuable discussions. I would like to thank my wife, the love of my life and a true friend, Avilasha for walking with me in thick and thins. I would like to thank my parents for their unconditional love and support.

Table of Contents

List of Tables

List of Figures

List of Symbols and Abbreviations

α	Crack angle
α_k	Stiffness calibration factor
α_t	Strength calibration factor
δ_j	Dilation angle
β	Ligament length
φ_j	Joint friction angle
φ_b	Basic friction angle
φ_{fjp}	Peak friction angle of flat joint
φ_{fjr}	Residual friction angle of flat joint
φ_p	Peak joint friction angle
φ	Friction angle
σ_1	Major principal stress
σ_3	Minor principal stress
$\acute{\sigma}_{3\max}$	Upper limit of confining stress
σ_0	Stress level on the sliding surface which is related to slope height
σ_t	Tensile strength
σ_{tj}	Joint tensile strength
σ^2_{P32}	Variance of fracture volumetric intensity
σ_2	Intermediate principal stress
σ_n	Normal stress
σ_{ci}	Crack initiation stress
σ_c	Uniaxial compressive strength of intact rock
σ_m	Rock mass strength
σ_d	Standard deviation of equivalent fracture diameter
σ_{cmic}	Lattice compressive strength
$(\sigma_t)_{mic}$	Lattice tensile strength
σ_{cd}	Crack damage stress
θ	Joint dip (angle)
λ	Joint dip direction (angle)
γ	Rock mass density
ω_i	Angular velocities of component i (i = 1, 2, 3)

μ	Coefficient of friction of the joint
μ_{P32}	Mean fracture volumetric intensity
τ	Joint shear strength
$2a$	Crack length
$2b$	Ligament length
a	Rock mass parameter dependent on the magnitude of GSI and D
A_d	Discontinuity or fracture area
A_{rb}	Area of rock bridge
A_{min}	Minimum fracture area
A_{max}	Maximum fracture area
c	Cohesion
c_j	Joint cohesion
CLD	Cumulative length distribution
CAD	Cumulative area distribution
D	H–B disturbance factor for jointed rock mass
d_e	Equivalent fracture diameter
d	Lattice contact gap
E_i	Intact rock modulus
E_m	Rock mass modulus
E_{mpp}	Post peak deformation modulus of rock mass
E_{mic}	Lattice Young's modulus
E_{mac}	Macroscopic Young's modulus
FS	Factor of safety
F^{Nmax}	Maximum normal strength
F^N	Normal spring force
F_i^S	Shear spring force
$\sum F_i$	Sum of all force-components
GSI	Geological strength index
h	Slope height
H	Pillar height
I	Moment of inertia
i	Joint roughness component

j_f	Joint factor
j_n	Joint frequency
JRC	Joint roughness coefficient index
K	Discontinuity persistence
k	Ratio of *in-situ* stress to rock strength
K_0	Ratio of horizontal to vertical *in-situ* stress
k^S	Spring's shear stiffness
k^N	Spring's normal stiffness
K_R	Bulk modulus
k_f	Fisher constant
k_{nj}	Joint normal stiffness
k_{sj}	Joint shear stiffness
$MRMR$	Modified rock mass rating
$\sum M_i$	Sum of all moments-components
m	Mass
m_i	Intact rock parameter fitted to Hoek–Brown (H–B) strength parameter
m_b	Rock mass parameter fitted to H–B strength parameter
n	Coefficient of influence of joint inclination
n_j	Reduction factor related to joint configuration and failure mode
Δn	Number of sampled fractures
n_{min}	Number of fractures above the maximum fracture area threshold
n_{max}	Number of fractures above the minimum fracture area threshold
n_{rg}	Number of fractures in a region group
n_i	Unit normal vector
N	Number of cracks
p	Parameters related to pillar and laboratory sample
P_{10}	Number of fractures per unit length
P_{11}	Length of fractures per unit length
P_{20}	Number of fractures per unit area
P_{21}	Length of fractures per unit area
P_{22}	Area of fracture traces per unit area
P_{30}	Number of discontinuities per unit volume

P_{32}	Area of fractures per unit volume
P_{33}	Volume of fractures per unit volume
Q	Rock mass quality
r	Coefficient of joint strength
RQD	Rock quality designation
RMR	Rock mass rating
RMi	Rock mass index
RM	Radius multiplier
R_n	Range of random number generator
R	Lattice resolution
s	Rock mass parameter dependent on the magnitude of GSI and D
s’	Parameters related to pillar and laboratory sample
SD	MoFrac slope deviation parameter
S_A	Sample area generating function
Δt	Time step
$u_i(t)$	Position of the components of nodes i (i = 1, 2, 3) at time t
$v_i(t)$	Velocity of the components of nodes i (i = 1, 2, 3) at time t
v_p	Pillar volume
v_s	Laboratory sample volume
WD	Degree of weathering of discontinuities
W	Pillar width

Preface

This research work has been undertaken at MIRARCO Mining Innovation and Bharti School of Engineering, Laurentian University, under the supervision of Dr. Ming Cai. This research was supported by Ontario Trillium Scholarship at Laurentian University, Natural Sciences and Engineering Research Council (NSERC CRD 470490 - 14) of Canada, Nuclear Waste Management organization (NWMO), Rio Tinto, and Itasca Consulting Group through its Itasca Education Partnership (IEP) program, and MIRARCO Mining Innovation.

The results presented in Chapter 3 are published in the proceedings of the 52nd US Rock Mechanics Symposium, 2018, which was organized by American Rock Mechanics Association at Seattle, USA (Bastola & Cai, 2018b). The results shown in Chapter 4 are published in the journal of *Computer and Geotechnics* (Bastola & Cai, 2019). The results presented in Chapter 5 are partially published in the proceedings of the 2nd International Discrete Fracture Network Engineering Symposium, 2018, which was organized by American Rock Mechanics Association at Seattle, USA (Bastola & Cai, 2018a) and a content-extended paper is accepted for publication in *International Journal of Rock Mechanics and Mining Sciences*. A paper based on the slope stability study results in Chapter 6 is submitted with minor revision to the *Journal of Rock Mechanics and Geotechnical Engineering*. A manuscript is being prepared for submission to the journal of *Rock Mechanics and Rock Engineering* based on the results in Chapter 7.

Chapter 1

1 Introduction

1.1 Background

The determination of the mechanical properties of rock mass is a major concern in geotechnical engineering design (Brown, 2008). It is impractical to perform direct loading tests of rock mass structures. Instead, empirical design approaches are commonly used in the stability assessment of geotechnical structures such as mine excavations, tunnels, pillars, open pit slopes, etc. (Mark, 2016). These empirical design approaches may not be universally applicable in all geological settings because of the inherent heterogeneity and anisotropy of rock mass associated with discontinuities in the form of joints, bedding planes, faults, etc. (Brady & Brown, 2006).

Numerical modeling approach provides an alternative to the empirical methods for the investigation of strength and deformation behaviors of jointed rock mass (Jing, 2003). A representative numerical model is the one that can explicitly incorporate most of the rock mass features in three dimensions. Rock discontinuities are often characterized with the natural undulating surface which can interlock the movement of the sliding blocks and in turn influence the strength and deformation behaviors of jointed rock mass. The reason is that with the application of external load, fracturing of the intact rock occurs simultaneously with the breaking of asperities and the deterioration of pre-existing discontinuities (Barton, 1973). Hence, it is imperative to investigate the influence of rough discontinuities on the strength and deformation of jointed rock mass. This requires realistic numerical models that can properly simulate the physics of the of the rock masses with rough discontinuities under natural loading condition.

The synthetic rock mass (SRM) modeling method is very robust in realistic representation of the rock masses because the discontinuities are explicitly represented as discrete fracture network (DFN) in the intact rock matrix. The DFN models are often used for the realistic representation of discontinuities in the rock mass (Jing & Stephansson, 2007; Lei et al., 2017). DFNs are often represented using discontinuities with planar surface geometry, but in nature discontinuities manifest as non-planar features which can be characterized using large-scale waviness and small-scale roughness (Barton & Choubey, 1977). Due to interlocking, a rock mass containing discontinuities with large-scale waviness can have higher strength and deformation modulus. Study needs to be conducted to generate realistic rock mass models such as SRM using DFN with rough discontinuity surface to assess the stability of structures built in or on jointed rock masses.

In addition, a full-span or ubiquitous wedge approach is often used to design rock support to stabilize wedges in the roof of underground openings (Diederichs et al., 2000; González-Palacio et al., 2005) and in the unstable rock slopes (Wyllie, 2017a). This worst-case scenario analysis often leads to conservative rock support design. A realistic geometrical representation of discontinuity surface would allow for more representative kinematic analysis that would aid in a reliable, safe, and economical geotechnical design.

1.2 Motivation

Mechanical properties (strength and stiffness) of rock discontinuities are strongly influenced by the roughness of the discontinuity surface. In blocky rock masses, intersecting discontinuities form wedges and these rock blocks are free to rotate, translate and deform. The displacement along the block interface depends on the physical (degree of weathering, water content) and mechanical properties (cohesion and friction) of the interface. Shear strength of rock masses depends on the

cohesion and frictional resistance of these interfaces. The frictional resistance of the block interface depends on the surface geometry and it increases with the increase of the degree of waviness. Thus, block interfaces with the non-planar surface may be significantly stronger and stiffer than the ones with the planar surface because of the interlocking of asperities along the block interface with the rough surface. Rock structures containing discontinuities with large-scale waviness could exhibit a higher strength, thus, reducing the support system requirements to stabilize these structures. For safe and economical geotechnical design, it is imminent to have a reliable estimate of the strength and deformational properties of jointed rock mass.

The mechanical properties of a rock mass can be estimated using numerical models based on the SRM approach. Existing SRM models employ either bonded particle model (BPM) in particle flow code (PFC) or bonded block model (BBM) in universal distinct element code (UDEC or 3DEC). These modeling approaches often represent discontinuities as smooth or planar features only and the explicit representation of non-planar discontinuities in existing SRM models is very complicated. To the author's knowledge, studies have not been conducted to investigate the mechanical behaviors of jointed rock mass by explicitly incorporating the large-scale roughness (waviness) of natural rock discontinuities.

In this thesis, a lattice-spring-based synthetic rock mass (LS-SRM) modeling approach is used to investigate the strength and deformation behaviors of jointed rock mass. Itasca's SRMTools is employed to perform numerical modeling because it can easily incorporate complex DFN model with non-planar discontinuities into the lattice spring model. Details on the SRMTools are provided in Section 2.5.3. Three-dimensional DFN model with non-planar discontinuities are

generated in MoFrac, a DFN software developed by MIRARCO Mining Innovation, and are imported into SRMTools for mechanical modeling.

1.3 Objective

The primary objective of the work presented in this thesis is to characterize the mechanical behavior of jointed rock and rock masses using the LS-SRM modeling approach. Some of the specific tasks that need to be addressed for the fulfillment of this primary objective are:

a) Perform sensitivity analysis of lattice model parameters and develop a calibration methodology for LS-SRM modeling.

b) Investigate the behavior of crack evolution (initiation and propagation) of a pre-cracked rock and the influence of pre-existing cracks on the mechanical properties (strength and deformability) of the pre-cracked rock.

c) Study the influence of pre-existing joint set properties (orientation, intensity, roughness, and persistence) on the mechanical response of jointed rock under confined compression.

d) Investigate the scale effect on the strength and deformability to determine the representative elementary volume (REV) of a jointed rock mass.

e) Examine the influence of volumetric discontinuity intensity (P_{32}) and confining pressure on the strength and deformability of jointed rock mass.

f) Assess the influence of discontinuity waviness, intensity, and size on the slope stability and deformation of an open pit mine.

1.4 Thesis summary

This thesis has been prepared in accordance with the requirements outlined by the School of Graduate Studies at Laurentian University, Sudbury, Canada. Some of the results have been published in peer-reviewed conference proceedings and scientific journals. Other results have been submitted to journals for publication. The document consists of eight chapters and the main research topics are shown in Figure 1-1.

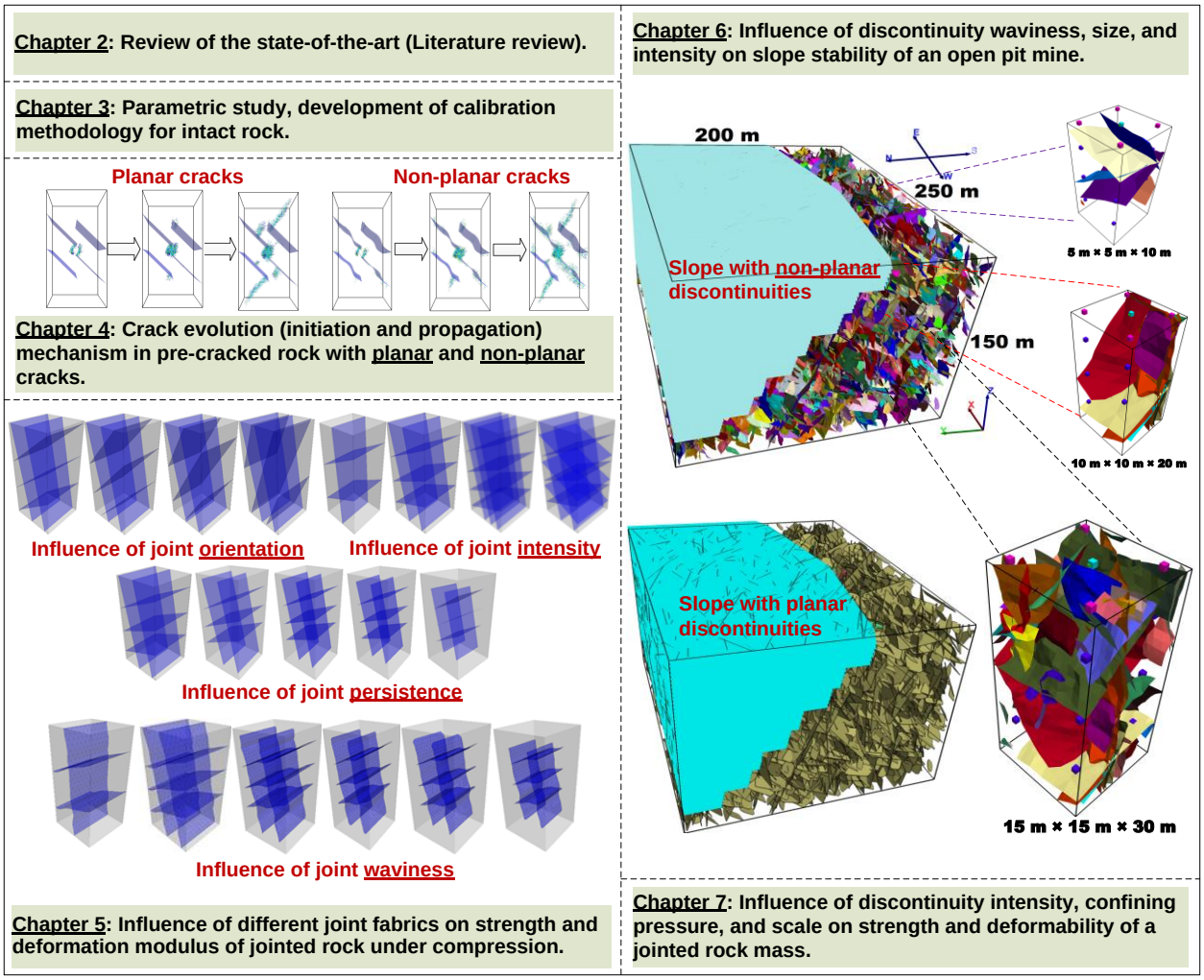

Figure 1-1 Main research topics.

Research problem, motivation, objective, and thesis content are summarized in Chapter 1.

In Chapter 2, existing state-of-the-art related to this research are discussed. Rock mass failure modes are discussed with the focus on mine pillars and slopes. In addition, failure mechanisms are also examined in pre-cracked rocks using laboratory testing and numerical modeling. Utility of empirical and numerical modeling approaches for the estimation of mechanical properties (strength and deformation modulus) of jointed rock mass are discussed with a focus on the application of SRM and DFN modeling techniques. The LS-SRM modeling approach is introduced and a comprehensive review of existing SRM methods is conducted with the comparison of LS-SRM with other DEM-based SRM approaches. DFN modeling methodology using MoFrac for the generation of DFN with non-planar discontinuities is also discussed.

Because the lattice spring-based tool (SRMTools) used in this research is relatively new, a parametric study is conducted to understand the influence of lattice micro-parameters on the macroscopic properties of intact rock and a calibration methodology is developed in Chapter 3. SRMTools (Itasca, 2016b) comprises of two software modules (SRMLab and Slope Model) which is developed by Itasca Consulting Group, Inc. SRMLab is a software within SRMTools which allows for the mechanical modeling of SRM models to understand the mechanical behavior of both intact and jointed rock mass. SRM models generated in SRMLab software are validated by performing direct tension, unconfined compression, and triaxial compression simulations.

Unconfined and confined compression simulations are performed on synthetic models of laboratory-scale pre-cracked marble to understand the crack evolution (initiation and coalescence) mechanism from non-persistent cracks with both planar and non-planar surface geometry in Chapter 4. In addition, the influences of crack length, crack angle, crack ligament angle, crack

ligament length, crack persistence, crack roughness, and the number of cracks on the mechanical response of pre-cracked marble under compression are also examined.

In Chapter 5, unconfined and confined compression simulations are conducted to investigate the mechanical behavior of laboratory-scale jointed granite with persistent joints. Influence of joints with different orientation, intensity, persistence, and waviness on strength and deformability of jointed granite is investigated under triaxial loading conditions. In addition, the strength and deformability of jointed granite with both planar and non-planar joints are investigated under true-triaxial loading condition.

A slope stability case study is conducted for the south wall of Cadia Hill open pit mine in Chapter 6. Stability and deformation behavior of the slope excavated in the rock mass with different discontinuity configuration (waviness, size, intensity) are investigated using Itasca's Slope Model software. The capability of the Slope Model software in assessing the stability of slope with both planar and non-planar discontinuity is validated before performing any simulations.

Influence of rock mass scale on strength and deformability is investigated to determine the REV of the rock mass in Chapter 7. Influence of P_{32} and confining pressure on mechanical properties of rock mass under compression are investigated using REV-sized rock mass samples.

Based on the research results, conclusions are made, and future works are recommended in Chapter 8. References are formatted as American Psychological Association 6th edition.

Chapter 2

2 Literature review

2.1 Introduction

This chapter provides a review of the state-of-the-art on the mechanical behavior of jointed rock mass and their implication on the geotechnical stability analysis of rock mass structures such as mine pillars and open pit mine slopes. The importance of combining numerical modeling methods such as discrete element method and DFN modeling techniques for the estimation of mechanical properties of jointed rock mass is highlighted. Other topics reviewed include:

a) Characterization of jointed rock masses.

b) Failure modes in jointed rock mass (mine pillar, slope) and pre-cracked rocks.

c) Application of empirical and numerical modeling approaches in the estimation of mechanical properties of rock mass, assessment of slope stability, estimation of strength and deformability of mine pillars, etc.

d) Application of BPM-based-SRM and BBM-based-SRM modeling approaches in the estimation of mechanical behaviors of jointed rock masses.

e) Usefulness of the LS-SRM modeling approach for the investigation of mechanical properties of jointed rock masses.

f) Generation of DFN with non-planar discontinuities in MoFrac.

2.2 Characterization of rock mass

Rock mass is primarily composed of the intact rock with small-scale defects in the forms of flaws that are not visible to the naked eye and large-scale discontinuities that may or may not contain infillings. Based on the properties of intact rock and discontinuities, rock masses are characterized considering rock blocks, rock bridges, discontinuity orientation, discontinuity spacing, discontinuity persistence, number of discontinuity sets, discontinuity wall strength, discontinuity aperture, discontinuity infilling, etc. as shown in Figure 2-1.

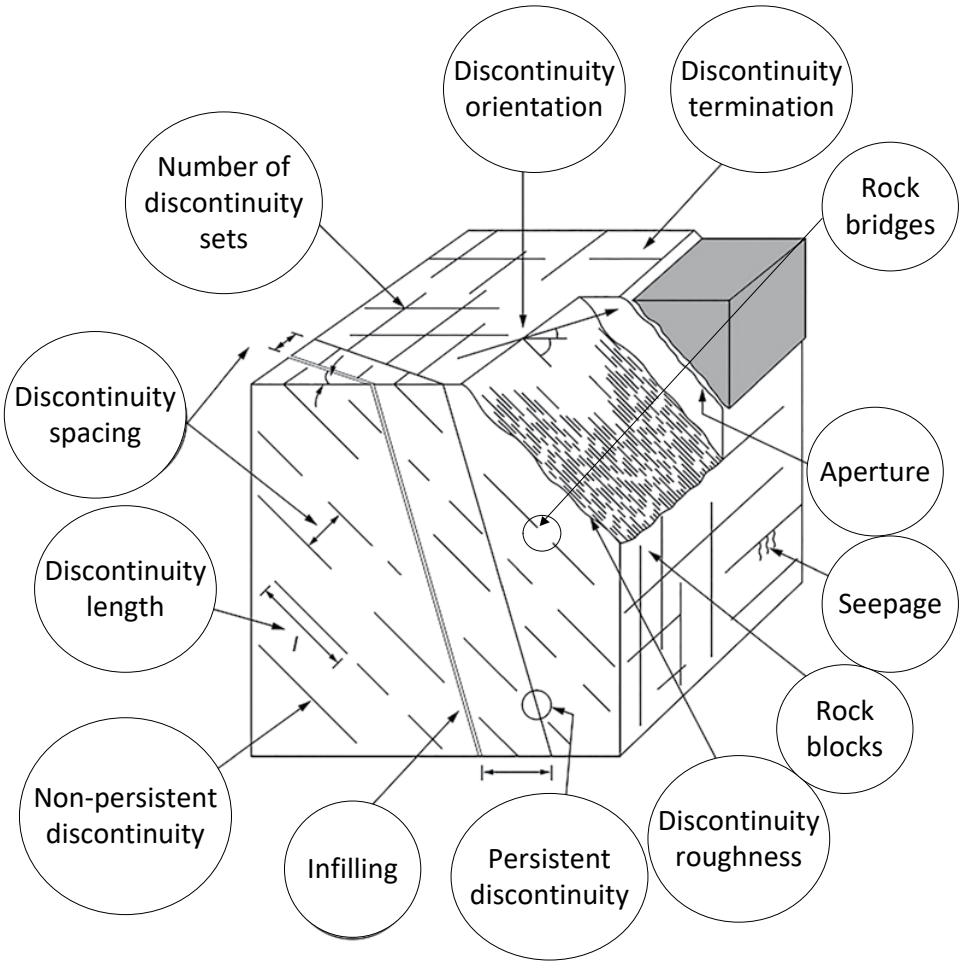

Figure 2-1 Characteristics of a jointed rock mass (Wyllie, 2017c).

Mechanical failure of any engineering system occurs at the weakest component or link when the external force applied to the system reaches the inherent strength. In the case of rock mass, these weak components are discontinuities in the form of joints, faults, bedding plane, veins, weak infillings, schistosity, etc. (Wyllie, 2017c). The discontinuity properties (orientation, spacing, intensity, persistence, roughness, infilling, water content, etc.) have a large influence on the strength and deformability of rock masses and these need to be accurately characterized by means of detailed field mapping. Discontinuities are also more vulnerable to weathering and corrosion because they are the pathway for groundwater and other corrosive fluids. Thus, it is very important to quantify the influences of discontinuities on the mechanical properties of jointed rock masses.

2.2.1 Discontinuity set

The first step in the characterization of discontinuities is the classification of these into a number of sets based on the orientation distribution, and then identify the ones that are unfavorably oriented and critical for the stability of a rock mass structure such as a mine pillar or a slope. This information can be collected by means of surface and underground mapping. The discontinuity orientation is expressed in terms of dip (the maximum angle made by the discontinuity with the horizontal axis) and dip direction (the direction of the horizontal trace of the line of the dip, measured clockwise from North) (Wyllie, 2017d). Fisher distribution is generally used to quantify the dispersion of the mean orientation of a discontinuity set (Fisher, 1953). Spherical projections (stereonet) are generally used to represent the discontinuity orientation and are preferred over rose diagram because they can accurately plot the spatial distribution of orientation data, identify major discontinuity sets, and are more convenient for kinematic analysis.

In the next step, discontinuity properties such as spacing, persistence, roughness, aperture, and water content are characterized for each discontinuity set. These discontinuity properties can be used as input parameters to generate DFN models.

2.2.2 Discontinuity spacing and size

Discontinuity spacing is the average perpendicular distance between the discontinuities within the same set and is related inversely to discontinuity density and frequency (Singhal & Gupta, 2010b); it controls the block size distribution of the jointed rock mass. Because the rock mass is opaque, the extent of the discontinuity inside the rock mass is not known; therefore, the size of a discontinuity is usually reported in terms of length rather than area. Distribution of discontinuity spacing and length are found to be either log-normal or negative exponential (Priest & Hudson, 1976, 1981).

2.2.3 Discontinuity persistence and rock bridge

Discontinuity persistence (*K*) is the measure of the extension (size) of a discontinuity into the rock and it significantly influences the strength and deformability of a jointed rock mass. In rock masses with non-persistent discontinuities, rock bridges provide additional strength and stiffness. Einstein et al. (1983) defined *K* as the ratio of total discontinuity area within a plane to the total area of the analyzed plane as,

$$K = \frac{\sum A_d}{\sum A_d + \sum A_{rb}} \tag{2-1}$$

where A_d and A_{rb} are the areas of discontinuity and rock bridge on the plane, respectively.

True persistence of the discontinuity is difficult to be measured because of the following challenges (Singhal & Gupta, 2010b):

a) It is difficult to measure the extent of the discontinuity inside the rock mass.

b) Truncation (censoring) and orientation bias of the measured area or scanline cannot be avoided.

The length of these discontinuities can be estimated using the scanline and circular window mapping techniques (Kulatilake & Wu, 1984; Zhang & Einstein, 1998; Mauldon et al., 2001) which can eliminate the bias (orientation and censoring) to some extent.

The very existence of non-persistent discontinuities gives rise to the concept of rock bridge. In simple terms, rock bridge is the volume of intact rock separating discontinuities within the rock mass and is defined as the fraction of discontinuity surface area that is discontinuous (Eq. (2-1)) (Einstein et al., 1983). Elmo et al. (2018) argue that the characterization of rock bridges is rather complex and suggest that it should be based on the block forming potential.

2.2.4 Discontinuity intensity

Discontinuity intensity or density is the non-directional intrinsic measure of the degree of jointing of rock mass which incorporates discontinuity frequency, persistence, and size (Rogers, 2015). Based on the dimension of the measured region and discontinuity size, Dershowitz (1984) classified discontinuity intensities into P_{10}, P_{11}, P_{20}, P_{21}, P_{22}, P_{30}, P_{32}, and P_{33} (Figure 2-2). The first and second subscripts represent the dimension of the measurement region and discontinuity size attribute, respectively. For example, P_{10} is the number of discontinuities per unit length of a scan line or borehole and is also referred as linear intensity, P_{21} is the length of fractures per unit

area of the mapping window and is also referred as areal intensity, and P_{32} is the total area of discontinuities per unit rock mass volume and is also referred as volumetric intensity. P_{32} is reported to be the most reliable measure of fracture intensity because it does not have a directional bias (Dershowitz & Herda, 1992). In a similar manner, discontinuity intensity also needs to be estimated because of the biases related to discontinuity size and persistence. Some studies suggested approaches to estimate the discontinuity intensity from traces in boreholes (Zhang & Einstein, 2000) and cylindrical exposures (Wang, 2005) such as tunnel walls and outcrops on slopes.

		Dimension of feature				
		0	**1**	**2**	**3**	
Dimension of sampling region	**0**	**P_{00}** Length^0 Number of fractures				Point Measure
	1	**P_{10}** Length^{-1} Number of fractures per unit length of scanline (Frequency or linear intensity)	**P_{11}** Length^0 Length of fractures intersects per unit length of scanline			Linear Measure
	2	**P_{20}** Length^{-2} Number of traces per unit area of sampling plane (Areal density)	**P_{21}** Length^{-1} Length of fracture traces per unit area of sampling plane (Areal intensity)	**P_{22}** Length^0 Area of fractures per unit area of sampling plane		Areal Measure
	3	**P_{30}** Length^{-3} Number of fractures per unit volume of rock mass (Volumetric density)		**P_{32}** Length^{-1} Area of fractures per unit volume of rock mass (Volumetric intensity)	**P_{33}** Length^0 Volume of fractures per unit volume of rock mass	Volumetric Measure

Figure 2-2 Quantification of fracture parameters (Dershowitz & Herda, 1992; Elmo, 2006).

2.2.5 Discontinuity waviness and roughness

The roughness components of a non-planar discontinuity can be classified into the large-scale waviness and small-scale roughness (Barton & Choubey, 1977). Both the discontinuity waviness and the discontinuity roughness play an important role in influencing the shear response of discontinuities and in turn the mechanical response of a jointed rock mass. For example, for rough, unweathered, and unfilled discontinuities, their shear strength and stiffness are very high (Barton & Choubey, 1977), which significantly increase the strength and reduce the deformability of the jointed rock mass. Despite the limitations of two-dimensional and subjective analysis of joint traces, the joint roughness coefficient (*JRC*) index approach suggested by Barton & Choubey (1977) has been widely used in the characterization of discontinuity roughness. In Barton's roughness scale, *JRC* increases from 0 to 20 with the increase of the degree of roughness.

The friction angle of a rough discontinuity (φ_j) is the sum of the of the basic friction angle of the intact rock material and the roughness component (i) which is the angle made by interlocking asperities with the shearing surface (Patton, 1966):

$$\varphi_j = \varphi_b + i \tag{2-2}$$

where φ_b is the basic friction angle of the planar joint and i can be related to *JRC* as,

$$i = JRC \cdot log_{10}\left(\frac{JCS}{\sigma_n}\right) \tag{2-3}$$

where *JCS* is the joint compressive strength and is equal to the compressive strength of the intact rock for an unweathered discontinuity, and σ_n is the effective normal stress acting on the discontinuity surface.

JRC is related to the discontinuity shear strength (τ) through (Barton, 1973),

$$\tau = \sigma_n \cdot \tan\left(\varphi_b + JRC \cdot log_{10}\left(\frac{JCS}{\sigma_n}\right)\right) \quad (2\text{-}4)$$

Large-scale waviness is often correlated to *JRC* using an upscaling approach based on empirical relation (Bandis et al., 1981). However, the influence of discontinuity waviness on strength and deformability is not clear. Bandis et al. (1981) found that the shear strength of rough discontinuity decreased with the increases of discontinuity length; however, based on the experimental work of both the laboratory and field scale discontinuities, Tatone & Grasselli (2013) found that both roughness and shear strength increase with the increase of discontinuity length. These results warrant the need for a detailed investigation to study the influence of the discontinuity roughness and waviness at different scales on the mechanical response of jointed rock masses.

2.3 Failure modes in jointed rock mass

Failure of jointed rock mass may occur in three ways: structure-controlled (discontinuity) failure, stress-controlled (intact rock) failure, and both. The structure-controlled failure mode is generally observed in rock mass with discontinuities oriented in unfavorable orientations at low confining pressure mainly in unstable slopes and shallow underground openings. As the confining pressure increases with the increase of depth, the natural discontinuities are clamped, and the rock mass is more brittle leading to stress-controlled failure. Stress-controlled failure is mainly driven by the redistribution of stress when an excavation is made in highly stressed grounds (Figure 2-3).

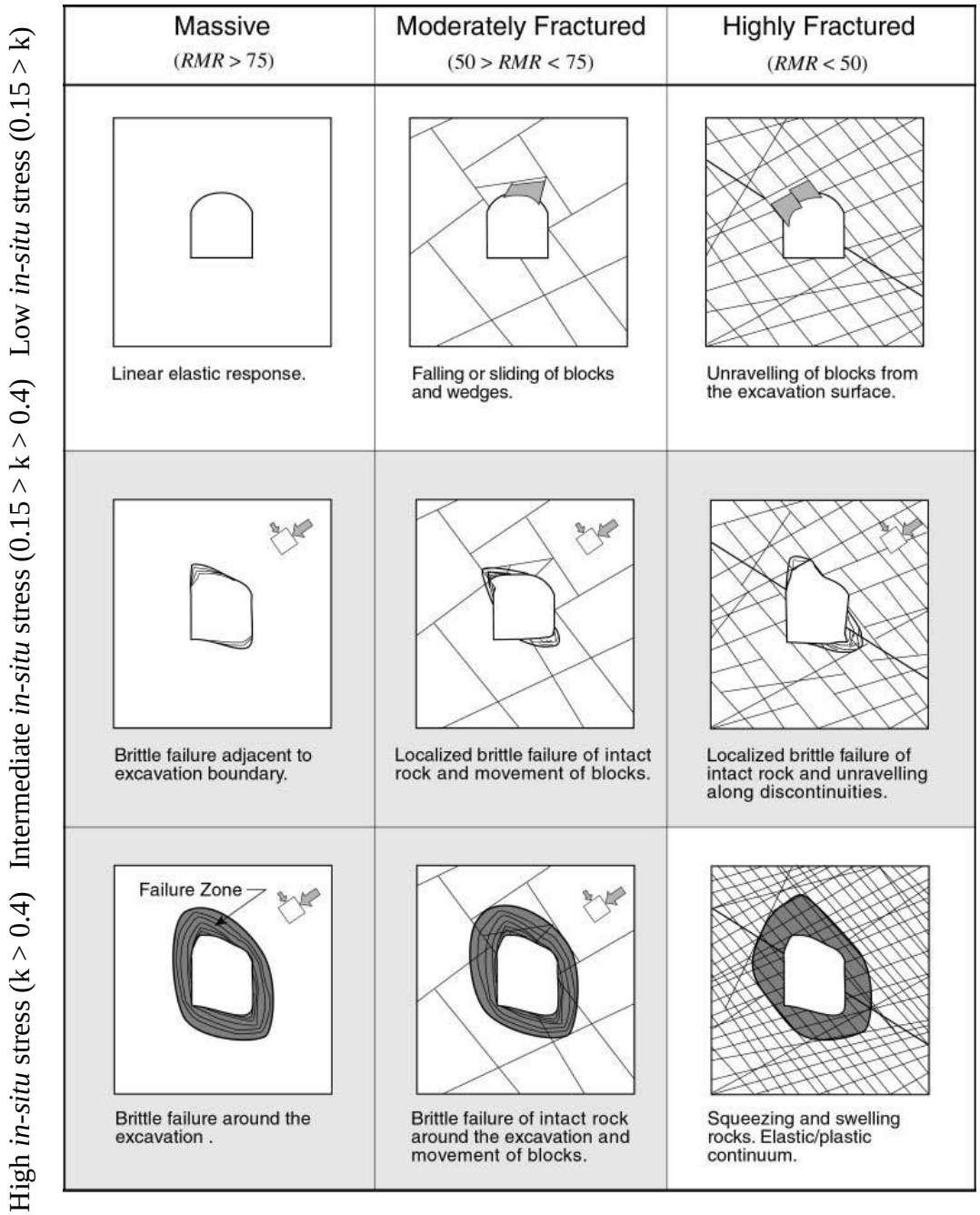

Figure 2-3 Examples of tunnel instability and failure observed in the hard rock as a function of the rock mass rating and the ratio of *in-situ* stress to rock strength (k) (Hoek et al., 1995; Martin et al., 1999; Kaiser et al., 2000).

Therefore, the failure of underground excavations in hard rocks is a function of the ratio of the *in-situ* stress to rock strength (*k*) and the mechanical properties of the rock mass (Kaiser et al., 2000).

At intermediate depths, stress induced failure zones are localized near the boundary of the excavation but at greater depth, extensive failure occurs which involves the entire perimeter of the excavation.

2.3.1 Pillar failure modes

Failure modes in mine pillar can be categorized into five, (i) spalling of pillar walls into mine opening (Figure 2-4a), (ii) shear failure along a discrete plane (Figure 2-4b), (iii) internal axial pillar splitting due to pillar deformation along the weak interface on roof and floor (Figure 2-4c), (iv) shear failure along the transgressive discontinuities (Figure 2-4d), and (v) buckling failure on a pillar with joints along the vertical axis (Figure 2-4e), as reported by Brady & Brown (2006). Structure-controlled failure of a mine pillar may occur along the critically oriented large discontinuity (Figure 2-5a) or crack coalescence along two or more discontinuities (Figure 2-5b).

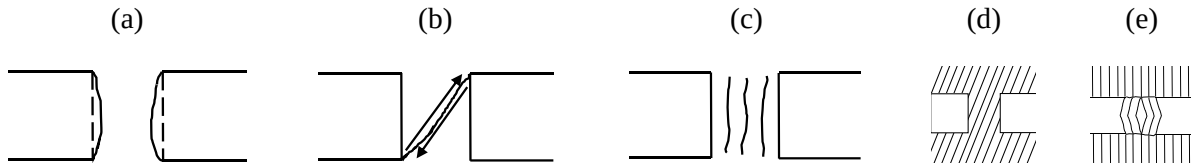

Figure 2-4 Different modes of failures of mine pillar: (a) spalling of pillar walls into mine opening, (b) shear failure along a discrete plane, (c) internal axial pillar splitting due to the movement of pillar along the weak interface on roof and floor, (d) shear failure along the transgressive discontinuities, and (e) buckling failure on a pillar with joints along the vertical axis (Brady & Brown, 2006).

(a) (b)

Figure 2-5 (a) Pillar bisected by a large angular discontinuity; (b) crack coalescence along two angular discontinuities in a limestone pillar (Esterhuizen et al., 2011).

2.3.2 Rock slope failure modes

Slope failure occurs along the surface when the shearing force is reaching the shear strength of the resisting surface. Four types of failure modes, wedge, planar, toppling, and circular (Wyllie, 2017d) are generally observed in a jointed slope, and these are controlled by the orientation and intensity of discontinuity sets (Wyllie, 2017d).

(a) (b) (c) (d)

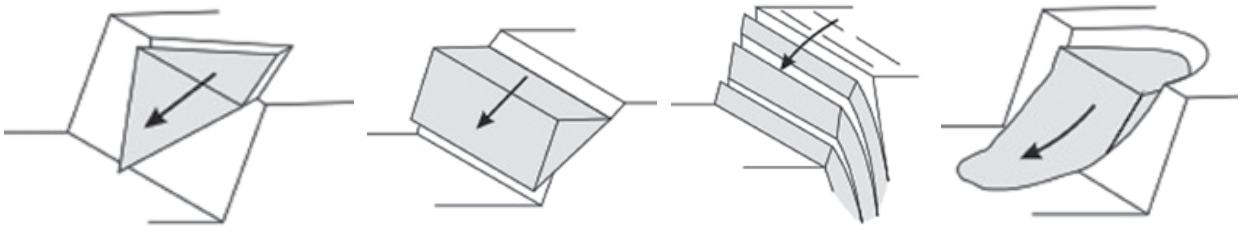

Figure 2-6 Types of slope failure (a) wedge failure; (b) plane failure (c) toppling failure (d) circular failure (Wyllie, 2017d).

In wedge failure, sliding takes place along the line of intersection of two planar discontinuities; however, in-planar failure sliding occurs along the single discontinuity plane. For a wedge failure, contact is maintained on both planes and sliding occurs along the line of intersection between the

two planes. For both planar and wedge failure, the dip of the failure plane should be larger than the overall slope face angle. For a toppling failure to occur, the dip direction of the steeply dipping discontinuities must be within about 20° of the dip direction of the slope face. Circular failure occurs in slopes with heavily broken rocks (near zero cohesion).

Depending on the scale of the problem analyzed and discontinuity persistence, slope failure modes can be complex where the failure mode is the combination of the ones mentioned earlier and the failure of intact rock bridges. In the moderately fractured slope, step-path failure mechanism (Camones et al., 2013; Sjoberg, 1992) is more frequent where the failure of intact rock bridges leads to the coalescence (Figure 2-7) and interconnection of the cracks developed on the tip of the non-persistent discontinuities and subsequently lead to the formation of failure surface.

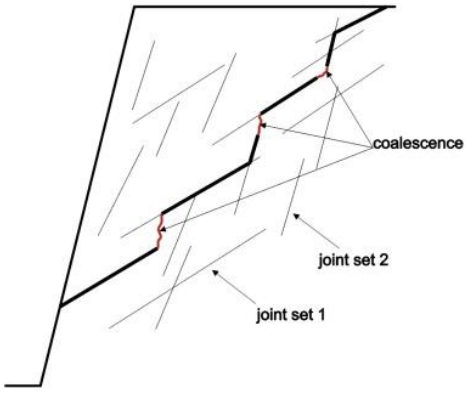

Figure 2-7 Step-path failure mechanism in a jointed slope with non-persistent discontinuities (Camones et al., 2013).

Scholtès & Donzé (2012) investigated the crack propagation mechanism in jointed rock slopes to identify the critical failure surface using the DEM-DFN approach in Yade (Kozicki & Donzé, 2008). Camones et al. (2013) used PFC^{3D} to assess slope failure due to the step-path failure of a fractured rock masses with co-planar and non-co-planar fractures and concluded that the slope models with non-co-planar fractures had lower safety factors than the models with co-planar

fractures. They further argued that the 3D models permit the consideration of the persistence of discontinuities in all directions and allow for a realistic comparison of results from numerical modeling with the physical experiments Further, the large-scale discontinuity waviness causes interlocking between the rough surfaces which could add more complexity in the slope failure mode and stability. More studies need to be conducted to understand the failure mechanism caused by these complexities.

2.3.3 Failure modes in pre-cracked rocks

Numerous laboratory and numerical studies have been carried out to investigate the failure modes of pre-cracked rocks. Four types of failure modes (splitting, shearing, rotational, and sliding) were observed during the laboratory testing of rock-like jointed material (Singh et al., 2002).

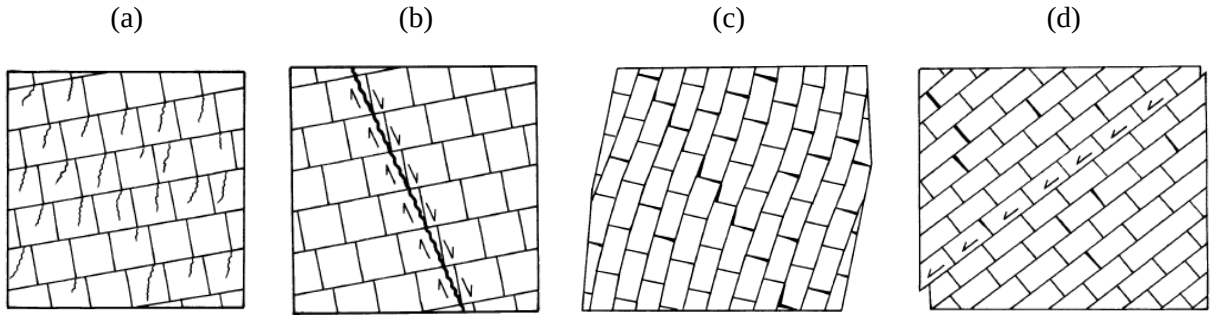

Figure 2-8 Failure modes observed in rock-like jointed material: (a) splitting, (b) shearing, (c) rotational, and (d) sliding, after Singh et al. (2002).

Many studies have been conducted to study crack evolution in pre-cracked natural rocks such as marble (Wang et al., 1987; Jiefan et al., 1990; Chen et al., 1995; Martinez, 1999; Li et al., 2005; Yang et al., 2008, 2009; Wong & Einstein, 2009a) and granite (Lee & Jeon, 2011; Martinez, 1999; Miller & Einstein, 2008; Wong & Einstein, 2009c). Because it is difficult to prepare natural rock specimens containing cracks, it is common to perform experimental investigation using pre-cracked rock-like materials (Hoek & Bieniawski, 1965; Reyes & Einstein, 1991; Germanovich et

al., 1994; Bobet & Einstein, 1998; Wong & Chau, 1998; Wong et al., 2001; Sagong & Bobet, 2002; Wong & Einstein, 2009c; Lee & Jeon, 2011; Zhang & Wong, 2012; Haeri et al., 2014; Cao et al., 2015; Xu et al., 2018; Zhou et al., 2018). The constraint of the experimental study is that the development of cracks is only visible on the outer surface of a specimen and the crack propagation inside the specimen can only be inferred from other indirect monitoring techniques such as acoustic emission monitoring. Wong & Einstein (2009b) investigated the crack development using the slices of the cracked specimen that was subjected to compressive load and they suggested using numerical modeling technique because of the difficulty to distinguish between the micro-cracks developed by loading and the ones induced during the slicing of the pre-loaded specimens.

Crack initiation and propagation inside the rock can be predicted using 3D numerical models. Although some studies on crack progression have been conducted in 3D (Scholtès & Donzé, 2012; Camones et al., 2013; Wang et al., 2014; Lee et al., 2017), the majority of the numerical studies were performed in 2D (Scavia, 1995; Vásárhelyi & Bobet, 2000; Tang et al., 2001; Cai & Kaiser, 2004; Lee & Jeon, 2011; Manouchehrian & Marji, 2012; Camones et al., 2013; Zhang & Wong, 2013; Haeri et al., 2014; Manouchehrian et al., 2014; Wang et al., 2017). Many investigations were conducted to study the crack development; however, only a few selected studies pertaining to 3D numerical modeling are reviewed.

Development of white patches are reported in the laboratory compression test conducted on Carrara marble specimens with both single (Wong & Einstein, 2009c) and stepped pair flaws (Wong & Einstein, 2009b). Length and width of these patches increased with the increase of the applied load. With further increase of loading, wing cracks initiated along the direction of the white patches, predominately in the vertical direction. The microscopic observations of the slices of the

samples with white patches and virgin samples suggested that the white patches were due to the intra-grain failure (Wong & Einstein, 2009b). Based on the coalescence behavior, nine types of cracks were identified with the failure mechanism of tensile (Figure 2-9), shear (Figure 2-10), and the combination of both. The experimental results also reported that a series of en-echelon cracks appeared on the rock bridge between the crack pair and concluded that the coalescence of the pre-existing cracks resulted in the formation of the macroscopic cracks. Yin et al. (2014) identified four surface crack coalescence patterns using the digital speckle correlation method and attributed the evolution of the white patches in the cracked marble to the development of the petal cracks.

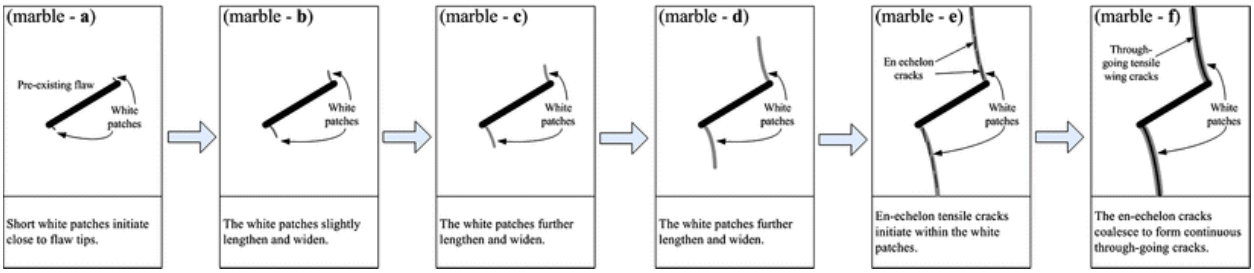

Figure 2-9 Different types of crack coalescence in tensile mode observed in the experimental study of flawed Carrara marble (Wong & Einstein, 2009a).

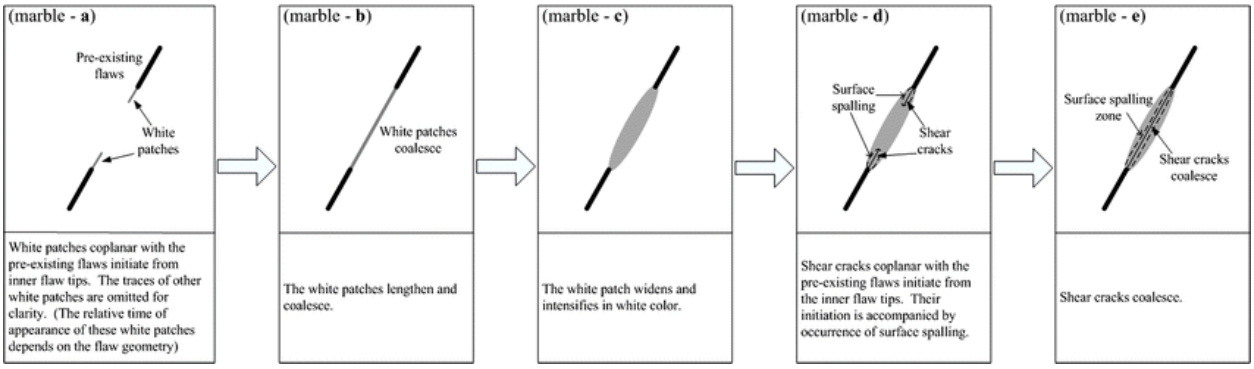

Figure 2-10 Different types of crack coalescence in shear mode observed in the experimental study of flawed Carrara marble (Wong & Einstein, 2009a).

In another study, crack evolution was investigated using 2 to 4 open cracks (Figure 2-11) in the two opposite corners of a specimen (Yang et al., 2009, 2008) as opposed to the center as in the studies conducted by Wong & Einstein (2009c, 2009a, 2009b). Crack length ($2a$) is the length of the crack along the inclination plane, ligament length ($2b$) is the distance between the internal tips of the two cracks, crack angle (α) is the angle made by the external tip of the crack with the vertical plane, and ligament angle (β) is the angle made by the imaginary line joining the internal tips of two cracks with the horizontal plane. Because of the locations of the cracks, crack initiation and propagation occur only at the internal tips of the flaws. The failure modes depend on the geometrical configuration of the flaws as shown in Figure 2-12. All studies concluded that the peak strength and the deformation modulus of the pre-cracked marble rock depend on $2a$, $2b$, α, β, and the number of cracks.

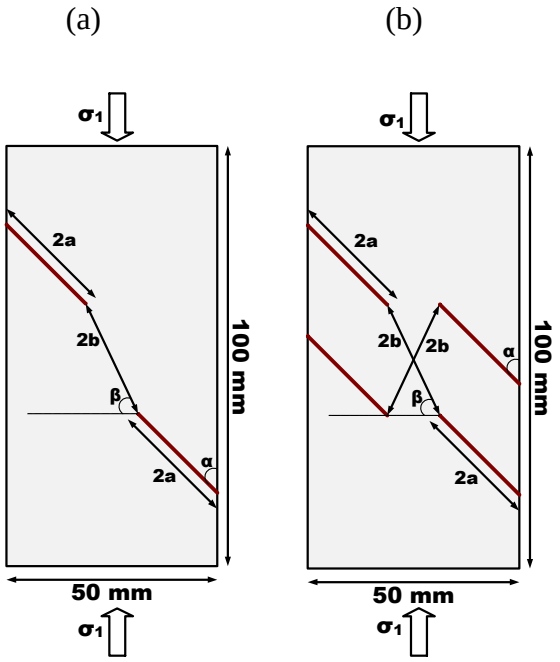

Figure 2-11 Illustration of crack geometry in the pre-cracked marble (a) Type B and (b) Type J, modified after Yang et al. (2009) where $2a$ = crack length, $2b$ = ligament length, α = crack angle, and β = ligament angle.

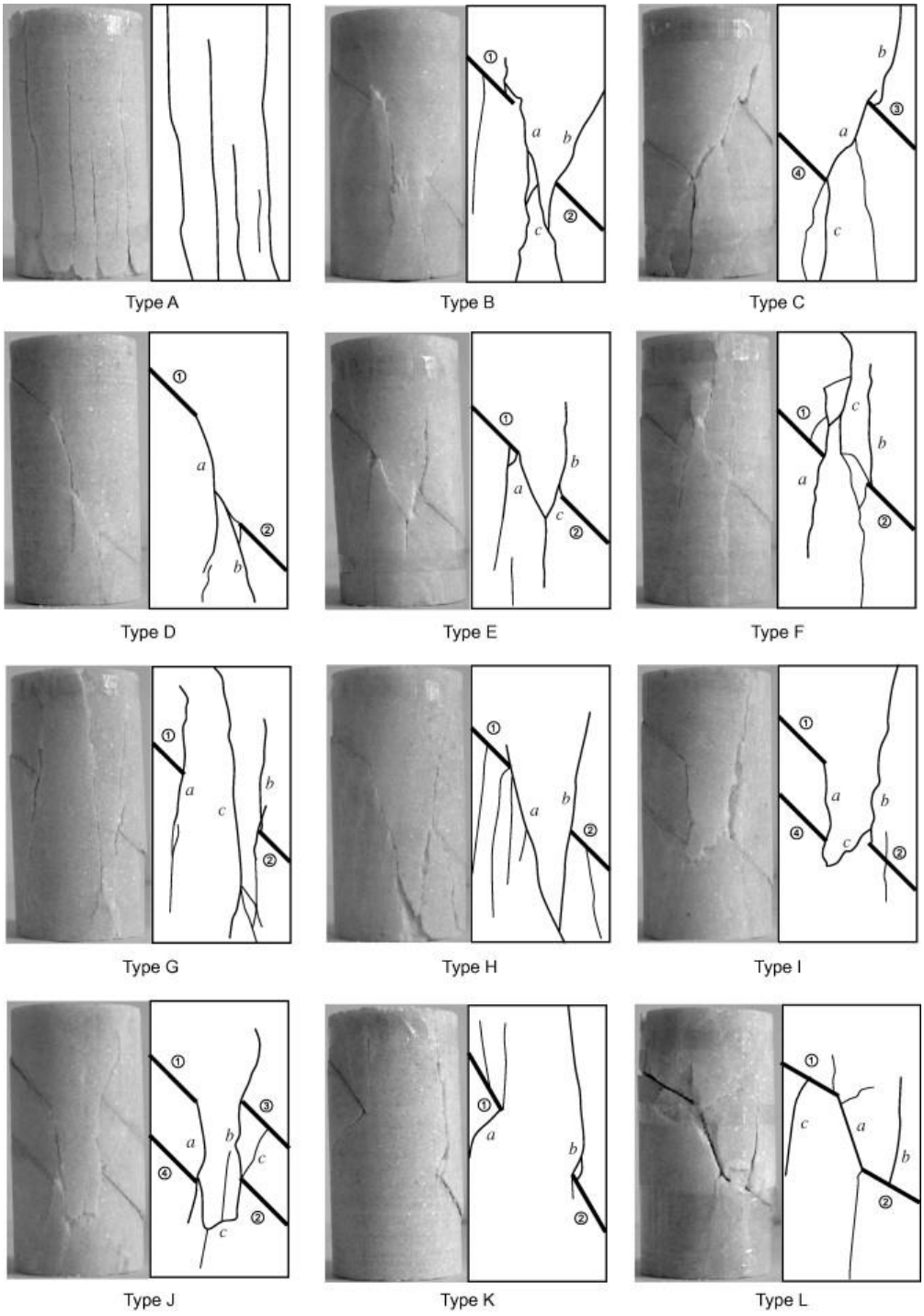

Figure 2-12 Failure modes of marble specimens with different crack configurations under uniaxial compression, after Yang et al. (2009).

Lee & Jeon (2011) observed a decrease in the crack initiation stress (σ_{ci}) with the increase of crack angle (α) when $\alpha \geq 15°$ and σ_{ci} was constant when $\alpha \leq 15°$ during laboratory uniaxial compression

of a double-flawed granite. They argued that this was due to the shielding effect of the horizontal flaw against the vertical load. However, in the numerical simulation in PFC^{2D}, they observed that σ_{ci} increased until the value of $\alpha = 30°$ was reached and then decreased when $30° \leq \alpha \leq 60°$, which could be attributed to the parallel bond contact law and two-dimensional nature of the numerical models.

Wang et al. (2014) investigated the fracturing process of the cylindrical specimen with two macroscopic cracks using RPFA^{3D} (Tang & Tang, 2011); however, the modeling results were not comparable to the laboratory test results because of the mesh dependency and the uncertainty associated with the homogeneous index parameter.

Sharafisafa & Nazem (2014) observed that UDEC was able to simulate all types of cracking mechanism in pre-cracked rock, such as the wing and secondary cracks, as well as the crack linkage between two adjacent flaws and their subsequent coalescence; however, results from extended finite element method (XFEM) could only represents tensile wing cracks without shear cracks.

Lee et al. (2017) simulated the fracturing process of a pre-cracked sandstone with three flaws using parallelized peridynamic technique coupled with the finite element method and indicated that the crack coalescing behavior is influenced by newly created cracks. The peridynamic formulation uses integral-differential operators for the simulation of the fracturing process.

2.4 Estimation of mechanical properties of jointed rock mass using empirical methods

Reliable estimates of mechanical properties of jointed rock mass are required for the assessment of geotechnical stability of any engineering structures built in or on rock mass. The mechanical properties of small-scale jointed rocks can be determined in laboratory using unconfined and

confined compression tests (Ramamurthy, 2001; Arzua et al., 2014; Alejano et al., 2017). However, the determination of strength and deformability of rock mass is a major challenge in solving geotechnical problems both in the subsurface (e.g., pillar stability) and surface (e.g., slope stability) operations. Strength, deformability, and failure depend on the mechanical properties and spatial location of pre-existing discontinuities. The engineering properties of rock mass can be estimated using empirical and numerical (Section 2.5.2) methods.

It is difficult to perform large-scale physical laboratory and *in-situ* tests to determine the mechanical properties of rock masses due to logistic and economic difficulties. Therefore, the mechanical properties of rock masses are often estimated using empirical methods. Strength and deformation modulus of rock masses are correlated to their corresponding intact rock properties and the indexes of rock mass classification systems such as Rock Quality Designation (RQD) (Deere et al., 1966), Rock Mass Rating (RMR) (Bieniawski, 1973), Modified Rock Mass Rating (MRMR) (Laubscher & Jakubec, 2001), Rock Mass Quality (Q) (Barton et al., 1974), Rock Mass Index (RMi) (Palmstrøm, 1996), Geological Strength Index (GSI) (Hoek, 1994), etc. Details on the empirical approach for the estimation of rock mass deformation modulus can be found in Zhang (2017). Empirical relations between rock mass deformation modulus and indexes of some rock mass classification systems and some other parameters such as intact rock modulus E_i and uniaxial compressive strength σ_c and joint properties are summarized in Table 2-1. The empirical relations are only applicable to isotropic and homogeneous rock masses.

The peak strength of a rock mass can also be estimated from the empirical approach using both laboratory and field test data. Laboratory tests (unconfined/confined compression) are often performed on intact and jointed rocks and the test results are used in conjunction with the rock

mass classification indexes. Some empirical relations for the estimation of rock mass strength are shown in Table 2-2.

Table 2-1 Empirical relations for the estimation of rock mass deformation modulus (E_m)

Equation	Reference
$2RMR - 100$ (GPa)	Bieniawski (1978)
$\sqrt{0.01\sigma_c 10^{(GSI-10)/40}}$ (GPa)	Hoek & Brown (1997)
$0.1\left(\frac{RMR}{10}\right)^3$ (GPa)	Read et al. (1999)
$E_i exp^{-0.00115 j_f}, j_f = j_n/rn$ (GPa)	Ramamurthy (2001)
$5.6RMi^{0.375}$ (GPa) (0.1 < RMi < 1) $7RMi^{0.4}$ (GPa) (1 < RMi < 40)	Palmström & Singh (2001)
$10(Q\sigma_c/100)^{1/3}$ (GPa)	Barton (2002)
$0.1423\left[\frac{E_i(1+0.01RQD)}{WD}\right]^{1.1747}$ (GPa)	Kayabasi et al. (2003)
$0.001\left[\frac{\left(\frac{E_i}{\sigma_c}\right)(1+0.01RQD)}{WD}\right]^{1.5528}$ (GPa)	Gokceoglu et al. (2003)
$E_i exp^{(RMR-100)/17.4)}$ (GPa)	Ramamurthy (2004)
$E_i 10^{(0.0186RQD-1.91)}$ (GPa)	Zhang & Einstein (2004)
$E_i\left(0.02 + \frac{1-\frac{D}{2}}{1+e^{\left(\frac{60+15D-GSI}{11}\right)}}\right)$ (GPa)	Hoek & Diederichs (2006)
$\tan(\ln(GSI))\log(\sigma_c)(RQD)^{1/3}$ (GPa) $\tan\left(\sqrt{1.56 + (\ln(GSI))^2}\right)(\sigma_c)^{1/3}$ (GPa)	Beiki et al. (2010)

E_i – intact rock modulus (GPa), j_f – joint factor, j_n – joint frequency (number of joints per meter), n – coefficient of influence of joint inclination, r – coefficient for joint strength (frictional component), WD – degree of weathering of discontinuities, D – Hoek–Brown (H–B) disturbance factor for jointed rock mass, σ_c – intact rock UCS (uniaxial compressive strength) (MPa).

Table 2-2 Empirical relations for the estimation of rock mass strength (σ_m)

Equation	Reference
$\sigma_c exp^{\frac{7.65(RMR-100)}{100}}$ (MPa)	Yudhbir et al. (1983)
$0.5exp^{0.06RMR}$ (MPa)	Trueman (1988); Zhang (2010)
$\sigma_c \left(\frac{E_m}{E_i}\right)^{n_j}$ (MPa)	Mehrotra (1992)
$\sigma_c exp^{\frac{7.65(RMR-100)}{24}}$ (MPa)	Kalamaras & Bieniawski (1993)
$0.7\gamma Q^{1/3}$ (MPa)	Bhasin & Grimstad (1996)
$\sigma_c exp^{\frac{7.65(RMR-100)}{20}}$ (MPa)	Sheorey (1997)
$7\gamma Q^{1/3}$ (MPa)	Singh et al. (1997)
$\sigma_c \frac{RMR}{600-5RMR}$ (MPa)	Aydan & Dalgic (1998)
$\sigma_c exp^{-0.008j_f}, j_f = j_n/rn$ (MPa)	Ramamurthy (2001)
$5\gamma \left(\frac{Q\sigma_c}{100}\right)^{1/3}$ (MPa)	Barton (2002)
$\sigma_c exp^{\frac{GSI-100}{9-3D}\left[0.5+\frac{1}{6}\left(exp^{-\frac{GSI}{15}}-exp^{\frac{20}{3}}\right)\right]}$ (MPa)	Hoek et al. (2002)
$\sigma_c \left(0.039 + 0.893exp^{\left(-\frac{j_f}{160.99}\right)}\right)$ (MPa)	Jade & Sitharam (2003)
$\sigma_c exp^{\frac{RMR-100}{25}}$ (MPa)	Ramamurthy (2004)
$\sigma_c 10^{0.013RQD-1.34}$ (MPa)	Zhang (2010)

σ_c – intact rock strength (MPa), E_m – rock mass modulus (GPa), E_i – intact rock modulus (GPa), n_j – reduction factor related to joint configuration and failure mode, γ – rock mass density (t/m^3).

Studies have been conducted to estimate the strength of mine pillar using the empirical approach based on case histories and back analysis. The published pillar formulas suggest that the pillar strength depends on three major parameters: pillar load, compressive strength of rock, and width to height ratio. A summary of existing empirical formulas for the estimation of hard rock pillar strength is shown in Table 2-3.

Table 2-3 Strength formulas for hard rock pillars, after González-Nicieza et al. (2006)

Pillar strength formula	σ_c (MPa)	No. of pillars	Reference
$133\frac{W^{0.5}}{H^{0.75}}$ (MPa)	230	28	Hedley & Grant (1972)
$\sigma_c\left(\frac{v_p}{v_{s\prime}}\right)^{-0.118}\left(\frac{W_p}{H_p}\frac{W_{s\prime}}{H_{s\prime}}\right)^{0.833}$ (MPa)	-	-	Hardy & Agapito (1982)
$65\frac{W^{0.46}}{H^{0.66}}$ (MPa)	94	7	Von Kimmelmann et al. (1984)
$35.4\left(0.778+0.222\frac{W}{H}\right)$ (MPa)	100	14	Krauland & Soder (1987)
$0.42\sigma_c\frac{W}{H}$ (MPa)		23	Potvin et al. (1989)
$74\left(0.778+0.222\frac{W}{H}\right)$ (MPa)	240	9	Sjoberg et al. (1992)
$0.44\sigma_c(0.68+0.52k)$ (MPa)		178	Lunder & Pakalnis (1997)
$0.27\sigma_c\left(\frac{1}{H_p}\right)^{0.36}+\left(\frac{H_p}{250}+1\right)\left(\frac{W_p}{H_p}-1\right)$ (MPa)		-	Sheorey et al. (2000)

W and *H* are width and height of pillar in meters, respectively; v_p and v_s are volumes of pillar and laboratory samples, respectively; *k* is a confinement-dependent empirical constant, and subscripts *p* and *s*' refer to the parameters related to pillar and laboratory samples.

These empirical formulas have been derived from the case studies of mine pillars between 600 and 1000 m depths with *W/H* ratios between 1.5 and 2. Thus the application of these formulas to pillar design in deeper grounds and with *W/H* > 2 could be misleading and conservative (Kaiser et al., 2011). Moreover, reliance on a few failed pillar cases with a high dependence on site-specific rock type and lack of information on pillar deformation are some of the limitations of using the empirical approach in pillar design.

The Hoek–Brown (H–B) failure criterion (Hoek & Brown, 2018) is widely used in the field of rock mechanics and rock engineering involving both experimental and numerical studies. For the estimation of rock mass strength, the H–B strength criterion is used in conjunction with the *GSI* value because it considers the influence of the intact rock strength, blockiness of rock mass, and joint conditions. The failure criterion can be summarized as,

$$\sigma_1 = \sigma_3 + \sigma_c \left(m_b \frac{\sigma_3}{\sigma_c} + s \right)^a \tag{2-5}$$

$$m_b = m_i exp\left(\frac{GSI - 100}{28 - 14D}\right) \tag{2-6}$$

$$s = exp\left(\frac{GSI - 100}{9 - 3D}\right) \tag{2-7}$$

$$a = 0.5 + \frac{1}{6}\left(e^{-\frac{GSI}{15}} + e^{-\frac{20}{3}}\right) \tag{2-8}$$

where σ_1 and σ_3 are the major and minor principal stresses. Intact rock strength parameters (m_i and σ_c) are derived by fitting triaxial test data to the H–B strength criterion. The value of m_b is a reduced value of m_i based on the *GSI* value and the degree of disturbance (*D*). *GSI* is the geological characterization of the blockiness of rock mass and the surface condition of discontinuities. Other

rock mass parameters *s* and *a* are also dependent on the magnitude of *GSI* and *D* as shown in Eqs. (2-7) and (2-8), respectively.

Rock mass strength for the assessment of slope stability can be estimated by back analysis of failed or failing slope using the available information (geometrical, groundwater, external force, etc.) at the time of failure. The cohesion (*c*) and friction angle (φ) of the failed surface are computed by keeping the factor of safety at 1. These estimates can be used for future slope designs in the same or similar location. Alternatively, the strength of rock mass for slope design can be estimated using the empirical methods such as H–B and Mohr–Coulomb (M–C) criteria (Wyllie, 2017b). Shear strength of a jointed slope is expressed in terms of *c* and φ. The *c* and φ values that are equivalent to the H–B failure criterion can be determined using the following equations (Wyllie, 2017b):

$$\varphi = sin^{-1}\left[\frac{6a \cdot m_b(s + m_b \cdot \sigma'_{3n})^{a-1}}{2(1+a)(2+a) + 6a \cdot m_b(s + m_b \cdot \sigma'_{3n})^{a-1}}\right] \tag{2-9}$$

$$c = \frac{\sigma_c[(1+2a)s + (1-a)m_b \cdot \sigma'_{3n}](s + m_b \cdot \sigma'_{3n})^{a-1}}{(1+a)(2+a)\sqrt{1 + (6a \cdot m_b(s + m_b \cdot \sigma'_{3n})^{a-1}/((1+a)(2+a))}} \tag{2-10}$$

where $\sigma'_{3n} = \sigma'_{3max}/\sigma_c$ and σ'_{3max} is the upper limit of confining stress over which the relationship between the H–B and M–C criteria is considered and can be determined as:

$$\frac{\sigma'_{3max}}{\sigma_m} = 0.72\left(\frac{\sigma_m}{\sigma_0}\right)^{-0.91} \tag{2-11}$$

where σ_m is rock mass strength and σ_0 is the stress level on the sliding surface which is related to slope height (*h*) and unit weight of rock (γ) as,

$$\sigma_0 = h \cdot \gamma \tag{2-12}$$

The M–C shear strength (τ), for given normal stress (σ_n), is calculated by substituting the values of c and φ from Eqs. (2-9) and (2-10) into Eq. (2-13):

$$\tau = c + \sigma_n \cdot tan\,\varphi \tag{2-13}$$

Similarly, σ_m is computed as:

$$\sigma_m = \frac{2c \cdot cos\,\varphi}{1 - sin\,\varphi} = \sigma_c \cdot \frac{(m_b + 4s - a(m_b - 8)) \cdot (\frac{m_b}{4} + s)^{a-1}}{2(1+a)(2+a)} \tag{2-14}$$

The main limitation of the H–B strength criterion is that the rock mass under consideration should be homogeneous and isotropic. Because of these assumptions, the criterion ignores the effect of stress concentration and localized failures around fractures before the peak strength is reached. The applicability of *GSI* is more effective for the rock mass with closely spaced and persistent discontinuities (i.e., 30 < *GSI* < 65). Thus, care should be taken when the failure criterion is applied in the cases where the stability is structurally controlled (Hoek & Marinos, 2007). The criterion is also not applicable for the rock mass with sparsely jointed to massive rock mass (i.e., 65 < *GSI*) with rough discontinuity surfaces and highly jointed rock mass (i.e., 30 > *GSI*) (Hoek & Brown, 2018). Another important limitation of the H–B criterion is that it ignores the influence of intermediate principal stress (σ_2). Several true triaxial compression test results clearly indicate that the peak strength (σ_1) of rock increases with the increase of σ_2 for a constant minor principal stress (σ_3) up to a certain value of σ_2 and then starts to decrease (Haimson, 2006; Mogi, 1967, 1971; Tiwari & Rao, 2004).

2.5 Analysis methods

2.5.1 Limit equilibrium method

Traditionally, limit equilibrium methods have also been carried out to perform slope stability analyses. Limit equilibrium analysis is performed in the slopes with simple failure modes such as plane, wedge, circular, and toppling failure (Wyllie, 2017a). The slope stability analysis is based on a factor of safety which is defined as the ratio of the resisting to displacing forces acting on the failed surface (Jennings, 1970).

The main limitations of this method are that rock mass is assumed to be rigid, the shear strength is mobilized at the pre-defined failure surface, cannot include the effect of *in-situ* stresses, and are, therefore, incapable of computing displacements and/or deformation (Wyllie, 2017a). That is why numerical methods are the preferred method of slope stability analysis because they are capable of computing displacement/deformation and incorporate complex material models. Two main advantages of numerical methods over limit equilibrium methods for stability analysis are: (i) potential failure surface is automatically determined and the failure surface does not need to be pre-defined, and (ii) translational and rotational equilibrium is satisfied (Wyllie, 2017a).

2.5.2 Numerical methods

Numerical methods are used to solve geotechnical problems such as stability assessments of open pit slopes (Sainsbury et al., 2016; Sainsbury et al., 2007) and pillars (Zhang, 2014) in underground mines. Numerical methods are often preferred to cumbersome laboratory and field tests because of the versatility and reproducibility of the simulation results for the estimation of mechanical properties of intact and jointed rocks. The numerical models are evolving to a more complex state that can incorporate many aspects of the rock mass such as realistic structural geometry, geology,

and groundwater data, thanks to the development in intelligent software and resources such as super-computers and cloud computing. Numerical methods used in geomechanics can be categorized into the continuum, discontinuum, and hybrid methods. A comprehensive review of these methods can be found in Jing (2003, 2007).

2.5.2.1 Continuum method

Continuum-based methods simulate the mechanical behaviors of jointed rock mass by reducing the strength and deformation modulus of the intact rock. These approaches are suitable for modeling jointed rocks with a homogeneous distribution of discontinuities. Continuum methods used in geomechanics are Finite Element Method (FEM), Boundary Element Method (BEM), and Finite Difference Method (FDM) (Jing, 2003). The most common continuum approaches are FEM and FDM. The only difference between the two is the methodology by which the partial differential equations are solved. BEM has an advantage over the FEM and FDM methods in terms of computational expense because it does not require the full domain discretization of the model and only divides elements on the boundaries. Some of the examples of commercially available continuum modeling tools are FLAC and FLAC^{3D} (FDM); RFPA^{2D}, RFPA^{3D}, RS^{2}, RS^{3}, Abaqus (FEM); Examine^{2D}, Examine^{3D}, Map^{3D} (BEM). The main disadvantages of these methods are the inability or inefficiency to (i) explicitly represent the discontinuities, and (ii) handle crack propagation and the development of macroscopic discontinuity. Thus, fracture opening, sliding, and complete block detachment cannot be simulated.

2.5.2.2 Discontinuum method

In discontinuum methods both intact rock and rock discontinuities can be represented discretely in such a way that allows realistic mechanical modeling of the jointed rock mass. These methods

allow explicit representations of pre-existing discontinuities on a bonded block or bonded particle assembly. One method is called the distinct element method (DEM) (Cundall, 1971) and the other is called discontinuous deformation analysis (DDA) (Shi, 1988). In a DEM, the contacts between blocks or particles are constantly updated with the change in stress and displacement. DEMs can simulate complex failure mechanisms such as fracture opening, sliding, and complete detachment of blocks in rock masses containing multiple intersecting discontinuities (Camones et al., 2013). DEM is preferred over other modeling approaches due to its capability to incorporate many discontinuities and handle them as distinct structures. Commonly used DEM codes are Itasca's PFC and UDEC, and their respective three-dimensional versions PFC3D and 3DEC.

PFC includes granular and bonded materials as well as interfaces that can be inserted into the bonded materials (Potyondy & Cundall, 2004). PFC materials consist of rigid bodies and contacts. The force–displacement relation of the bonded particle model follows Newton's second law of motion and the constitutive law of the contacts.

3DEC is a 3D numerical modeling code for advanced geotechnical analysis of discontinuous media such as jointed rock masses (Itasca, 2016a). A discontinuous material is represented as an assembly of discrete blocks (rigid or deformable) and the discontinuities are treated as the boundaries between the blocks. Large displacements along the discontinuities and rotation of blocks are allowed. The bonded block method (BBM) approach differs from particle-based methods in its ability to represent zero-porosity condition, as well as interlocked irregular block shapes that provide resistance to block rotation after contact breakage (Garza-Cruz et al., 2014; Turichshev & Hadjigeorgiou, 2017).

Discontinuities are represented as Discrete Fracture Network (DFN) in bonded block or bonded particle assemblies. In general, rock mass modeling is performed using BPM- or BBM-based SRM modeling approach, which will be discussed in detail in Section 2.5.4. The major limitations of BPM- and BBM-based discontinuum methods are the long computation time and difficulties to explicitly represent non-planar discontinuities.

2.5.2.3 Hybrid method

Both continuum and discontinuum methods are used to model a large-scale rock mass in the hybrid method. Because the hybrid method is an integrated approach, it carries advantages and disadvantages of both the continuum and the discontinuum approaches. The FEM-DEM combined approach has been used to simulate progressive rock failure process (Pine et al., 2006) and assess the stability of a mine pillar (Elmo & Stead, 2010). The FEM-DEM combined approach has also been used to simulate tensile splitting in indirect tensile simulations incorporating heterogeneity (Cai & Kaiser, 2004; Mahabadi et al., 2010; Cai, 2013) and investigate directional rock fracturing under true-triaxial loadings (Cai, 2008).

2.5.3 Lattice spring method

Another rock mass modeling approach is lattice spring method (LSM). The LSM discussed here is based on SRMTools, Itasca's lattice code. The code was developed as part of the Large Open Pit (LOP) project administered by the Commonwealth Scientific and Industrial Research Organization (CSIRO) in Brisbane, Australia. Discontinuities in the LSM code are derived from a user-specified discrete fracture network (DFN). The LSM code is designed to simulate the deformation behaviors of rock masses, in which failure is a combination of slip or opening of joints and intact rock failure. The LSM in SRMTools is formulated for both mechanical and coupled

fluid-mechanical simulations; however, for the relevance of the intended study in this thesis, only the formulation of the mechanical model is discussed here.

2.5.3.1 Mechanical formulation

In LSM, intact rock is represented as a random assembly of nodes that are connected to each other with massless springs in 3D space. The formulation of the lattice spring model in SRMTools is similar to the BPM model in PFC except that the particles are represented as concentrated point masses at the lattice nodes and contacts are represented by springs in both the normal and the shear directions. Node locations are derived from the centroids of a packed assembly of particles in the periodic-space mode in PFC. Displacement of a lattice node is computed using Newton's second law of motion and a linear force–displacement relation is used for springs (Cundall, 2011).

A simulation is carried out by solving the equations of motion (three for translations and three for rotations) for all nodes in the model using the explicit numerical method. Central difference equations for the translational degrees of freedom are,

$$v_i^{(t+\Delta t/2)} = v_i^{(t-\Delta t/2)} + \sum F_i^{(t)}\,\Delta t/m \tag{2-15}$$

$$u_i^{(t+\Delta t)} = u_i^{(t)} + v_i^{(t+\Delta t/2)}\Delta t \tag{2-16}$$

where $v_i(t)$ and $u_i(t)$ are the velocity and position of the components of nodes i (i = 1, 2, 3) at time t respectively, $\sum F_i$ is the sum of all force-components acting on the node of mass (m), within time step (Δt) and it also includes local damping force. The angular velocities, ω_i, of component i (i = 1, 2, 3) at time t are calculated from the following central difference equations:

$$\omega_i^{(t+\Delta t/2)} = \omega_i^{(t-\Delta t/2)} + \frac{\sum M_i^{(t)}}{I}\Delta t \tag{2-17}$$

where $\sum M_i$ is the sum of all moments-components acting on the node with the moment of inertia I. In quasi-static simulations, the only effect of spins (i.e., angular velocities) is to "dissipate" the unbalanced moments at nodes. The default calculation mode includes all six degrees of freedom (three translational and three rotational). However, an alternate mode, in which it is assumed that nodes have three translational degrees of freedom but no rotational degrees of freedom, is also available.

After all the nodes are applied with Equations (2-15) and (2-16), then the following calculations are performed at time t for all unbroken springs,

$$v_i^{\mathrm{rel}} = v_i^{\mathrm{A}} - v_i^{\mathrm{B}} \tag{2-18}$$

$$v^{\mathrm{N}} = v_i^{\mathrm{rel}} n_i \tag{2-19}$$

$$v_i^{\mathrm{S}} = v_i^{\mathrm{rel}} - v^{\mathrm{N}} n_i \tag{2-20}$$

where the superscript "rel" denotes "relative", "A" and "B" denote the two particles connected by the spring, "N" denotes "normal", "S" denotes shear, and n_i is the unit normal vector. Then, the normal and shear forces are updated using,

$$F^{\mathrm{N}} \leftarrow F^{\mathrm{N}} + v^{\mathrm{N}} k^{\mathrm{N}} \Delta t \tag{2-21}$$

$$F_i^{\mathrm{S}} \leftarrow F_i^{\mathrm{S}} + v_i^{\mathrm{S}} k^{\mathrm{S}} \Delta t \tag{2-22}$$

where k^{N} and k^{S} are the spring's normal and shear stiffnesses, respectively. New spring forces are then added to the sum of nodal forces as,

$$F_i^{\mathrm{A}} \leftarrow \sum F_i^{\mathrm{A}} - F^{\mathrm{N}} n_i - F_i^{\mathrm{S}} \tag{2-23}$$

$$F_i^{\mathrm{B}} \leftarrow \sum F_i^{\mathrm{B}} + F^{\mathrm{N}} n_i + F_i^{\mathrm{S}} \tag{2-24}$$

For the intact rock, the unit normal vector (n_i) from node A to node B is computed as,

$$n_i = (v_i^{\mathrm{A}} - v_i^{\mathrm{B}}) / \left| v_i^{\mathrm{A}} - v_i^{\mathrm{B}} \right| \tag{2-25}$$

If a joint plane passes through the spring, then n_i is the unit normal to the joint plane.

During each iteration, the spring force remains zero ($F^{\mathrm{N}} = 0$) while the gap between the contacts is positive ($d > 0$) and is calculated as,

$$d \leftarrow d + v^n \Delta t \tag{2-26}$$

For a spring that is part of a joint segment, when the normal force is compressional ($F^{\mathrm{N}} < 0$) the shear force is limited to the maximum frictional force as,

$$\text{If } \left| F_i^{\mathrm{S}} \right| > \mu \left| F_i^{\mathrm{N}} \right| \text{ then } F_i^{\mathrm{S}} \leftarrow F_i^{\mathrm{S}} \frac{\mu |F^{\mathrm{N}}|}{\left| F_i^{\mathrm{S}} \right|} d + v^n \Delta t \tag{2-27}$$

where μ is the coefficient of friction of the joint.

The calibrated normal strength (F^{Nmax}) and stiffness (k^{N}) of the springs are computed as,

$$k^{\mathrm{N}} = \alpha_k K_R R \tag{2-28}$$

$$F^{\mathrm{Nmax}} = \alpha_t \sigma_t R^2 \tag{2-29}$$

where K_R is the bulk modulus, R is the resolution, σ_t is the rock mass's tensile strength, α_k and α_t are the stiffness and strength calibration factors, respectively, which are built-in in the code and depend on the arrangement of the nodes. The effective Poisson's ratio of the lattice model is a function of the ratio k^S/k^N; for $k^S/k^N = 1$, the Poisson's ratio of the lattice model is zero. Spring normal force is positive in tension. After the normal force is calculated using Equation (2-21), it is tested for breakage. If force reaches the calibrated spring strength either in tension or in shear, the spring breaks, resulting in the formation of a micro-crack, i.e., if $F^N > F^{Nmax}$, then $F^N = 0$, $F_i^S = 0$, and a "fracture flag" is set. For lattice with flat joint contact model, $k^S/k^N = 1$ and the calibrated shear strength is determined using the built-in relation between the assigned UCS/σ_t and contact shear strength multiplier (see Section 2.5.3.2).

2.5.3.2 Contacts in LSM

Contacts in SRMTools can be modeled as parallel bonds or flat-joint contacts. Lattice springs with parallel bond contacts have two major limitations: one is that the compressive to tensile strength ratio (σ_c/σ_t) is less than 4, which is uncharacteristic for rock; the other is that the maximum friction angle of intact rock is only around 30°. The reason is that when a parallel bond breaks, the particles can roll relative to each other without resistance. To address these limitations, FJMs (Flat-Joint Models), which are similar to the "Flat-Joint" in PFC (Figure 2-13a), are developed. A FJM mimics the microstructure of angular, interlocked grains and it represents the contacts between rigid polygonal or polyhedral particles (Itasca, 2017). Using the FJM formulation, each spring is split into sub-springs which allows resistance against rotation by means of normal forces in the sub-springs even after the springs are broken. As a result, this allows proper simulations of uniaxial compressive strengths (*UCS, or* σ_c) and σ_c/σ_t ratios of intact rock. Force–displacement relations of a FJM interface exhibit from a fully bonded state to a fully unbonded and frictional state after the

contact is broken (Potyondy, 2015). Sub-contacts are arranged around the circumference of the contact disk with a minimum of three sub-contacts (Figure 2-13b).

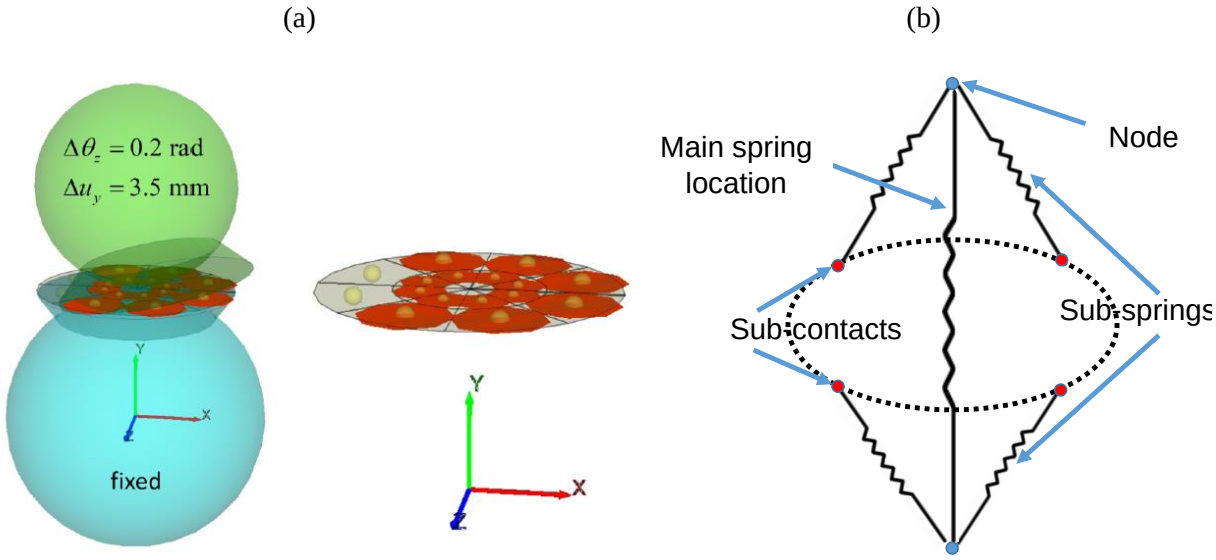

Figure 2-13 Representation of flat joint contact in Itasca's (a) PFC (Potyondy, 2017) (b) SRMTools, after Itasca (2017).

The flat-joint's peak friction angle is assigned to unbroken sub-contacts. When a sub-contact breaks, the flat-joint's friction angle is mobilized, and the flat-joint's residual friction angle is assigned to broken sub-contacts. The relative motion at each sub-contact is computed from the translational and rotational motions of the two nodes considering the vector directions from nodes to sub-contacts. The main spring and sub-springs are represented as resistors (Figure 2-13b). Resultant normal and shear forces are computed from the normal and shear displacements at the sub-contacts. When the forces attain the tensile and shear strength limits, breaking, sliding or opening may occur at each sub-contact. Sub-contact forces are then resolved into nodal forces and moments.

When the flat joint (FJ) contact model is used, the simulated tensile strength of the rock is the same as the input tensile strength. Contact shear strength of the spring is computed as the product of the tensile strength and a multiplier which is called "contact shear strength multiplier". This multiplier has a positive linear relationship with the σ_c/σ_t ratio. This relation has been built into the lattice code (Figure 2-14) and the user-assigned *UCS* is translated automatically into a contact shear strength (Itasca, 2017). Thus, for models with higher input values of σ_c/σ_t, the resultant multiplier increases, which increases the contact's shear strength and the resultant compressive strength.

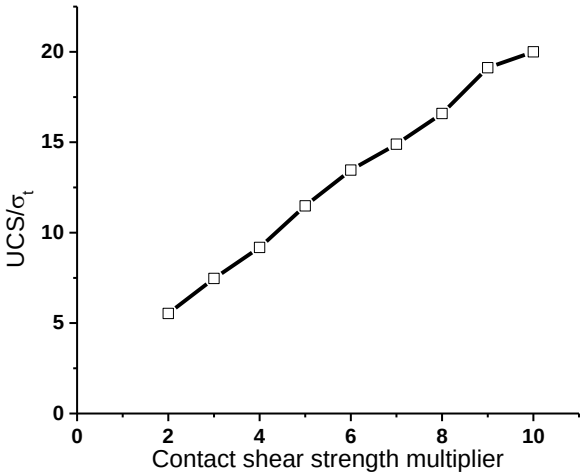

Figure 2-14 Relation between the contact shear strength multiplier and σ_c/σ_t for a flat joint contact (Itasca, 2017).

In SRMTools, pre-existing discontinuities can be incorporated as smooth joint (SJ) contacts into the lattice assembly (Figure 2-15a). The spatial orientation of the lattice springs through which a pre-existing discontinuity passes is the same as that of the discontinuity, and these springs are also called joint springs (Cundall, 2011). In addition, the SRMTools can represent realistic geometry of a natural undulating joint surface easily (Figure 2-15b). This is one of the reasons that the SRMTools is chosen for the thesis research. Mechanical response of a jointed rock mass is the

emergent behavior caused by the interaction of resultant force and displacement of joint springs and intact lattice springs.

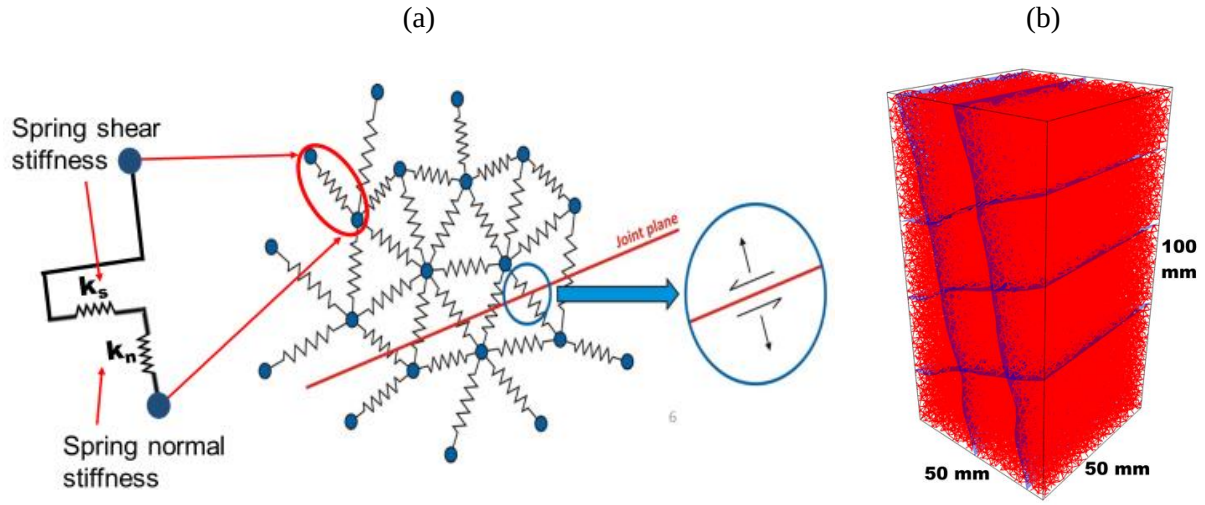

Figure 2-15 (a) A discontinuity plane cutting through a lattice spring assembly (Cundall, 2011); (b) a LS-SRM model in SRMTools with two non-planar joint sets (Bastola & Cai, 2018a).

2.5.4 Discrete Fracture Network

A Discrete Fracture Network (DFN) is a computational model that explicitly represents the geometrical properties (orientation, size, position, shape, and aperture) of discontinuities. It is commonly applied in discontinuum numerical methods for solving advanced rock mechanics problems relating to rock mass discontinuities (Jing, 2003). DFN models explicitly represent faults and joints within the rock mass, which helps in the understanding of the failure mechanism such as sliding along a major structure and fracturing of intact rock bridges. DFNs are also used as a constituent part in synthetic rock mass (SRM) modeling to estimate rock mass strength and deformation properties, rock fragmentation distributions, kinematic block stability, and groundwater contaminant flow (Lorig et al., 2015).

DFN models can be categorized into three geological, stochastic, and geomechanical models based on the approaches for geometrical representation of discontinuities (Lei et al., 2017). DFNs generated from geologically mapped data can preserve the realism of the discontinuity geometry but the use of two-dimensional data from analog mapping, borehole logging, aerial photographs, lidar scanning, photogrammetry, seismic survey, etc., to solve three-dimensional problems is challenging. The stochastic DFN modeling approach is simple and efficient but the models are only as reliable as the input DFN parameters. Similarly, geomechanical DFN models depend on the accuracy of the rock mass properties and *in-situ* stress as well as the mechanical simulation model. Detailed discussion on DFN generation methodologies can be found in Jing & Stephansson (2007) and Lei et al. (2017).

2.5.4.1 Existing DFN software

Several DFN software packages such as FRACMAN 7.5 (Golder, 2018), 3DEC & PFC3D (Itasca, 2016a), DFNWORKS (Hyman et al., 2015), FracSim3D (Xu & Dowd, 2010), MP_FRAC (Erhel et al., 2009), DFNModeler (Jin & Pashin, 2007), GEOFRAC (Ivanova et al., 2014), NAPSAC (Porter et al., 1992), RESOBLOK (Merrien-Soukatchoff et al., 2012), Jointstats (JKMRC, 2000), 3FLO (Billaux et al., 2006), SIMBLOC (Hamdi & du Mouza, 2005), MoFrac (Janeczek, 2015; Junkin et al., 2017), and ADFNE (Alghalandis, 2017) have been reported in the literature. Out of these tools, FracMan is the widely used commercial DFN modeling software. Most of these tools typically simplify the realistic undulating fracture surface into planar facets except for FracMan and MoFrac. In general, fractures generated by most of these tools are planar polygonal features with uniform spatial distribution using conventional Poisson's or Beacher's model (Dershowitz, 1984). In nature, however, fracture position is not uniform, and fractures exhibit geological features such as clustering, intersection, and termination (truncation). In addition, fracture surfaces

are usually non-planar with natural waviness as opposed to planar surfaces. Improper representation of DFNs can have a large implication in the assessment of groundwater flow, stress distribution, and strength of fractured rock masses.

Uncertainty in DFN modeling is unavoidable with the currently available DFN modeling tools. However, efforts should be made to minimize the variability using a deterministic-stochastic DFN modeling approach; for example, 2D trace data from the tunnel wall or slope could be constrained such that the mapped traces are always reproduced in the DFN model.

MoFrac is a DFN software that can be used to generate 3D fracture networks in rock mass based on field mapping data. MoFrac, developed by MIRARCO – Mining Innovation in Canada, is based on the FXSIM3D code previously developed by Srivastava (2002). DFN models in MoFrac are guided by geological rules and constrained by field data (Janeczek, 2015). The resulting DFN honors the known field data from fracture mapping and generates stochastic fractures in the unknown area (area without mapped fracture information). Fracture data can be derived from the surface or underground mapping, remote sensing, core logging and/or borehole imaging. MoFrac DFN models can range from meter scale for underground tunnel and pillar studies, to kilometer scale for regional groundwater flow studies.

2.5.4.2 DFN generation in MoFrac

A fracture is represented in MoFrac by an equilateral triangle grid mesh composed of vertices and faces (Janeczek, 2015). MoFrac can generate both deterministic and stochastic fractures. Fractures generated from the field mapped trace elements are deterministic fractures and fractures generated from pure statistical distribution are stochastics fractures. First, deterministic fracture elements are turned into deterministic fracture seeds which germinate into fractures. Based on the deterministic

trace length and aspect ratio (strike length to dip length ratio), all germinated deterministic fracture seeds are propagated in sequence (Janeczek, 2015). Larger fractures are prioritized to smaller ones and stochastic fractures are generated only after the completion of the deterministic ones. Stochastic fractures are germinated and propagated until the fracture intensity parameters for the region group are satisfied. The collection of these propagated fractures forms the DFN. Deterministic fractures can preserve their natural waviness and depend on the resolution of the triangles (Figure 2-16).

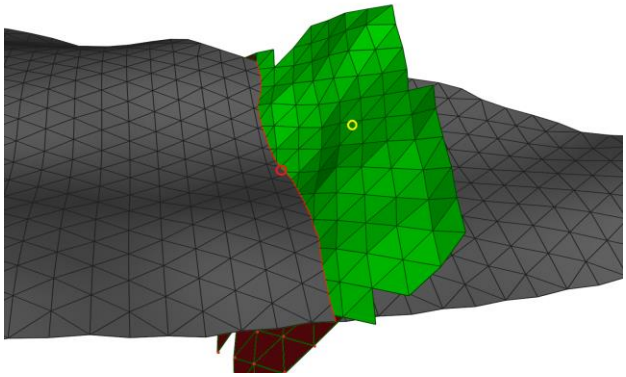

Figure 2-16 Illustration of deterministic fracture generated in MoFrac (Janeczek, 2015).

Input data required for DFN modeling in MoFrac include geological mapping information such as fracture traces on tunnel walls and surface outcrops, the size of experimental volume, the number of fracture groups, fracture orientation, size, shape, intensity, termination rules, and undulation or waviness. Geological mapping information is preserved during fracture propagation, and no fractures are propagated in the section of known unfractured rock.

Fracture orientation is the mean plane that the fracture follows during propagation. It is described by two angles (Dip/Dip Dir., Dip/Strike, or Trend/Plunge) using the Fisher or Gaussian distribution.

The real size and shape of a fracture in 3D space is unknown. As a simplification, a fracture can be modeled as a circular, elliptical, square, and rectangular shape of an estimated area using a simple empirical equation. For example, the fracture area (A_d) can be estimated from the fracture trace length using the equivalent diameter (d_e) approach of a circular fracture (Singhal & Gupta, 2010a) as,

$$A_d = \left(\frac{\pi}{4}\right) \cdot (d_e^2 + \sigma_d) \tag{2-30}$$

where σ_d is the standard deviation of the mapped fracture length.

P_{32} is reported to be the most reliable measure of fracture intensity (Dershowitz & Herda, 1992). Both P_{32} equivalent Cumulative Area Distribution (*CAD*) and P_{21} equivalent Cumulative Length Distribution (*CLD*) can be used as an input fracture intensity parameter in MoFrac (Janeczek, 2015). *CAD* is estimated for each fracture group from a linear trend line (slope) which is derived from a log–log plot (Figure 2-17) of P_{30} (number of fractures greater than area threshold per unit volume) and fracture area threshold as,

$$\frac{\text{No. of fractures} > \text{Area threshold}}{\text{Volume}} \text{ vs. Area threshold} \tag{2-31}$$

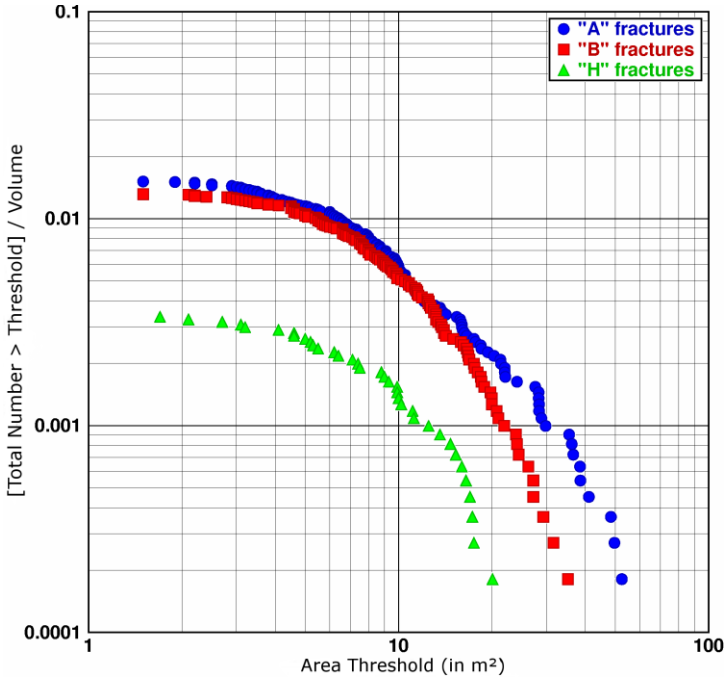

Figure 2-17 Illustration of CADs in a log–log plot for three fracture sets (Janeczek, 2015).

The slope is defined with two coordinates with four parameters (A_{min}, $(P_{30})_1$) and (A_{max}, $(P_{30})_2$)). *CAD* characterizes both the number of fractures and fracture area distribution of each fracture group. The simulated number of fractures in a region group (n_{rg}) depends on the slope of the *CAD* and the range of the area component of the slope and is computed as,

$$n_{rg} = V_r \times [CAD_{rg}(A_{min}) - CAD_{rg}(A_{max})] \tag{2-32}$$

where V_r is the region volume, A_{min} and A_{max} are the minimum and maximum fracture areas respectively assigned to that fracture group. An inverse cumulative area distribution function (CAD^{-1}) is used to generate fracture area using a sample area generating function (S_A) as,

$$S_A = CAD^{-1}\left(n_{min} - R_n \times (\Delta n)\right) \tag{2-33}$$

$$n_{min} = CAD(A_{min}),\ \ n_{max} = CAD(A_{max}),\ \ \Delta n = n_{min} - n_{max} \tag{2-34}$$

where 'Δn' is the actual number of fractures sampled for that area range, 'R_n' is the range of the random number generator [0.0, 1.0], and n_{max} and n_{min} are numbers of fractures above the maximum and minimum fracture area thresholds, respectively. Only *CAD* is discussed here for illustration; however, for calculations involving *CLD*, the area field can be replaced by length.

Fracture undulation characterizes the natural waviness and surface roughness of fractures. Two fracture undulation schemes (stripe and slope deviation) are available in MoFrac. In the stripe undulation scheme, 2D mapped traces are extended to the third dimension preserving the original waviness. In the slope deviation scheme, a fracture can randomly deviate along the mean orientation plane. For the deterministic fracture, the deviation is limited to the maximum known height or amplitude of the 2D trace; however, for the stochastic fracture, the deviation from the mean orientation plane is governed by the user-defined parameter. Although both approaches generate non-planar fractures, neither of them is validated using numerical or field experiments. Robust characterization and quantification of natural fracture surface geometry parameter in 3D should be made using the field mapping data of discontinuity surface.

Fracture truncation rules provide the probability for a fracture group in a region to terminate or to propagate to another fracture group or a region boundary. Fracture truncation relates to the connectivity of fractures and has more significance on the contaminant flow in hydrogeological modeling.

2.5.5 Synthetic Rock Mass Model

The Synthetic Rock Mass (SRM) (Ivars et al., 2011; Pierce et al., 2007) modeling approach has been developed with the objective of a more realistic representation of the mechanical behavior of a fractured rock mass than conventional numerical models. It is also termed as the 'virtual

laboratory' (Ivars et al., 2007) that complements the empirical approach in the estimation of rock mass properties. The SRM approach simulates complete stress–strain curves for synthetic rock masses with imbedded fracture network. A SRM model comprises of intact rock matrix with embedded fracture network. The intact rock matrix is usually represented in 3D by a DEM model and the discontinuities are represented with a DFN model. Three main components in the workflow of the SRM modeling approach (Figure 2-18) are data collection of intact rock and discontinuities, discrete fracture network (DFN) modeling, and geomechanical modeling of SRM models.

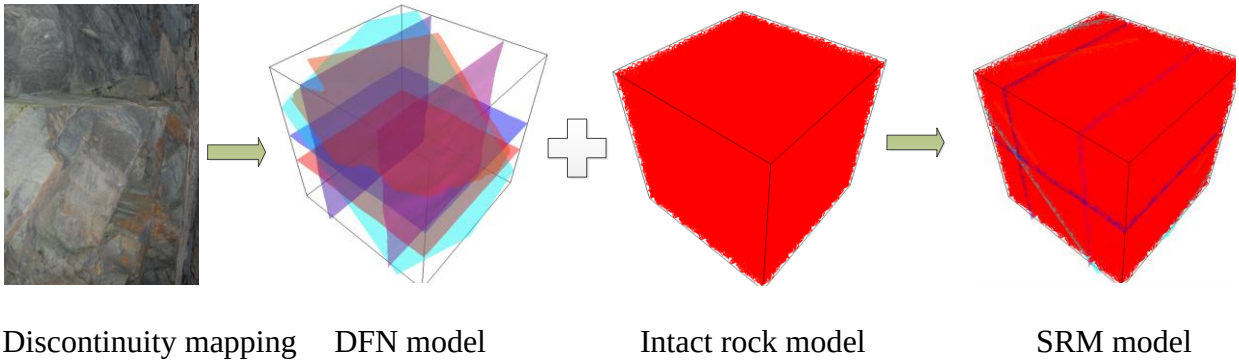

Figure 2-18 Workflow for model development using the SRM modeling approach.

Some of the important considerations for SRM modeling as outlined by Elmo (2006) are:

a) Collection and analysis of discontinuity data should be conducted diligently because the accuracy of the DFN model influences the realism of the SRM model.

b) The scale of the representative elementary volume (REV) of the SRM model should be enough to emulate the problem domain.

c) Reliability in the calibration of laboratory-scale SRM models can be maintained but care should be taken for the calibration of large-scale models.

The majority of the 3D SRM modeling has been performed using Itasca's DEM codes (PFC^{3D}, 3DEC) (Pierce et al., 2007; Ivars et al., 2008; Ivars et al., 2011), Rockfield's FEM-DEM code ELFEN (Rockfield, 2016), and open source DEM code YADE (Kozicki & Donzé, 2008, 2009). In current engineering practice, rock mass properties at a larger scale are determined by degrading the mechanical properties of laboratory-scale intact rock specimens using empirical formulas. However, in the SRM modeling approach, the rock mass properties depend on the model size and the properties of intact rock and discontinuities. Thus, it is not necessary to rely on empirical relations to estimate the rock mass properties at different scales.

The most important aspect of SRM modeling is that the mechanical properties are not defined by the constitutive laws; instead, these are the cumulative outcome of the mechanical properties of the intact rock matrix and the fracture network. Several works had been performed using the SRM modeling approach in the past using planar discontinuities. In one study, the DFN model generated in FracMan (Golder, 2018) is imported into ELFEN to study the influence of the discontinuities on rock mass strength (Pine et al., 2006). For similar applications, SRM modeling has also been performed using PFC^{3D} (Pierce et al., 2007; Esmaieli et al., 2010; Ivars et al., 2011; Zhang, 2014; Vallejos et al., 2016), 3DEC (Garza-Cruz et al., 2014; Turichshev & Hadjigeorgiou, 2017), and more recently SRMTools (Poulsen et al., 2015).

2.5.5.1 BPM-based SRM Model

In BPM-based SRM modeling, intact rock and discontinuities are represented as bonded particles and smooth joint contact model (SJCM), respectively. BPMs simulate the movement and interaction of many finite-sized particles using Newton's second law of motion (Potyondy & Cundall, 2004). Particles are rigid bodies with the finite mass that can move independently of one

another and can translate and rotate (Potyondy, 2017). Particles interact at the contacts by means of internal force and moment. Particle-interaction laws or contact laws update the internal force and moment because all the deformation occurs at the contacts. The three basic entities of the PFC model are ball, clumps, and wall. Clumps are aggregates of balls that act as a single entity and walls are surfaces that are used to apply velocity and boundary condition to the particle assembly.

Contacts between the particles are assigned tensile and shear bond strengths. The contacts in BPM models are oriented in the direction of the line connecting the centers of the particles involved in the contacts. Material properties of a BPM are governed by the contact-model properties (Potyondy & Cundall, 2004). The contacts between the particles can be contact-bonded, parallel-bonded or flat jointed contact (Potyondy, 2015). When the inter-particle forces and moments reach the bond strengths, the contacts break, and they behave as parallel bond contacts. Flat joint bonds have advantages over the regular parallel bonds because of their capability to simulate the realistic values of compressive to tensile strength ratio of rock (Potyondy, 2015).

The complex interactions between the particles and contacts give rise to the overall macroscopic mechanical response of the BPM assembly. Extensive calibration of micro-parameters is required to achieve the target macroscopic mechanical properties of a jointed rock. Discontinuities are represented as a DFN which is discussed in detail in Section 2.5.4 and the tool uses the SJCM logic in which the contacts are oriented perpendicular to the discontinuity plane irrespective of the spatial location of the particles. Consequently, the particles can slide relative to each other along the discontinuity plane as if it was perfectly smooth. The components of a BPM-based SRM model are shown in Figure 2-19.

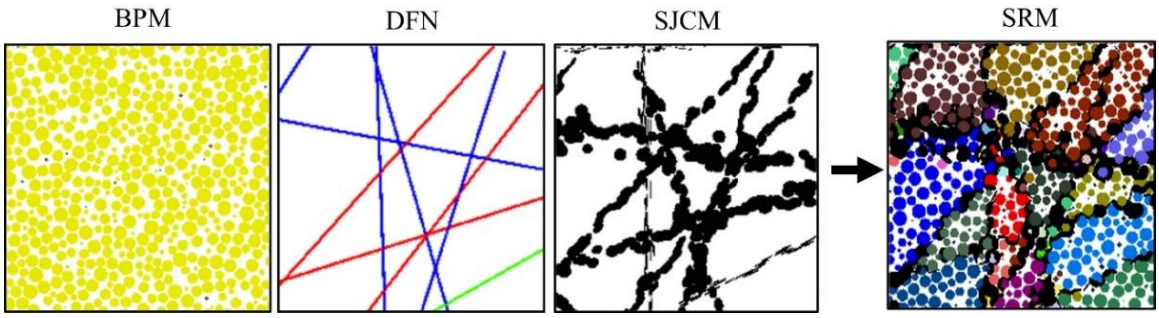

Figure 2-19 Components of a BPM-based SRM model, after Vallejos et al. (2016).

The BPM-based SRM modeling approach has been used to characterize the mechanical properties of intact rock and jointed rock mass, anisotropy, and scale effects (Pierce et al., 2007; Ivars et al., 2008; Ivars et al., 2011). The BPM-based SRM modeling approach has also been applied to reproduce the mechanical behavior of veined core samples under laboratory uniaxial compression tests (Vallejos et al., 2016), to estimate the geometrical and mechanical REV of a jointed rock mass in an underground mine (Esmaieli et al., 2010), and to evaluate the slope stability in a jointed rock mass (Lorig et al., 2015).

Esmaieli et al. (2010) investigated the mechanical properties of rock mass samples of different size and concluded that the rock mass of dimensions 7 m × 7 m × 14 m is the mechanical REV of the rock mass based on numerous UCS simulation results.

Bahrani (2015) investigated the influence of the roughness on the strength of the heavily jointed rock mass analogs without explicitly considering the real geometry of the discontinuity surface using the BPM-based SRM modeling approach in PFC2D.

Vallejos et al. (2016) concluded that the BPM-based SRM approach reasonably reproduced the peak strength, elastic parameters, and failure mode of the veined core samples. Although being

one of the extensively used approaches, the BPM-based SRM modeling approach has the following limitations as outlined by Vallejos et al. (2016):

a) The Poisson's ratio of intact rock cannot be matched in models with brittle post-peak deformation behavior.

b) Discontinuities are modeled as smooth discs without considering the details of the discontinuity surface waviness.

c) Computation times of the numerical models increase exponentially with the increase of the number of particles.

Zhang (2014) employed BPM-based SRM in PFC3D to investigate the mechanical properties and cracking mechanism of the hypothetical jointed pillar under compression and concluded that pillar strength and deformation modulus decrease with the increase of the discontinuity size and density; however, the parallel bond contacts were used to glue the particles which has the limitation of not being capable of matching the compressive to tensile strength ratio of rock in addition to the limitations outlined by Vallejos et al. (2016).

The laboratory triaxial test results of both intact (Castro-Filgueira et al., 2016) and jointed (Castro-Filgueira, 2019) Blanco Mera granite were simulated using the flat-joint contact model in PFC3D and concluded that both the elastic behavior and the strength levels derived from the models are very closely matched to the response of the laboratory samples; however, the post-peak deformational behavior of the jointed granite was not reasonably captured.

The particle-based SRM approach based on an open-source tool YADE (Kozicki & Donzé, 2008, 2009) has also been used to study the mechanical properties of jointed rock mass (Harthong et al.,

2012) and analyze the slope stability in a fractured rock mass (Bonilla-Sierra et al., 2015b, 2015a; Scholtès & Donzé, 2012).

Harthong et al. (2012) investigated the mechanical properties of jointed rock mass using the DFN-DEM approach and concluded that the clustering of fractures has variable influence on the mechanical properties with the change in scale.

Scholtès & Donzé (2012) identified the critical failure surface without any assumptions regarding its location and concluded that the extension of the failure surface across the rock bridges results from the complex interaction between deformation along existing discontinuities and fracture propagation in the intact rock.

Camones et al. (2013) investigated the step-path failure mechanism in a jointed rock slope using the BPM-based SRM approach in PFC and concluded that the tensile crack coalescence is the result of the union of secondary cracks and the shear failure in intact rock portion of the rock slope occurs under the influence of high confining pressure.

2.5.5.2 BBM-based SRM Model

In a BBM, rock mass is represented as an assembly of discrete polyhedral blocks which can either be rigid or deformable. These blocks are bordered with discontinuities and a contact is formed when two blocks come in contact. A force–displacement law dictates the deformations of contacts and sub-contacts. A contact breaks in tension once the limiting tensile strength is reached. In the elastic range, the contact behavior is governed by the normal and shear stiffness parameters. Dilatation properties may be assigned to the contact once it starts to slip. Similar to the BPM-based SRM, discontinuities can be represented as a DFN in the BBM-based SRM. Material properties of block assembly and DFNs are independent to each other.

Bidgoli & Jing (2014) investigated the anisotropy of strength and deformability of fractured rock mass using BBM-based SRM approach in UDEC and argued that the laboratory test results of intact rock materials can only be used to estimate elastic or elastoplastic behaviors of intact rock materials but these results cannot be used to estimate the mechanical properties of fractured rock system.

Le Goc et al. (2014) investigated the influence of DFN of different configurations on the deformability of jointed rock mass in 3DEC and concluded that the elastic modulus depends on the cubic fracture size parameter.

Turichshev & Hadjigeorgiou (2017) reproduced the key experimental behaviors of intact veined rock under compression and calibrated the mechanical properties (modulus, strength) of veined core granite using BBM-based SRM models in 3DEC.

Recently, Wang & Cai (2018a) performed multiple scale modeling in 3DEC to investigate the stress distribution during tunnel excavation by dividing the tunnel zones into three, highly damaged zone (HDZ), excavation damaged zone (EDZ), and excavation disturbed zone (EdZ) and argued that the modeling approach captured the tunnel deformation behavior more accurately than the traditional equivalent continuum modeling approach.

Based on the BBM-based SRM modeling analysis in 3DEC, Brideau et al. (2011) and Havaej et al. (2016) concluded that the slope stability is influenced by the slope topography, discontinuity friction angle, and discontinuity persistence. Kulatilake & Shu (2015) simulated the slope deformation of an open pit mine using the BBM-based SRM approach and indicated that the lateral stress ratio influences the model displacements. Using the BBM-based SRM models in 3DEC, Sainsbury et al. (2016) demonstrated that the intermediate discontinuity structures have a

significant influence on the stability of mine-scale slope. A typical BBM-based SRM model, generated using 3DEC, is shown in Figure 2-20.

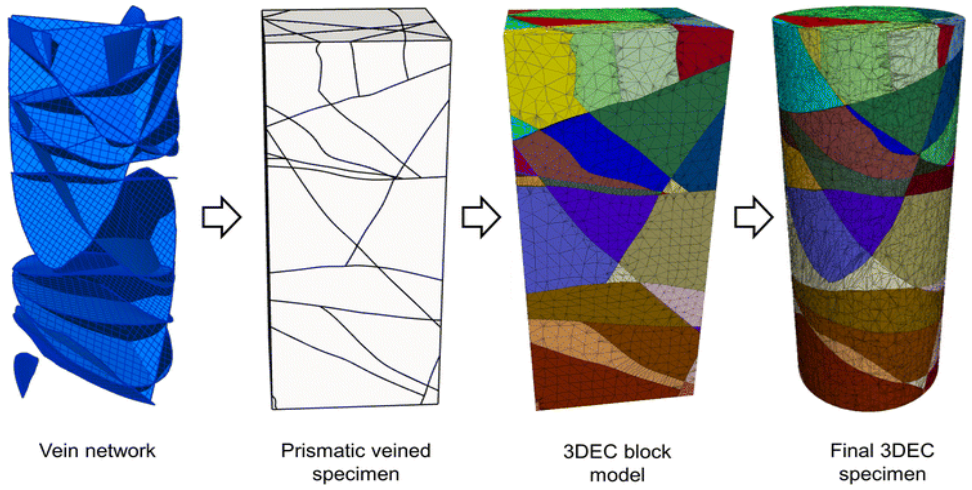

Figure 2-20 BBM-based SRM model of the intact veined specimen in 3DEC, after Turichshev & Hadjigeorgiou (2017).

Some BBMs have also been used to perform SRM modeling without the consideration of DFN. Instead, these models consist of grains generated using the Voronoi tessellation algorithm (Ghazvinian et al., 2014; Li et al., 2016) and the trigon logic (Gao & Stead, 2014) and inter and intra-grain contacts (Wang & Cai, 2018b) that can fail in both tension and shear. Blocks generated by coupling the trigon logic offers advantages over the Voronoi algorithm by providing more freedoms for block rotation and sliding.

Similar to the BPM models, the complex interactions between the bonded blocks dictate the overall macroscopic mechanical response of a BBM assembly and extensive calibration of micro-material parameters is required to achieve the target macroscopic response of a jointed rock. Like the BPM-based SRM models, BBM-based SRM models also have the disadvantages of longer running time (longer than BPM models) and difficulties in explicitly representing DFN with non-planar discontinuities.

2.5.5.3 LS-SRM Model

The lattice-spring-based synthetic rock mass (LS-SRM) modeling approach is efficient in terms of computational time because it is formulated in small strain which does not require contact detection as in classical DEM modeling. Unlike other DEM modeling approaches, calibration of some micro parameters is not required in the lattice code because calibration factors are built-in and most of the desired macroscopic properties can be provided as model inputs. The basic principle of LS-SRM modeling is similar to the BPM- and BBM-based SRM modeling approach except that the intact rock matrix is represented as a lattice assembly and the discontinuity geometry can be either planar or non-planar. Calibration is easier for LS-SRM models because there are fewer lattice micro-parameters as shown in Table 2-4. Detailed calibration approaches for intact and jointed LS-SRM models are discussed in Chapters 3 & 4, respectively.

Table 2-4 Lattice micro-parameters for intact rock and joints

Intact lattice matrix	Lattice joint set properties
E_{mic} (GPa)	Joint tensile strength, σ_{jt} (MPa)
σ_{cmic} (MPa)	Joint friction angle, φ_j (°)
$(\sigma_t)_{mic}$ (MPa)	Joint cohesion, c_j (MPa)
Density, ρ (kg/m^3)	Joint dilation angle, δ_j (°)
Porosity (%)	Joint normal stiffness (GPa/m)
φ_{fjp} (°)	Joint shear stiffness (GPa/m)
φ_{fjr} (°)	Joint dip, θ (°)
Radius multiplier	Joint dip direction, λ (°)

E_{mic} – lattice elastic modulus, σ_{cmic} – lattice compressive strength, $(\sigma_t)_{mic}$ – lattice tensile strength, φ_{fjp} – peak friction angle of flat joint, φ_{fjr} – residual friction angle of flat joint.

Furthermore, the lattice code is efficient in handling discontinuities by avoiding the formation of very small blocks due to ill-conditioned meshing. Details on the lattice spring modeling approach can be found in Cundall (2011), Damjanac et al. (2016), and (Bastola & Cai, 2019). A comparison of LS-SRM and other DEM-based SRM modeling approaches are shown in Table 2-5.

Table 2-5 Comparison of SRM modeling approaches

Method	Advantages	Disadvantages
BPM-based SRM	Easy to simulate crack propagation and slip on discontinuities	Cumbersome calibration approach
	Can incorporate DFNs	Particles are rigid and it is difficult to incorporate non-planar discontinuities
	Can incorporate non-persistent discontinuity easily	High computational cost
BBM-based SRM	Easy to simulate crack propagation and slip on discontinuities	Cumbersome calibration approach
	Can incorporate DFNs	Difficult to incorporate non-planar and non-persistent discontinuities
	Blocks can be both rigid and deformable	High computational cost
Lattice-spring-based SRM	Simple calibration of model parameters	Particle detachment cannot be visualized
	Easy to incorporate non-planar and non-persistent discontinuities	Poisson's ratio of intact rock is low for flat-joint contact model
	Computational time is 5 to 10 times less than BPM- and BBM-based SRM	Model cross-section is rectangular in SRMTools

The lattice-spring-based synthetic rock mass (LS-SRM) modeling approach has been used to study the brittle fracturing and stability assessment of rock slopes (Herrero, 2015; Cundall et al., 2016; Havaej & Stead, 2016) using the SRMTools-Slope Model software (Itasca, 2016b). Herrero (2015)

found that both the stability and the failure mode of the slopes are influenced by the *in-situ* stress in deep open pit mines. Havaej & Stead (2016) quantified the rock damage intensity due to brittle rock fracturing and highlighted the close relationships among kinematics, failure surface, and rock damage. Cundall et al. (2016) argued that the slope failure is the outcome of the brittle fracturing of the intact rock bridges and that the assumption of equivalent shear strength of the slope is not justified. Comparative studies on the results from LS-SRM using SRMTools and the H–B strength criterion suggest that joint persistence and joint intensity are critical for the estimation of rock mass strength (Poulsen et al., 2015).

2.6 Remarks

In this Chapter, a comprehensive review of the state-of-the-art pertaining to the rock mass failure modes, estimation of mechanical properties of rock mass using empirical and numerical modeling approaches are presented. Existing empirical formulas for the estimation of strength and deformability of rock mass and mine pillars are also reviewed. Failure mechanisms observed in both the laboratory-scale pre-cracked rocks and large-scale jointed rock masses such as slope and mine pillars are discussed.

Numerical modeling method is often preferred in the characterization of mechanical properties of jointed rock mass and in the assessment of slope stability because of the difficulty in performing the large-scale testing of rock mass and the lack of universal applicability of empirical approaches. Based on an exhaustive analysis of the numerical modeling approaches, discontinuum numerical modeling approaches, especially the ones based on the SRM approach, are better suited for modeling the mechanical response of jointed rock mass because of their ability to explicitly represent pre-existing discontinuities.

Of all the SRM approaches, the LS-SRM modeling approach is chosen for the simulation of jointed rock mass because of its capability to represent non-planar discontinuities easily and relatively shorter computation time than other DEM-based SRM modeling approaches. The mechanical formulation and the application of the LS-SRM modeling approach in SRMTools are also discussed. Complex DFN models with realistic non-planar discontinuities can be generated using DFN software MoFrac and integrated to mechanical models to synthesize more robust SRM models in SRMTools for a better representation of jointed rock mass systems. General description and application of the DFN software, MoFrac is also provided.

Because SRMTools is a relatively new software tool, an extensive sensitivity study of the lattice model parameters of intact marble is performed in Chapter 3. In Chapter 4, the influence of discontinuity surface geometry on the cracking mechanism and mechanical properties of pre-cracked rocks is investigated using the LS-SRM modeling approach under unconfined and confined compressions, using eight different models with planar and non-planar crack configurations. The mechanical behavior of laboratory-scale jointed granite with different joint configurations (orientation, intensity, waviness, and persistence) are investigated under triaxial compression using the LS-SRM modeling approach in Chapter 5. In Chapter 6, slope stability of the Cadia Hill Open Pit mine is assessed using LS-SRM modeling approach in Slope Model. In Chapter 7 the mechanical response of the rock mass of different scale, discontinuity intensity are investigated under unconfined and confined compression.

Chapter 3

3 Calibration of LS-SRM models for intact rocks[1]

In this Chapter, the mechanical behavior of intact Zhenping marble is studied using the LS-SRM modeling approach with Itasca's SRMTools software. The investigated marble samples are from a copper mine in Zhenping City, located in Henan Province, China. This marble is chosen because the stress–strain curves are highly affected by the confining pressure and the post-peak responses exhibit a typical brittle-to-ductile-to-plastic deformation behavior with the increase of confining pressure during laboratory triaxial tests. The average *UCS* and density of the rock are 70.1 MPa and 2700 kg/m^3, respectively (Peng et al., 2017). The mechanical response of the rock is assessed using stress–strain relations under unconfined and confined compressions. Under unconfined loading condition, specimens exhibit a typical brittle failure behavior and the strength drops to zero immediately after the peak. Under confined loading condition and when the confinement is above 30 MPa, the stress–strain curves exhibit ductile behavior and at 40 MPa of confining pressure, the specimens exhibit a nearly perfect plastic deformation behavior. Because of the homogeneity of the rock, Young's moduli (*E*) are similar under all confining pressures. Because SRMTools is a relatively new tool, a sensitivity analysis is conducted first in Section 3.2 to understand the influence of lattice micro-parameters on the macro-mechanical parameters and a calibration approach is outlined. Calibration of the mechanical properties of Zhenping marble is performed using the laboratory test results from Peng et al. (2017) (Section 3.3). The numerical

[1] Originally published as 'Bastola, S. and Cai, M. Simulation of stress–strain relations of Zhenping marble using lattice-spring-based synthetic rock mass models. In *52nd U.S. Rock Mechanics/Geomechanics Symposium*. Seattle, USA: American Rock Mechanics Association; 2018.

modeling results are used to capture the macroscopic properties of Zhenping marble such as elastic modulus, crack initiation stress, crack damage stress, tensile strength, strength envelope, etc., and these are compared with the ones derived from laboratory test results.

3.1 Model development

Synthetic marble models, 100 mm × 50 mm × 50 mm in dimension (Figure 3-1), are generated. The model contains 38,784 lattice nodes that are connected to each other by 192,436 lattice springs.

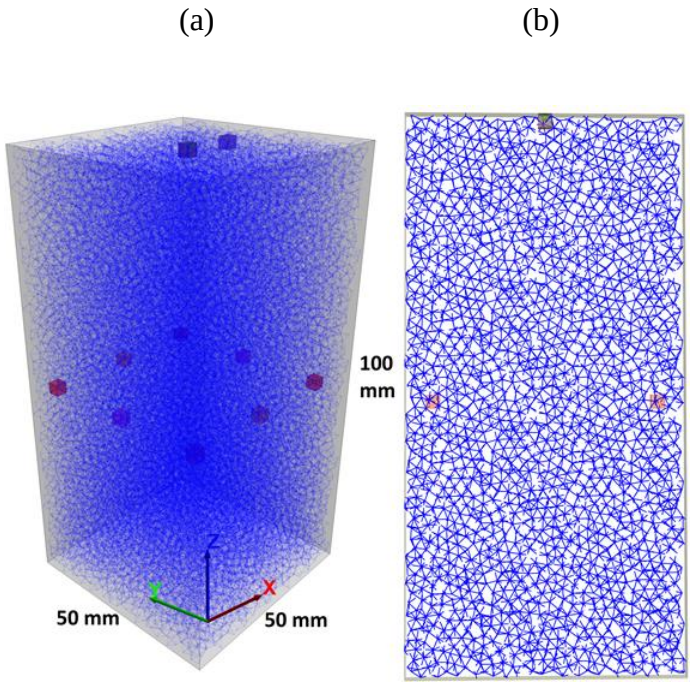

Figure 3-1 Synthetic intact rock model of Zhenping marble (a) and a longitudinal section at the center of the model (b) illustrating the connectivity of lattice springs; red cubes indicate force and displacement monitoring points.

Specimens are loaded axially in the vertical displacement control mode (constant velocity). The optimum velocity of loading is established by performing a series of *UCS* simulations with different displacement rates as discussed in Section 3.2.1. Vertical and lateral confining forces are applied simultaneously during triaxial loading. Vertical force, vertical displacement, lateral

displacement, and the number of cracks are measured using the monitoring points shown in Figure 3-1 in all numerical experiments. Axial stress is calculated based on the total reaction forces on the specimen which depends on the contact area between the lattice nodes (Itasca, 2016b). Contact areas between the lattices are directly influenced by the lattice resolution.

3.2 Sensitivity study

Numerical models are idealized replicas of physical models; hence, the results from a realistic numerical model should reasonably agree with the results from experimental studies conducted in laboratory or *in-situ*. Modeling parameters such as boundary condition, model resolution, and material properties all influence the outcome of a numerical simulation. Before the actual simulation of the mechanical behavior of Zhenping marble, a sensitivity analysis of LS-SRM model parameters is performed. In the sensitivity analysis, the studied model parameter is changed while keeping other parameters unchanged. The insight gained from the sensitivity study is useful for model calibration.

3.2.1 The sensitivity of loading rate, lattice resolution, and lattice structure

The influences of loading rate, lattice resolution, and lattice shape on *UCS* and Young's modulus (*E*) are studied first. The sensitivity analysis of loading rate is performed at loading velocities of 0.001, 0.01, 0.03, and 0.05 m/s, using a resolution of 0.2 cm lattice size, which results in 25 lattices in the shortest dimension of the synthetic specimen. The lattice resolution is the ratio of the shortest dimension of the synthetic specimen to the lattice size (with the same unit) used in modeling. The sensitivity analysis of lattice size is performed using lattice sizes of 0.1, 0.2, 0.3, 0.4, and 0.5 cm at the loading rate of 0.01 m/s. Both Voronoi Lattice (V_L) and spherical lattice (referred to as Regular Lattice (R_L) in this thesis) are employed in the sensitivity analysis. Other lattice model

parameters are lattice compressive strength (σ_{cmic}) = 50 MPa, lattice tensile strength $(\sigma_t)_{mic}$ = 5.2 MPa, lattice Young's modulus E_{mic} = 32 GPa, peak flat joint friction angle φ_{fjp} = 40°, and residual flat joint friction angle φ_{fjr} = 8°, which are unchanged in the sensitivity analyses.

It is seen from Figure 3-2a that loading rate does not influence *UCS* and *E* significantly for both the R_L and the V_L models. *UCS* and *E* are slightly higher for the V_L model. This is because the number of springs in V_L models is 1.39 times more than the number of springs in R_L models with the same lattice size and the V_L model has a crystalline shape which offers more interlocking between the lattice springs than the spherical shaped R_L models.

The influence of lattice resolution and size on *UCS* and *E* is presented in Figure 3-2b&c. Both *UCS* and *E* increase with the increase of lattice resolution or the decrease of lattice size for the R_L model. However, for the V_L model, *UCS* increases with the increase of lattice resolution in the range of 5 to 25 but eventually decreases at higher resolutions. A logarithmic decay in *E* is observed with the increase of the lattice resolution for the V_L model; however, *E* increases with the increase of lattice resolution for the R_L model. Low *UCS* and *E* for the V_L model at high resolutions could be attributed to the reduction of the relative size of the interlocking Voronoi structures

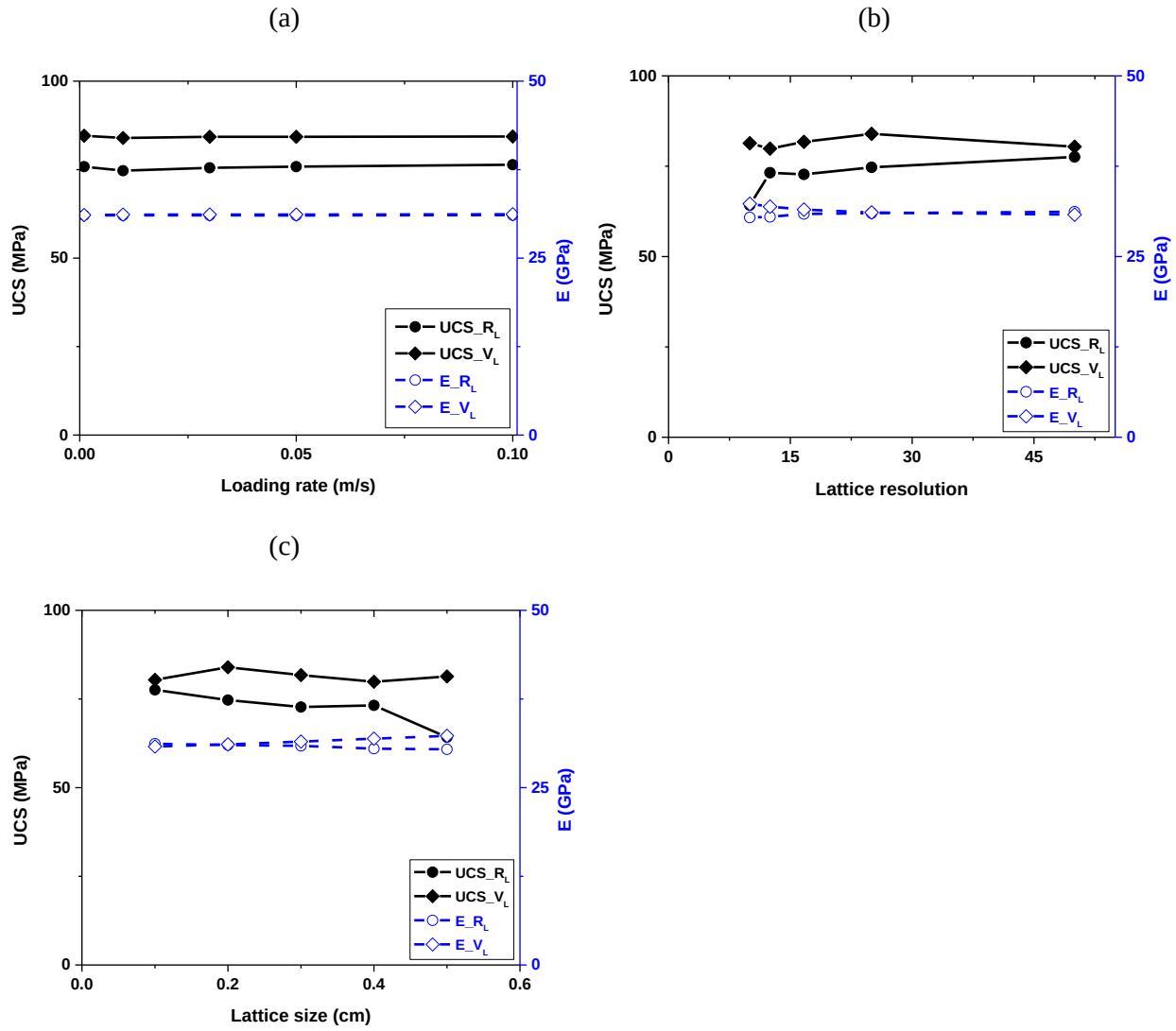

Figure 3-2 Influence of loading rate (a), lattice resolution (b), and lattice size (c) on *UCS* and *E*.

In both the R_L and the V_L models, an increase in lattice resolution or a decrease in loading rate increases the computation time significantly. Hence, an intelligent selection of suitable loading rate and lattice size should be made such that the modeling is feasible, and the results are not influenced by these parameters. Although the small loading rate does not affect the simulation results significantly, an optimized loading rate should be used to avoid shock loading during simulations for confining pressures greater than 10 MPa. From the sensitivity analysis, a lattice

resolution of 25 is used, which is above the recommended minimum resolution of 20 by Itasca, and the loading rate of 0.01 m/s is used in all simulations. The R_L models are used in this study because the computation time is longer for the V_L models.

3.2.2 The sensitivity of radius multiplier

Radius multiplier (*RM*) is the ratio of the flat joint contact diameter to the particle diameter. For instance, a multiplier of 1.0 corresponds to the condition when the flat joint contact diameter is equal to the particle diameter (Itasca, 2017). The influence of *RM* on *UCS*, σ_t, and the angle of internal friction (φ) is studied for *RM* values of 0.1, 0.5, and 0.9 and the results are presented in Figure 3-3. A non-linear increase in *UCS* is observed with the increase of *RM*. However, σ_t and φ increase slightly with the increase of RM. A *RM* of 0.9 is used in all model simulations because *RM* = 1.0 is not recommended for triaxial simulation (Itasca, 2017).

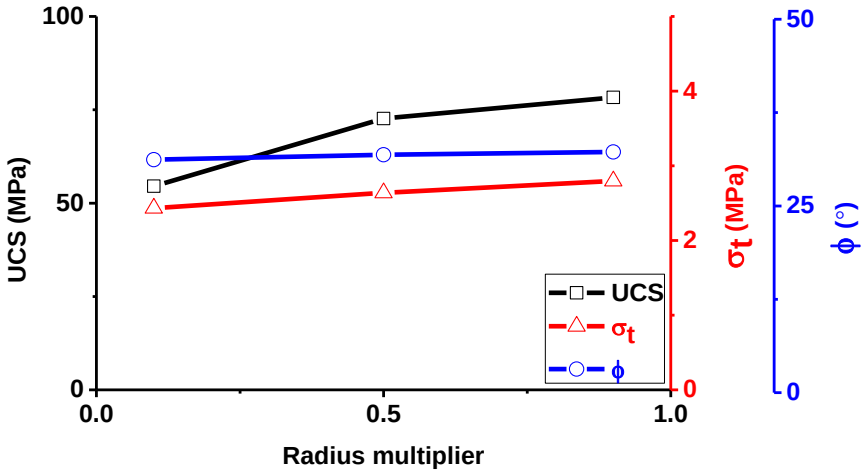

Figure 3-3 Influence of radius multiplier on *UCS*, σ_t, and φ.

3.2.3 The sensitivity of elastic modulus

To examine the influence of the elastic modulus (E_{mic}) of the lattice particles on the macroscopic elastic modulus (E_{mac}) of the intact rock, three sets of *UCS* simulations are conducted with E_{mic} =

32, 42, and 52 GPa, while keeping other parameters the same as those used in the sensitivity analysis in Section 3.2.1. E_{mac} increases linearly with the increase of E_{mic} and E_{mac} is approximately 0.97 times of E_{mic}; however, E_{mic} shows no significant influence on the *UCS* (Figure 3-4).

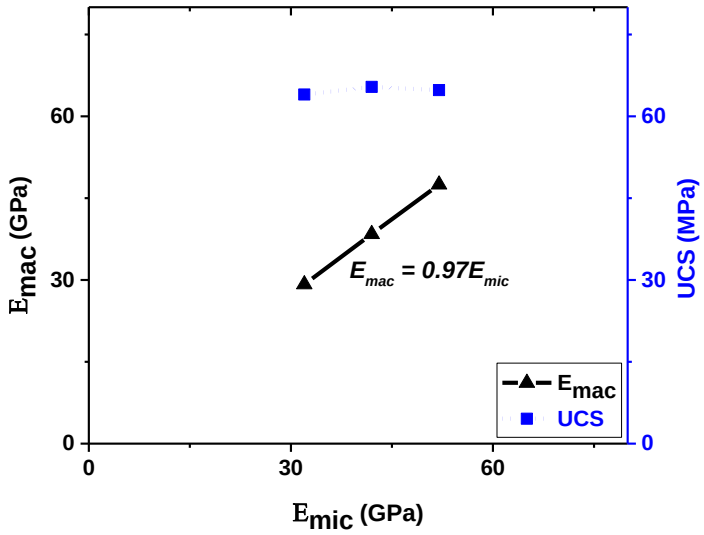

Figure 3-4 Influence of E_{mic} on E_{mac} and *UCS*.

3.2.4 The sensitivity of friction angle of flat joints

The flat joint contact model was adopted in this study because of its ability to simulate realistic values of σ_c/σ_t for rock. Each flat joint spring contact can be discretized into sub-springs with a minimum of three. When one sub-spring breaks, other sub-springs can remain intact. A flat joint contact has two parameters: peak (φ_{fjp}) and residual (φ_{fjr}) flat joint friction angles. These frictional properties only get mobilized after cracks are formed. The φ_{fjp} is assigned to intact flat jointed sub-spring(s) and the φ_{fjr} is assigned to broken flat jointed sub-spring(s).

Sensitivity analyses of both φ_{fjp} and φ_{fjr} on the compressive strength are conducted under 5, 10, and 15 MPa confining pressures. Sensitivity analyses of φ_{fjp} are conducted at 30°, 40°, and 50° while keeping φ_{fjr} at 0° and sensitivity analyses of φ_{fjr} are conducted at 5° and 10° while keeping φ_{fjp} at 40°. Both φ_{fjp} and φ_{fjr} have a positive influence on rock strength. The φ_{fjp} and φ_{fjr} have more

influence on the peak and post-peak strengths, respectively. The φ value also increases with the increase of φ_{fjp} (Figure 3-5a). At $\varphi_{fjr} = 0°$, φ is approximately 90% of φ_{fjp} for $30° \leq \varphi_{fjp} \leq 50°$. The φ_{fjr} has a very small or no influence on φ (Figure 3-5b). The increase of φ_{fjr} results in higher post-peak strengths and more ductile-plastic post peak deformation behavior. Strain-hardening occurs when the confining stress is greater than 10 MPa for flat joint contacts with $\varphi_{fjr} = 10°$ and $\varphi_{fjp} = 40°$ as shown in Figure 3-6.

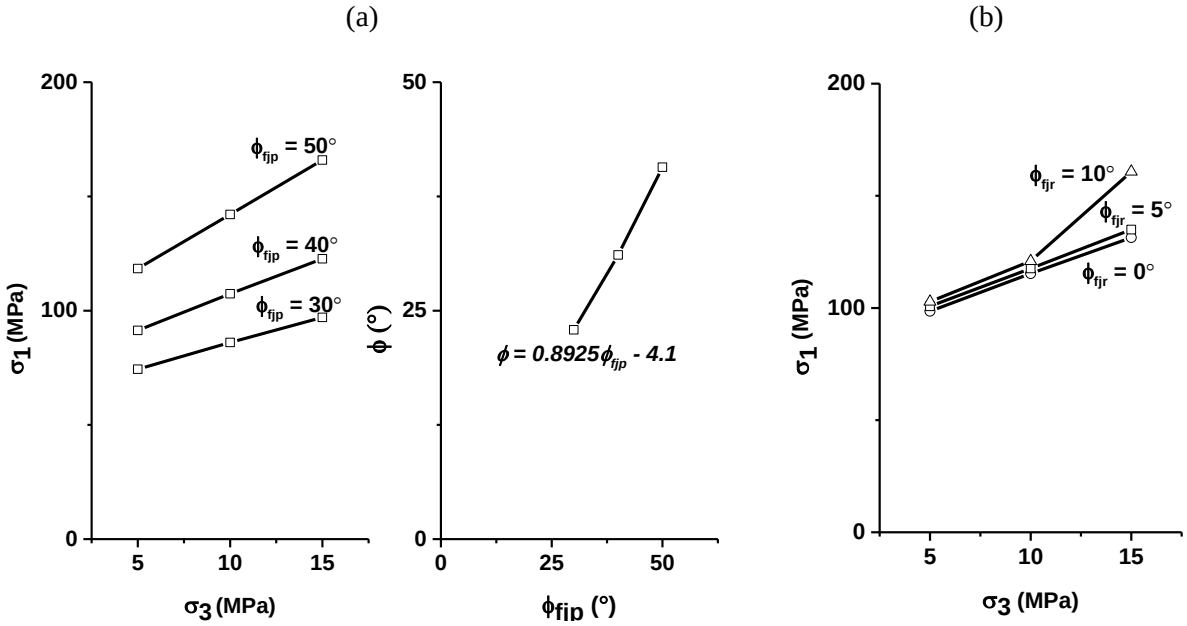

Figure 3-5 Influence of (a) φ_{fjp} on σ_1 and φ (b) φ_{fjr} on σ_1.

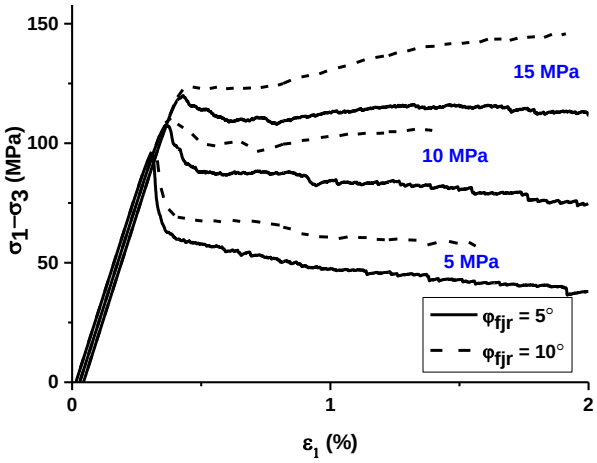

Figure 3-6 Differential stress–axial strain plot of Zhenping marble with φ_{fjr} = 5° (solid line) and φ_{fjr} = 10° (dotted line) under different confining pressures.

3.2.5 The sensitivity of lattice compressive to tensile strength ratio

Sensitivity analyses of the microscopic compressive to tensile strength ratio $(\sigma_c/\sigma_t)_{mic}$ on *UCS* and the macroscopic compressive to tensile strength ratio $(\sigma_c/\sigma_t)_{mac}$ are performed at microscopic tensile strengths $(\sigma_t)_{mic}$ of 1, 2.7, and 5 MPa while keeping other micro-parameters the same as those used in the sensitivity analysis presented in Section 3.2.1. As can be seen from Figure 3-7, both *UCS* and $(\sigma_c/\sigma_t)_{mac}$ increase with the increase of $(\sigma_c/\sigma_t)_{mic}$. A positive linear relationship is observed between $(\sigma_c/\sigma_t)_{mac}$ and $(\sigma_c/\sigma_t)_{mic}$ because the simulated tensile strength $(\sigma_t)_{mac}$ using the flat joint model is always equal to $(\sigma_t)_{mic.}$ This simplifies the calibration process for achieving the desired ratio of $(\sigma_c/\sigma_t)_{mac}$. A non-linear relationship is observed between the UCS and $(\sigma_c/\sigma_t)_{mic}$.

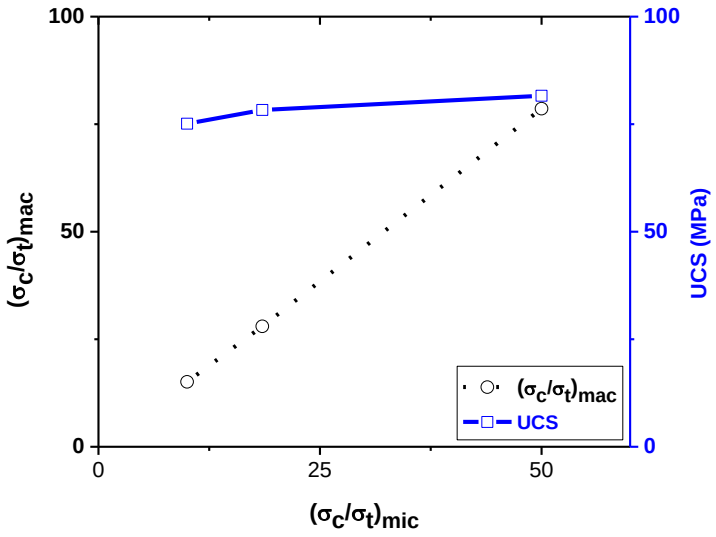

Figure 3-7 Influence of $(\sigma_c/\sigma_t)_{mic}$ on *UCS* and $(\sigma_c/\sigma_t)_{mac}$.

3.3 Calibration of intact marble models

To use the SRMTools to simulate the mechanical properties of intact rock, microscopic lattice model parameters need to be calibrated. The goal of the calibration process is to obtain a set of model parameters that can reproduce the macro-mechanical properties of the intact rock. The insight gained from the sensitivity study in Section 3.2 is used for calibration.

Calibration of Zhenping marble is performed by carrying out a series of unconfined and confined compression and direct tension simulations and comparing the modeling results with the laboratory test results from Peng et al. (2017). An acceptable range of the flat joint friction angles that resemble the physics of the contacts between the particles are used and these remain unchanged throughout the simulation process for all models. In this study, φ_{fjp}, and φ_{fjr} of 40° and 0°, respectively, are used. One might find the choice of φ_{fjr} somewhat unrealistic, but the sensitivity analysis infers otherwise. The residual friction angle of the flat joint contact model must be very small (0° in this case) to compensate the interlocking effect in the post-peak deformation stage if the laboratory post-peak stress–strain curves are to be simulated. The lattice parameters used for

the simulation of the laboratory test results of Zhenping marble are shown in Table 3-1. The loading rate and lattice size used in all simulations are 0.01 m/s and 0.2 cm, respectively.

Because the lattice code SRMTools has fewer micro parameters compared with other DEM codes, the calibration procedure using the lattice flat joint contact model is less complicated (Figure 3-8). The detailed calibration approach can also be found in Bastola & Cai (2018b).

Table 3-1 Lattice parameters for the simulation of laboratory test results of Zhenping marble

Lattice parameters	Value
E_{mic} (GPa)	35
σ_{cmic} (MPa)	50
$(\sigma_t)_{mic}$ (MPa)	2.7
Density, ρ (kg/m^3)	2700
Porosity (%)	2
φ_{fjp} (°)	40
φ_{fjr} (°)	0
Radius multiplier	0.9

E_{mic} – lattice elastic modulus, σ_{cmic} – lattice compressive strength, $(\sigma_t)_{mic}$ – lattice tensile strength, φ_{fjp} – peak friction angle of flat joint, φ_{fjr} – residual friction angle of flat joint

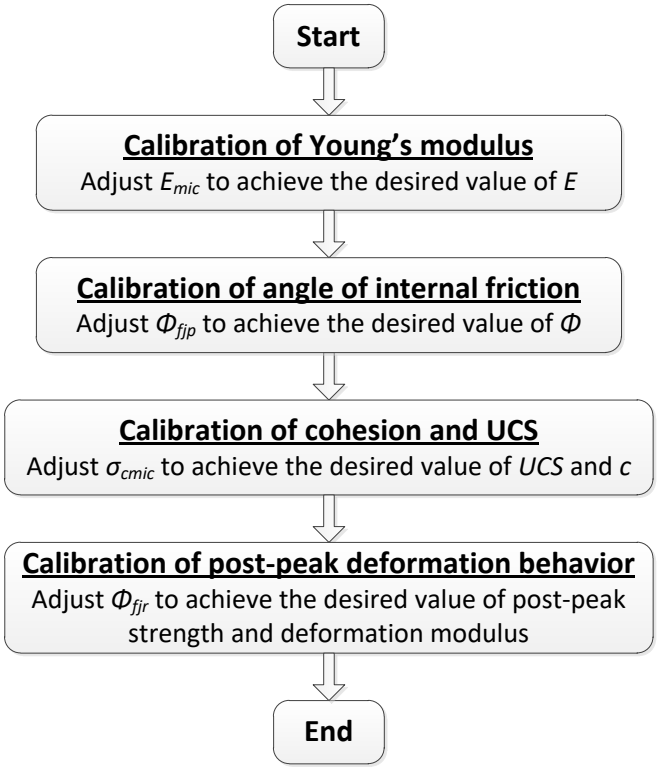

Figure 3-8 Flowchart illustrating the procedure for calibrating the mechanical properties of intact rock for LS-SRM models with flat joint contacts.

3.3.1 Calibration of Young's modulus

The relation between E_{mic} and E_{mac} derived from the sensitivity analysis in Section 3.2.3 is used to calibrate the model to the desired value of E_{mac}. The relation between E_{mic} and E_{mac} is established using the following steps: (i) three UCS simulations are performed at $E_{mic} = E_{target}$, $E_{target}+10$, and $E_{target}-10$, (ii) E_{mac} is derived from the modeling results by calculating the tangent modulus at 50% of σ_{mac} from the axial stress–axial strain curve, (iii) a regression analysis is performed between E_{mic} and E_{mac} and the equation with the R^2 value of at least 90% is chosen; (iv) E_{mic} value is calculated from the equation generated in step (iii) by replacing E_{mac} with E_{target}. Using these steps, Young's modulus of Zhenping marble is calibrated to E_{mac} = 33.9 GPa using E_{mic} = 35 GPa.

3.3.2 Calibration of tensile strength

This is the simplest step of calibration because in the flat joint contact model the value of target tensile strength is always equal to $(\sigma_t)_{mic}$. The tensile strength is calibrated to the laboratory tensile strength of 2.8 MPa. Failure occurs shortly after crack initiation and both the crack initiation (σ_{ci}) and the crack damage (σ_{cd}) stresses are near the peak strength (Figure 3-9).

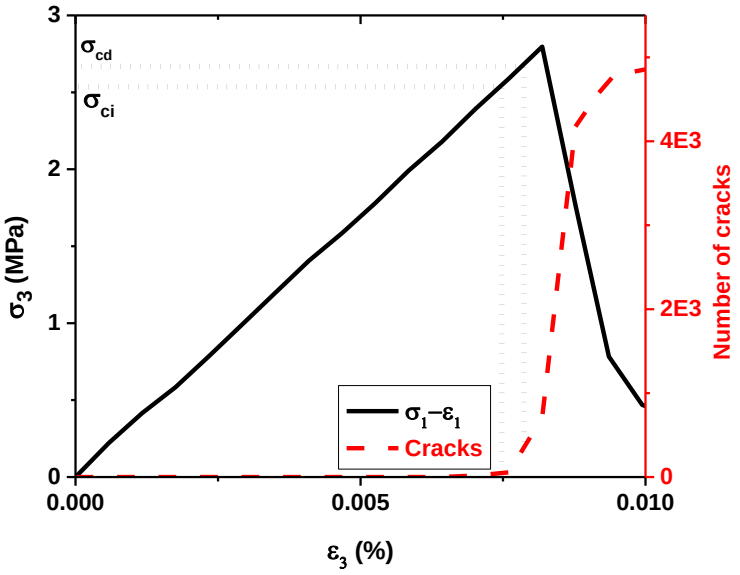

Figure 3-9 Axial stress–axial strain and axial strain–number of cracks relations of Zhenping marble under direct tension.

3.3.3 Calibration of strength envelope

To achieve the desired value of φ, the relation between φ_{fjp} and φ derived in Section 3.2.4 is used. At a zero φ_{fjr}, φ_{fjp} = 40° is required to reach a φ value of 31.7°. A non-zero φ_{fjr} as low as 1° causes strain-hardening in models that are under confining pressures greater or equal to 30 MPa. Thus, φ_{fjr} is adjusted within the range of $0° \leq \varphi_{fjr} \leq 10°$ for $0 \leq \sigma_3 \leq 30$ MPa for the calibration of strength envelope at φ_{fjp} = 40°. The calibrated c and φ values are 17.4 MPa and 37.5°, respectively.

3.3.4 Calibration of UCS

The cohesion of an intact material is controlled by $(\sigma_c)_{mic}$. In addition, both φ_{fjp} and φ_{fjr} influence the macroscopic compressive strength $(\sigma_c)_{mac}$. As a result, all three parameters need to be adjusted carefully to simulate the *UCS*. Calibration to the target *UCS* is carried out by keeping φ_{fjp} = 40°, which was achieved at the previous calibration stage in Section 3.3.3. Using the relation between $(\sigma_c)_{mic}$ and $(\sigma_c)_{mac}$ that was derived in the sensitivity study in Section 3.2.5, $(\sigma_c)_{mic}$ is adjusted to obtain the desired macroscopic value of *UCS*. *UCS* is calibrated to 78.3 MPa using $(\sigma_c)_{mic}$ = 50 MPa and σ_t = 2.8 MPa. The crack initiation stress (σ_{ci}) is reported at the point in the axial stress–cumulative number of cracks plot, from which acoustic emission (AE) event count increases significantly for the first time. The crack damage stress (σ_{cd}) is reported at the point where the AE event count diverges from the first linear slope and increases rapidly. σ_{ci} is around 35 MPa or 45% of σ_c, which is within the range 40 to 60% of σ_c observed for most hard rocks (Martin, 1993; Cai et al., 2004). The σ_{cd} is around 73 MPa, which is near the peak compressive strength. This value is higher than the range of 70 to 90% of σ_c because of the limitation of the tool and it explains why the volumetric strain reversal point occurs near the peak strength (Figure 3-10). The failure of the intact Zhenping marble is accompanied by typical axial splitting and shearing (Figure 3-11).

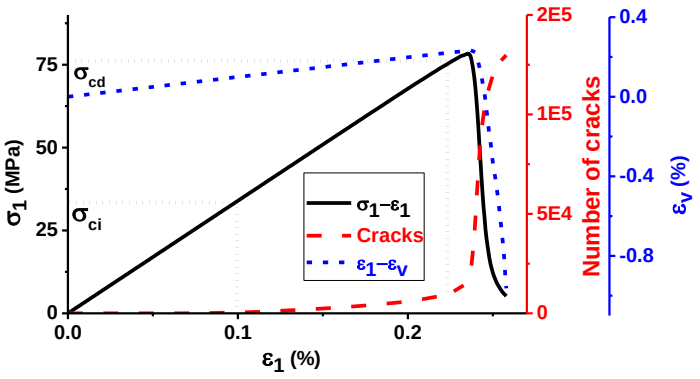

Figure 3-10 Axial stress–axial strain, axial strain–number of cracks, axial strain–volumetric strain plots of Zhenping marble under unconfined compression.

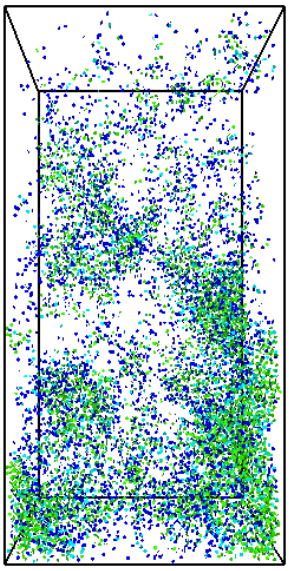

Figure 3-11 Crack development in intact marble at failure (peak axial stress).

3.3.5 Calibration of post-peak deformation behavior

Matching the post-peak deformation behavior is the final stage of calibration. This calibration stage can be optional if the focus is only on pre-peak deformation behavior and peak strength. Zhenping marble exhibits a high degree of plastic deformation near the peak and in the post-peak deformation stage with the increase of confining pressure. This phenomenon can be reproduced to some extent with the SRMTools. The post-peak deformation behavior is highly sensitive to φ_{fjr} with the increase of confining pressure as shown in Section 3.2.4. Lattice models exhibit very high post-peak strengths under high confinements even at $\varphi_{fjr} = 0°$. Adjustment of φ_{fjr} is made within the range of $0° \leq \varphi_{fjr} \leq 10°$ for $0 \leq \sigma_3 \leq 30$ MPa to achieve realistic post-peak stress–strain curves. To capture the post-peak strength of Zhenping marble, φ_{fjr} is gradually decreased with the increase of confinement. For instance, φ_{fjr} of 8° and 1° simulates realistic post-peak stress–strain behaviors of intact Zhenping marble at 5 and 25 MPa confinements, respectively.

Input lattice parameters and resultant macro-mechanical parameters for the calibrated Zhenping marble model are shown in Table 3-1 and Table 3-2, respectively. Axial stress–axial strain curves from the laboratory triaxial test and numerical models are reasonably close to each other as shown in Figure 3-12a. The target values for each parameter are derived from the H–B and M–C strength envelope fits of the laboratory triaxial test results. The triaxial simulation results are also fitted to the H–B and M–C strength envelopes as shown in Figure 3-12b. H–B and M–C model parameters from both laboratory test and numerical modeling are very close (within 10%) to each other as shown in Table 3-2. The calibrated lattice parameters should yield the simulation results that are reasonably close (± 10%) to the calibration targets.

Table 3-2 Comparison of mechanical properties of Zhenping marble from laboratory test (target) with numerical models

Parameters	Target value (lab test)	Numerical modeling
E (GPa)	31.7	33.9
σ_c (MPa)	70.1	78.3
σ_t (MPa)	2.7	2.8
m_i	9.8	7.9
σ_{ci}, σ_{cd} (MPa)	28-42, 49-63	35, 73
c (MPa)	16.9	17.4
φ (°)	36.9	37.5

E – Elastic Modulus, σ_t – tensile strength, (σ_c, m_i) – H–B strength parameters, σ_{ci} – crack initiation stress, σ_{cd} – crack damage stress, c – cohesion, φ – angle of internal friction

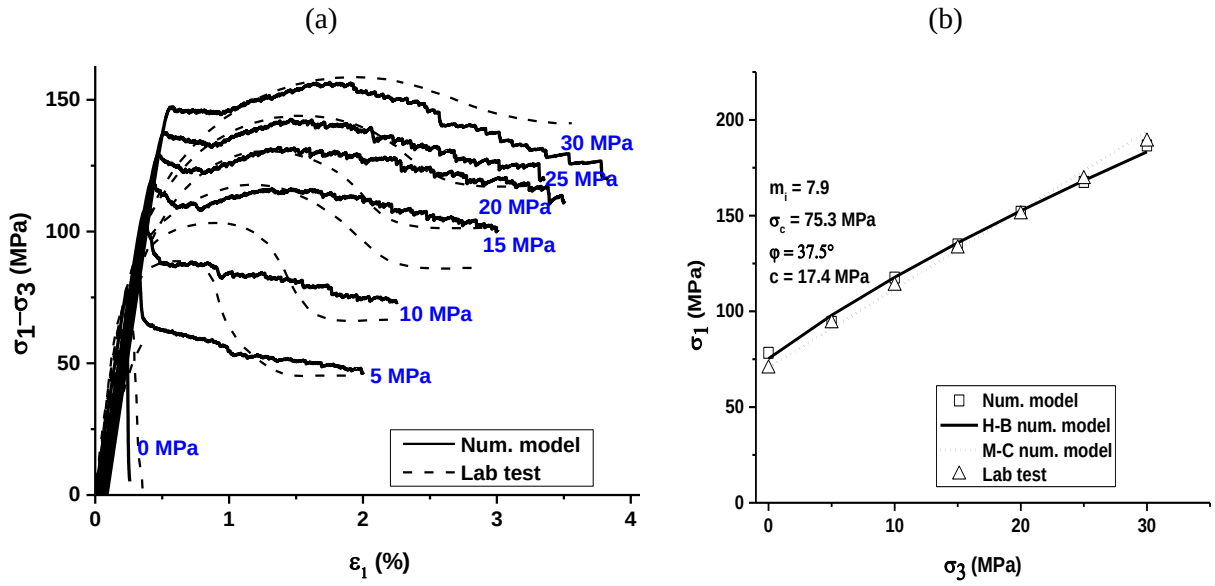

Figure 3-12 (a) Deviatoric stress–axial strain curves from laboratory triaxial test (dashed line) and numerical modeling (solid line) of Zhenping marble; (b) triaxial simulation results (unfilled square) of Zhenping marble fitted to H–B (solid line) and M–C (dotted line) strength envelopes. Laboratory test results are shown as unfilled triangles for comparison.

Compared with other hard rocks, marble exhibits a unique post-peak behavior, especially under high confining pressures. The post-peak curves of Zhenping marble exhibit a brittle to ductile transition with the increase of confinement. Close to perfect plastic deformation is evident when the confinement is above 30 MPa. The residual strength depends on φ_{fjr} which is the only frictional component that gets mobilized after all the flat jointed springs are broken. The magnitude of φ_{fjr} dictates the slopes of the post-peak stress–stain curves and the magnitude of the residual strength. An intelligent choice of φ_{fjr} should be made because the post-peak stress–stain curves change from brittle-ductile-plastic to a roughly bi-linear curve as φ_{fjr} increases. The sensitivity analysis conducted in Section 3.2.4 illustrates clearly that for a model with φ_{fjp} = 40° and φ_{fjr} = 10°, strain-hardening is observed when the confining pressure is higher than 10 MPa (Figure 3-6). This is due to high interlocking caused by infinitely stiff lattice particles. Use of a very high lattice resolution

might solve some of the issues but the computation time would be very long. Hence, employing low φ_{fjr} values is a reasonable trade-off to reduce the influence of interlocking on post-peak behavior. In this study, φ_{fjr} as low as 0° is used to simulate the $(\sigma_1–\sigma_3)–\varepsilon_1$ curve for the model under the confining pressure of 30 MPa.

3.4 Remarks

Because SRMTools is a relatively new software tool, an extensive sensitivity study is conducted to understand the influence of the lattice micro parameters on the macro-mechanical properties of intact rock in this Chapter. Using the results of the sensitivity analysis and the laboratory test results of Zhenping marble, a methodology is developed for the calibration of intact rock and the capability of SRMLab in the simulation of mechanical behavior of intact rock is validated.

The sensitivity study suggests that the strength of intact rock is dependent on the lattice size when the spherical shaped lattice structure is used and the dependence on lattice size is low for Voronoi-shaped lattice structure. Both strength (compressive and tensile) and angle of internal friction increases non-linearly with the increase of the radius multiplier. The intact rock's deformation modulus increases linearly with the increase of the lattice deformation modulus. Similarly, the intact rock compressive to tensile strength ratio increases linearly with the increase of the lattice compressive to tensile strength ratio. The angle of internal friction of the intact rock increases linearly with the increase of peak friction angle of the flat joint and the post-peak deformation behavior is controlled by the residual friction angle of the flat joint. Based on the results of the sensitivity study, a methodology is developed for the calibration of intact rock which is used in subsequent chapters.

Chapter 4

4 Crack evolution and mechanical behavior of pre-cracked rock under compression[2]

Pre-existing discontinuities occur in the forms of flaws, cracks, joints, bedding planes, shears, faults, etc. in rock masses. These discontinuities provide favorable conditions for crack propagation along intact rock bridges and significantly influence the mechanical properties of jointed rock masses. A detailed understanding of crack initiation, propagation, and coalescence in jointed rock can not only benefit in the characterization of rock mass but also aid in the geotechnical design of stable rock slopes, tunnels, and mine pillars in jointed rock masses.

Previous experimental and numerical studies on pre-cracked rocks and rock-like materials demonstrate that there is a good correlation between the crack angle (α), ligament angle (β), crack length ($2a$), ligament length ($2b$) (Figure 2-11), and the number of cracks (n) to the mechanical properties of cracked rocks. However, these tests were performed on specimens with cracks having planar surfaces. In nature the crack surfaces in a rock mass have waviness. The crack evolution mechanism of a cracked rock with rough crack surfaces could be different compared with that of a cracked rock with planar crack surfaces and hence manifests different mechanical response under compression. Although the influence of joint roughness on the strength and deformability of joint has been investigated using laboratory direct shear tests, more attention is required to understand the influence of these non-planar cracks on crack evolution and mechanical properties of jointed

[2] Originally published as: Bastola, S. and Cai, M. (2019) 'Investigation of mechanical properties and crack propagation in pre-cracked marbles using lattice-spring-based synthetic rock mass (LS-SRM) modeling approach', *Computers and Geotechnics*, 110, pp. 28–43

rocks and rock masses. The influence of persistent undulate crack on the progressive failure of a pre-cracked rock was investigated using contours of a stress concentration factor in FLAC^{3D} (Guo & Qi, 2015); however, this continuum modeling approach does not explicitly capture real crack initiation and propagation.

In this Chapter, crack initiation, propagation, and coalescence at or near the pre-existing open crack of a cracked marble are investigated under unconfined and confined compressions using the LS-SRM modeling approach. LS-SRM models are built using SRMTools because it allows the explicit representation of pre-existing discontinuities (both planar and non-planar) and the crack evolution process under external loading. Details on lattice spring method and SRMTools can be found in Cundall (2011), Damjanac et al. (2016), and Bastola & Cai (2018b, 2019) (see Section 2.5.3). Models are calibrated by comparing the simulation results with the laboratory uniaxial compression test results reported in Yang et al. (2009) on pre-cracked marble with planar cracks. Then the calibrated model parameters are used to simulate unconfined and confined compression on the models with non-planar cracks of different configurations. In the following discussion, model development is described in Section 4.1. Calibrations of intact and pre-cracked marbles are performed in Sections 4.2 and 4.3, respectively. The modeling results are discussed in Sections 4.4–4.6 and concluding remarks are presented in Section 4.7.

4.1 Model development

Eight pre-cracked LS-SRM models of marble are generated using the information reported in Yang et al. (2009). The synthetic marble models are 100 mm × 50 mm × 50 mm in dimension and contain 38,784 lattice nodes that are connected to each other by 192,436 lattice springs. Non-persistent and planar cracks are introduced into the intact rock model to mimic the geometry of the cracked

rock specimens used in the laboratory test. The dimension and location of the cracks and nomenclature of the specimens are based on the information given in Yang et al. (2009). Schematics of Type B and Type J models are shown in Figure 2-11 to illustrate the crack geometry in the pre-cracked marble specimens, in which $2a$ is the crack length, $2b$ is the ligament length, α is the crack angle, and β is the ligament angle. Other model types are shown in Figure 4-1.

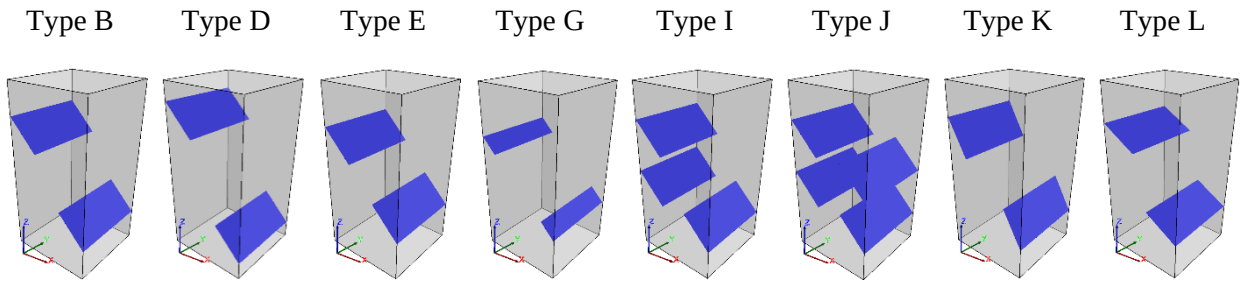

Figure 4-1 LS-SRM models of pre-cracked marbles with different crack configurations of planar cracks based on the information from Yang et al. (2009).

Table 4-1 Crack patterns in the pre-cracked marbles based on Yang et al. (2009)

Model description	α (°)	β (°)	$2a$ (mm)	$2b$ (mm)	N
Type B	45	61	24	33	2
Type D	45	70	24	48	2
Type E	45	48	24	24	2
Type G	45	34	16	33	2
Type I	45	61	24	33	3
Type J	45	61	24	33	4
Type K	30	38	24	33	2
Type L	60	75	24	33	2

α – crack angle, β – ligament angle, $2a$ – crack length, $2b$ – ligament length, N – the number of cracks.

As shown in Figure 4-1 and Table 4-1, all the specimens have a crack length of 24 mm except for the Type G specimen, which has a crack length of 16 mm. All the specimens have a crack angle of 45° except for the Type K (30°) and Type L (60°) models, and all the specimens have two cracks except for Type I (three cracks) and Type J (four cracks). All the cracks shown in Figure 4-1 have planar surfaces.

To investigate the influence of non-planar cracks on the mechanical properties and crack evolution, all the cracks in the cracked marble specimens shown in Figure 4-1 are substituted by non-planar cracks with a joint roughness coefficient (*JRC*) of 18 to 20 (Barton & Choubey, 1977) and the models are shown in Figure 4-2. Enlarged images of Model J with planar and non-planar cracks are illustrated in Figure 4-3.

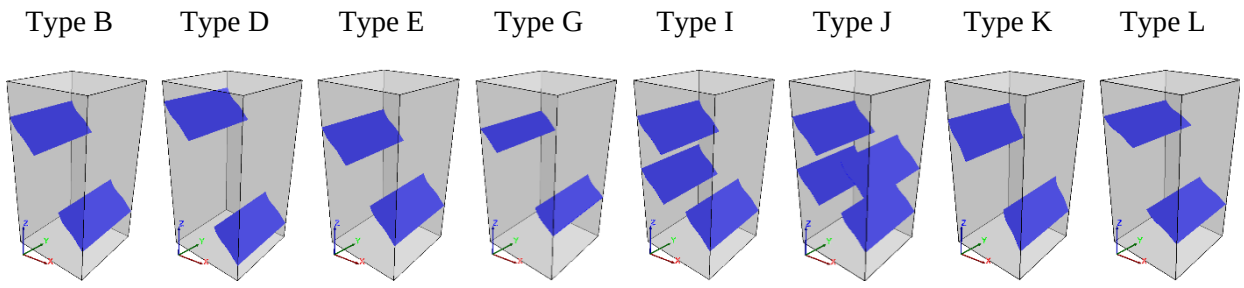

Figure 4-2 LS-SRM models of pre-cracked marbles with different non-planar crack configurations.

The roughness of the non-planar surface corresponds to Barton's *JRC* index of 18 to 20 (Figure 4-4) and are generated using MoFrac (see Section 2.5.4.2). Using the 2D traces, 3D triangulated meshes are generated in MoFrac using the semi-deterministic approach. A 2D trace is extruded to the third dimension while keeping the same waviness of the 2D profile. Mechanical properties and spatial locations of cracks are specified when importing the cracks into the SRMTools during model development. Non-planar crack surfaces generated in MoFrac differ with each other for each realization. To ensure that the surface geometry of the non-planar crack does not change,

mesh simplification and rotation are performed using third-party software such as Paraview and MeshLab. The flow chart for the generation of a single non-planar crack is shown in Figure 4-5.

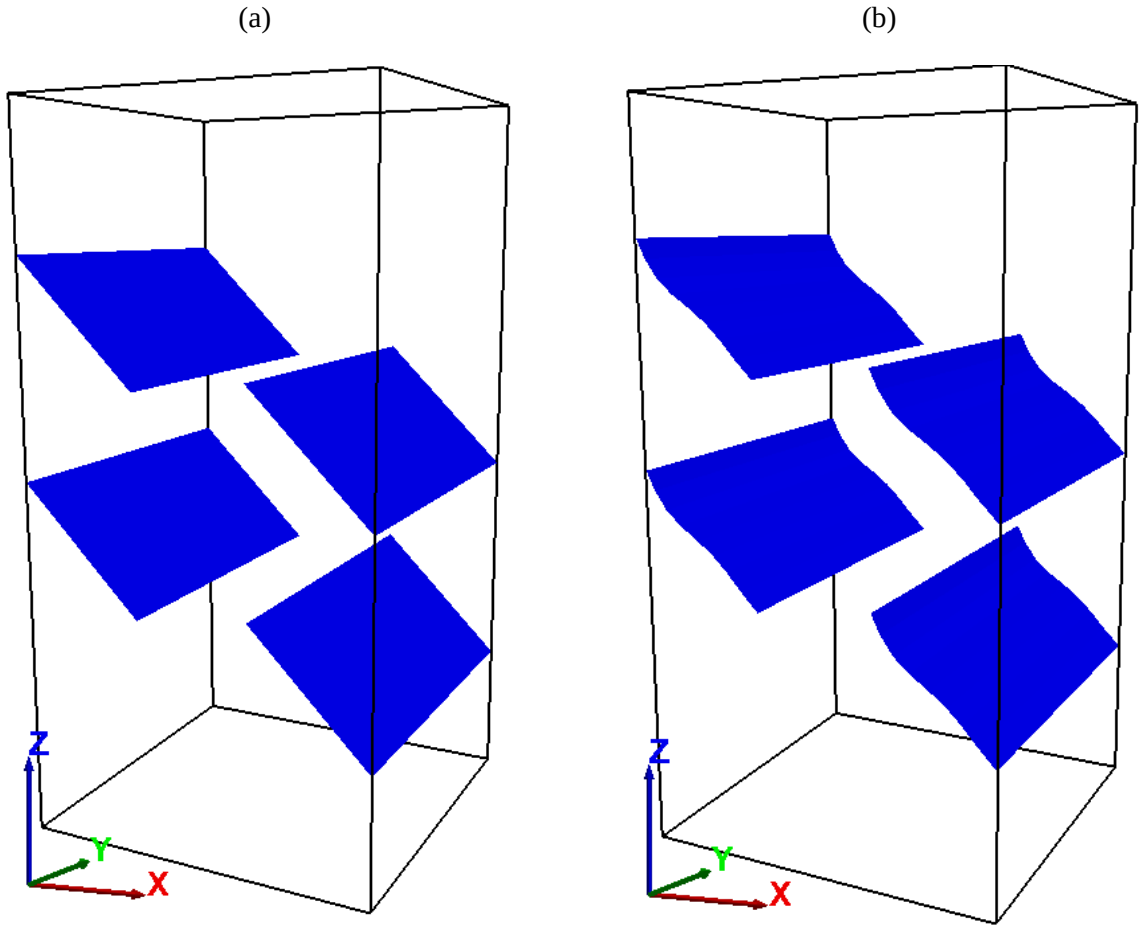

Figure 4-3 Enlarged Model J with (a) planar and (b) non-planar cracks with 2*a* = 24 mm.

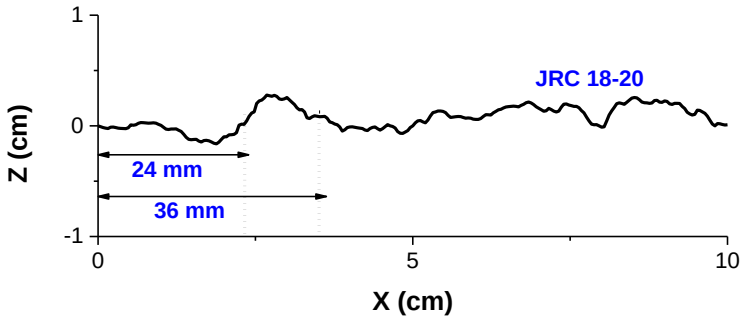

Figure 4-4 Joint surface roughness profile used to generate non-planar crack surface corresponding to the *JRC* index of 18 to 20, modified after Barton & Choubey (1977) and Li & Huang (2015).

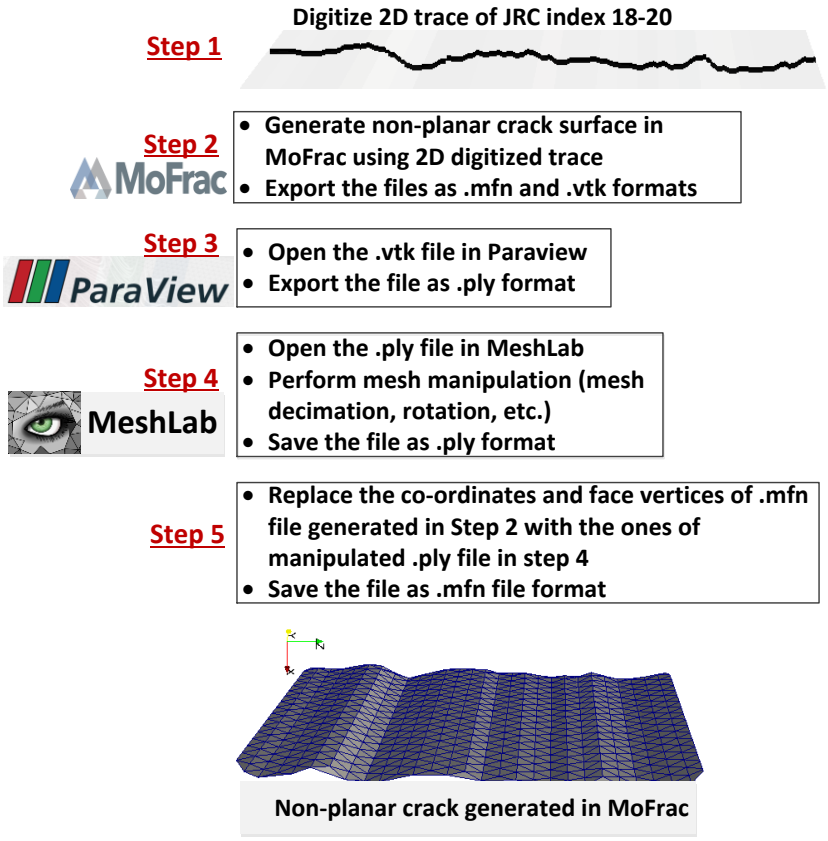

Figure 4-5 Procedure for generating a single non-planar crack surface.

The models are loaded axially in the displacement control mode (constant velocity). The optimum velocity of loading is established by performing a series of unconfined compressive strength (*UCS*) simulations with different displacement loading rates. Vertical and lateral confining forces are applied simultaneously during initial loading in triaxial compression simulation. Once the confining pressure reaches the target value, it is kept constant and the vertical force is increased until the computation is terminated by the user. Vertical force, vertical displacement, lateral displacement, and the number of cracks is recorded for all numerical experiments. Test results reported in Yang et al. (2009) are used to calibrate the LS-SRM models under unconfined compression only. Then the calibrated model parameters are used to perform compression simulations on pre-cracked marbles with planar or non-planar cracks. Because the experimental

studies used specimens with open cracks, the numerical simulations are also performed using through-going open cracks along the y-axis (Figure 4-1 and Figure 4-2). Through-going cracks whose ends are visible on the outer surface of the specimen are called open cracks and the ones that are enclosed inside the specimen and the crack ends cannot be seen from outside are called closed cracks. The fracture mechanisms for open and closed cracks are similar; the only difference is that the stresses at which cracking (i.e. crack initiation and coalescence) occurs are higher for rocks with closed cracks than for the ones with open cracks (Park, 2008).

4.2 Calibration of intact marble

Calibration of the model parameters of the intact marble is carried out using the approach proposed in Bastola & Cai (2018b) and Figure 3-8 by performing a series of *UCS* simulations and comparing the modeling results with the laboratory test results. Based on the laboratory test results reported in Yang et al. (2009), the intact rock model is calibrated to the *UCS* of 89.2 MPa (Figure 4-6) and the deformation modulus (*E*) of 35.9 GPa, which are close to the target laboratory *UCS* and *E* values of 83.5 MPa and 36.0 GPa, respectively. The axial stress–axial strain curves for intact marble under unconfined compression during laboratory test and numerical modeling do not coincide with each other because of the initial curvature due to the initial crack closure in laboratory specimens. The calibrated model parameters (Table 4-2) are used for the compression simulations of the intact and the cracked marbles under unconfined and confined loading conditions. The loading rate and the lattice size used in all simulations are 0.01 m/s and 0.2 cm, respectively. Spherical lattice structure with flat joint contact is used.

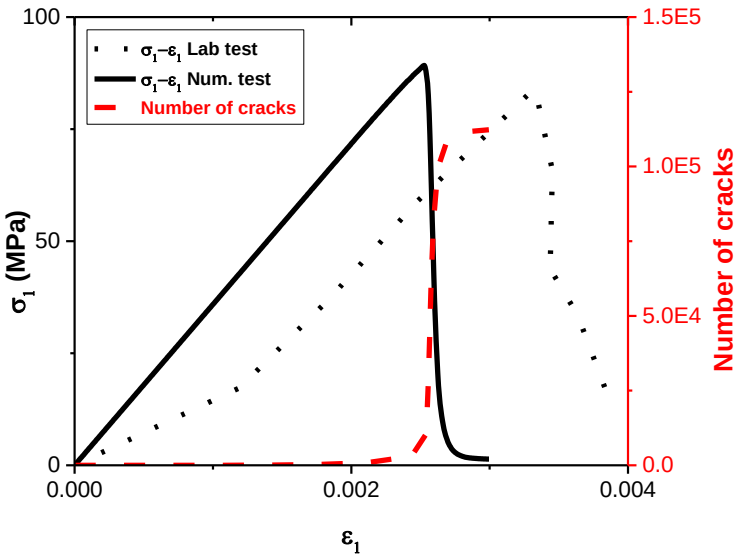

Figure 4-6 Axial stress–axial strain & axial strain–number of cracks plot for intact marble model under unconfined compression. Axial stress–axial strain plot for the laboratory test is shown as a dotted line.

Table 4-2 Input lattice parameters for the simulation of laboratory test results of intact marble

Model parameters	Value
E_{mic} (GPa)	37
σ_{cmic} (MPa)	64
$(\sigma_t)_{mic}$ (MPa)	5.4
ρ (kg/m^3)	2700
Porosity (%)	2
φ_{fjp} (°)	35
φ_{fjr} (°)	0
Radius multiplier	0.9

E_{mic} – lattice elastic modulus, σ_{cmic} – lattice compressive strength, $(\sigma_t)_{mic}$ – lattice tensile strength, ρ – rock density, φ_{fjp} – peak friction angle of flat joint, φ_{fjr} – residual friction angle of flat joint

4.3 Sensitivity of joint stiffness & calibration of pre-cracked marble

Mechanical properties of discontinuities such as joint friction angle and joint stiffness influence the mechanical properties of jointed rocks. In the calibration process, it is important to quantify the influence of joint properties on the macro-mechanical properties of cracked rocks. The calibration of cracked rock is performed using the calibration approach (Figure 4-7) developed for the jointed rock after the intact rock is calibrated using the procedure outlined in Section 3.3.

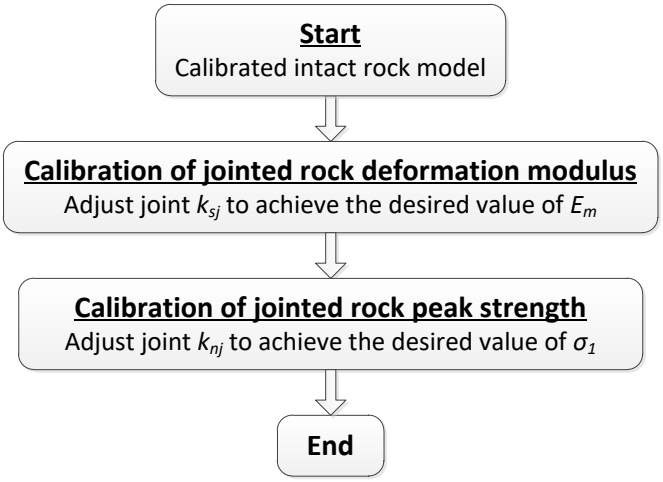

Figure 4-7 Flowchart illustrating the procedure for calibrating the mechanical properties of jointed rock for LS-SRM models with flat joint contacts.

To this end, uniaxial compression simulations are performed on the Types K and L specimens with two cracks of variable joint stiffness. These specimens are selected because they encompass all the range of crack angles (30°–60°) investigated in the laboratory experiments. Sensitivity analyses are conducted at a joint shear stiffness (k_{sj}) range of 10–100 GPa/m and a joint normal stiffness (k_{nj}) range of 100–1000 GPa/m. The crack friction angle (φ_j) is set to 30°. Because the cracks are filled with gypsum, crack tensile strength and crack cohesion are set to 1 MPa and 0.5 MPa, respectively. The crack dilation angle is set to zero.

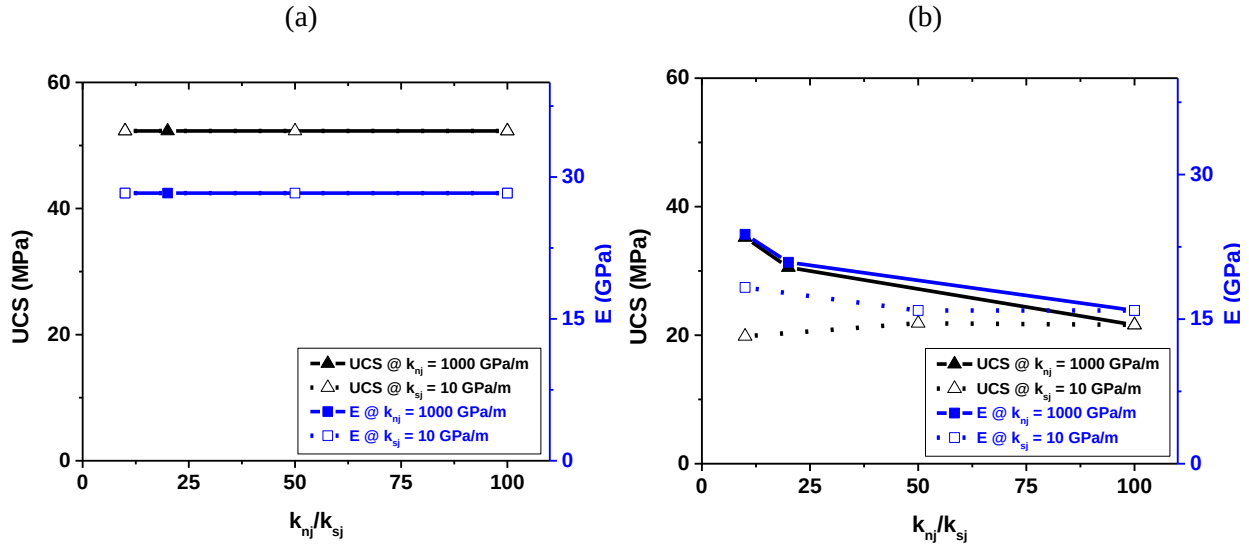

Figure 4-8 Influence of k_{nj}/k_{sj} on *UCS* and *E* for (a) Type K and (b) Type L cracked marble.

The sensitivity study results suggest that the mechanical properties of the cracked models are highly influenced by the magnitude of joint stiffness if $\alpha \geq 60°$. *E* and *UCS* depend on the k_{nj}/k_{sj} ratio for the Type L model (Figure 4-8b); however, *E* and *UCS* are independent of the k_{nj}/k_{sj} ratio for the Type K model (Figure 4-8a). The reason is that with the decrease of α, the intact rock bridge between the internal tips of the cracks increases, increasing the influence of the intact rock and reducing the influence of the joint properties on the overall mechanical response of the cracked rocks. The values of k_{nj} and k_{sj} that result in *E* and *UCS* values of the cracked models that are reasonably close to their experimental counterparts are adopted for the numerical modeling. Based on the results of this sensitivity analysis, k_{nj} and k_{sj} values of 100 GPa/m and 10 GPa/m, respectively, are used for subsequent modeling in Sections 4.4, 4.5, and 4.6.

4.4 Mechanical behavior of pre-cracked marble with planar cracks

Uniaxial compression simulations are performed on the eight cracked marble models with non-persistent planar cracks. Calibrated mechanical properties for pre-cracked marbles are adopted

based on the results of the detailed sensitivity study performed in Section 4.3. The simulation results, summarized in Table 4-3 along with the laboratory test results (target), suggest that the geometry of the cracks has a large influence on *UCS* or σ_c and *E* of the cracked marble.

Table 4-3 Comparison of mechanical properties of intact and cracked marbles from laboratory test (target) in Yang et al. (2009) and numerical modeling

Model	Modeled value		Target value	
	σ_c (MPa)	*E* (GPa)	σ_c (MPa)	*E* (GPa)
Intact	89.2	35.9	83.5	36.0
Type B	32.2	22.2	50.7	27.7
Type D	30.0	22.0	31.3	22.5
Type E	34.6	22.5	41.5	27.7
Type G	61.2	32.1	66.7	35.5
Type I	30.5	21.5	35.4	24.6
Type J	27.9	20.3	16.8	14.1
Type K	52.3	28.3	57.1	30.1
Type L	19.8	18.2	15.2	15.9

The *UCS* and *E* of the cracked marbles decrease with the increase of crack length (2*a*), crack angle (α), ligament angle (β), ligament length (2*b*), and the number of cracks. For instance, The Type G cracked marble has the shortest 2*a* among all the specimens and consequently, it has the highest σ_c (61.2 MPa) and *E* (32.1 GPa). Similarly, the Types I and J specimens have three and four cracks, respectively, and they have lower σ_c and *E* when compared with the specimens with two cracks.

This could be attributed to the localized failure due to the proximity of the cracks to the loading end of the specimens. The Type L cracked specimen, which has a α of 60°, has lower σ_c and E compared with other cracked specimens. The numerical values of σ_c decrease with the increase of the 2b and β. This is due to the reduction of the extent of the rock bridge along the direction of applied principal stress with the increase of 2b and β. Among the specimens with two cracks (Types B, D, and E) with equal crack lengths of 24 mm, the Type D specimen has the lowest σ_c and E because it has the highest values of β and 2b among the three specimens. The discrepancies between the laboratory test results (Yang et al., 2009) and the numerical simulation results (see Table 4-3) could be due to the inherent anisotropy and heterogeneity associated with the laboratory specimens, damage to the specimens during sample preparation, etc.

Differential stress–axial strain relations and crack initiation, propagation, and coalescence under both unconfined and confined (10 MPa) compression conditions at five axial strains ($\varepsilon_{0.25peak}$, $\varepsilon_{0.5peak}$, $\varepsilon_{0.75peak}$, ε_{peak}, $\varepsilon_{1.1peak}$) for all cracked specimens with planar cracks are shown in Figure 4-9. The stress–strain curves derived from the LS-SRM model simulation (shown as a solid line) of cracked marbles with planar cracks under unconfined compression are reasonably close to the ones obtained from the laboratory tests (shown as dotted line).

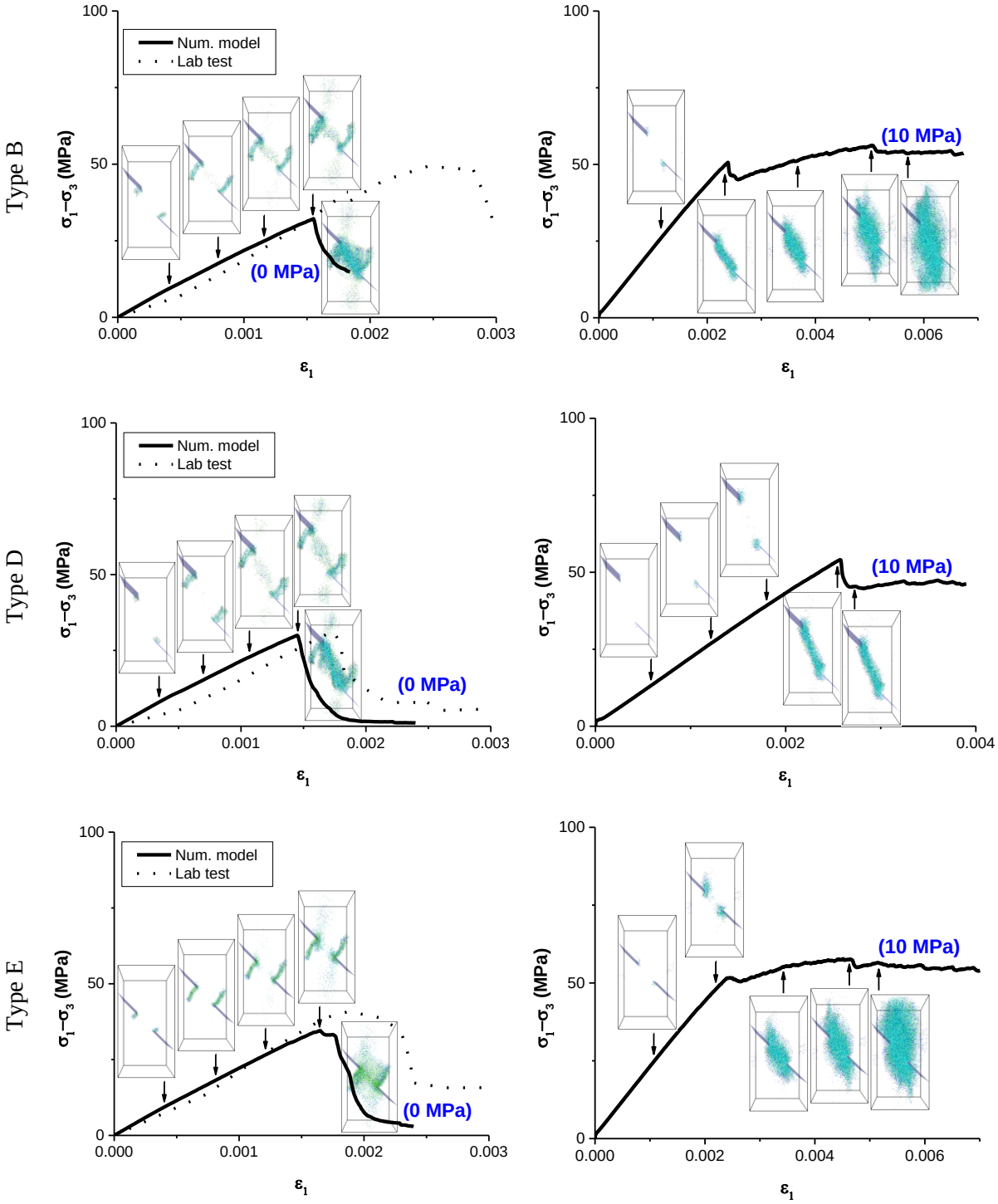
Type B
Type D
Type E
Num. model
Lab test
(0 MPa)
(10 MPa)
σ1–σ3 (MPa)
ε1
0
50
100
0.000
0.001
0.002
0.003
0.004
0.006

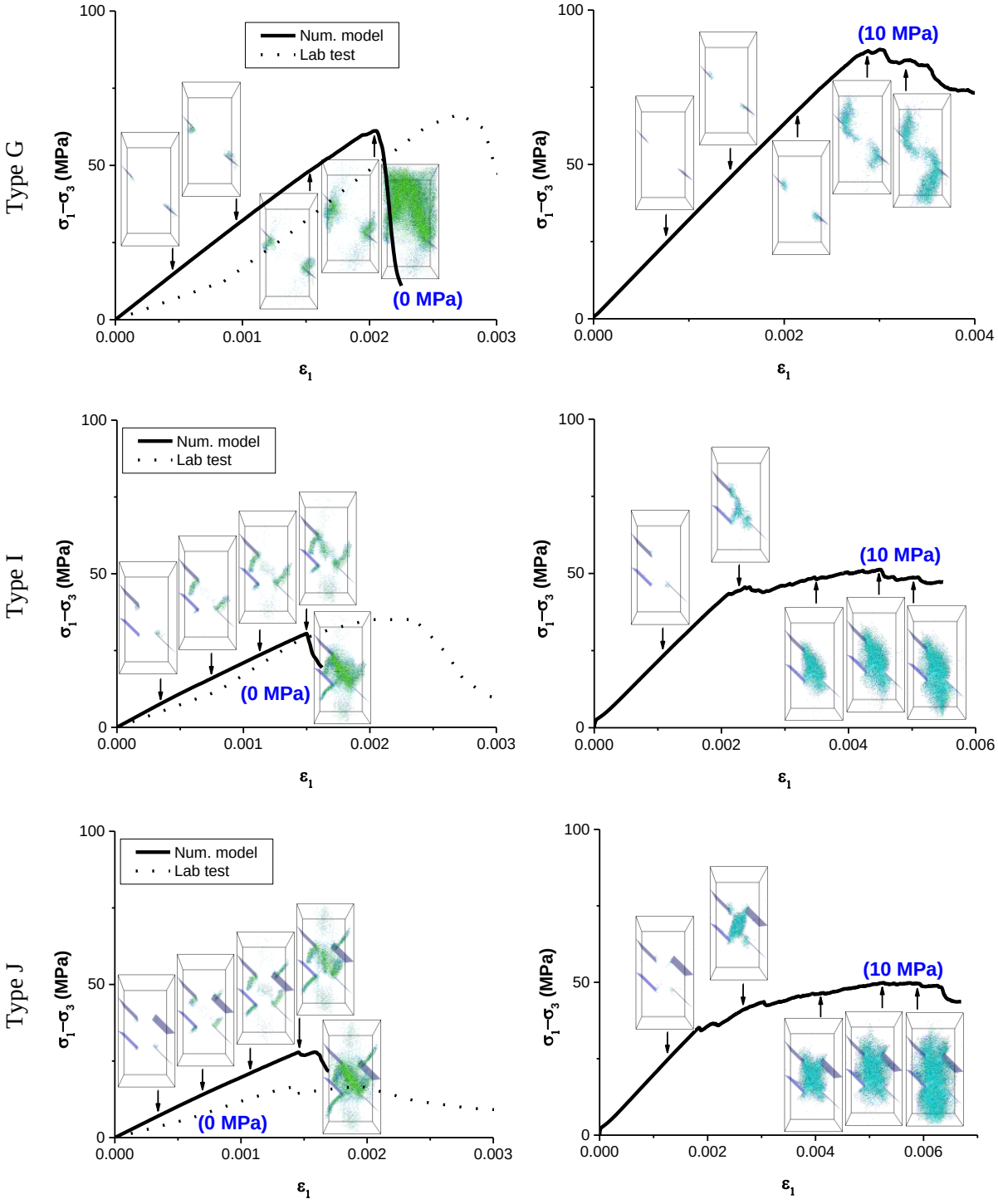
Type G
Num. model
Lab test
(0 MPa)
(10 MPa)
Type I
Num. model
Lab test
(0 MPa)
(10 MPa)
Type J
Num. model
Lab test
(0 MPa)
(10 MPa)
σ1–σ3 (MPa)
ε1

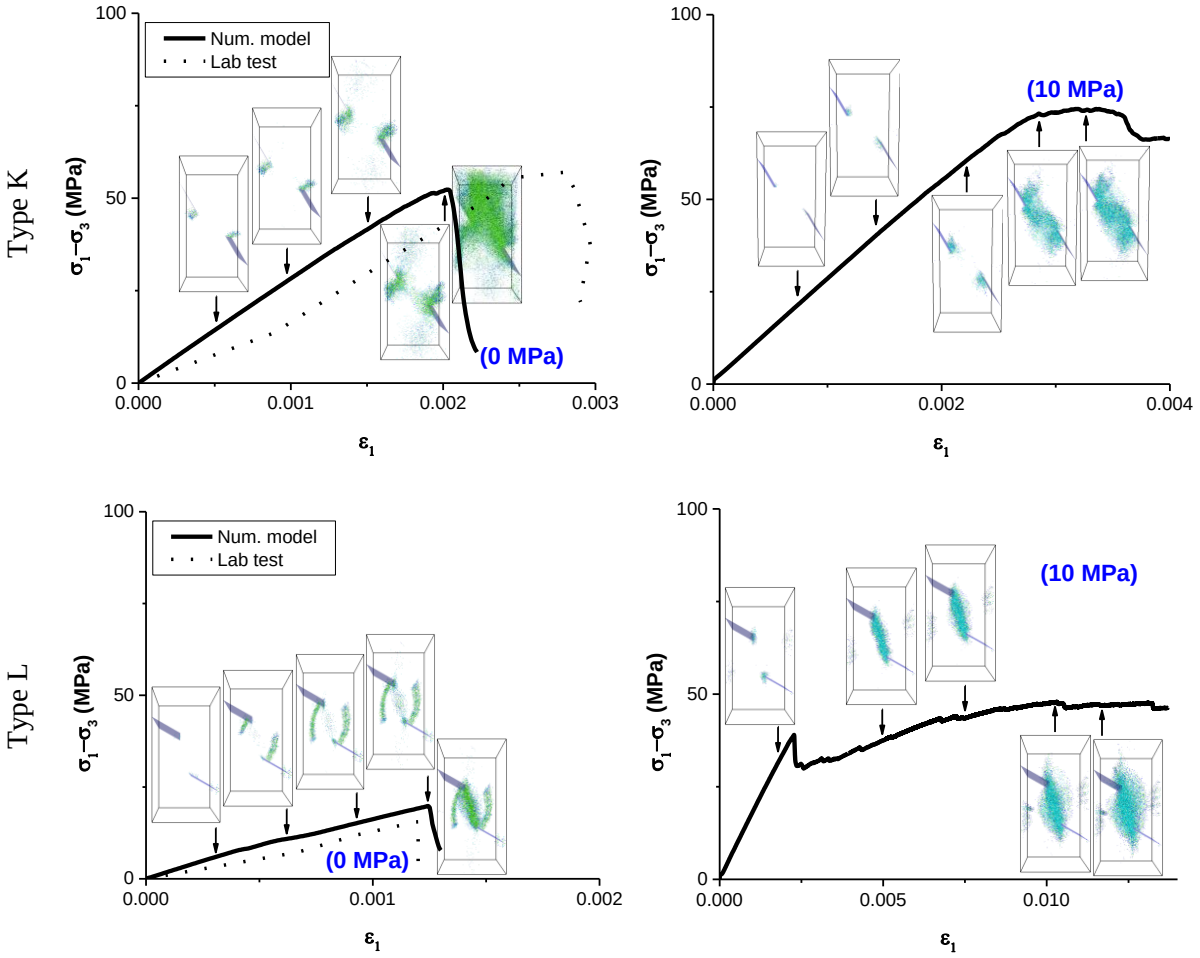

Figure 4-9 Illustration of crack propagations in cracked synthetic marbles with planar cracks of different configurations at different axial strains along the differential stress–axial strain plots under unconfined compression (left) and confined compression at 10 MPa (right). Laboratory test results of the cracked marble under unconfined compression are shown as a dotted line.

For the pre-cracked specimens under the unconfined loading condition (σ_3 = 0 MPa), five types (Types 1–5) of cracking mechanisms are observed (Figure 4-10). In terms of the types of cracking, Types 1–2 are tensile, Types 3–4 are shear, and Type 5 is the mix of tensile and shear.

In Type 1 cracking, tensile wing cracks initiate simultaneously from the internal tips of the pre-existing cracks along the orthogonal direction of the crack angle and then along the major principal stress direction and there is no crack coalescence (Figure 4-10a). Type 2 cracks develop during the

later stage of loading (mostly in the post-peak deformation stage); thus, they are not as clearly visible as Type 1 cracks. The relative size of the micro-cracks to that of the specimen also clouds the existence of Type 2 crack. For instance, the size of micro-cracks was reduced to 20% of their original size for clarity, and this could have also contributed to indistinctness of Type 2 cracks. In Type 2 cracking, anti-wing cracks grow from the tips of the pre-existing cracks along the direction of the major principal stress but they are in the opposite direction compared with the Type 1 cracks and there is no crack coalescence either (Figure 4-10b). In Type 3 cracking, shear cracks propagate towards each other and finally coalesce (Figure 4-10c). In Type 4 cracking, shear cracks initiate from the internal tips of the pre-existing cracks in the direction of their inclination (Figure 4-10d). Type 5 secondary cracks initiate randomly from the pre-existing cracks and they may be either tensile or shear (Figure 4-10e). Type 5 cracking occurs at the later stage of crack evolution (i.e. usually after Type 1–4 cracks occur).

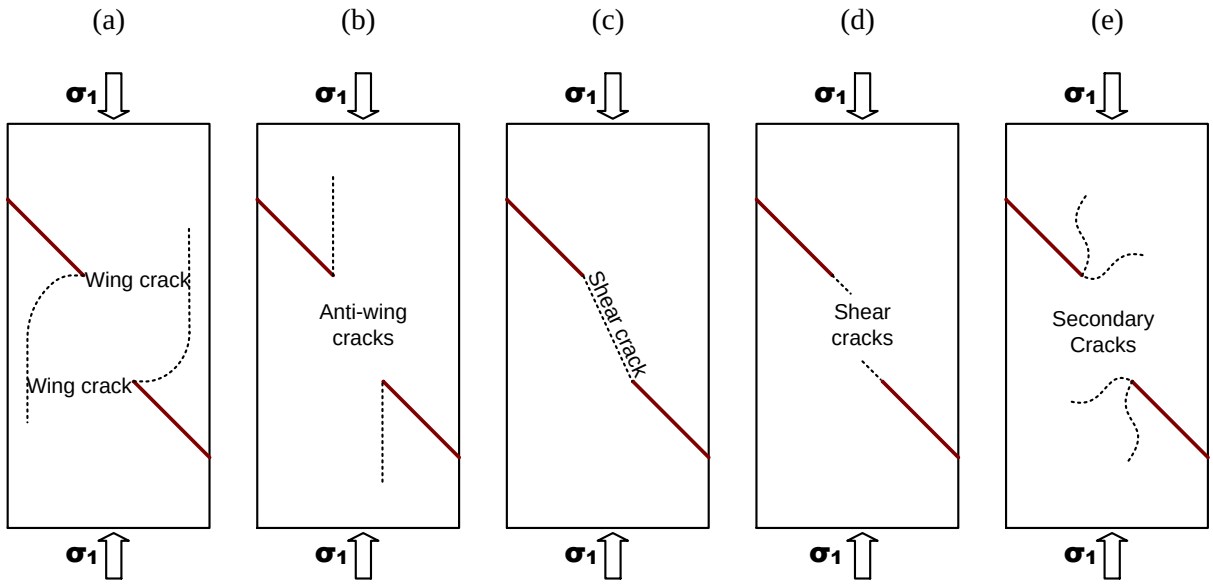

Figure 4-10 Types of cracking pattern (shown as dots) observed in this study (a) Type 1 (b) Type 2 (c) Type 3 (d) Type 4 (e) Type 5.

The crack coalescence patterns of the cracked rocks under unconfined compression result from a combination of axial splitting and shear failure. Based on the observed cracking mechanisms, the crack initiation and coalescence processes for each type of cracked marble can be attributed to a combination of these types of cracking under uniaxial compression. For instance, the cracking patterns in Types B, D, E, and L models are the combination of Types 1–4 cracks. The cracking patterns in Types G and K models are dominated by Type 2 anti-wing cracking leading to axial splitting failure of the specimen. The cracking patterns of Types I and J models are characterized by the coalescence of Types 1–5 cracks. The observed crack coalescence mechanisms are in agreement with those observed in Wong & Einstein (2009a) and Yang et al. (2009) (see Figure 2-9, Figure 2-10, and Figure 2-12).

The crack evolutions of these cracked marbles are also recorded under confined compression condition at a confining pressure of σ_3 = 10 MPa (Figure 4-9). As expected, under the confined compression condition, the growth of tensile wing cracks is suppressed due to the confining pressure and the dominant failure mode is the coalescence of Type 3 and Type 4 shear cracks and Type 5 random secondary cracks. Some lateral tensile cracking is observed in Type L marble (Figure 4-9) on the opposite side of the pre-existing cracks under confinement. These lateral cracks initiate when the applied axial stress is around 50% of UCS and are oriented perpendicular to the major principal stress and parallel to the minimum principal stress.

4.5 Mechanical behavior of pre-cracked marble with non-planar cracks

Both unconfined and confined (σ_3 = 10 MPa) compression simulations are performed on the eight cracked specimens with non-planar cracks to study the influence of non-planar cracks on crack propagation and mechanical properties of cracked rocks. All the model parameters are the same as

those of the models with planar cracks except that the planar cracks are replaced with the non-planar ones (see Section 4.1).

Lattice size could influence the strengths of both the cracked marble and the intact marble. A study conducted by Bastola & Cai (2018b) suggests that the lattice resolution influences the strength of intact Zhenping marble. Hence, a sensitivity of lattice size on peak strength is conducted for both the intact (Figure 4-11a) and the cracked marbles (Type B and Type J) with non-planar cracks (Figure 4-11b&c) for the lattice sizes of 4, 3, 2, 1, and 0.75 mm. The results show that the normalized peak strength (Figure 4-11e) decreases with the decrease of lattice size up to the lattice size of 1 mm and then increases slightly for the lattice size of 0.75 mm. Although there is some influence of the lattice resolution on the peak strength of the pre-cracked marble with non-planar cracks, the relative difference between the normalized peak strengths is small for the lattice sizes of 2 and 0.75 mm. This is illustrated with axial stress–axial strain curves and the lattice size sensitivity analysis plots (Figure 4-11a,b&c). The time required for the simulation of the cracked marble models are 0.5, 1, 12, 48, and 168 hours for the models with the lattice sizes of 4, 3, 2, 1, and 0.75 mm, respectively; The estimated time for the cracked marble model with a lattice size of 0.5 mm is approximately 1 month (the run was aborted due to the extremely long runtime). The ideal model would be the one that can represent the rock to the microscopic scale; however, there is a significant computational expense associated with it. Thus, as a preliminary parametric study of the influence of non-planar cracks on the model response, the lattice size of 2 mm is adopted as a reasonable trade-off between the lattice resolution and computation time.

(a)

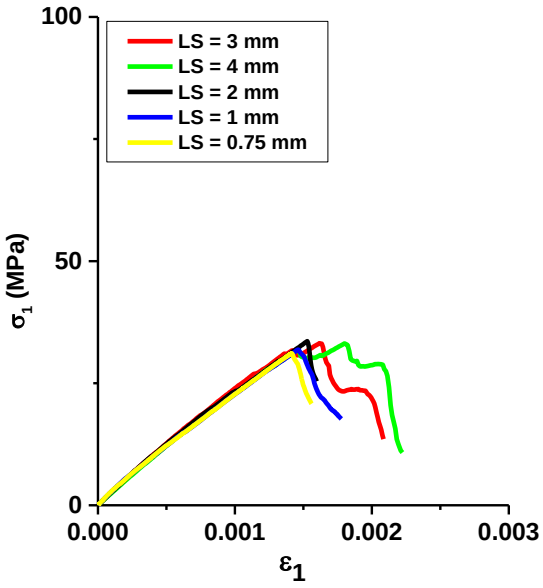
LS = 3 mm
LS = 4 mm
LS = 2 mm
LS = 1 mm
LS = 0.75 mm
σ1 (MPa)
ε1
100
50
0
0.000
0.001
0.002
0.003

(b)

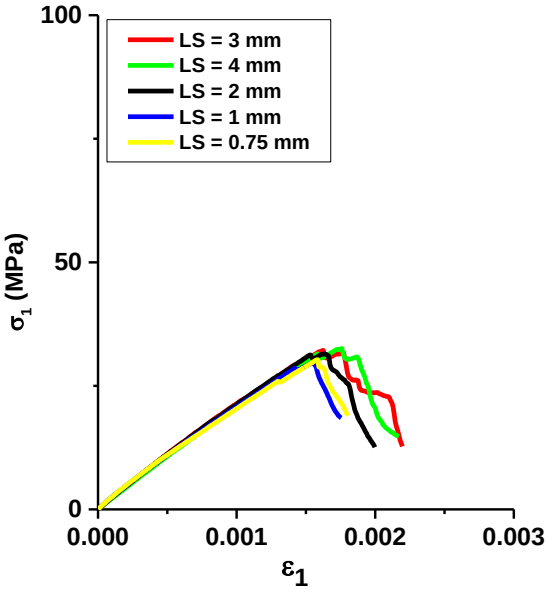
LS = 3 mm
LS = 4 mm
LS = 2 mm
LS = 1 mm
LS = 0.75 mm
σ1 (MPa)
ε1
100
50
0
0.000
0.001
0.002
0.003

(c)

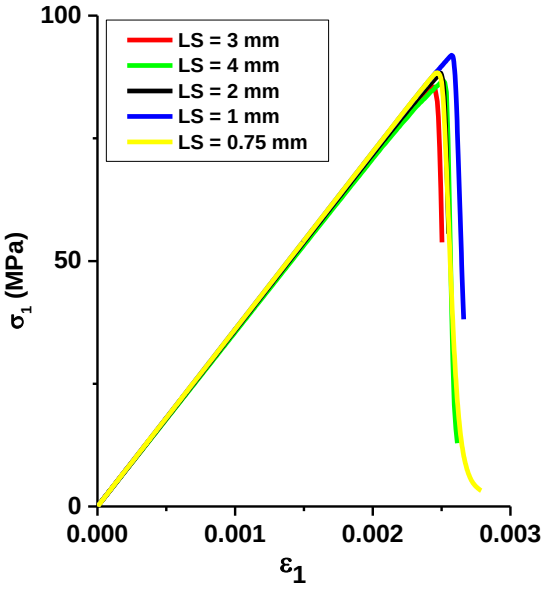
LS = 3 mm
LS = 4 mm
LS = 2 mm
LS = 1 mm
LS = 0.75 mm
σ1 (MPa)
ε1
100
50
0
0.000
0.001
0.002
0.003

(d)

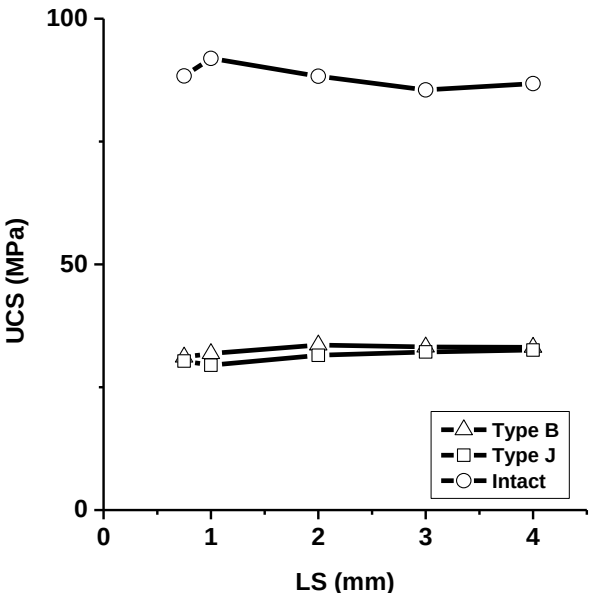
Type B
Type J
Intact
UCS (MPa)
LS (mm)
100
50
0
0
1
2
3
4

(e)

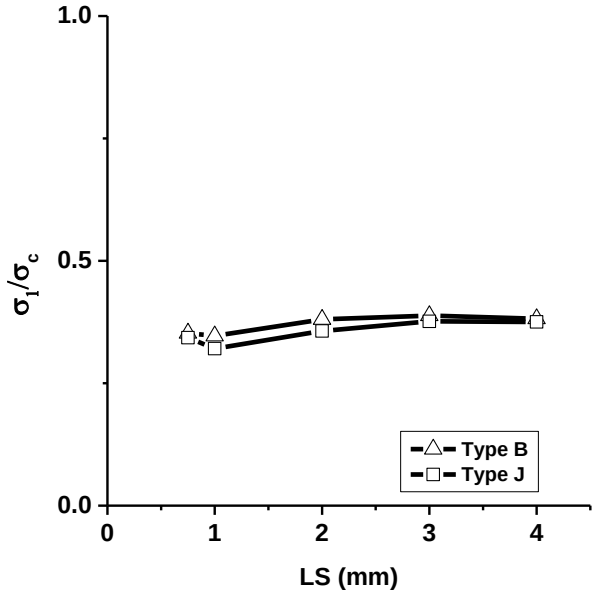

Figure 4-11 (a) Axial stress–axial strain curves for intact marble with different lattice size; (b) Axial stress–axial strain curves for Type B marble with non-planar cracks and with different lattice size; (c) Axial stress–axial strain curves for Type J marble with non-planar cracks and with different lattice size; (d) Influence of lattice size on the peak strength of intact and cracked marbles with non-planar cracks; (e) Influence of lattice size on the normalized peak strength of cracked marbles with non-planar cracks.

Differential stress–axial strain relations and crack evolutions at five axial strains ($\varepsilon_{0.25peak}$, $\varepsilon_{0.5peak}$, $\varepsilon_{0.75peak}$, ε_{peak}, $\varepsilon_{1.1peak}$) are shown in Figure 4-12. The numerical modeling results show that the peak strengths and the deformation moduli of the cracked marbles with non-planar cracks are only slightly higher than the corresponding ones with planar cracks except for Type L marble. This is due to the low crack persistence ($2a \leq 24$ mm relative to the 50 mm width of the specimens) used in the study. The influence of crack persistence on the mechanical response of the cracked marbles is investigated in Section 4.6. In the case of Type L marble with non-planar cracks, its peak strength under 10 MPa of confining pressure is about 43% higher than that for the model with planar cracks because of the high crack angle ($\alpha = 60°$).

For the models with non-planar cracks, complex crack evolution is observed because of the localized stress concentration and damages on the wavy surfaces of the cracks. In addition to the failure modes observed in the cracked marbles with planar cracks (Figure 4-10), secondary cracks propagate from the wavy section of the pre-existing cracks in the models with non-planar cracks.

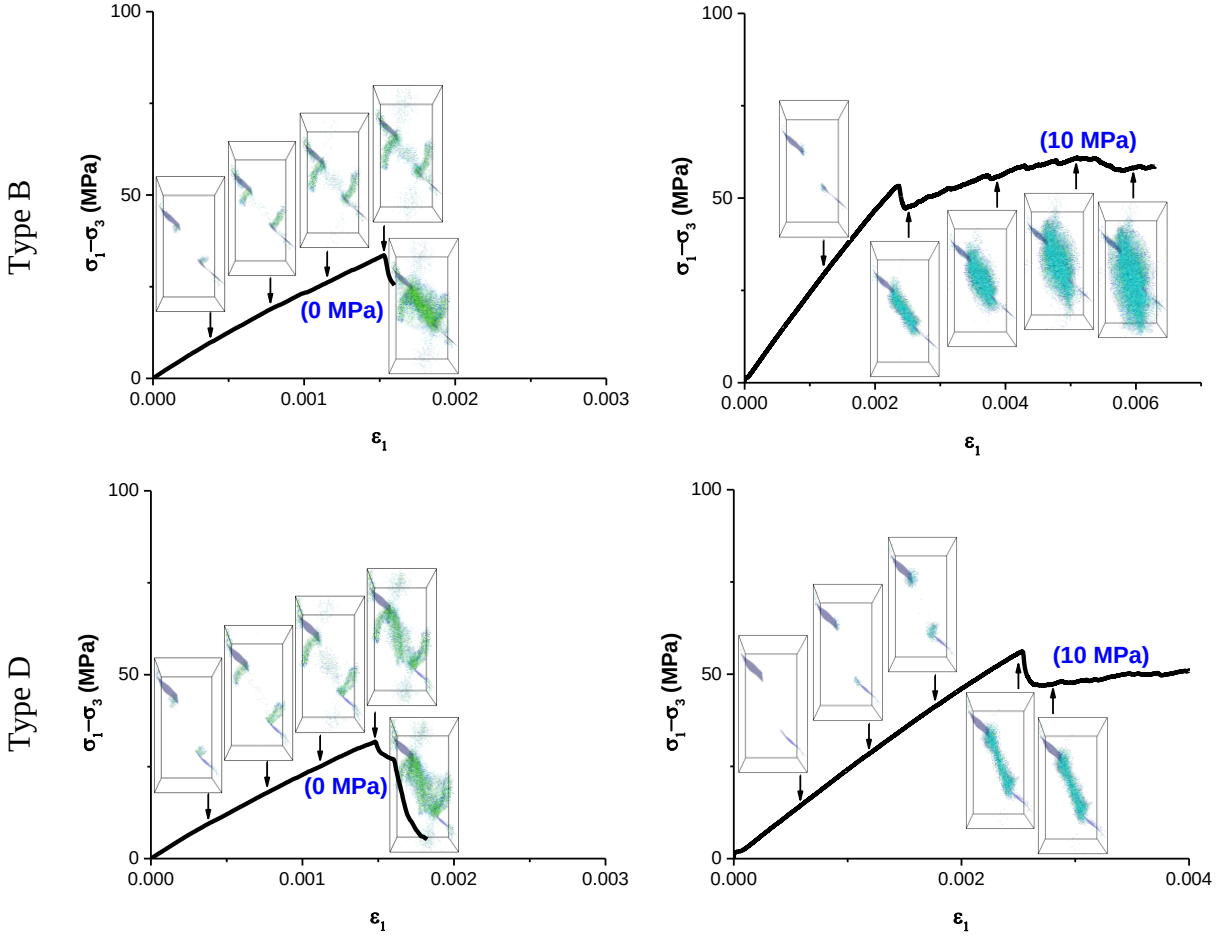

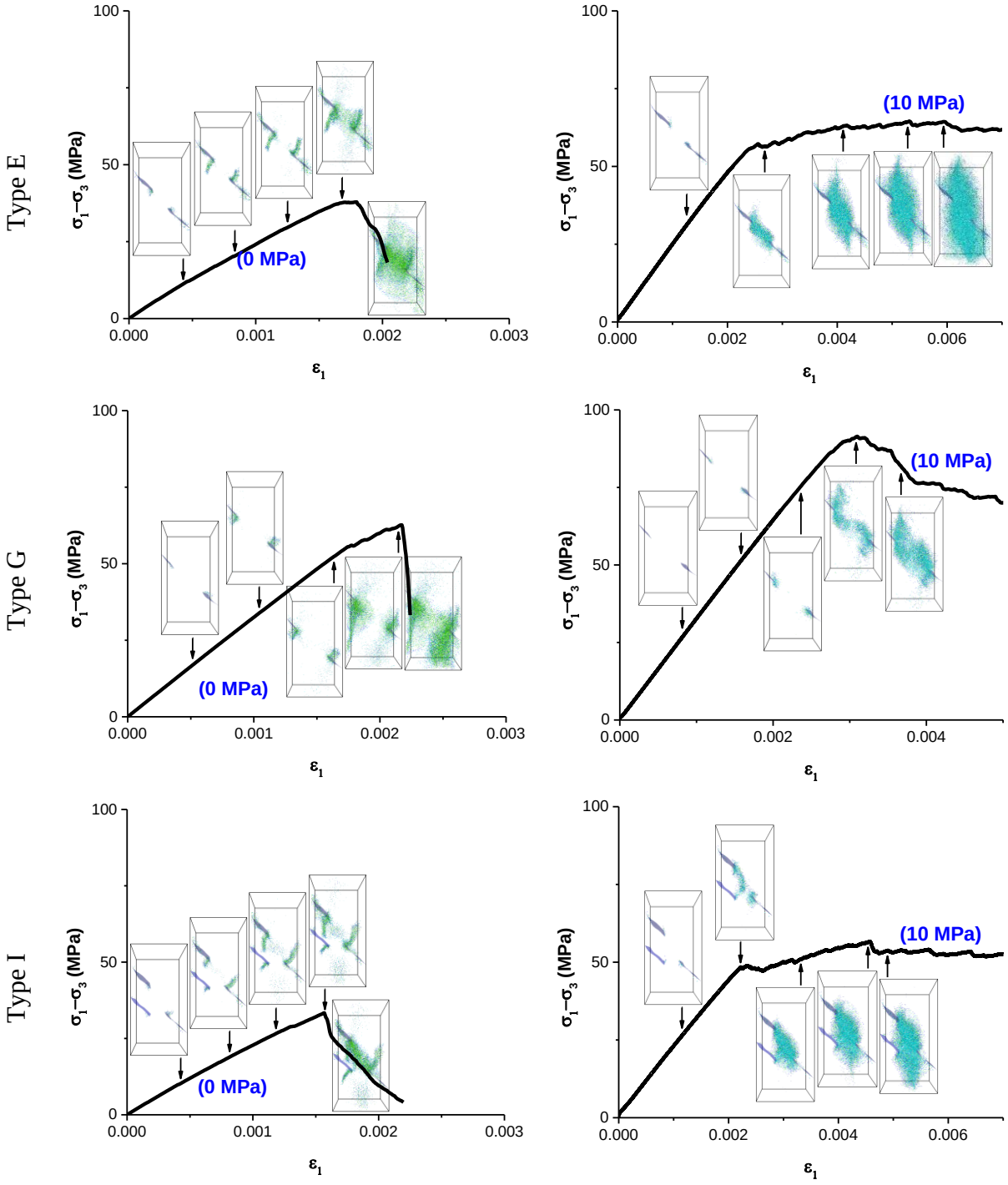
Type E
Type G
Type I
σ1–σ3 (MPa)
ε1
(0 MPa)
(10 MPa)
0
50
100
0.000
0.001
0.002
0.003
0.004
0.006

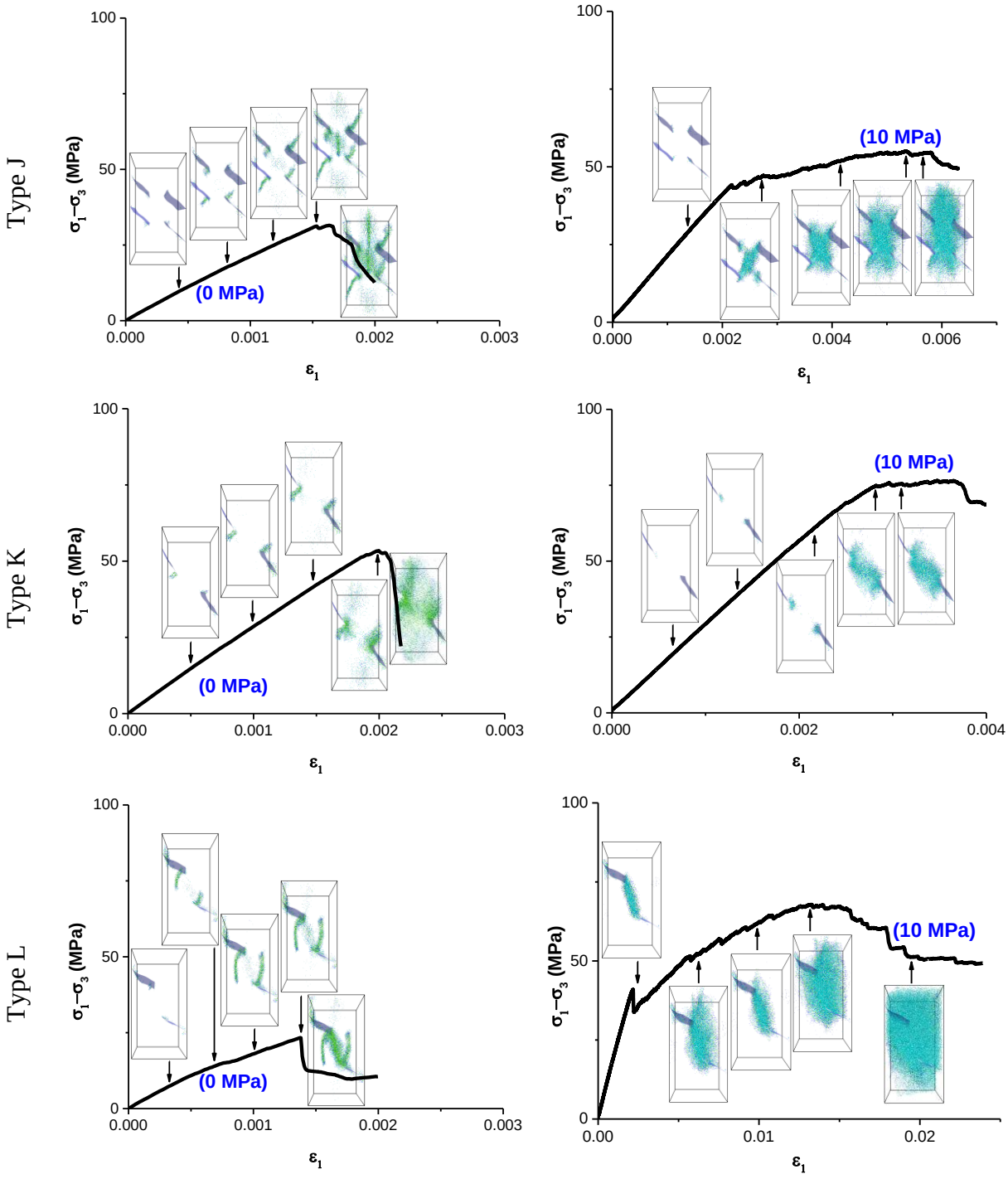

Figure 4-12 Illustration of crack propagations in cracked synthetic marble models with non-planar cracks of different configurations at different axial strains along with the differential stress–axial strain plots under unconfined compression (left) and confined compression at 10 MPa (right).

4.6 Influence of crack persistence on the mechanical behavior of pre-cracked marble

It is seen from the results presented in Sections 4.4 and 4.5 that the mechanical properties of the cracked marbles with a large number of cracks and large crack angles are highly influenced by the mechanical properties of the cracks. For the models with 24 mm long cracks, there is a small difference in the mechanical properties between the cracked specimens with planar and non-planar cracks because of the low persistence of the cracks. To investigate the influence of crack persistence and waviness on the mechanical response of the cracked marbles, 2*a* is increased to 36 mm for the Type B and Type J models with both planar and non-planar cracks. The non-planar cracks are generated from the first 36 mm of Barton's *JRC* profile with a *JRC* index of 18 to 20 (Figure 4-4). The models with 36 mm long cracks are subjected to both unconfined (σ_3 = 0 MPa) and confined (σ_3 = 10 MPa) compressions.

The modeling results suggest that both σ_c and E decrease with the increase of 2*a*. This is because as the 2*a* increases, the volume of the rock bridge between the cracks is reduced. Consequently, the force required to overcome the strength provided by the rock bridge is reduced for specimens with longer cracks. Because the stress–strain plot is highly nonlinear, E is determined by measuring the secant modulus in the stress–strain curve at 50% of σ_c. The σ_c and E of Type B and Type J cracked marbles with 36 mm long planar and non-planar cracks are shown in Table 4-4 and differential stress–axial strain relations are shown in Figure 4-13. For the Type B model with planar cracks, the σ_c and E decrease from 32.2 MPa and 22.2 GPa to 4.6 MPa and 9.3 GPa, respectively, when 2*a* is increased from 24 mm (Figure 4-9) to 36 mm (Figure 4-13a) under unconfined compression. The σ_c and E decrease from 27.9 MPa and 20.3 GPa to 4.4 MPa and 8.1 GPa, respectively, when *2a* is increased from 24 mm (Figure 4-9) to 36 mm (Figure 4-13a) for the Type

J model with planar crack under unconfined compression. The σ_c and E also decrease for both Type B and Type J marble specimens with planar cracks when $2a$ is increased from 24 (Figure 4-9) to 36 mm (Figure 4-13b) under confined compression at σ_3 = 10 MPa.

Table 4-4 Summary of mechanical properties of Type B and Type J models with 36 mm long planar and non-planar cracks under compression

Cracked model ($2a$ = 36 mm)	σ_c at σ_3 = 0 MPa	σ_c at σ_3 = 10 MPa	E (GPa)
Type B planar	4.6	28.6	9.3
Type B non-planar	7.0	53.3	14.3
Type J planar	4.4	35.6	8.1
Type J non-planar	6.6	52.7	11.5

An increase in the σ_c and E is also observed for the pre-cracked marbles (Type B and Type J) with 36 mm long cracks when the planar cracks are replaced with non-planar ones under unconfined compression (Figure 4-13). In models with non-planar cracks, the applied force must overcome the strength of intact rock asperities along the wavy surface in addition to the intact rock bridge between the cracks. For the Type B model with 36 mm crack length, the σ_c and E increase from 4.6 MPa and 9.3 GPa to 7.0 MPa and 14.3 GPa, respectively, when the crack surface geometry is changed from planar to non-planar under unconfined compression (Figure 4-13a). Similarly, for Type J marble the σ_c and E increase from 4.4 MPa and 8.1 GPa to 6.6 MPa and 11.5 GPa, respectively, when the crack surface geometry is changed from planar to non-planar under unconfined compression. The σ_c and E also increase for both Type B and Type J marble specimens with 36 mm long cracks when the planar cracks are replaced with non-planar ones under confined compression at σ_3 = 10 MPa (Figure 4-13b).

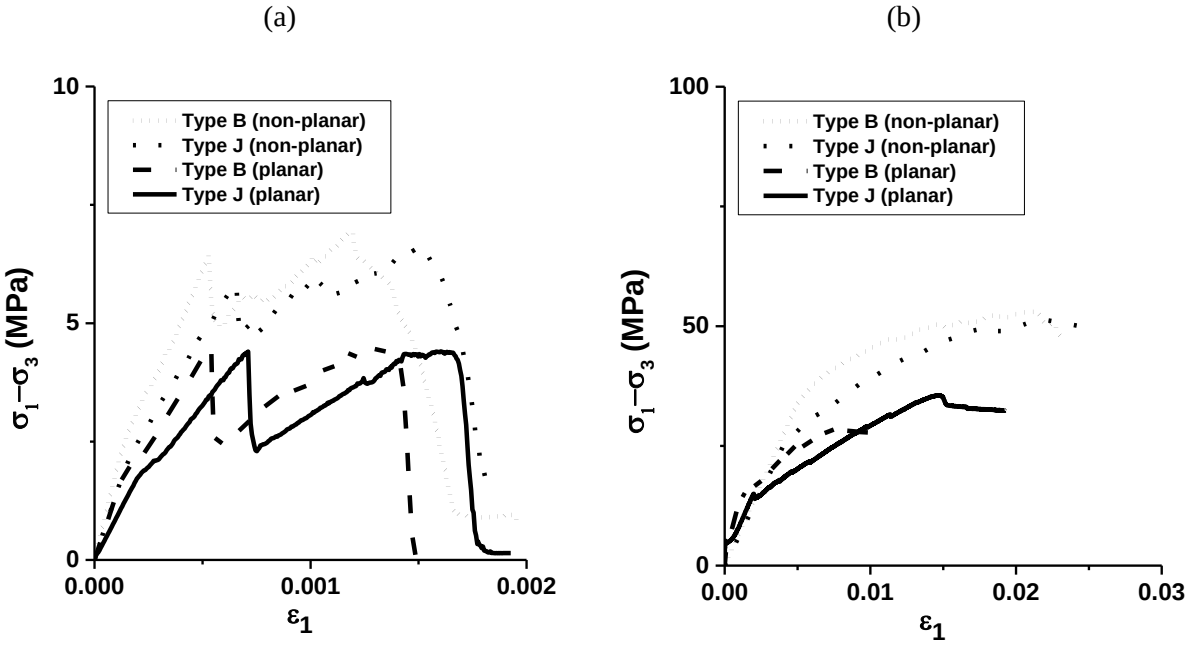

Figure 4-13 Comparison of differential stress–axial strain plots for the Type B and Type J models with 36 mm long planar and non-planar cracks under (a) unconfined compression (b) confined compression at σ_3 = 10 MPa.

Cracks initiate around the inner tips of the pre-existing cracks for the pre-cracked marbles with 36 mm long planar cracks, in the similar manner as in the models with 24 mm long planar cracks. However, in the models with 36 mm long planar cracks, crack coalescence occurs shortly after the development of a few tensile wing cracks (Figure 4-14a); this causes a reduction in both the σ_c and E of the pre-cracked marbles. However, in the models with 36 mm long non-planar cracks, a complex cracking pattern is observed. In addition to the development of the tensile wing cracks and the coalescence of these cracks, additional cracks initiate from the wavy sections of the cracks (Figure 4-14b). This leads to the cracking of both the intact rock bridge between the cracks and the rock asperities along the wavy sections of cracks, which increases the strength and stiffness of the pre-cracked marble with non-planar cracks. This comparison is relative to specimens with planar cracks of the same crack length. In the Type J model with 36 mm long cracks, wing cracks

initiate between the cracks with the shortest rock bridge span that are closer to the middle of the specimen and then propagate towards the internal tips of other cracks with coalescence (Figure 4-14c&d). The cracks in Type J marble whose internal tips are located away from the center of the specimens also exhibit tensile wing cracking mechanism.

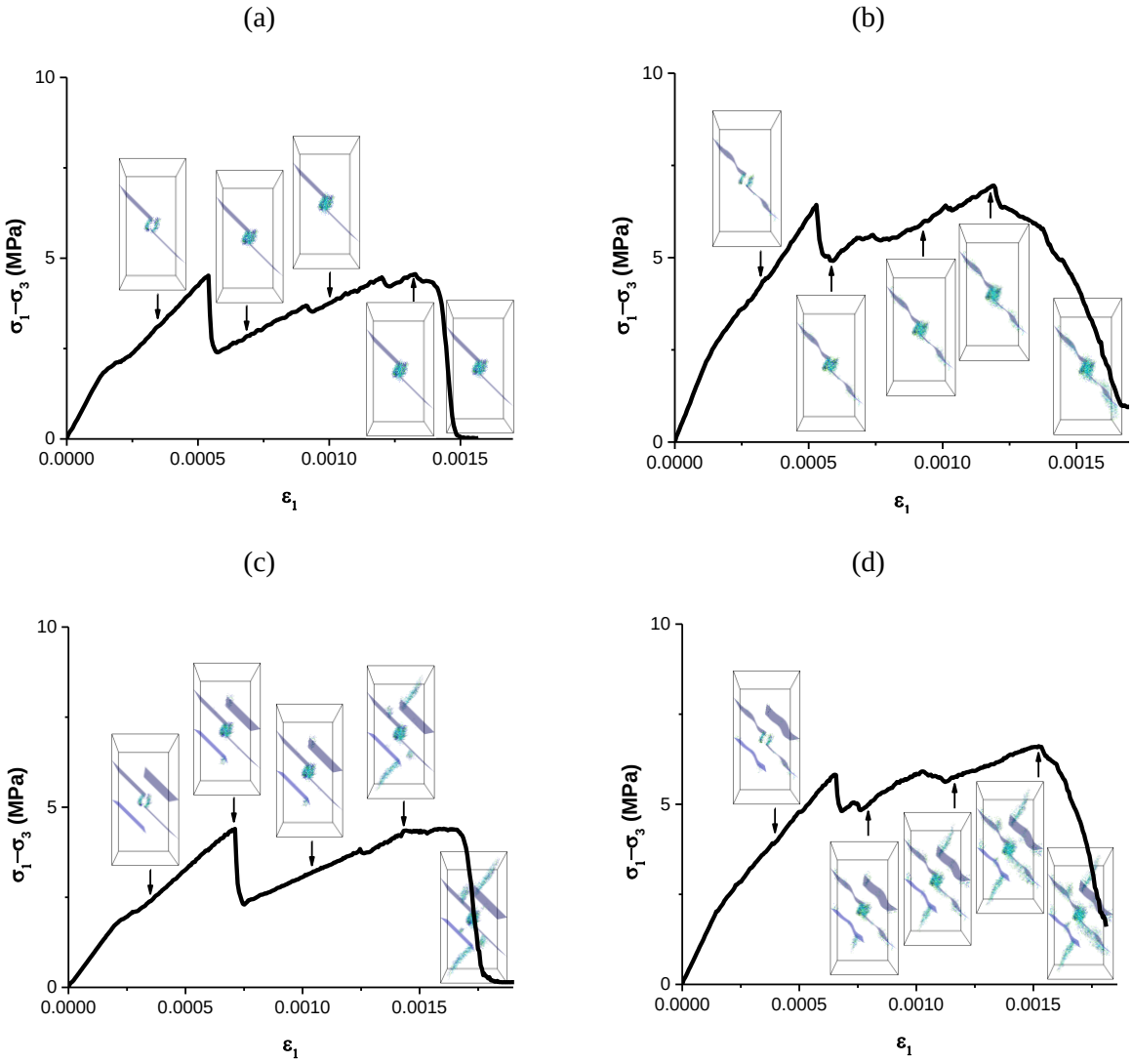

Figure 4-14 Illustration of crack propagation for pre-cracked marbles with 36 mm long cracks at different axial strains along with differential stress–axial strain plots under unconfined compression for (a) Type B with planar cracks, (b) Type B with non-planar cracks, (c) Type J with planar cracks, and (d) Type J with non-planar cracks.

4.7 Remarks

In this Chapter, the influence of crack surface geometry on the cracking mechanism and mechanical properties of pre-cracked rocks has been investigated using the LS-SRM modeling approach under unconfined and confined compressions, using eight synthetic rock models with different planar and non-planar crack configurations. The mechanical properties and cracking patterns of pre-cracked rocks are highly dependent on the spatial location, persistence, waviness, and the number of pre-existing cracks.

The numerical modeling results suggest that in the cracked rock models with planar cracks, initiation of tensile wing cracks from the internal crack tips is accompanied with the breakage of intact rock bridges between the cracks. However, in the cracked rock models with wavy or non-planar cracks, slipping along the cracks is hindered by the asperities with the initiation of secondary cracks from the wavy section of the cracks along with the tensile wing-cracks from the internal crack tips. The failure mode is mixed tensile splitting and shearing failures in uniaxial compression. Under the confined condition, shear failure dominates because tensile damage is largely suppressed.

As expected, compared with the intact marble, the cracked marbles have lower strength and smaller deformation modulus. Both the peak strength and the deformation modulus decrease with the increase of the crack angle, crack length, ligament angle, and the number of cracks. The strength and the stiffness of the cracked marble with non-planar crack are higher than the ones with planar cracks when the crack persistence is high, indicating that the influence of crack waviness on rock properties is high only when the crack persistency is large. The results from this numerical

investigation are reasonably consistent with the results of previous experimental studies (Yang et al., 2009, 2008) and numerical simulation (Wang et al., 2014).

Chapter 5

5 Influence of joint configuration on the mechanical response of jointed granite under compression[3,4]

Many experimental studies have been conducted to investigate the strength and deformability of rock-like materials (Brown & Trollope, 1970; Einstein et al., 1969; Einstein & Hirschfeld, 1973; Fan et al., 2015; Kulatilake et al., 1997; Kulatilake et al., 2001; Prudencio & Van Sint Jan, 2007; Ramamurthy, 2001; Ramamurthy & Arora, 1994; Singh et al., 2002; Tiwari & Rao, 2004; Tiwari & Rao, 2006). These synthetic rock-like materials are not representative of strong natural rock in terms of mechanical properties and cracking mechanism. Very few studies have been conducted to investigate the strength and deformability of real jointed rock such as sandstone (Ramamurthy & Arora, 1994) and granite (Arzua et al., 2014; Alejano et al., 2017).

Arzua et al. (2014) and Alejano et al. (2017) conducted extensive laboratory triaxial tests on both intact and jointed Blanco Mera granite samples and concluded that both the strength and deformation modulus of the jointed granite decrease with the increase of the number of joints. The laboratory triaxial test results of both intact (Castro-Filgueira et al., 2016) and jointed (Castro-Filgueira, 2019) Blanco Mera granite were simulated using the flat-joint contact model in PFC3D; however, the post-peak deformational behavior of the jointed granite was not reasonably captured. In those studies, joints were idealized as planar features. However, in nature, rock joints are

---

[3] Originally published as 'Bastola, S. and Cai, M. Investigation of strength and deformation behaviors of intact and jointed granite using lattice-spring-based synthetic rock mass models. In *2nd International Discrete Fracture Network Engineering Symposium*. Seattle, USA: American Rock Mechanics Association; 2018'.

[4] The manuscript is accepted for publication in the *Int. J. of Rock Mech.& Min. Sci*.

characterized with some degree of roughness which could directly influence the mechanical behavior of jointed rocks.

The influence of roughness or waviness on the strength and deformability of jointed rocks can be accounted for by increasing the effective joint friction angle without explicitly integrating the non-planar joints in SRM models (Bahrani, 2015). While this approach is simple in terms of modeling, it is evident that the mechanical properties and crack evolution mechanism are also controlled by the surface geometry of pre-existing non-persistent cracks (Bastola & Cai, 2019; Chapter 4). Oversimplification may lead to inaccurate results. Thus, it is vital to include realistic geometry of the non-planar joints in SRM models.

In this Chapter, the mechanical behaviors of intact and jointed Blanco Mera granite with fully persistent joints of different configurations are investigated using LS-SRM modeling approach under unconfined and confined compressions. Both the intact rock model and the jointed granite models with planar joints are calibrated (Section 5.2) using the laboratory triaxial test results reported by Alejano et al. (2017). The calibrated lattice model parameters are used to investigate the influences of joint intensity, waviness, orientation, and persistence on the mechanical properties of jointed granite under conventional triaxial loading (Section 5.3). In addition, the mechanical response of jointed granite with both planar and non-planar joints under true-triaxial loading are also investigated (Section 5.4). Itasca's SRMTools is used for numerical modeling.

5.1 Model development

LS-SRM models are constructed based on the information reported in the laboratory triaxial test results of intact and jointed Blanco Mera granite (Alejano et al., 2017) because the database consists of a suite of results for intact, sparsely jointed (1+2), and moderately jointed (2+3) rock.

This rock is coarse-grained granite and all the jointed block pieces were derived from a homogeneous block of granite. The triaxial test was conducted with the confining pressure between 1 MPa and 12 MPa. Triaxial test results suggest that both the strength and deformation modulus decrease with the increase of the number of joints. Each synthetic rock model is 100 mm × 50 mm × 50 mm in dimension and contains 38,784 lattice nodes that are connected to each other by 192,436 lattice springs. Persistent joints are introduced into the intact rock model to mimic the geometry of the jointed rock specimens in the laboratory test. Numerical models with two types of joint configurations, (1+2) and (2+3) joint patterns, are constructed to emulate the dimension and location of the joints in the laboratory study (Alejano et al., 2017).

In this Chapter, synthetic jointed models with (1+2) and (2+3) planar joint configurations are referred to as Model A (Figure 5-1a) and Model B (Figure 5-1b), respectively. In Model A, the mean dips are 23° for the sub-horizontal joints and 85° for the sub-vertical joints. In Model B, the mean dips of the sub-vertical and the sub-horizontal joints are 78° and 23°, respectively. The sub-horizontal joint spacings in Models A and B are 4.0 cm and 2.5 cm, respectively. Model B has a joint spacing of 2.0 cm for the sub-vertical joints. The spacings of the vertical and horizontal joints in Model C (Figure 5-1c) are 1.0 and 2.0 cm, respectively. In Model D (Figure 5-1d), the spacings of the vertical and the horizontal joints are same as these in Model B, except that the model has an additional sub-horizontal joint set with a spacing of 2.5 cm. Model E (Figure 5-1e) and Model F (Figure 5-1f) are generated by replacing the planar joints in Models A and B with non-planar joints, respectively. The geometries of Model G (Figure 5-1g), Model H (Figure 5-1h), Model I (Figure 5-1i), and Model J (Figure 5-1j) are the same as that of Model F except that the length of the non-planar joints is reduced to generate jointed rock models of different persistence. Models G, H, I, and J have a persistence of 0.8, 0.7, 0.6, and 0.5, respectively. Similarly, Model K (Figure 5-1k),

Model L (Figure 5-1l), Model M (Figure 5-1m), and Model N (Figure 5-1n) have a persistence of 0.8, 0.7, 0.6, and 0.5, respectively, except that the joints are planar. Additional eight models are created by varying the dip at 35°, 45°, 55°, 67° for the sub-horizontal joint set of Model B (Figure 5-1o,p,q&r) and Model F (Figure 5-1s,t,u&v) while keeping the dip of the sub-vertical joint set the same at 78°.

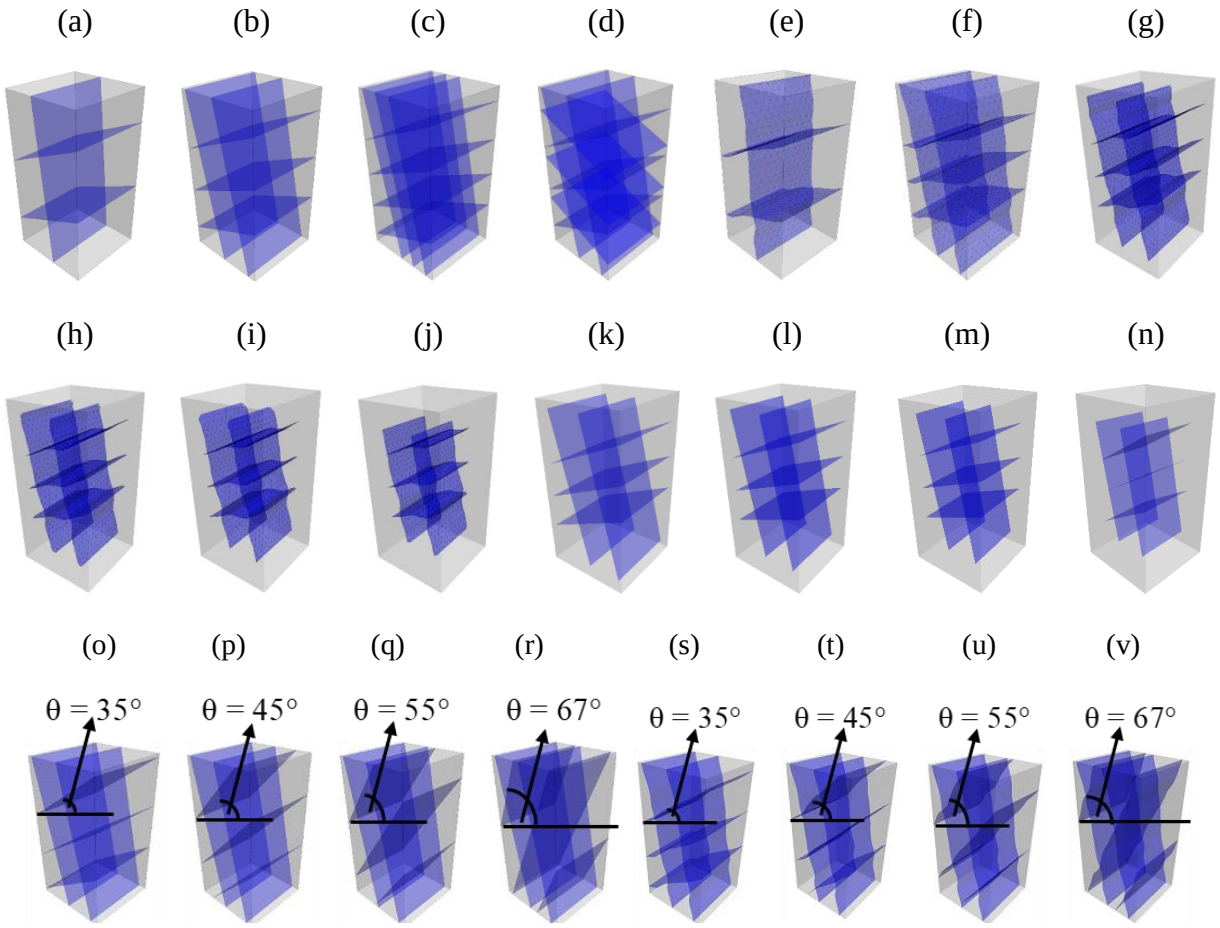

Figure 5-1 Synthetic jointed rock models (a) Model A and (b) Model B, created based on the joint configuration in laboratory test (Alejano et al., 2017); additional models with different joint intensities: (c) Model C, (d) Model D; joint waviness & persistence: (e) Model E, (f) Model F, (g) Model G, (h) Model H, (i) Model I, (j) Model J; and joint persistence: (k) Model K, (l) Model L, (m) Model M, (n) Model N; and different orientations (o) Model B with joint set dip θ = 35°, (p) Model B with θ = 45°, (q) Model B with θ = 55°, (r) Model B with joint set dip (θ) = 67°, (s) Model F with θ = 35°, (t) Model F with θ = 55°, (u) Model F with θ = 55°, (v) Model F with θ = 67°.

The joint configuration matrix for all the jointed models are shown in Table 5-1.

Table 5-1 Joint configuration matrix in LS-SRM models

Model	x_h (cm)	x_v (cm)	θ_h (°)	θ_V (°)	P_{32} (m^2/m^3)	JRC	K
A	4.0	-	23	85	41.8	0	1.0
B	2.5	2.0	23	78	73.5	0	1.0
C	2.0	1.0	23	78	104.8	0	1.0
D	2.5	2.0	23	78	106.1	0	1.0
E	4.0	-	23	85	41.8	18-20	1.0
F	2.5	2.0	23	78	73.5	18-20	1.0
G	2.5	2.0	23	78	58.8	18-20	0.8
H	2.5	2.0	23	78	51.4	18-20	0.7
I	2.5	2.0	23	78	44.1	18-20	0.6
J	2.5	2.0	23	78	36.7	18-20	0.5
K	2.5	2.0	23	78	58.8	0	0.8
L	2.5	2.0	23	78	51.4	0	0.7
M	2.5	2.0	23	78	44.1	0	0.6
N	2.5	2.0	23	78	36.7	0	0.5
O	2.5	2.0	35	78	73.5	0	1.0
P	2.5	2.0	45	78	73.5	0	1.0
Q	2.5	2.0	55	78	73.5	0	1.0
R	2.5	2.0	67	78	73.5	0	1.0
S	2.5	2.0	35	78	73.5	18-20	1.0
T	2.5	2.0	45	78	73.5	18-20	1.0
U	2.5	2.0	55	78	73.5	18-20	1.0
V	2.5	2.0	67	78	73.5	18-20	1.0

Note: x_h – spacing of sub-horizontal joints, x_v – spacing of sub-vertical joints, θ_h – dip of sub-horizontal joints, θ_v – dip of sub-vertical joints, P_{32} – volumetric joint intensity, JRC – joint roughness coefficient index, K – joint persistence

5.2 Model calibration

The goal of the calibration process is to obtain a set of lattice parameters that can reproduce the macroscopic properties (σ_c and E) of both intact and jointed granite with planar joints. All LS-SRM models (intact and jointed) have a lattice size and a flat joint radius multiplier of 0.2 cm and 0.9, respectively, and are subjected to a loading rate of 0.01 m/s. The calibrated lattice parameters for both the intact and the jointed granite are derived using the methodology based on the extensive sensitivity studies conducted by Bastola & Cai (2018b, 2019) (see also Sections 3.3 & 4.3).

5.2.1 Calibration of intact granite

The intact granite is calibrated using the procedure outlined for the LS-SRM models with flat joint contacts in Figure 3-8. Calibration of the intact Blanco Mera granite is performed by carrying out direct tension simulation (Figure 5-2a), unconfined compression simulation (Figure 5-2b), and confined compression simulations (Figure 5-2c), and comparing the simulation results with the laboratory test results (Alejano et al., 2017).

(a) (b)

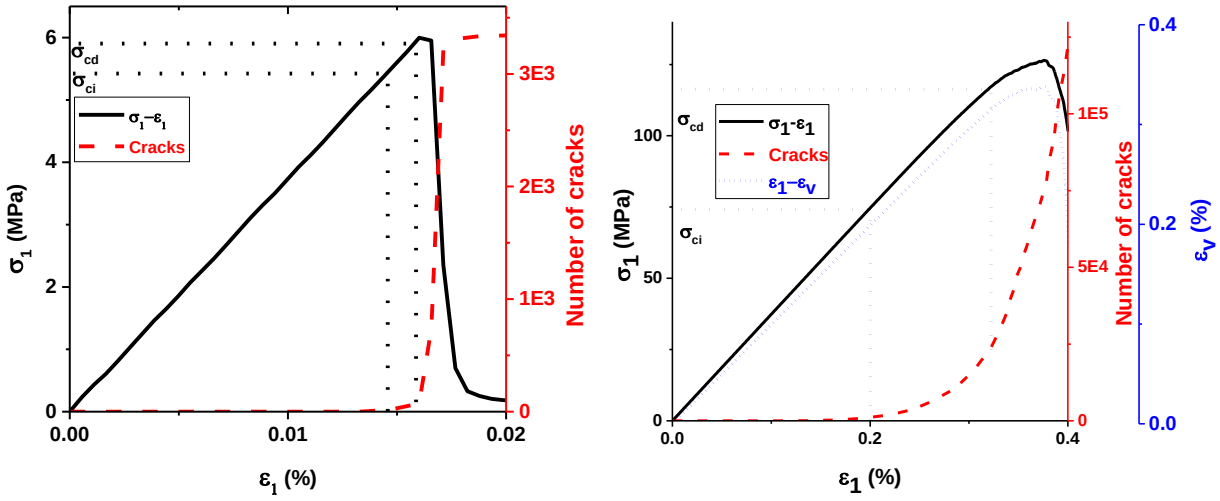

(c) (d)

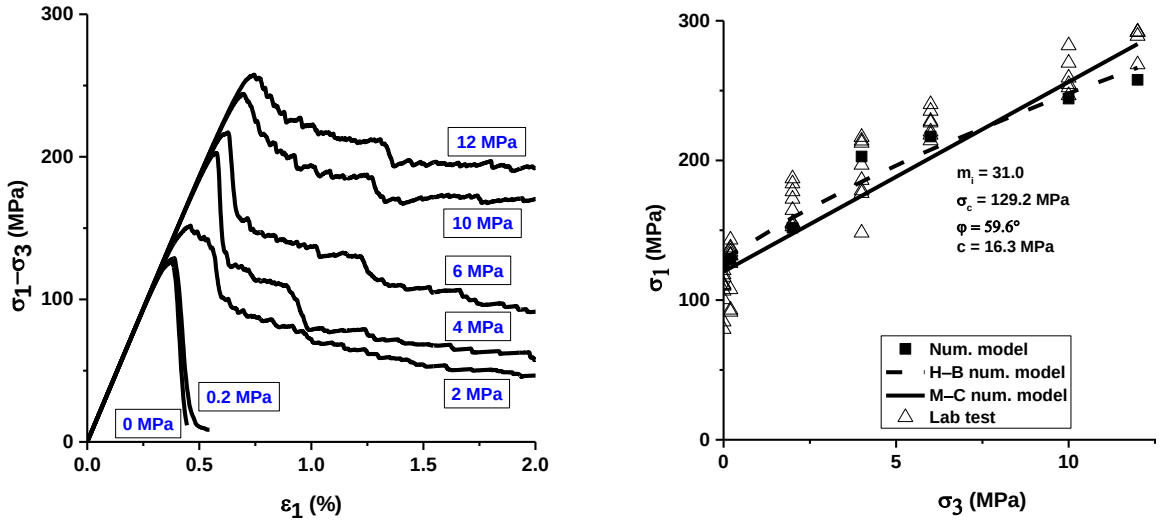

Figure 5-2 (a) Axial stress (σ_1)–axial strain (ε_1) and number of cracks – ε_1 relations of intact Blanco Mera granite under direct tension; (b) σ_1 – ε_1, volumetric strain (ε_v) – ε_1, and number of cracks – ε_1 relations of intact Blanco Mera granite under unconfined compression; (c) differential stress (σ_1–σ_3) – ε_1 relations of synthetic intact Blanco Mera granite under confined compression; (d) strength envelope of synthetic intact Blanco Mera granite with Hoek–Brown (H–B) and Mohr–Coulomb (M–C) fit of triaxial simulation results; laboratory test results are shown as unfilled triangles.

Note: σ_{ci} – crack initiation stress, σ_{cd} – crack damage stress, (m_i, σ_c) – H–B strength parameter, φ – the angle of internal friction, and c – cohesion.

Because of the high non-linearity of the strength envelope, a bilinear strength envelope calibration approach is adopted for the intact rock where the first part of the strength envelope covers the confinement range up to 2 MPa and the second part covers the confinement range from 2 to 12 MPa (Figure 5-2d). The lattice model parameters of the calibrated macro-mechanical model are shown in Table 5-2. Calibration targets (laboratory test results) and model results are shown in Table 5-3.

Table 5-2 Input lattice parameters used to calibrate the intact Blanco Mera granite

Model parameters	$0 \leq \sigma_3 \leq 2$ MPa	$2 < \sigma_3 \leq 12$ MPa
E_{mic} (GPa)	57.0	57.0
σ_{cmic} (MPa)	50.0	80.0
$(\sigma_t)_{mic}$ (MPa)	6.1	6.1
ρ (kg/m^3)	2650.0	2650.0
Porosity (%)	0.3	0.3
φ_{fjp} (°)	62.0	55.0
φ_{fjr} (°)	0	0

E_{mic} – lattice elastic modulus, σ_{cmic} – lattice compressive strength, $(\sigma_t)_{mic}$ – lattice tensile strength, ρ – rock density, φ_{fjp} – peak friction angle of flat joint, φ_{fjr} – residual friction angle of flat joint

Table 5-3 Summary of calibration targets and modeled values for intact Blanco Mera granite

Parameters	Target value	Modeled value
E (GPa)	37.0	37.4
UCS (MPa)	120.0	126.0
σ_t (MPa)	6.1	6.0
σ_{ci} (MPa)	50.0-75.0	75.0
σ_{cd} (MPa)	85.0-110.0	110.0
c (MPa)	14.0	16.3
φ (°)	62.0	60.0

E – elastic modulus, UCS – uniaxial compressive strength, σ_t – tensile strength, σ_{ci} – crack initiation stress, σ_{cd} – crack damage stress, c – cohesion, φ – the angle of internal friction

5.2.2 Calibration of jointed granite

The goal of calibration is to capture the peak confined compressive strength (σ_1) and the deformation modulus (E_m) of the jointed Blanco Mera granite. For all jointed models, the joint friction angle (φ_j) is kept constant at 30° based on the values reported in the literature for the basic friction angle of granite (Barton & Choubey, 1977; Barton, 1973). Joint cohesion (c_j), joint tensile strength (σ_{tj}), and joint dilation (δ_j) are all set to zero because all the joints were saw cut and were persistent with planar surfaces. The procedure for calibrating the mechanical properties of jointed rock for LS-SRM models with flat joint contacts is shown in Figure 4-7.

The strength and deformation modulus of a jointed rock depend on joint frictional resistance and joint stiffness. For the numerical modeling of jointed rock, the calibrated intact rock properties are used in conjunction with the calibrated joint properties. Joint properties are derived from the sensitivity analysis of joint stiffness parameters (k_{nj}, k_{sj}) on the strength and deformation modulus of Model A. The joint stiffness values that reproduce the strength and deformation modulus of both Models A and B are the calibrated joint properties and are used in all subsequent numerical modeling. In the calibration process, k_{sj} is adjusted to achieve the desired value of E_m; then, k_{nj} is adjusted to achieve the desired peak strength. Based on the result of the sensitivity analysis, k_{nj} = 3000 GPa/m is used in all jointed rock models because the influence of k_{nj} on the strength and deformation modulus is small for k_{nj} > 3000 GPa/m (Figure 5-3). Joint shear stiffness (k_{sj}) is adjusted to accommodate the influence of confining pressure on E_m. The joint properties used in the numerical modeling of the jointed granite are shown in Table 5-4.

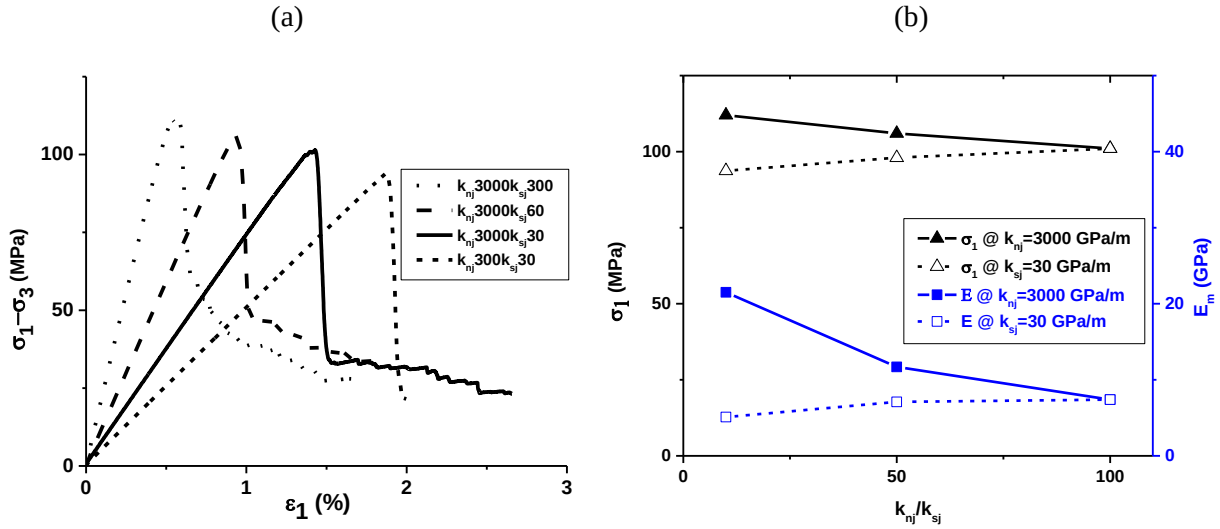

Figure 5-3 (a) Deviatoric stress–axial strain relation for Model A with different joint stiffness under 1 MPa of confining pressure; (b) sensitivity analysis of joint k_{nj}/k_{sj} on E and σ_1 (unit of k_{nj} and k_{sj} is in GPa/m) for Model A under 1 MPa of confining pressure.

Table 5-4 Joint properties used in jointed granite models

Joint parameter	Value
k_{nj} (GPa/m)	3000
k_{sj} (GPa/m)	$27\sigma_3 + 37$, for $1 \leq \sigma_3 \leq 10$ MPa
φ_j (°)	30
σ_{tj} (MPa)	0
c_j (MPa)	0
δ_j (°)	0

k_{nj} – joint normal stiffness, k_{sj} – joint shear stiffness, φ_j – joint friction angle, σ_{tj} – joint tensile strength, c_j – joint cohesion, δ_j – joint dilation

A series of triaxial simulations are performed using Models A and B with planar persistent joints under 1.0, 2.0, 4.0, 6.0, 10.0, and 12.0 MPa confining pressures. Model parameters used in both models (A and B) are the same. Under the confined condition, the synthetic jointed rock models

show degradation in both strength and deformation modulus with the increase of the number of joints, which is in agreement with the laboratory test results (Alejano et al., 2017). The differential stress (σ_1–σ_3)–axial strain (ε_1) relations from the numerical models of the intact and jointed granite under 4 and 10 MPa confining pressures show a very close resemblance to the laboratory test results (Figure 5-4). However, the post-peak strength from the numerical models is higher than the ones reported in the laboratory tests under high confinements ($\sigma_3 \geq 10$ MPa).

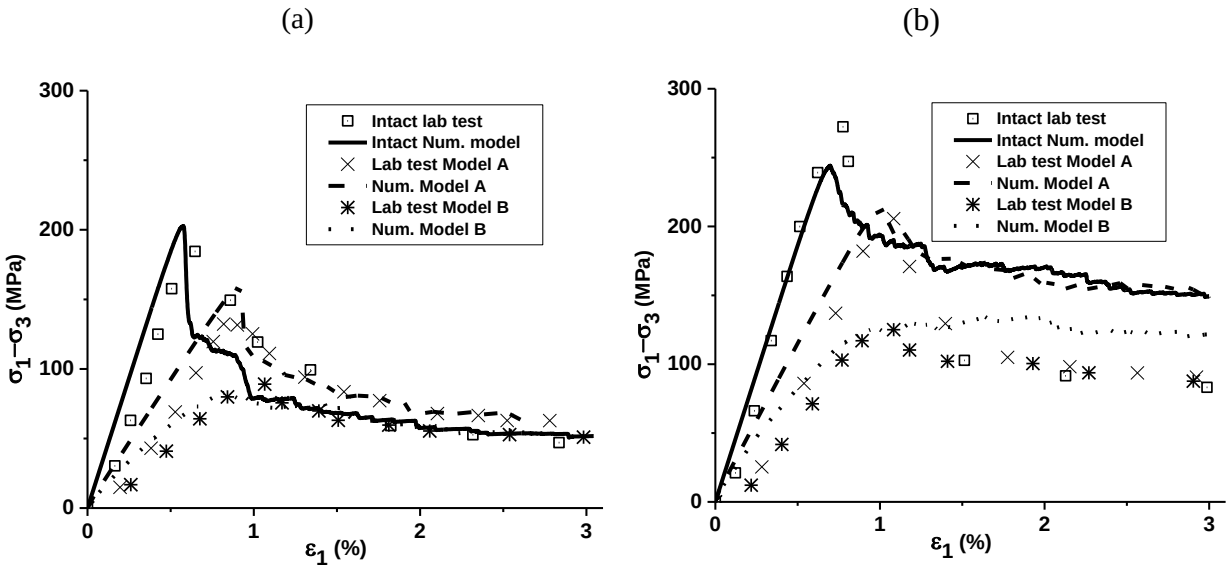

Figure 5-4 Comparison of (σ_1–σ_3)–ε_1 plots for intact and jointed Blanco Mera granite from numerical models with laboratory test results under triaxial compression at (a) 4 MPa and (b) 10 MPa confining pressures.

The peak strengths and deformation moduli of both jointed rocks (Models A and B) decrease with the increase of the degree of jointing. The Hoek–Brown (H–B) (σ_c and m_b) and Mohr–Coulomb (M–C) (c and φ) strength parameters derived from the triaxial simulation results for both Models A and B are reasonably close to the parameters determined for the laboratory test results as shown in Table 5-5 and Figure 5-5. For the jointed granite Models A and B, deformation modulus (E_m) increase with the increase of σ_3 and plateaus when $\sigma_3 \geq 10$ MPa, which is consistent with the

laboratory observation (Alejano et al., 2017). Similar results were also reported in studies on granulated Wombeyan marble (Rosengren & Jaeger, 1968) and damaged Lau du Bonnet granite (Martin & Stimpson, 1994).

Table 5-5 Comparison of the target and achieved macro-mechanical parameters for jointed Blanco Mera granite from numerical modeling

Parameters	Target value		Model value	
	Model A	Model B	Model A	Model B
σ_c (MPa)	55.5	42.1	92.7	31.0
m_b	50.0	45.9	36.0	46.5
c (MPa)	8.1	6.8	12.4	6.8
φ (°)	57.3	54.2	59.1	54.1

(a) (b)

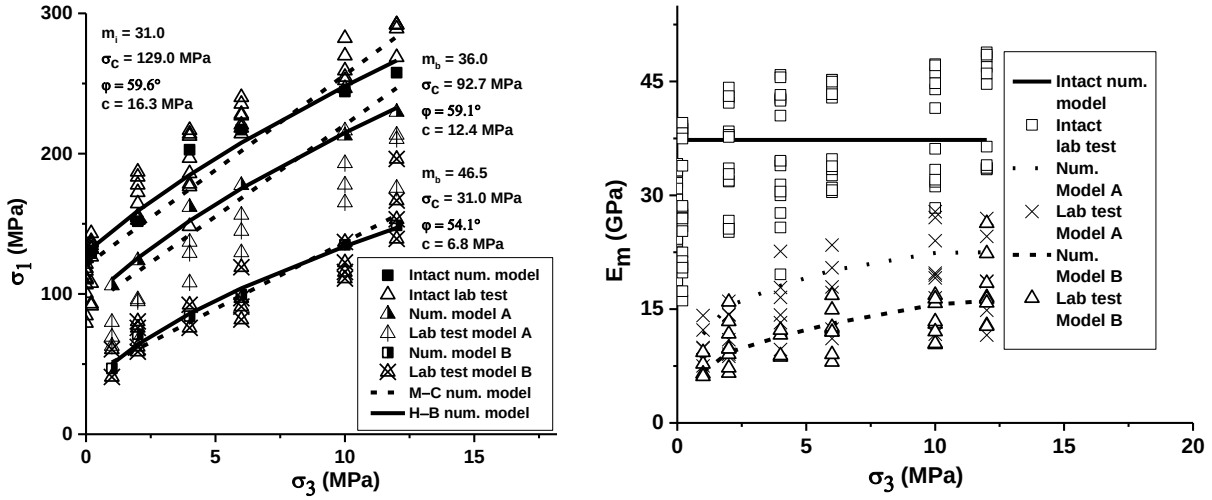

Figure 5-5 (a) Comparison of strength envelopes for intact and jointed Blanco Mera granite from numerical models and laboratory test. The numerical modeling results are fitted to the H–B and M–C strength envelopes. (b) Comparison of E_m–σ_3 plot for intact, Model A, and Model B from numerical modeling and laboratory test.

In laboratory triaxial test, the failure of the (2+3) jointed granite was accompanied with irregular cracking of the rock blocks, crushing of the block corners, and sliding along the pre-existing joints (Alejano et al., 2017). Macroscopic failure surface identified on the (2+3) jointed specimen in the laboratory (Figure 5-6a) triaxial test (Alejano et al., 2017) under 10 MPa of confinement is reasonably close to the failure pattern observed in numerical Model B (Figure 5-6b). The vertical displacement contour shown in Figure 5-6c presents a clear picture of cracking related movements of the rock.

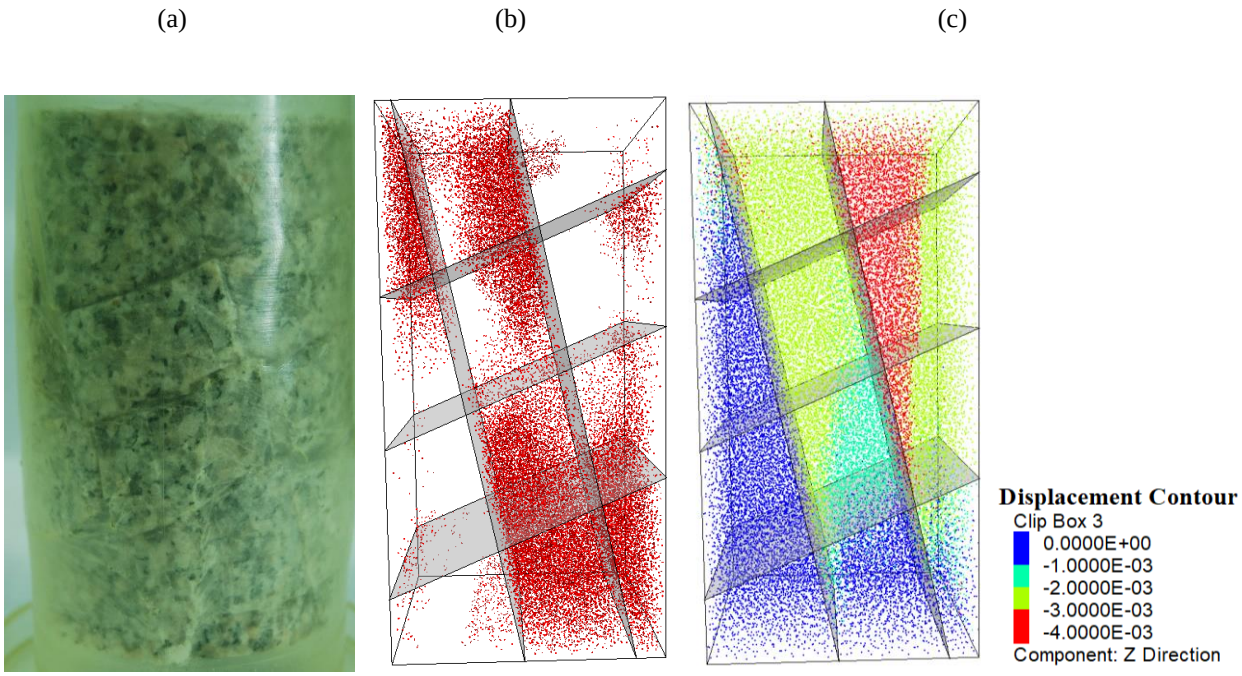

Figure 5-6 (a) Macrocracks observed in laboratory triaxial compression test of (2+3) jointed granite specimen (Alejano et al., 2017); (b) microcracks observed in triaxial compression simulation of Model B; (c) vertical displacement (in m) contour of Model B, under 10 MPa confinement.

5.3 Influence of joint configuration on the mechanical response of jointed granite under conventional triaxial loading

Rock joints have a large influence on the strength and deformation properties of the jointed rock as shown in Figure 5-5. In this section, further numerical simulations are performed to study the

influence of joints with different configurations (intensity, waviness, orientation, and persistence) on the mechanical properties of jointed rocks under conventional triaxial loading condition. All the models have the same intact rock and joint properties. The calibrated intact rock properties for $2 < \sigma_3 \leq 12$ MPa in Table 5-2 are used for the intact rock. This was done to ensure that all the jointed rock models have the same intact rock properties. For joints, k_{nj} = 3000 GPa/m, k_{sj} = 300 GPa/m, and all other joint properties are the same as those listed in Table 5-4. Triaxial compression simulations are conducted on these jointed rock models at different confining pressures.

5.3.1 Influence of joint intensity

Joint intensity, which is measured by joint spacing or frequency, is another important parameter that influences rock mass deformation behavior. In this section, the influence of joint density on the strength and deformability of jointed rocks is investigated using Models A, B, C, and D as shown in Figure 5-1. To quantify the joint intensity, the volumetric joint intensity (P_{32}) is computed for all four models. P_{32} is the total surface area of the joints per unit volume of a jointed rock. The P_{32} values for Models A, B, C, and D are 41.8 m^{-1}, 73.5 m^{-1}, 104.8 m^{-1}, and 106.1 m^{-1}, respectively.

The triaxial simulation results show that both the peak strength (Figure 5-7a & Figure 5-8a) and the normalized deformation modulus (E_m/E_i) (Figure 5-7b & Figure 5-8b) decrease with the increase of P_{32}. However, the peak strength is stagnant for models with $P_{32} \geq 73.5$ m^{-1}.

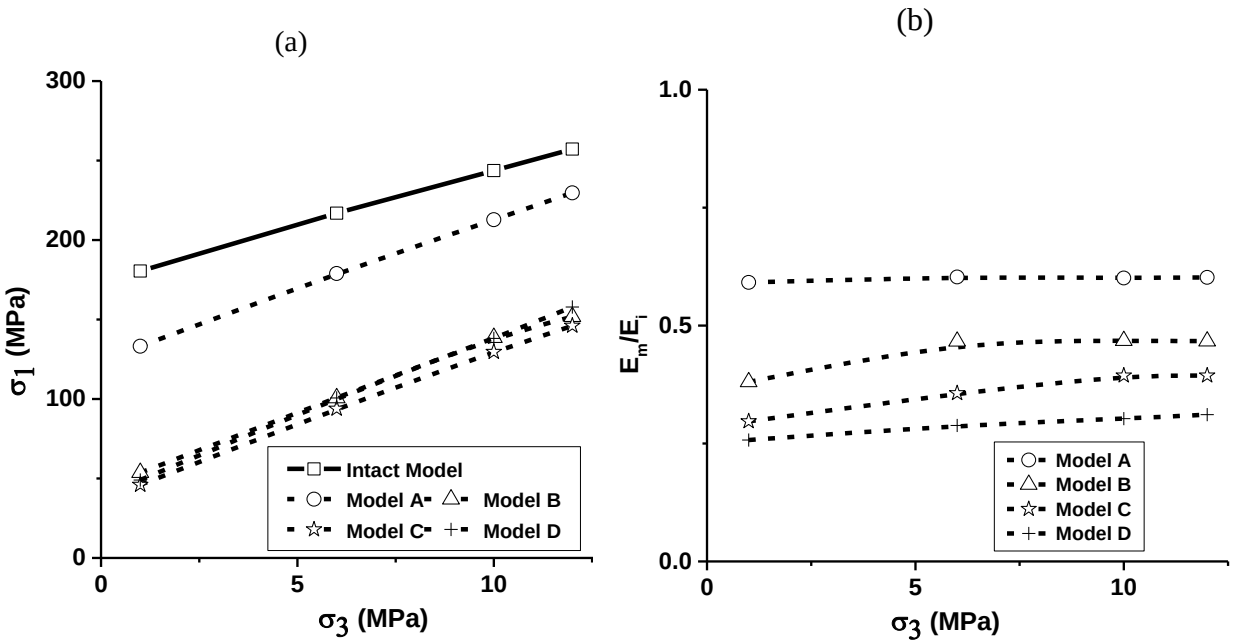

Figure 5-7 Comparison of (a) strength envelopes of jointed rock models with different P_{32} (strength envelope of the intact rock is shown for comparison); (b) normalized deformation modulus (E_m/E_i)–σ_3 plot for jointed rock models with different P_{32}.

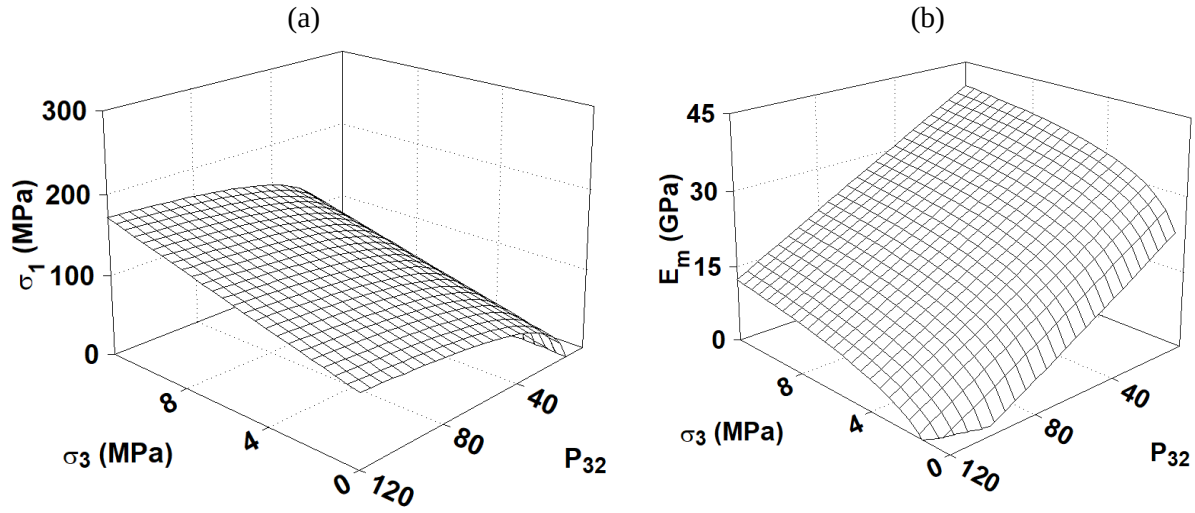

Figure 5-8 Influence of P_{32} on (a) σ_1 and (b) E_m for $\sigma_3 \leq 12$ MPa.

The influence of P_{32} on σ_1 is quantified by establishing a bi-variate relation between σ_1, σ_3, P_{32} as,

$$\sigma_1 = 7.1\sigma_3 - \frac{409.7}{\ln(P_{32})} + 172 \qquad \text{(MPa)} \tag{5-1}$$

$$\text{for } P_{32} \leq 105 \text{ m}^{-1}, \sigma_3 \leq 12 \text{ MPa, and } R^2 = 0.75$$

Similarly, a bi-variate relation between E_m, σ_3, and P_{32} is established as,

$$E_m = 5.5\ln(\sigma_3) - 0.23P_{32} + 26 \qquad \text{(GPa)} \tag{5-2}$$

$$\text{for } P_{32} \leq 105 \text{ m}^{-1}, \sigma_3 \leq 12 \text{ MPa, and } R^2 = 0.72$$

5.3.2 Influence of joint waviness

In most geotechnical investigations and numerical modeling, a joint is often idealized as a planar surface. However, rock joint surfaces are wavy and undulating in their natural states. If joints are smooth and planar, blocks can slide easily under small external forces. Joint surface asperities cause interlocking of blocks, resulting in a high load-bearing capacity of the jointed rock mass, which may reduce the demand on rock support. Thus, it is important to quantify the stiffness and strength of rock masses with non-planar joints.

Lattice resolution has some influence on the strength and deformation modulus of both intact rock (Section 3.2.1) and pre-cracked rock with non-planar discontinuities (Section 4.5). Non-planar discontinuities in the jointed rock model are represented as triangles. The size of these triangles controls the degree of representation of joint roughness and it might have some influence on the strength and deformability of the jointed rock with non-planar joints. Therefore, a sensitivity analysis is conducted to investigate the influence of joint triangle area on strength and deformation modulus of Type F jointed granite. Joints with three different areas, 50, 10, 5 mm^2, are generated in MoFrac using the joint trace with *JRC* of 18–20 from Barton's joint roughness profiles. Three

Type F jointed rock models are constructed using these joints and the calibrated intact rock model. These jointed rock models are subjected to triaxial loading at 1 MPa confining pressure.

The sensitivity study shows that the deformation modulus of Model F increases with the increase of the joint resolution i.e. with the decrease in the triangle size, however, significant influence is not observed in the magnitude of peak strength as shown in Figure 5-9.

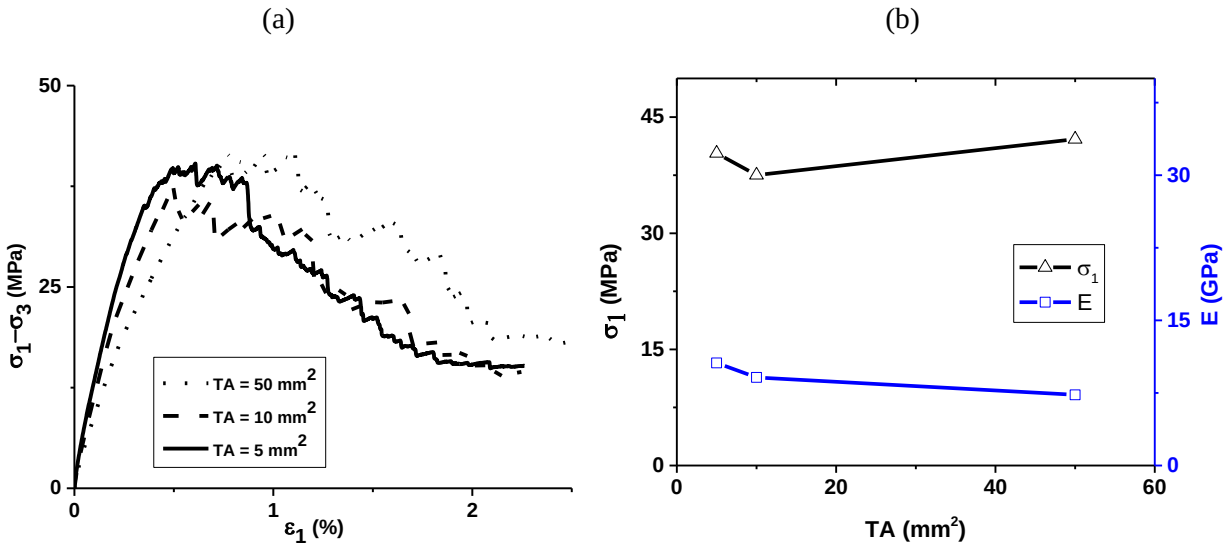

Figure 5-9 Sensitivity of joint resolution on (a) deviatoric stress–axial strain relation and (b) strength and deformation modulus under 1 MPa of confining pressure; TA is the area of the triangles that comprise the non-planar joint surface.

To investigate the influence of joint waviness on the strength and deformation behaviors of jointed rock, two models (Models A, B) with planar joints and two models (Models E, F) with very rough joints (Figure 5-1) are subjected to triaxial compression under 1, 6, 10, 12 MPa confining pressures. Models A and E have larger joint spacing than Models B and F.

The triaxial compression simulation results show that when the joint spacing is smaller, the strength of the jointed rock model with non-planar joints (Model F) is higher than that of the model with planar joints (Model B) (Figure 5-10a). This is due to additional frictional resistance provided

by the interlocking of the asperities of the non-planar joints as illustrated in Figure 5-13 (see the strength difference between Models B and F). As a result, any contribution of interlocking can increase the strength of jointed rock significantly.

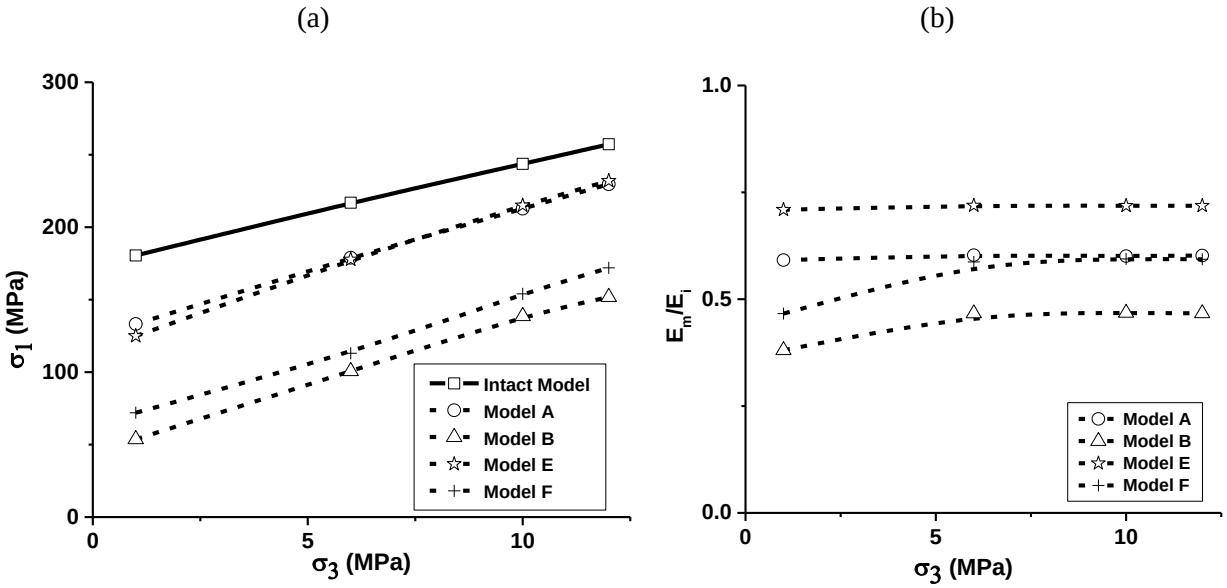

Figure 5-10 (a) Comparison of strength envelopes of jointed rock models with planar and non-planar joints; (b) comparison of E_m/E_i–σ_3 relations for jointed rock models with planar and non-planar joints.

However, in the models with larger joint spacing, the peak strength is less sensitive to the change of joint surface condition. For instance, in the case of Models A and E, the peak strengths of the models with planar and non-planar joints are similar. In comparison, in the case of Models B and F with smaller joint spacing, the peak strength of the model with non-planar joints is 18% higher than that with planar joints. As a result, any contribution of interlocking can increase the strength of jointed rocks significantly.

The E_m/E_i ratios of Models B and F increase with the increase of confining pressure, which agrees with the laboratory triaxial test results. In addition, the E_m/E_i ratio increases with the increase of joint surface roughness and decreases with the increase of joint intensity (Figure 5-10b). A 40%

reduction of the E_m/E_i ratio is observed for Model A; however, the reduction is only 28% for Model E. Similarly, the E_m/E_i ratio is reduced by 57% for Model B and the reduction is only 45% for Model F.

5.3.3 Influence of joint orientation

One of the most important characteristics of joints is their orientations relative to each other or other geological structures in underground excavations or slopes. Joints are often classified based on their orientations because geological processes usually generate one or more clusters of nearly parallel joints in a rock mass (Priest, 1993). A model with a single plane of weakness yields a U-shaped strength–orientation curve when the angle of inclination of the joint is varied from 0° to 90°. A similar exercise is conducted in this section by varying the dip of the sub-horizontal joint set (θ_h) at 35°, 45°, 55°, 67° for models B & F (see Figure 5-1o-v). These models are subjected to triaxial compression under 1, 6, 10, 12 MPa confining pressures.

The triaxial simulation results are summarized in Figure 5-11, showing that both the strength and the deformation modulus are controlled by the orientation of the sub-horizontal joint set. A U-shaped surface between the peak strength, confining stress, and the joint set dip (θ) can be seen in Figure 5-11a. The peak strength decreases progressively with the increase of θ, with the lowest strength occurring at around 55° and then the strength increases with the further increase of θ. For this modeling case, failure occurs mostly by sliding of the sub-vertical joint set. This is roughly in agreement with the observations by some researchers (Priest, 1993) showing that shear failure along the plane of weakness occurs when the joint dip is about 60°. The deformation modulus is the lowest for models with joint dips smaller than 45°. For $\sigma_3 > 1$ MPa, the deformation modulus increases with the increase of joint dip when the joint dip is greater than 45° (Figure 5-11b). This

increase in the deformation modulus is due to the increase of stiffness caused by the alteration in the block kinematics and interlocking of the sliding blocks owing to the variation of the joint dip. As the joint dip increases the joint surface that is previously kinematically unstable becomes stable, resulting in a stiffer model response.

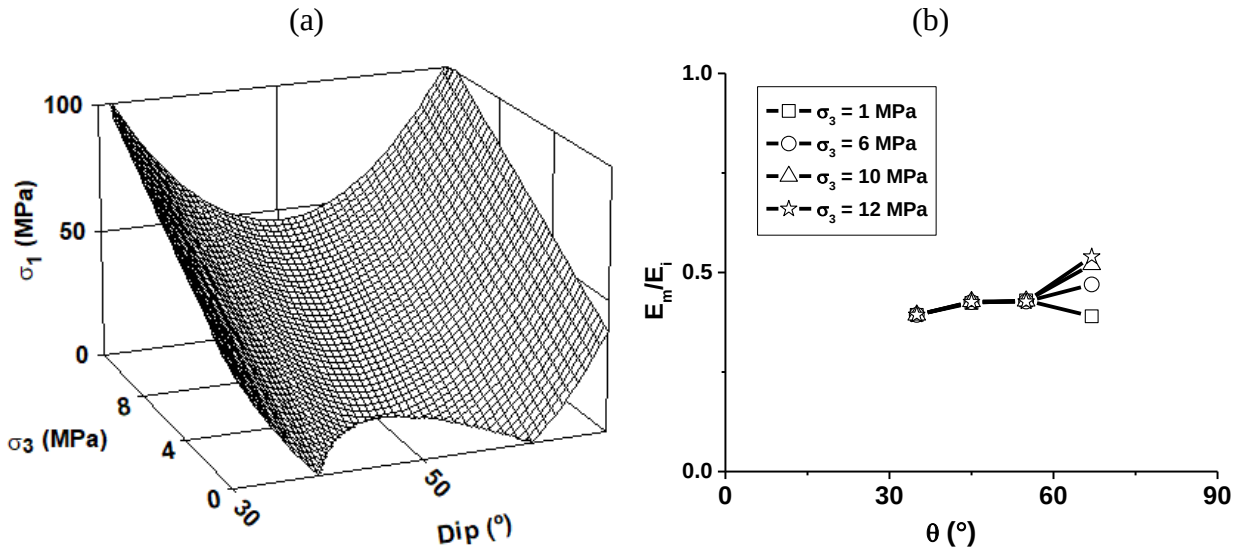

Figure 5-11 Influence of joint set dip (θ) on (a) peak strength and (b) normalized deformation modulus (E_m/E_i) under different confining pressures.

To quantify the influence of joint orientation on rock strength, empirical relations are derived among σ_1, σ_3, and θ using TableCurve3D (SYSTAT, 2016). The equation with a strong correlation ($R^2 \geq 90\%$) and the least number of parameters is chosen, which is a bi-variate second-degree polynomial function shown below,

$$\sigma_1 = 0.13\theta^2 - 13.2\theta + 5.4\sigma_3 + 315 \quad \text{(MPa)} \tag{5-3}$$

for $\sigma_3 \leq 12$ MPa, $45° \leq \theta \leq 67°$, and $R^2 = 0.90$

where the unit of stress is MPa and the unit of θ is degree. The normalized deformation modulus (E_m/E_i) increases with the increase of dip (θ) and confining pressure (σ_3); however, it is not

influenced by σ_3 when the failure occurs purely by sliding of joint. The E_m/E_i ratio does not change with the increase of σ_3 for $35° \leq \theta \leq 55°$. In the model with $\theta = 67°$, E_m/E_i increases with the increase of σ_3 because failure occurs both by joint deformation and intact rock breakage thus increasing the overall stiffness as the confining pressure increases. It is interesting to note that the value of E_m/E_i for the model with $\theta = 67°$ is equal to the value of E_m/E_i for the model with $\theta = 35°$ under 1 MPa confinement. This is because the total area of joints increases significantly for the model with $\theta = 67°$, which in turn increases the joint intensity and decreases the model stiffness under low confinement. The study conducted on the influence of joint intensity on the strength and elastic modulus also suggests that the model stiffness decreases with the increase of joint intensity (see Section 5.3.1).

A comparison of the $(\sigma_1–\sigma_3)–\varepsilon_1$ plots in Figure 5-12 shows that Model B displays an elasto-perfectly plastic deformation behavior, but Model F exhibits a mix of brittle-ductile-plastic and strain-softening deformation behavior. The strength of the jointed models with different joint dips increases when the planar joints are replaced with non-planar ones; however, E_m does not change significantly with such a change of the joint waviness. This is due to the additional strength provided by the intact rock asperities along the rough joint surface in Model F. The strength of Model B is purely governed by frictional sliding as no micro-cracks are developed during the failure process (Figure 5-13).

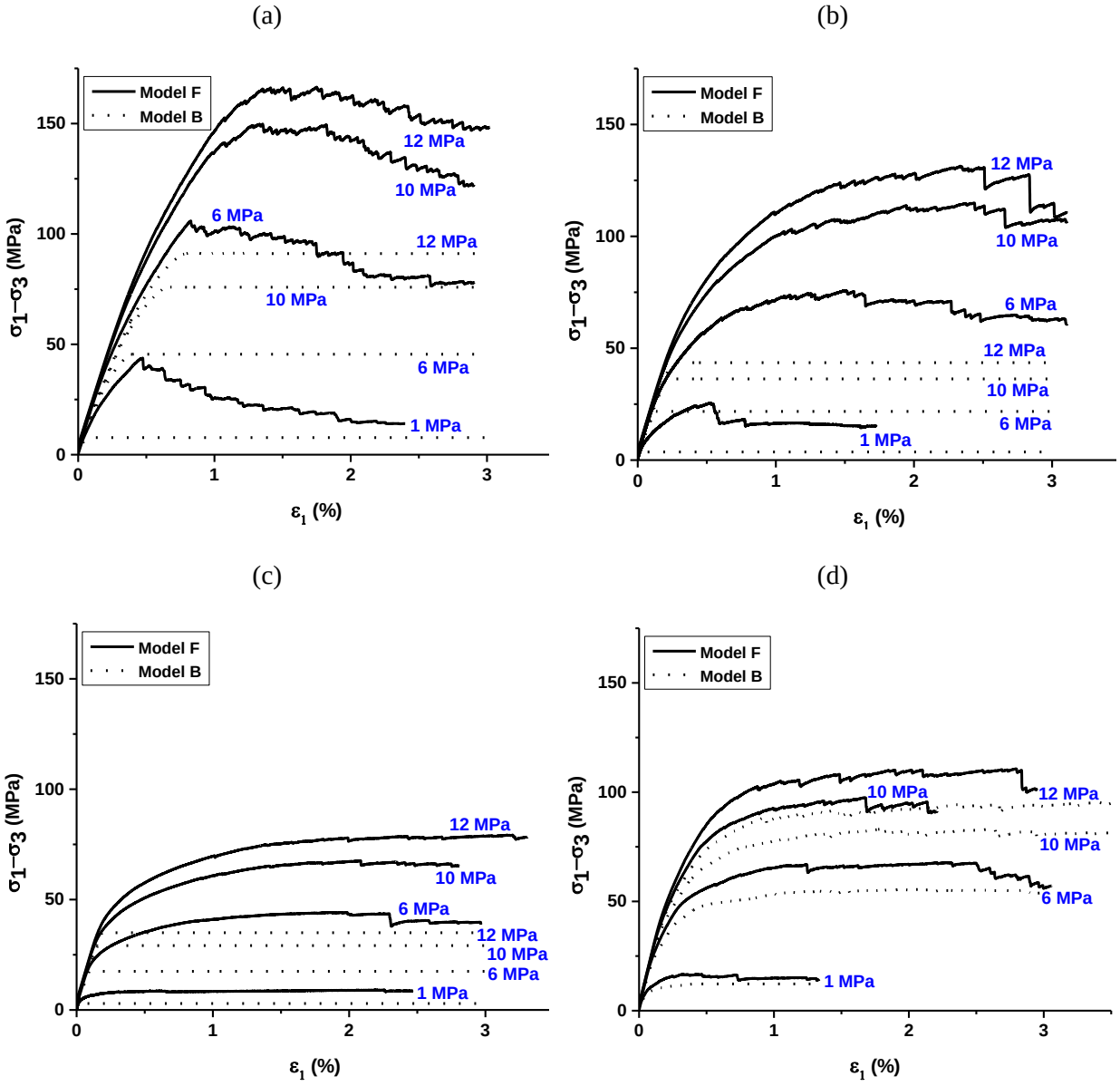

Figure 5-12 Comparison of (σ_1–σ_3)–ε_1 plots of Model B (dotted line) and Model F (solid line) with different joint dips: (a) θ = 35°, (b) θ = 45°, (c) θ = 55°, (d) θ = 67° under triaxial compression.

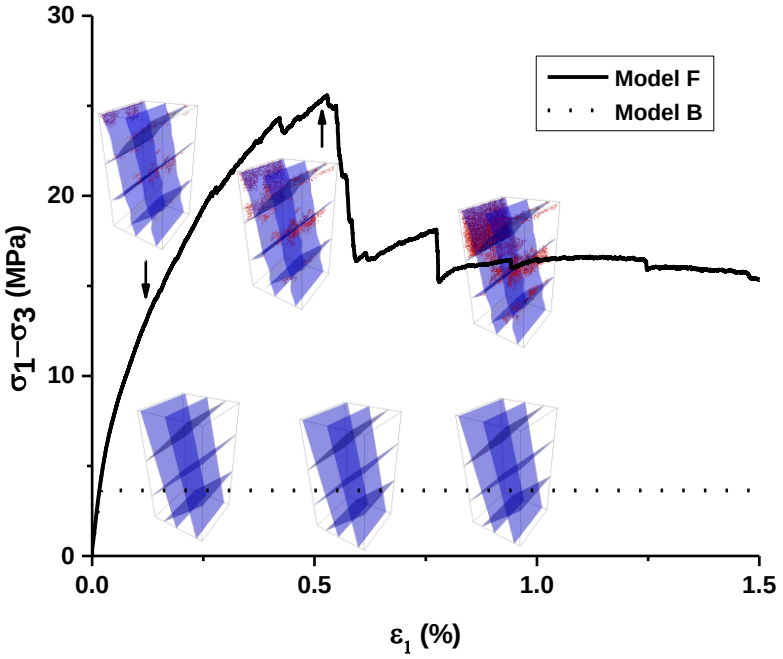

Figure 5-13 Illustration of crack propagation at different deformation stages along the (σ_1–σ_3)–ε_1 plots of Model B (dotted line) and Model F (solid line) with θ = 35° under 1 MPa confinement.

5.3.4 Influence of joint persistence

Joint persistence is of great importance for many rock-related engineering applications because it affects both the rock mass strength and the deformation modulus (Cai et al., 2004; Kim et al., 2006). Joint persistence (Section 2.2.3) is defined in terms of the extent of rock bridges (Section 2.2.3) in jointed rock masses.

In this section, the influence of joint persistence on the mechanical properties of jointed rocks is investigated by performing confined compression simulations on jointed rock models with both planar and non-planar joints of different areal persistence (K). Five jointed rock models with planar joints (Models B, K, L, M, and N; see Figure 5-1) and five jointed rock models with non-planar joints (Models F, G, H, I, and J) with different K are loaded under confined compression with σ_3 in the range of 1 to 15 MPa. Models B, K, L, M, and N have K of 1.0, 0.8, 0.7, 0.6, and 0.5,

respectively, with 1.0 meaning that the joint is fully persistent. Similarly, Models F, G, H, I, and J have K of 1.0, 0.8, 0.7, 0.6, and 0.5, respectively. The roughness of the non-planar joints correspond to the *JRC* range of 18–20 (Barton & Choubey, 1977) and the non-planar joints are generated using MoFrac.

The triaxial compression simulation results show that both σ_1 and E_m/E_i of the jointed rock decrease with the increase of K. For the jointed rock models with planar joints and $K \geq 0.8$, there is no significant decrease in σ_1 (Figure 5-14a). There is no significant influence of confining stress (σ_3) on E_m/E_i of the jointed rock with planar joints except the case with persistent joints (K = 1) as shown in Figure 5-14b. For the jointed rock models with equal K values, σ_1 (Figure 5-15a) and E_m/E_i (Figure 5-15b) of the jointed rock models with non-planar joints are higher than the ones with planar joints.

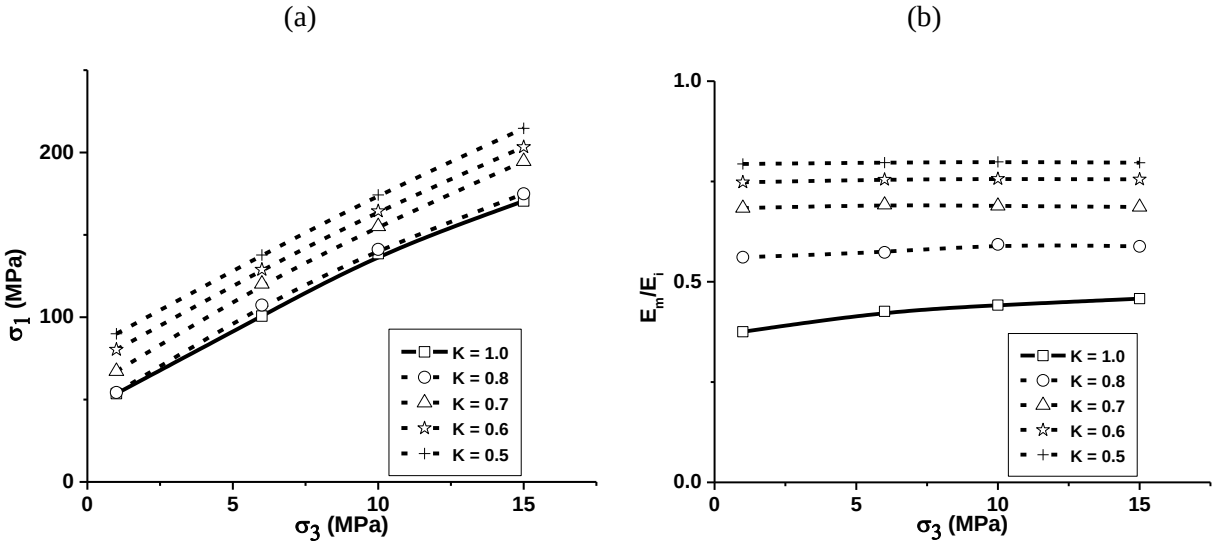

Figure 5-14 (a) Comparison of strength envelopes of jointed rock models with planar joints and different K; (b) (E_m/E_i)–σ_3 plots for jointed rock models with planar joints and different K.

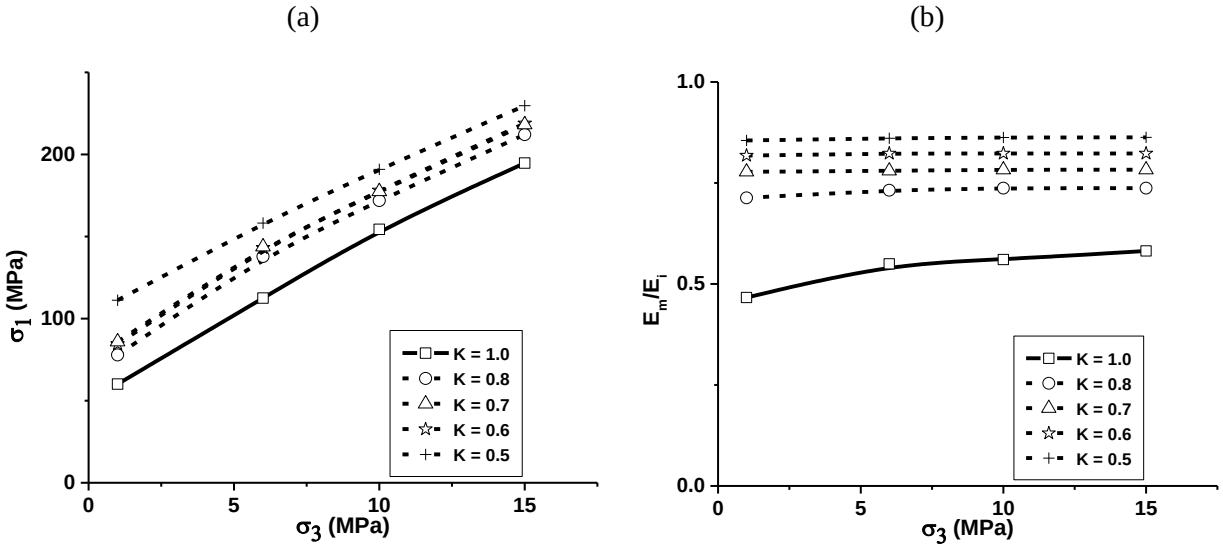

Figure 5-15 (a) Comparison of strength envelopes of jointed rock models with non-planar joints and different K; (b) E_m/E_i–σ_3 plots for jointed rock models with non-planar joints and different K.

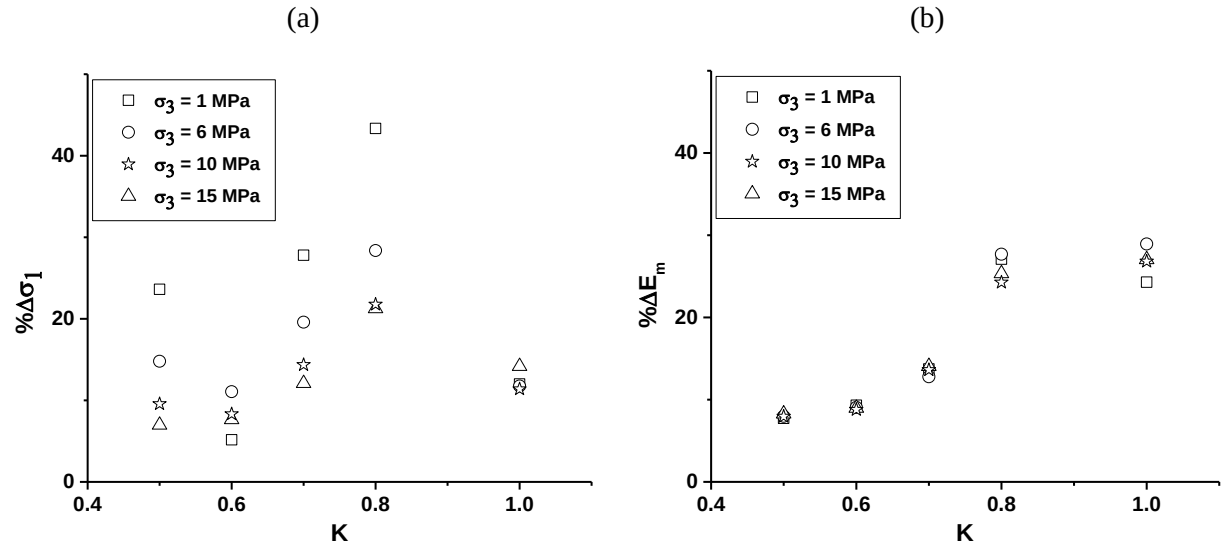

Figure 5-16 Percentage changes in (a) σ_1 and (b) E_m when the planar joints are replaced with non-planar joints for jointed rock models with different joint persistence.

The percentage changes of σ_1 and E_m of the jointed rocks when the planar joints are replaced by non-planar joints at different K values are presented in Figure 5-16. The percentage increments of σ_1 and E_m are proportional to the increase of K. The percentage increases of σ_1 and E_m are the

highest for the models with K = 0.8 and σ_3 = 1 MPa. The percentage increase of σ_1 decreases with the increase of σ_3; however, the percentage increase of E_m with the increase of σ_3 is relatively small.

The influence of joint persistence on the strength of jointed rocks with planar joints is quantified by deriving a bi-variate relation between σ_1, σ_3, and K as,

$$\sigma_1 = 42.26 - 59.47 \ln \mathrm{K} + 8.76\sigma_3 \quad \text{(MPa)} \tag{5-4}$$

for $0.5 \leq \mathrm{K} \leq 1.0$, $\sigma_3 \leq 15$ MPa, and $R^2 = 0.98$

Similarly, the influence of joint persistence on the deformability of the jointed rocks with planar joints is quantified by deriving a bi-variate relation between E_m and σ_3, K as,

$$E_m = 0.34 \ln(\sigma_3) - 28.7K + 44 \quad \text{(GPa)} \tag{5-5}$$

for $0.5 \leq \mathrm{K} \leq 1.0$, $\sigma_3 \leq 15$ MPa, and $R^2 = 0.98$

5.4 Mechanical response of jointed granite under true-triaxial loading

A rock mass in the field is under a true triaxial ($\sigma_1 > \sigma_2 > \sigma_3$) loading state. For convenience, conventional triaxial compression tests are usually conducted to investigate the mechanical behaviors of intact and jointed rocks. During a conventional triaxial compression test, the intermediate and the minor principal stresses are equal ($\sigma_1 > \sigma_2 = \sigma_3$). Studies have found that the intermediate principal stress (σ_2) has a large influence on the strength and deformability of intact rocks (Cai, 2008; Haimson, 2006; Mogi, 1967). Although some true triaxial tests were conducted on weak synthetic jointed rocks (Kulatilake et al., 2019; Tiwari & Rao, 2004), the influence of σ_2 on the strength and deformability of jointed hard rocks has not been studied experimentally.

In this section, the mechanical response of the jointed Blanco Mera granite is investigated numerically under the true triaxial loading condition. True triaxial compression simulations are

conducted on the same LS-SRM models (Models B and F, Figure 5-17) on which the conventional triaxial compression simulations were conducted except that the intact rock properties are used for the models with $2 < \sigma_3 \leq 12$ MPa as specified in Table 5-2; joint properties specified in Table 5-4 are used except that k_{nj} = 3000 GPa/m and k_{sj} = 300 GPa/m are used. Because the confinement range of interest in most civil and mining underground construction is between 0 and 15 MPa, the maximum σ_2 is limited to 15 MPa in the numerical simulation. The models are simulated under the confinement ranges of $2 \leq \sigma_2 \leq 15$ MPa and $2 \leq \sigma_3 \leq 10$ MPa, respectively. True triaxial compression simulations are conducted on the intact rock model, jointed rock Models B and F by varying σ_2 and σ_3 along x- and y-axis directions, respectively (Figure 5-17).

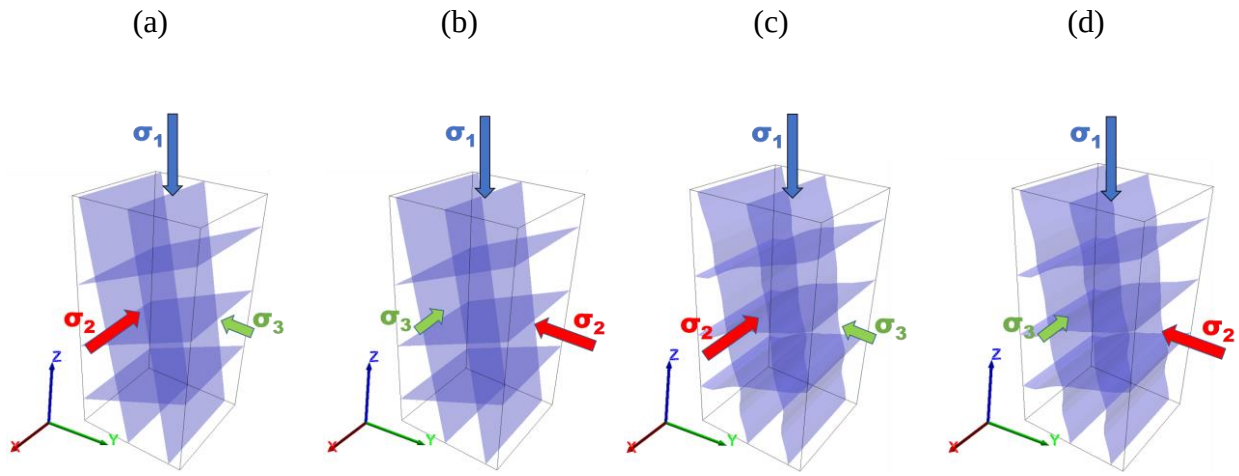

Figure 5-17 Illustration of true triaxial stress states: (a) Model B with σ_2 oriented perpendicular to the dip direction of the sub-vertical joint set; (b) Model B with σ_2 oriented parallel to the dip direction of the sub-vertical joint set; (c) Model F with σ_2 oriented perpendicular to the dip direction of the sub-vertical joint set; (d) Model F with σ_2 oriented parallel to the dip direction of the sub-vertical joint set.

The modeling results are presented in Figure 5-18, showing that the peak strengths (σ_1) of both the intact and the jointed granite (Figure 5-18) are affected by σ_2. At a constant σ_3, σ_1 increases with the increase of σ_2. As expected, the true triaxial strength of intact granite is higher than the true triaxial strength of jointed granite.

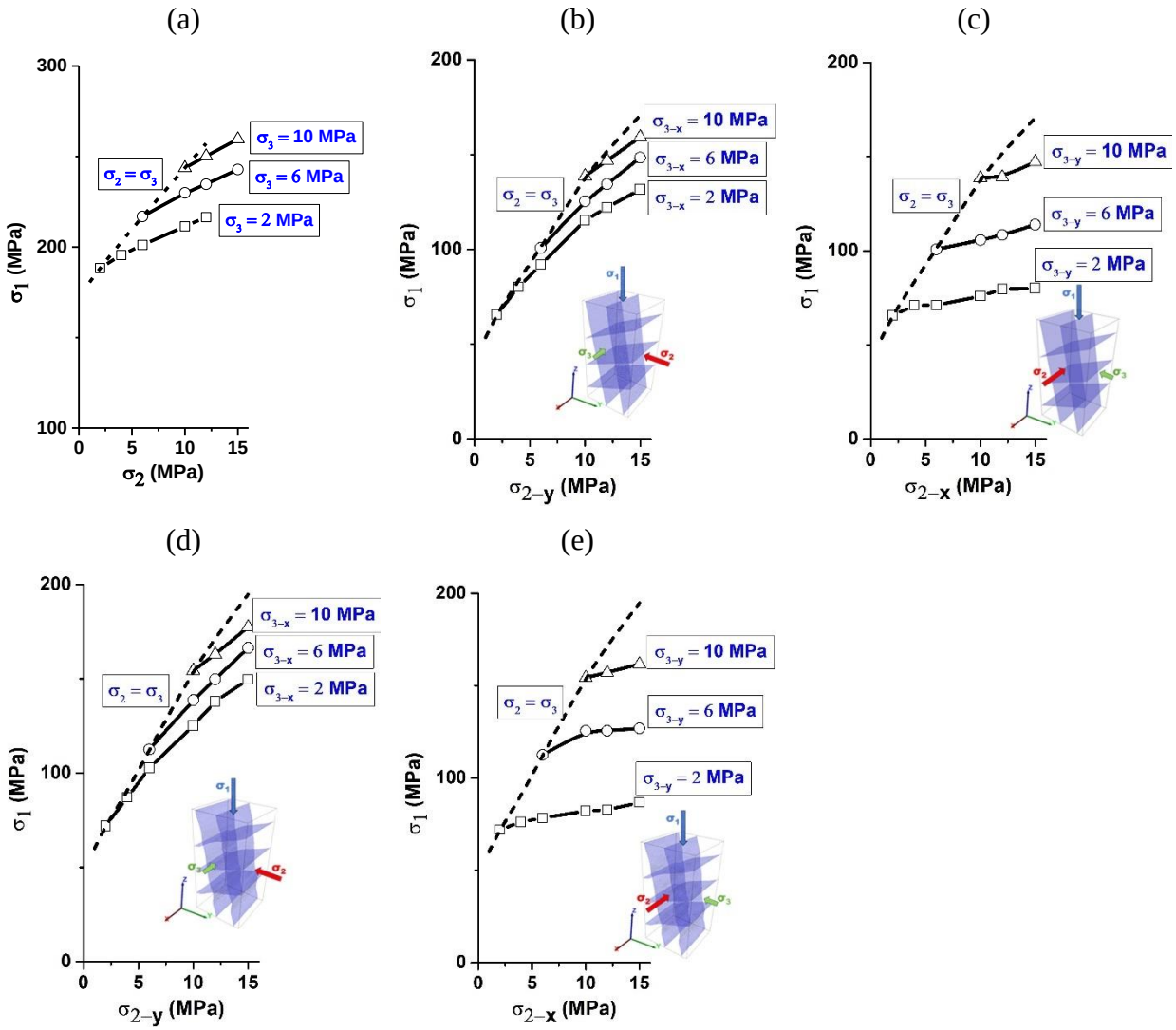

Figure 5-18 Strength envelopes under true triaxial loading condition: (a) intact rock model; (b) Model B with σ_2 along y-axis (see Figure 5-17 for the orientation of the coordinate system); (c) Model B with σ_2 along x-axis; (d) Model F with σ_2 along y-axis; (e) Model F with σ_2 along x-axis; strength envelope for conventional triaxial loading condition ($\sigma_2 = \sigma_3$) is shown as dashed lines.

For the jointed granite, σ_1 is influenced by the orientation of σ_2 relative to the joint sets. For instance, the rate of increase of σ_1 with the increase of σ_2 is higher for Model B (Figure 5-18b) and Model F (Figure 5-18d) when the dip direction of the sub-vertical joint set is orientated parallel to the direction of σ_2. This is due to the stiffening of the jointed rock due to joint closure and interlocking caused by σ_2. On the other hand, the rate of increase of σ_1 with the increase of σ_2 are

low for Model B (Figure 5-18c) and Model F (Figure 5-18e) when the dip direction of the sub-vertical joint set is orientated perpendicular to the direction of σ_2. Compared with Model B (Figure 5-18b&c), the peak strengths of Model F (Figure 5-18d&e) are higher.

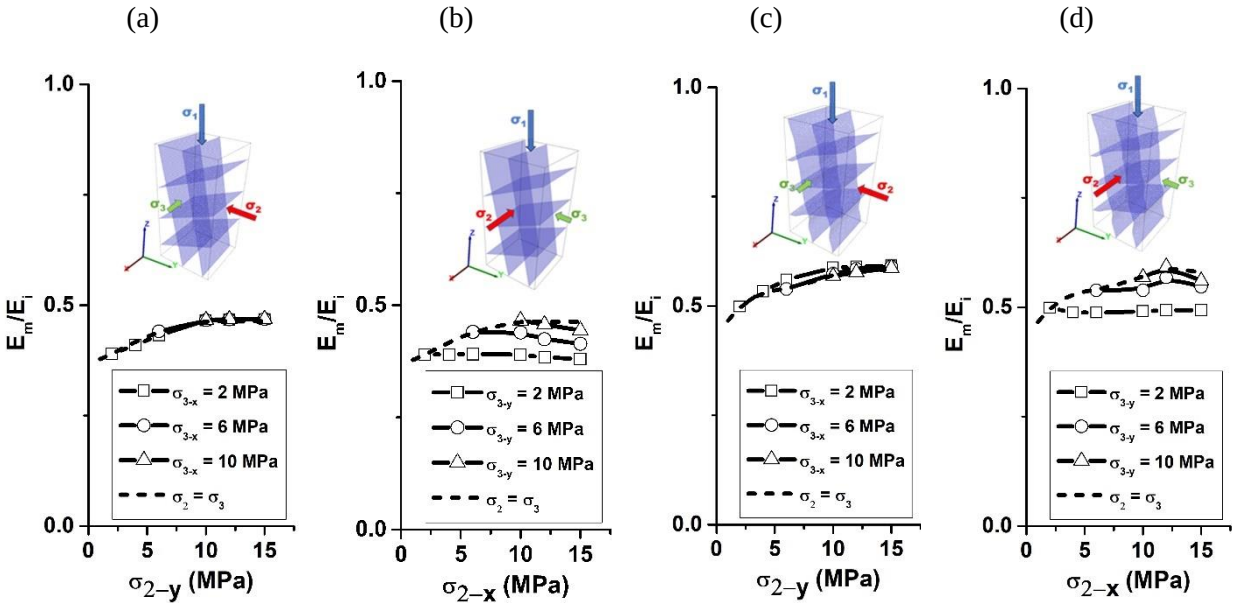

Figure 5-19 (a) E_m/E_i–σ_2 plot for Model B with σ_2 along y-axis; (b) E_m/E_i–σ_2 plot for Model B with σ_2 along x-axis; (c) E_m/E_i–σ_2 plot for Model F with σ_2 along y-axis; (d) E_m/E_i–σ_2 plot for Model F with σ_2 along x-axis; E_m/E_i–σ_2 plots for $\sigma_2 = \sigma_3$ are shown as dashed lines.

E_m/E_i remains constant for the intact rock model under the range of confining pressures used in this study. However, the E_m/E_i values of the jointed rocks (Models B and F) are influenced by both the magnitude and orientation of σ_2. The rate of increase of E_m/E_i with the increase of σ_2 is higher for Model B (Figure 5-19a) and Model F (Figure 5-19c) when the dip direction of the sub-vertical joint set (Figure 5-17b&d) is parallel to the direction of σ_2. On the other hand, the rate of increase of E_m/E_i with the increase of σ_2 is low for Model B (Figure 5-19b) and Model F (Figure 5-19d) when the dip direction of the sub-vertical joint set (Figure 5-17a&c) is perpendicular to the direction of σ_2. As expected, the value of E_m/E_i of Model F is higher than that of Model B.

The cracking mechanism is also influenced by the relative orientation of σ_2 with the dip direction of the sub-vertical joint set for both Models B and F. For the case where σ_2 is orientated perpendicular to the dip direction of the sub-vertical joint set, cracking is localized along the direction of σ_2; however, for the case where σ_2 is oriented parallel to the dip direction of the sub-vertical joint set, cracking is more uniform along all directions. Two examples are shown in Figure 5-20 to illustrate the cracking patterns at different deformation stages in Model F at σ_2 = 15 MPa and σ_3 = 2 MPa. The strength is higher for Model F with the orientation of σ_2 parallel to the dip direction of the sub-vertical joint set (Figure 5-20b).

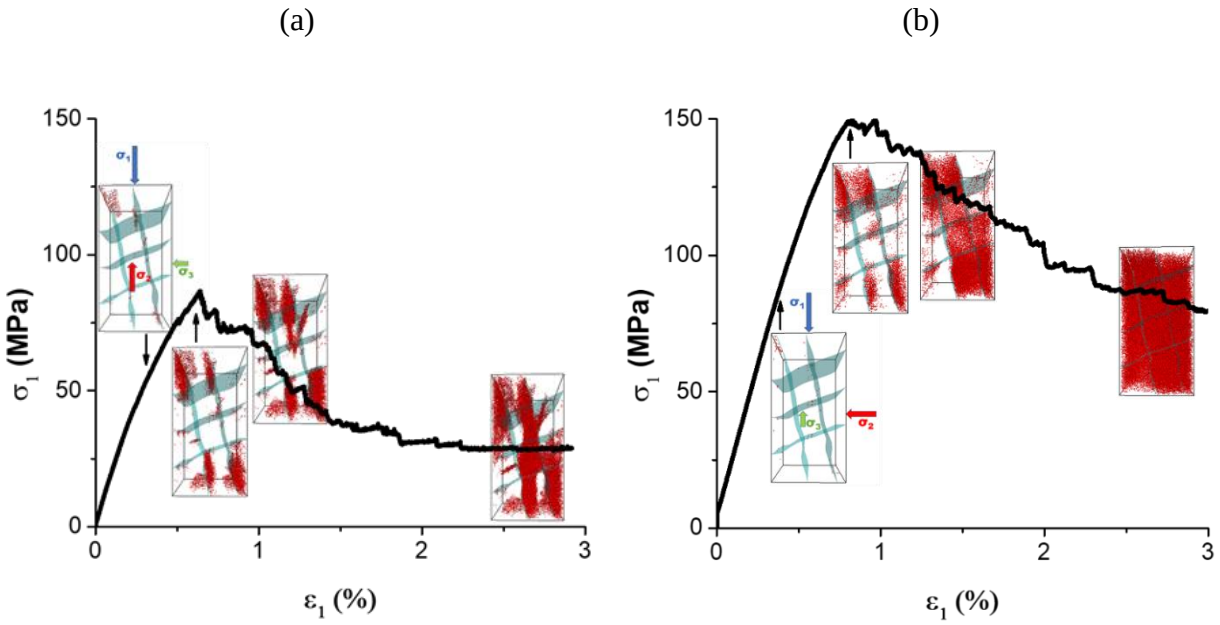

Figure 5-20 Illustration of crack propagation along the axial stress–axial strain curve for Model F under true triaxial loading condition at σ_2 = 15 MPa and σ_3 = 2 MPa: (a) σ_2 is oriented perpendicular to the dip direction of the sub-vertical joint set; (b) σ_2 is oriented parallel to the dip direction of the vertical joint set.

This is because that for the case that σ_2 is perpendicular to the dip direction of the sub-vertical joint set, the pre-existing sub-vertical joints dilate rather than close, which reduces the strength and

stiffness of the jointed rock. However, for the case that σ_2 is orientated parallel to the dip direction of the sub-vertical joint set, the pre-existing sub-vertical joints close, which increases the strength and stiffness of the jointed rock. This is more evident in the post-peak deformation stage.

5.5 Remarks

In this Chapter, the mechanical behavior of laboratory-scale jointed granite is investigated using the LS-SRM modeling approach. Intact and jointed granite models with planar joints are calibrated using laboratory triaxial test results. The lattice model parameters of the calibrated jointed rock model are used to investigate the mechanical response of jointed granite with different joint configurations (intensity, waviness, orientation, and persistence) under confined compression. The numerical modeling results suggest that the strength and deformability of the jointed rocks are highly depended on the orientation, intensity, waviness, and persistence of the joints.

As anticipated, the strength and deformation modulus of jointed granites are lower than those of the intact granite. Jointed granites exhibit a U-shaped strength curve with the increase of joint dip from 35° to 67° and the deformation modulus increases non-linearly with the increase of joint dip. Similarly, both the strength and deformation modulus decrease with the increase of joint intensity and persistence. The results of the numerical investigation are reasonably consistent with the laboratory test results (Arzua et al., 2014; Alejano et al., 2017).

In addition, the influences of joint waviness and the intermediate principal stress on the strength and deformability of jointed granite are studied. It is found that the strength and deformation modulus of the jointed rocks with non-planar joints are higher than the ones with planar joints. For both the intact and the jointed rock under true triaxial compression, it is shown that the strength and deformation modulus increase with the increase of the intermediate principal stress.

Furthermore, the cracking behavior and the degree of enhancement of strength and deformation modulus of jointed rocks depends on the relative orientation of the intermediate principal stress with the dip-direction of the dominant joint set, which influences the stiffening effect of the jointed rock due to joint clamping.

The numerical modeling investigations up to this Chapter focused on the mechanical behavior of laboratory scale intact and jointed rock. The next two chapters focus on the mechanical behavior of rock mass under compression and the influence of rock mass with different discontinuity properties on slope stability.

Chapter 6

6 Slope Stability of Cadia Open Pit Mine – A Case Study[5]

Slope stability is an important geotechnical issue in surface mining operation because slope failure can result in production halt, loss of mining machineries, and human casualties. Reliable slope design in civil and mining projects can not only improve safety but also avoid unexpected construction cost overrun due to slope failure. In the assessment of slope stability, the most important factors that need to be considered are the geometry of the slope and the mechanical properties of the jointed rock mass (intact rock and discontinuities). Structural discontinuities control the stability of a slope because these are the weakest component of the rock mass. Logically, the slope becomes increasingly unstable with the increase of unfavorably oriented discontinuities. Hence, it is vital to have a reliable estimate of the mechanical properties of intact rock and discontinuities to increase the reliability of rock slope engineering design. Mechanical properties of rock and discontinuities can be estimated by experimental and empirical methods and mechanical properties of jointed rock masses can be estimated using analytical, empirical, and numerical methods (Cai, 2010; Cai et al., 2007; Cai et al., 2004; Hoek & Brown, 2018). These mechanical properties can be used in slope design.

Slope design can be conducted using methods such as limit equilibrium method, empirical design method, numerical modeling method, physical model testing, and probabilistic-based design method (Sjoberg, 1996). Out of these design methods, the numerical modeling approach is the most popular in recent years. Among the numerical modeling methods, the discontinuum method

[5] The manuscript is submitted with minor revision to the Journal of Rock Mechanics and Geotechnical Engineering.

is better suited than the continuum method to simulate slope stability problems because the continuum method cannot simulate crack development, large deformation, and rotation of pre-existing discontinuities. Discrete element methods (DEM) such as the bonded particle method (BPM) and the bonded block method (BBM) are widely used. Synthetic rock mass (SRM) modeling methods based on BPM (Section 2.5.5.1), BBM (Section 2.5.5.2), and most recently lattice spring model (Section 2.5.5.3) have been traditionally used for the stability assessment because they can explicitly represent the pre-existing discontinuities and crack evolution from these discontinuities.

In all the previous studies, discontinuities are simplified into planar surfaces for convenience, which is clearly not the case in natural geological settings. There is a large influence of non-planar crack geometry on the cracking mechanism and mechanical properties (strength and deformability) of laboratory-scale pre-cracked rocks (Bastola & Cai, 2019). The influence of non-planar discontinuities on the strength and deformation behavior has been demonstrated from the LS-SRM modeling results in previous Chapters 4 and 5. Hence, it is hypothesized in this Chapter that the large-scale discontinuity waviness can have a large influence on slope stability and deformability.

In this Chapter, the south wall slope failure at Cadia Hill open pit mine in Australia is simulated using the LS-SRM modeling approach in the Slope Model. LS-SRM models are built using Slope Model because it allows explicit representation of pre-existing discontinuities (both planar and non-planar). The influence of the discontinuity of different configurations (intensity, size, waviness) and *in-situ* stress on the deformability and stability of the open pit slope are investigated.

The utility of Slope Model software is verified by comparing the model results of a hypothetical rock slope experiencing planar failure with the analytical solution (Section 6.1). An overview of

the mine site and the previous studies conducted on the open pit stability assessment is summarized in Section 6.2. Discrete fracture network (DFN) and the slope model for the slope are developed, and the mechanical properties of intact and jointed rocks are calibrated in Section 6.3. Using the calibrated slope model parameters, the influences of different discontinuity configurations and *in-situ* stresses on the stability of the slope are investigated in Section 6.4. The concluding remarks of the modeling results are presented in Section 6.5.

6.1 Validation of Slope Model

Extensive verification and validation of the Slope Model software had been conducted by Itasca, which demonstrated the capability of this software to perform slope stability assessment. The code was validated by comparing the numerical modeling results with analytical solutions, experimental results, and alternative numerical solutions (Varun & Damjanac, 2012; Cundall et al., 2016). Since the initial publication of the validation report (Varun & Damjanac, 2012), the software has been extensively updated.

In this section, a slope stability problem of a planar failure is simulated to validate the tool. In this revalidation exercise, the factor of safety is computed for the slope with a cohesionless persistent planar discontinuity and the modeling result is compared with the analytical solution.

The safety factor can be computed using the analytical solution as the ratio of resisting forces (friction) to the driving forces (gravity) acting parallel along the direction of sliding and can be written as (Wyllie, 2017b),

$$FS = \frac{\tan \varphi_j}{\tan \theta} + \frac{2c}{\gamma H \sin^2(\alpha)\,[\cot(\alpha) - \cot(\beta)]} \tag{6-1}$$

where φ_j, θ, and c are friction angle, dip angle, and cohesion, respectively of the sliding discontinuity surface. For a cohesionless and dry discontinuity surface where the failure occurs purely under the influence of gravity, the relation can be reduced to,

$$FS = \frac{\tan \varphi_j}{\tan \theta} \tag{6-2}$$

In the generated model, height, width, and the angle of inclination of the slope are 150 m, 100 m, and 75°, respectively (Figure 6-1). The dip angle is kept constant at 30° for both slopes with planar discontinuity (Figure 6-1a) and non-planar discontinuity (Figure 6-1b). The planar discontinuity is generated using the joint-set builder in Slope Model and the non-planar discontinuity is generated in MoFrac (see Section 2.5.4.2).

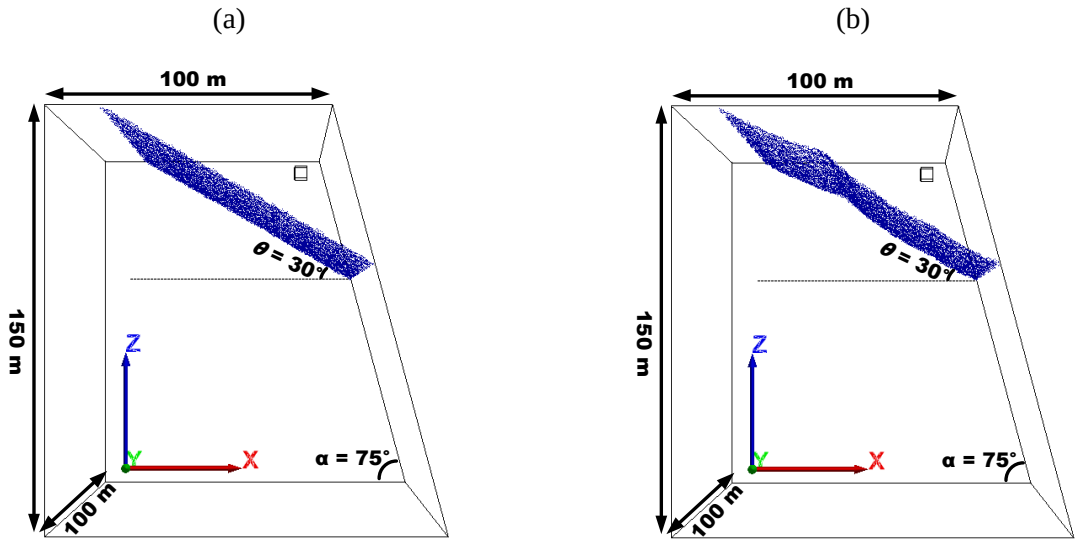

Figure 6-1 Schematics for the planar failure analysis of a slope with a single (a) planar and (b) non-planar discontinuity.

Stability of the slope is assessed by reducing the φ_j values in the order of 30.5°, 30.0°, 29.5°, 29.0°, and so on until the slope fails. The sliding occurs only under the influence of gravity. Velocity history is recorded with time to evaluate the failure of the slope. In the case of the stable slope,

velocity converges to zero; however, in the case of the unstable slope, velocity increases progressively with time. Based on Eq.(6-2), $FS = 1$ for a cohesionless, dry, and planar discontinuity with $\varphi_j = \theta$. Hence, the slope should be stable when both $\theta < (\varphi_j = 30.0°)$ for a cohesionless, dry, and planar discontinuity. Slope modeling result suggests that the slope with planar discontinuity is stable when $\varphi_j \geq 30°$ (Figure 6-2a & Figure 6-3a) and unstable when $\varphi_j < 30°$; for example, when $\varphi_j \leq 29.5°$, the slope with the planar discontinuity is unstable (Figure 6-2a & Figure 6-3b).

In addition, although no analytical solution is available, the stability of the slope with the non-planar discontinuity is assessed by reducing φ_j values in the order of 30.5°, 30.0°, 29.5°, 29.0°, and so on until the slope fails. The slope with a non-planar discontinuity is stable for $\varphi_j \geq 16.5°$ (Figure 6-2b & Figure 6-3c) because in this case the additional resisting force is provided due to interlocking on the asperities. The slope with a non-planar discontinuity is found to be unstable for $\varphi_j \leq 16°$ (Figure 6-2b & Figure 6-3d).

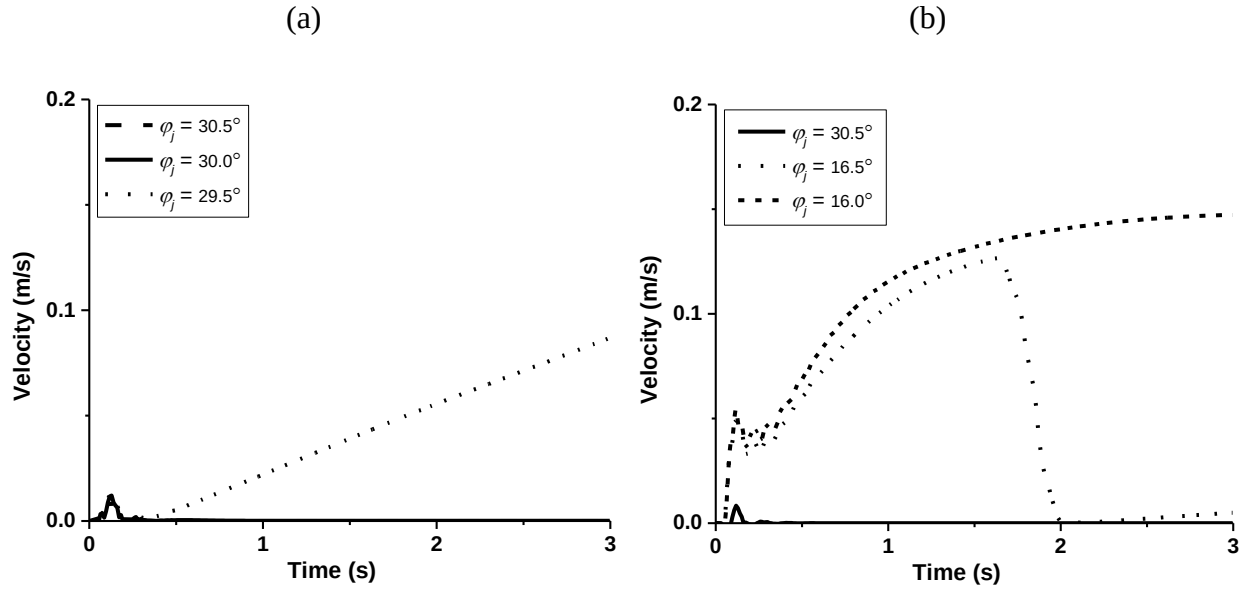

Figure 6-2 Velocity–time plot in x-direction for stable and unstable slope with (a) planar and (b) non-planar discontinuity.

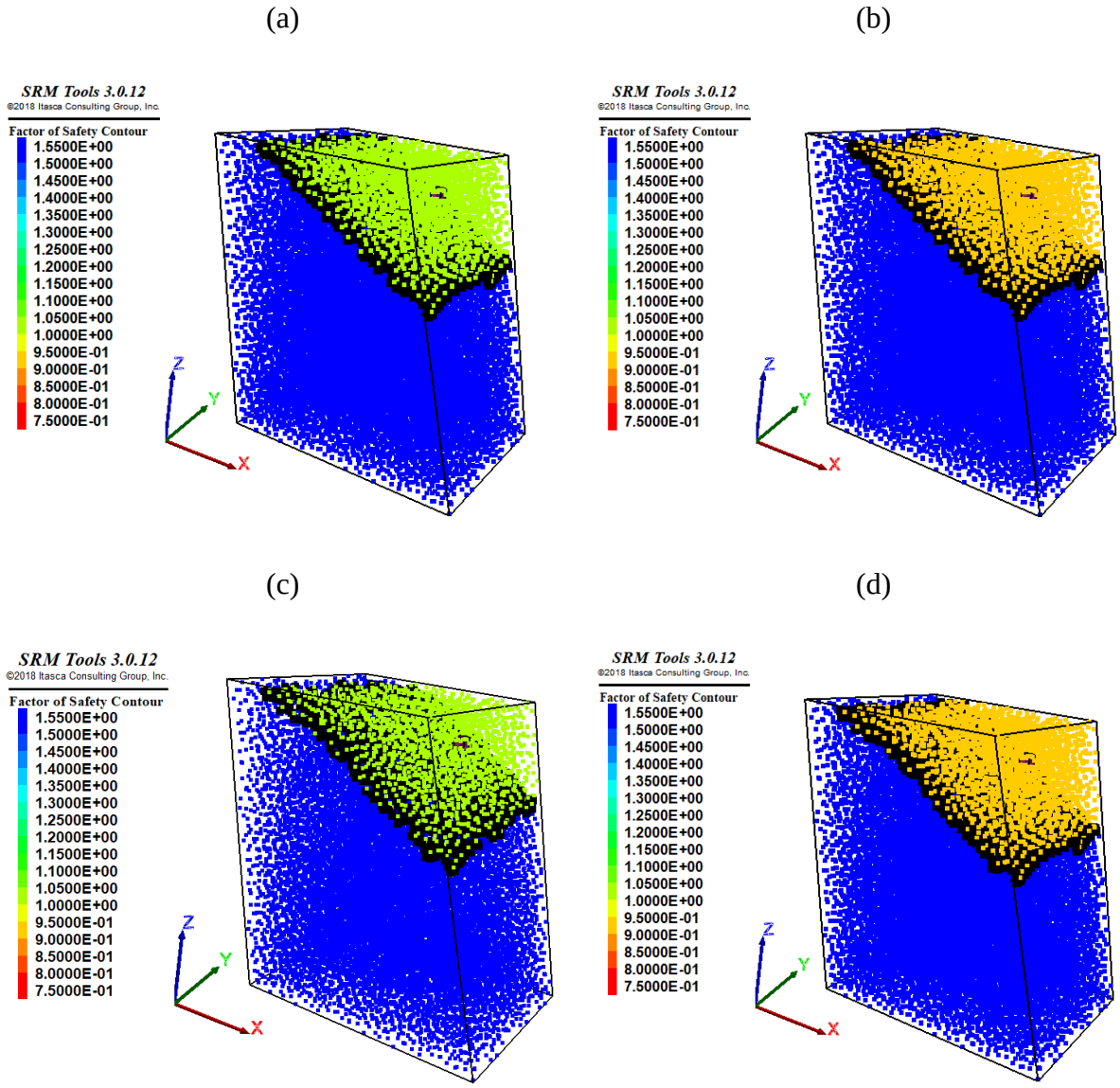

Figure 6-3 Factors of safety for the slope with planar discontinuity with (a) φ_j = 30° and (b) φ_j = 29.5°, and the one with non-planar discontinuity with (c) φ_j = 16.5° and (d) φ_j = 16°.

To ensure the capability of SRMTools to properly simulate the mechanical behavior of non-planar discontinuity, four direct shear simulations are conducted in SRMLab under the normal stress of 0.1, 0.5, 1, and 2 MPa using the lattice size of 100 cm on rock mass models of dimensions 150 m × 150 m × 15 m with the same non-planar discontinuity employed in the Slope Model validation. All the lattice material properties are same as the ones used in the planar failure validation using

Slope Model except that the joint friction angle is kept at 30° for all four simulations. Sensitivity analysis exercise performed in Section 6.3.4 suggest that the lattice size of 150 cm is sufficient to simulate the cracking mechanism on the wall of the rough discontinuity.

Direct shear simulation results show that the peak shear strength (Figure 6-4a) of the non-planar discontinuity increase with the increase of the confining normal stress as suggested by Patton (1966). In addition, peak joint friction angle (φ_p) (Figure 6-4b), and dilation angle (δ_j) (Figure 6-4c) also decrease with the increase of the confining normal stress. This is because that at low confining normal stress ($\sigma_n \leq 1$ MPa), shear strength is attributed to the dilation of the joints and riding of the asperities and at high confining normal stress ($\sigma_n \geq 1$ MPa), shear strength is attributed to the shearing off of the asperities and joint closure. Similar behavior was also observed by (Barton & Choubey, 1977; Barton, 1973) during laboratory shear tests of very rough fractures.

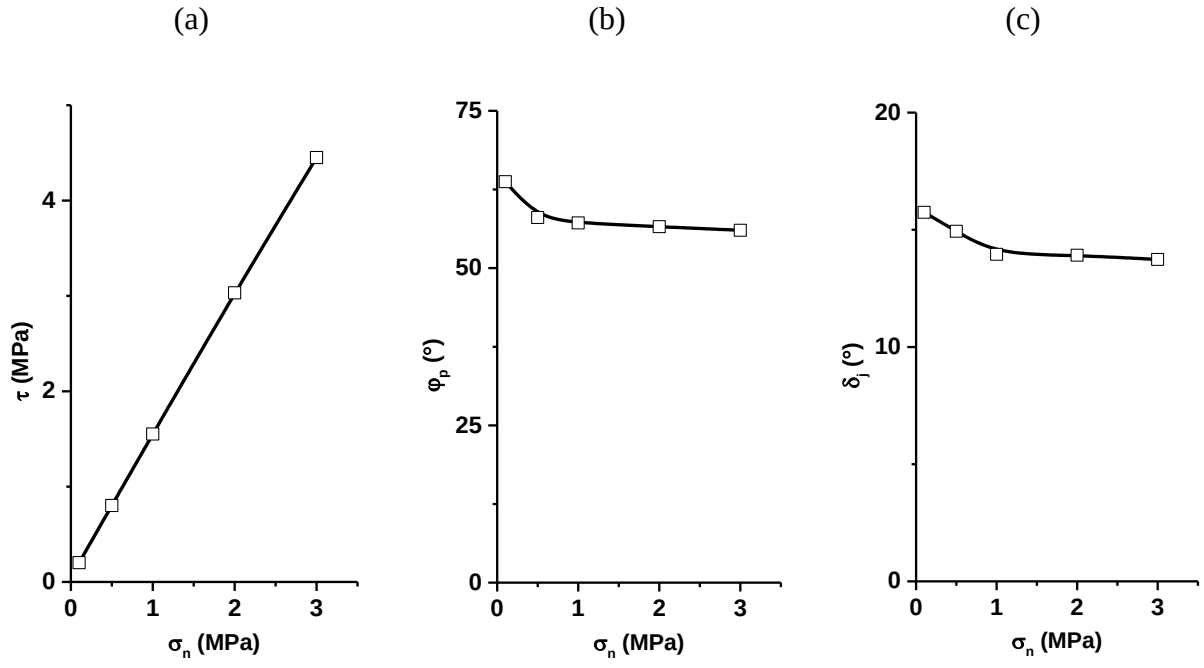

Figure 6-4 Influence of normal stress on the (a) peak shear strength (b) peak friction angle, and (c) dilation angle on the non-planar discontinuity.

6.2 A brief overview of Cadia Hill open pit

Cadia Hill Open Pit gold mine is operated by Cadia Valley Operations, a subsidiary of Newcrest Mining Limited (Sainsbury et al., 2007). The mine is located within a complex geological setting near Orange in New South Wales, Australia, approximately 250 km west of Sydney. Mining of the pit began in 1997. The pit width is about 1500 m and the final pit depth as per the design in 2005 is 580 to 720 m deep. The designed inter-ramp slope angle is 35°–65° depending on the strength of rock mass (Figure 6-5).

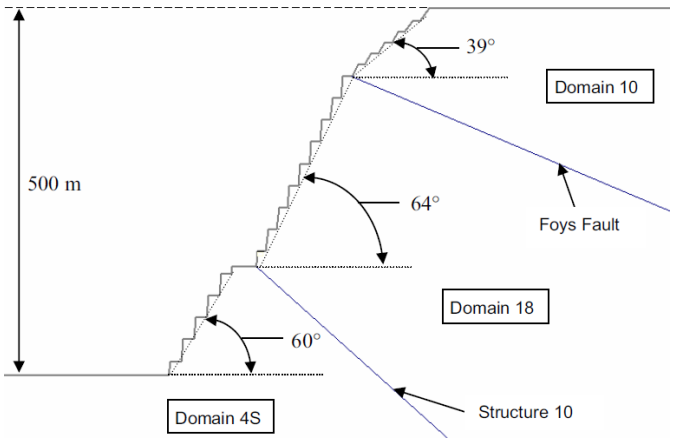

Figure 6-5 Cross-section of Cadia Hill open pit south slope (Franz, 2009).

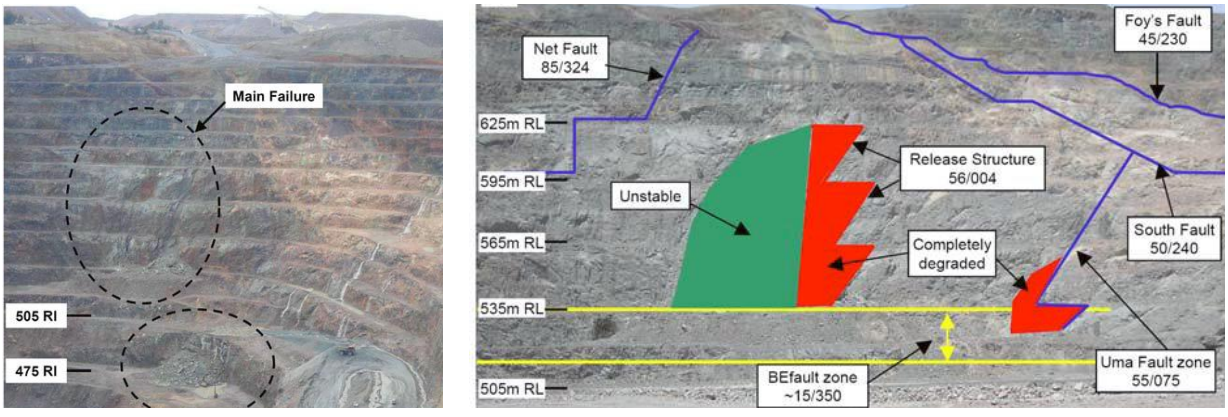

Figure 6-6 Failure location on the south wall of Cadia Hill open pit mine (Sainsbury et al., 2007).

In 2006, the mine experienced a multi-bench failure in the center of the south wall from 535–625 m RL levels (Domain 18) while mining at 505 m RL level (Figure 6-6). The rock mass at the failed location was composed of Monzonite. The failure mechanism involved was a combination of both the geological structure and rock mass failures. A large shear structure that was sub-parallel to the pit face at an orientation of 56°/004° formed a basal sliding failure plane (Figure 6-6). The failed structure does not form a daylighting wedge; hence, the failure cannot be back analyzed using the traditional limit equilibrium or the simple continuum models (Sainsbury et al., 2007). The conceptual model for the slope failure mechanism is shown in Figure 6-7, showing a combined failure of sliding along the shear structure and tensile and shear failures of the rock mass (Franz, 2009; D. Sainsbury et al., 2007). The prevalent lithology of the south wall is monzonite Volcanics and Silurian sediments associated with faulting. The rock mass at the south wall is characterized by moderate-to-high RQD values and high intact rock strength (120–160 MPa) (Sainsbury et al., 2007). Based on the drillhole and bench face mapping data, geological strength index (GSI) values for the rock mass at Domain 18 and the BE-Fault zone are 60–70 and 40–50, respectively. The structural geology of the south wall is complex because of four deformation episodes that have resulted in curvilinear discontinuity structures.

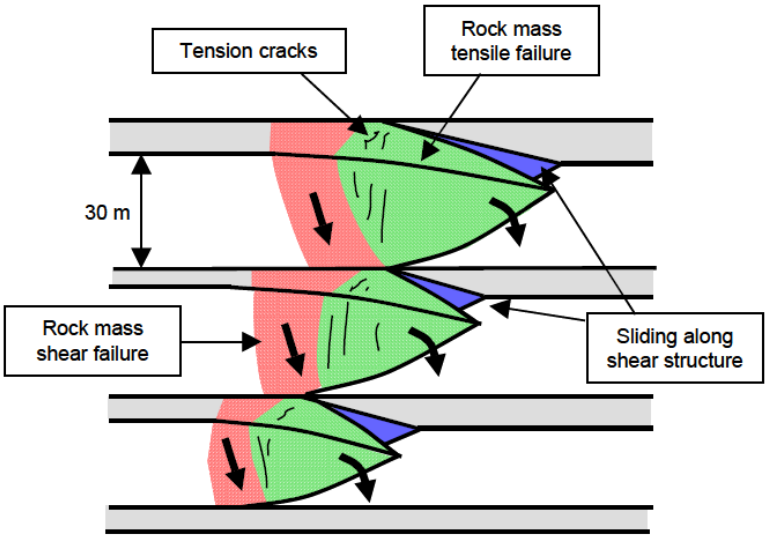

Figure 6-7 Conceptual model of the failure mechanism on the south wall of Cadia Hill open pit mine (Sainsbury et al., 2007).

Sainsbury et al. (2007) simulated the failure of the south wall using 3DEC. Although the model predicted slope displacements agreed, to some extent, with the field measured data, the model did not explicitly represent the discontinuities and the mechanical properties of the rock were downgraded using the GSI approach. Franz (2009) conducted a parametric study using various conceptual slope models of Cadia Hill open pit using both continuum and discontinuum modeling approaches and indicated that the slope stability is influenced more by discontinuity continuity (persistence) than by discontinuity spacing (intensity). Neither of these studies modeled discontinuities as non-planar features.

6.3 Model development and calibration

In this study, the Slope Model software is used to simulate the main failure of the south wall at Cadia Hill open pit mine. Discontinuities are represented as a DFN, which is generated using MoFrac that can represent both planar and non-planar discontinuities. First, the intact rock model is created, and the lattice micro-parameters are adjusted to match the reduced macro-mechanical

properties for the intact rock (Section 6.3.1). Then the DFN model (Section 6.3.2) that is representative of the discontinuity structures in Domain 18 is generated in MoFrac and is incorporated into the intact rock model to generate the LS-SRM models (Section 6.3.3).

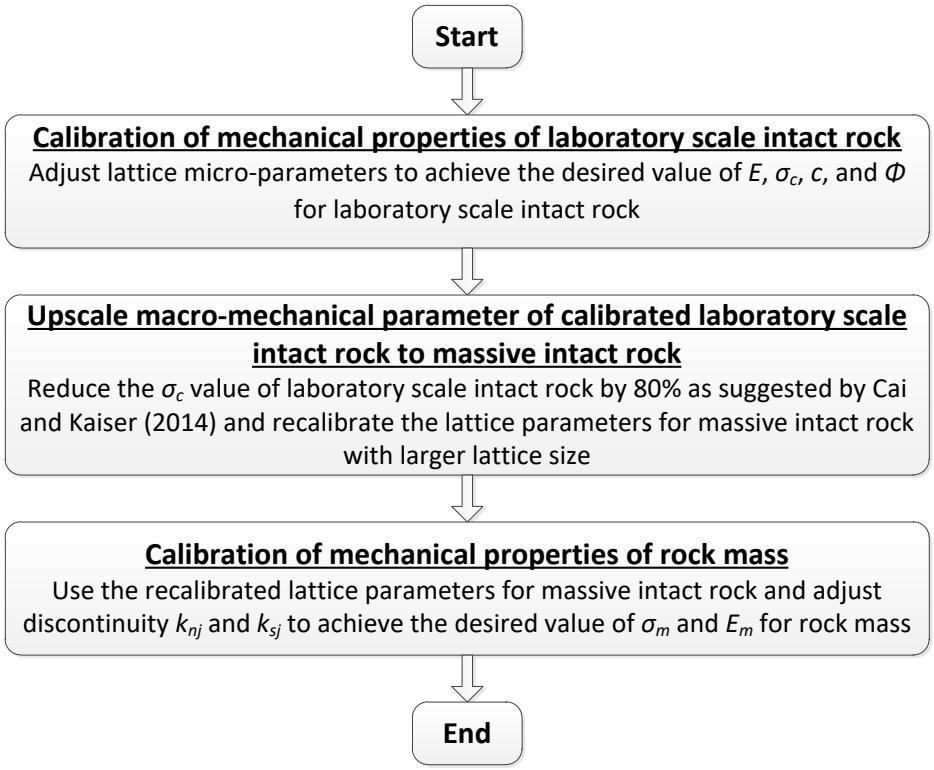

Figure 6-8 Calibration approach for upscaling the mechanical properties of laboratory-scale specimens to the ones that are equivalent for the massive rock mass, where E – Young's modulus of intact rock, σ_c – compressive strength of intact rock, c – cohesion of intact rock, φ – angle of internal friction of intact rock, k_{nj} – joint normal stiffness, k_{sj} – joint shear stiffness, σ_m – compressive strength of rock mass, and E_m – rock mass deformation modulus.

The calibration methodology previously established for the laboratory-scale jointed rock models (Bastola & Cai, 2019) is adjusted for the calibration of mechanical properties of large-scale rock mass models (Figure 6-8). The target mechanical properties of rock mass for the calibration of the LS-SRM model are derived from Sainsbury et al. (2007). The slope is excavated in the calibrated

LS-SRM model using Slope Model and the result is validated using the field displacement data (Section 6.3.4).

6.3.1 Intact rock model

The intact rock model is generated with a dimension of 5 m × 5 m × 10 m. The intact rock model is calibrated to two sets of lattice parameters, one for the intact monzonite, and the other for the slightly weaker rock within the BE-Fault zone. The size of the intact rock model that is to be calibrated is significantly larger than the size of conventional laboratory specimens. Cai & Kaiser (2014) suggested that the value of the peak *in-situ* strength of the massive intact rock should be about 80% of compressive strength (σ_c) that is measured in the laboratory-scale specimens. Thus, the calibration targets of σ_c for both the intact Monzonite and the BE-Fault material are reduced to 80% of their respective laboratory σ_c. Voronoi-shaped lattice is used because the lattice resolution of Voronoi-shaped lattice does not exhibit scale effect on σ_c and E for massive intact and jointed rocks (see Section 6.3.3). For initial model calibration, a lattice size of 18.75 cm is used, which results in about 26 lattices in the shortest dimension (5 m) of the synthetic specimen. A loading rate of 0.02 m/s is used along with the flat-joint contact model in the simulations.

Calibration of the massive intact rocks is performed by carrying out unconfined and confined compression simulations ($\sigma_3 \leq 6$ MPa) and comparing the simulation results with the scale-adjusted laboratory test results. The confinement limit of 6 MPa is sufficient because the *in-situ* stress in the pit is roughly in the range of 0 to 6 MPa. σ_c of the laboratory-scale intact Monzonite and the weaker BE-Fault material are (120–160) MPa and (80–120) MPa, respectively, as reported by Sainsbury et al. (2007) and Franz (2009). The uniaxial compressive strengths of the intact Monzonite and the weaker intact BE-Fault material are calibrated to σ_c of 116.5 and 85.3 MPa,

respectively (Figure 6-9a). Elastic moduli (E) of the intact Monzonite and the weaker BE-Fault material are calibrated to 63.1 and 43.6 GPa, respectively. Similarly, based on the triaxial compression test data of the intact Monzonite and the weaker BE-Fault material, c and φ values are calibrated to 19.4 MPa and 51.9° and 16.6 MPa and 46.5°, respectively for the two materials (Figure 6-9b). The calibrated lattice model parameters for both rocks are shown in Table 6-1.

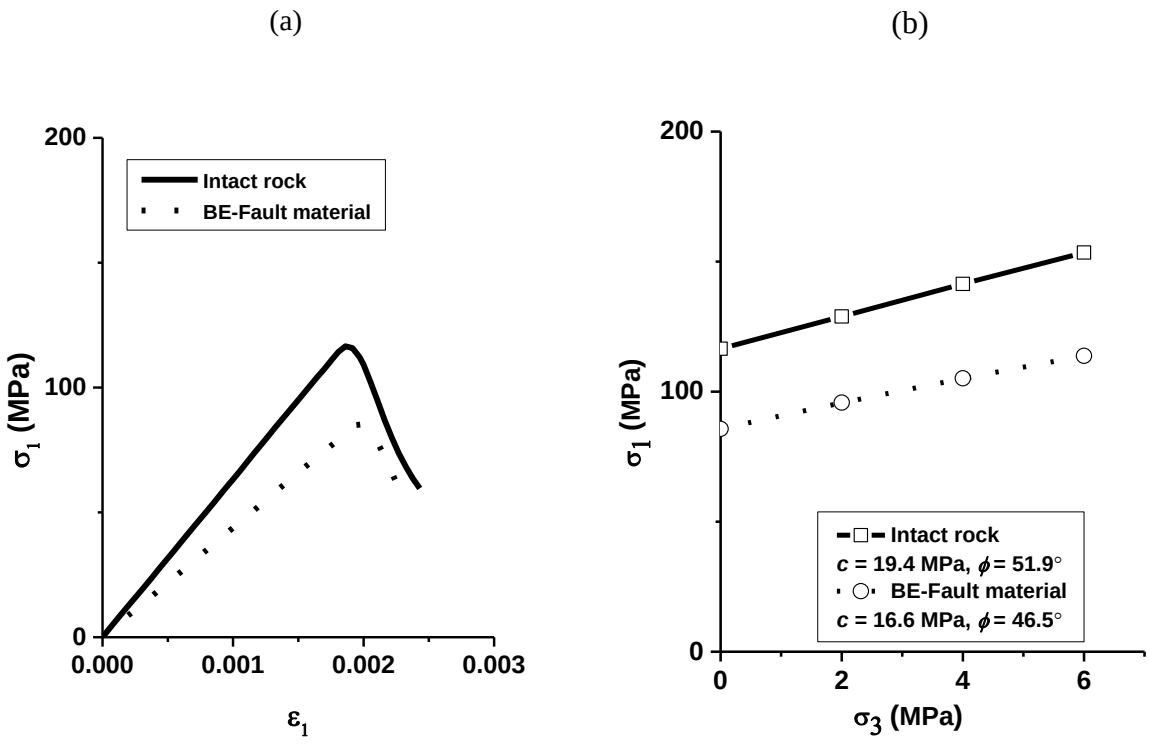

Figure 6-9 (a) Axial stress–axial strain relation for intact monzonite (solid line) and BE-Fault material (dotted line) under unconfined compression. (b) Strength envelopes for intact monzonite (solid line) and BE-Fault material (dotted line) under triaxial compression.

Table 6-1 Input lattice parameters used for the calibration of mechanical property of intact rock

Model parameters	Intact Monzonite	BE-Fault material
E_{mic} (GPa)	65	45
σ_{cmic} (MPa)	55	45
$(\sigma_t)_{mic}$ (MPa)	5	4
ρ (kg/m^3)	2700	2700
Porosity (%)	2	2
φ_{fjp} (°)	50	45
φ_{fjr} (°)	0	0
Radius multiplier	0.9	0.9

6.3.2 DFN model

The dimension of the DFN model generated in this study is 250 m × 200 m × 150 m. DFNs are generated using MoFrac because it can generate realistic non-planar discontinuities. To ensure that the spatial locations of all the discontinuities in the DFN with planar and non-planar discontinuities are the same, the DFN with non-planar discontinuities is exported to the Fracman file format (.fab) in MoFrac to generate planar discontinuities. Joint parameters such as joint orientation, intensity, size, and waviness factor are used to generate DFNs. The joint parameters for the DFN model generation are adapted from Sainsbury et al. (2007) and (Franz, 2009; Wilson, 2003). Discontinuities are stochastically represented as discontinuity sets based on orientation distribution. The discontinuity orientation data from (Franz, 2009; Wilson, 2003) were plotted in DIPS (Rocscience, 2016) and six discontinuity sets were identified (Figure 6-10). The dominant

joint set is south dipping with an average dip of 68°. All discontinuity sets are assigned a Fisher distribution value of k_f = 700 to reduce the dispersion of orientation distribution.

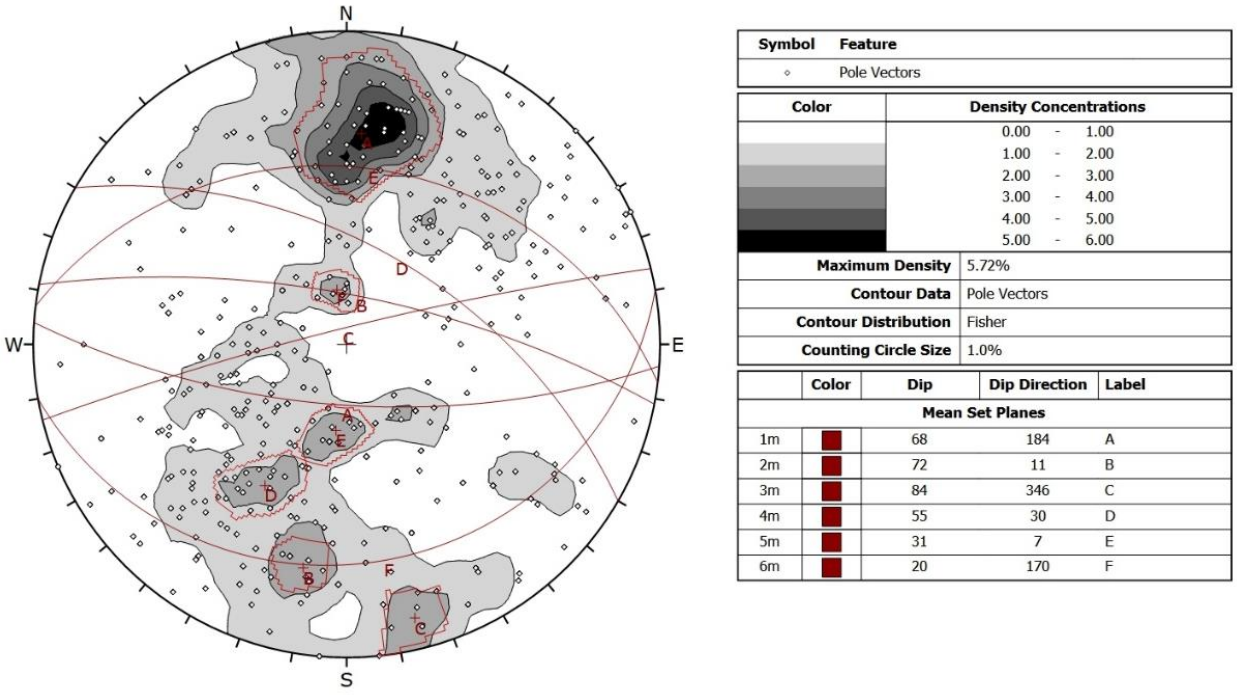

Symbol	Feature
◇	Pole Vectors

Color	Density Concentrations
	0.00 - 1.00
	1.00 - 2.00
	2.00 - 3.00
	3.00 - 4.00
	4.00 - 5.00
	5.00 - 6.00

Maximum Density	5.72%
Contour Data	Pole Vectors
Contour Distribution	Fisher
Counting Circle Size	1.0%

	Color	Dip	Dip Direction	Label
Mean Set Planes				
1m		68	184	A
2m		72	11	B
3m		84	346	C
4m		55	30	D
5m		31	7	E
6m		20	170	F

Figure 6-10 Stereonet for all six fracture groups.

The fracture intensity parameter, cumulative area distribution (CAD), is derived from the discontinuity length data (Franz, 2009; Wilson, 2003). In order to convert length into area, a discontinuity is assumed to have a length ratio of 2 along the strike and the dip direction. The number of discontinuities per volume (P_{30}) is extracted for each discontinuity set by weighting the discontinuity sets for the number and size of discontinuities within the experimental volume. Non-planar discontinuities are generated using the slope deviation parameter (SD) which allows the random deviation of the discontinuity along the orientation plane. The DFN parameters used to generate the base case DFN model are shown in Table 6-2.

Table 6-2 DFN parameters for the discontinuities at the south wall of Cadia Hill open pit mine

Set #	Dip (°)	Dip dir. (°)	k_f	A_1 (m^2)	A_2 (m^2)	$(P_{30})_1$ ($1/m^3$)	$(P_{30})_2$ ($1/m^3$)	SD	A_{min} (m^2)	A_{max} (m^2)
A	68	184	700	0.78	7854	0.627	6.27×10^{-7}	0.5	50	10,000
B	72	11	700	0.78	7854	0.076	7.6×10^{-8}	0.5	50	10,000
C	84	346	700	0.78	7854	0.091	9.1×10^{-8}	0.5	50	10,000
D	55	30	700	0.78	7854	0.144	1.44×10^{-7}	0.5	50	10,000
E	31	7	700	0.78	7854	0.144	1.44×10^{-7}	0.5	50	10,000
F	20	170	700	0.78	7854	0.100	1×10^{-7}	0.5	50	10,000

Note: k_f – Fisher constant, SD – Slope deviation parameter.

The DFN model with non-planar discontinuities generated using the field measured discontinuity parameters of the Cadia Hill south wall is referred to as base case DFN. The waviness of the non-planar discontinuities corresponds to the slope deviation of 0.5; slope deviation is the waviness parameter in MoFrac which allows the discontinuity to deviate along the mean orientation plane. The range of this parameter is 0-1.0. The mean value of 0.5 is estimated by back analyzing through trial and error. The close resemblance of the input and the output CAD parameters for all six discontinuity sets in Figure 6-11 validates the generated base case DFN model. The base case DFN model has a P_{32} value of 0.4 m^{-1}.

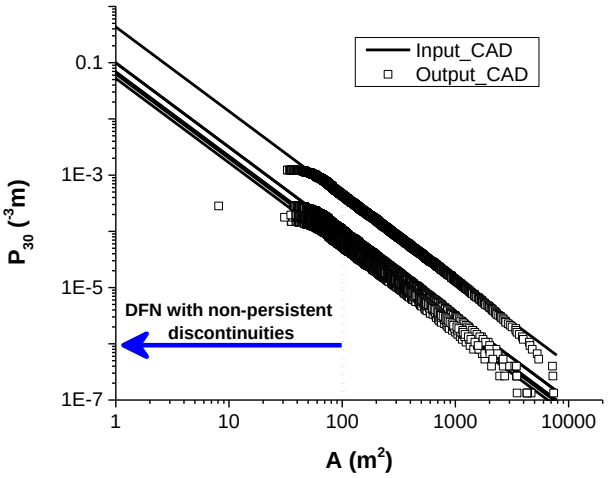

Figure 6-11 Comparison of input and output cumulative area distributions (CAD) for base case DFN.

In addition to the base case DFN model (Figure 6-12a), DFN models with smaller discontinuity size (Figure 6-12b) and higher discontinuity intensity (Figure 6-12c) are also generated. The DFN with smaller discontinuities is generated by reducing the value of A_{max} in Table 6-2 to 100 m^2 while keeping all the other parameters the same. The DFN with a higher discontinuity intensity (P_{32} = 0.72 m^{-1}) is generated by changing the values of A_1, A_2, and A_{max} in Table 6-2 to 1, 10,000, and 20,000 m^2 respectively while keeping all the other DFN parameters the same. The generated DFNs are also exported to the .fab file format to produce DFNs with planar discontinuities in the same spatial locations. It is noted that the DFNs generated in this study are purely stochastic and each realization is different from another. Hence, it is recommended to constrain the DFN to known spatial locations of the field mapped discontinuity trace data, if available.

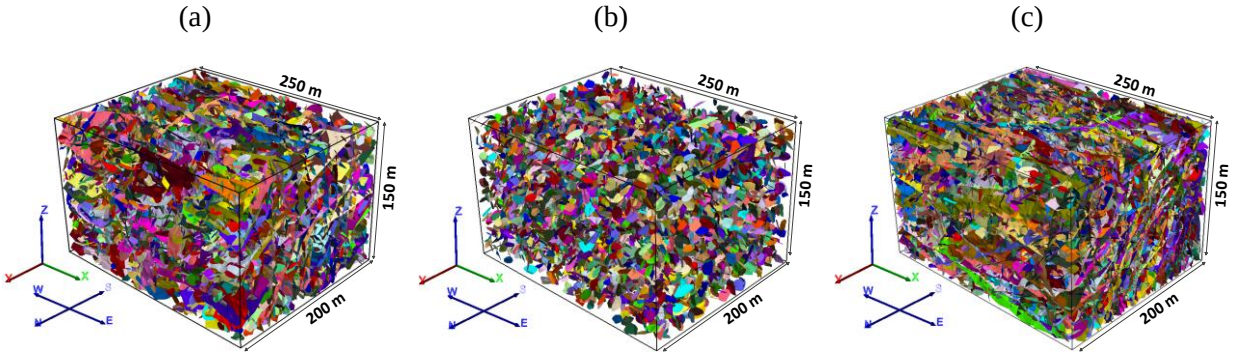

Figure 6-12 DFN models with non-planar discontinuities: (a) base case, (b) reduced discontinuity size, (c) increased discontinuity intensity.

6.3.3 Jointed rock mass model

The dimension of the pit slope model is 250 m × 200 m × 150 m, which is the same as the DFN model. Jointed rock mass models are generated by integrating the DFN models (Section 6.3.2) with the calibrated intact rock model (Section 6.3.1). Six jointed rock mass models are generated using DFNs with different discontinuity intensities, size, and waviness. The stability and deformability of the slope excavated in these rock mass models are assessed using Slope Model in Sections 6.3.4 and 6.4.

The generated base case SRM model is validated by performing UCS simulations on the representative elementary volume (REV) samples and comparing the corresponding strength and deformation modulus to the ones back-calculated from the empirical relations (Sainsbury et al., 2007). A study on the scale-effect of the mechanical properties of rock mass suggests that the rock mass sample size of 10 m × 10 m × 20 m is the REV size of the rock mass. The base case jointed rock mass model with non-planar discontinuities is calibrated to the peak compressive strength (σ_m) and the deformation modulus (E_m) of 3.2 MPa and 8.1 GPa, respectively using a joint friction angle of φ_j = 30°, joint normal stiffness k_{nj} = 1 GPa/m, and joint shear stiffness k_{sj} = 0.1 GPa/m, as

these reported by other researchers (Franz, 2009; Sainsbury et al., 2007). All other joint parameters such as tensile strength, cohesion, and dilation angle are set to zero.

6.3.4 Jointed Slope Model

The lattice model parameters of the validated SRM model are used in the slope stability assessment in Sections 6.3.4 and 6.4. As mentioned above, the calibrated lattice parameters for the intact rock are for Voronoi-shaped lattices with a lattice size of 18.75 cm and a model dimension of 5 m × 5 m × 10 m. The large-scale slope model with the dimension of 250 m × 200 m × 150 m cannot be simulated using this small lattice size with the currently available PCs to the author. To resolve this issue, the lattice size needs to be upscaled. To justify the use of the upscaled lattice size, a sensitivity study of Voronoi shaped lattice structure on strength and deformation modulus of rock mass is conducted. A sensitivity study on the laboratory-scale intact Zhenping marble shows that there is a small influence of lattice resolution on σ_c and E (Bastola & Cai, 2018b). A similar sensitivity study is conducted here to investigate the influence of lattice resolution of Voronoi-shaped lattice on strength and deformation modulus of both massive intact rock and rock mass that have a dimension of 40 m × 40 m × 80 m, which is 64 times the size of the rock mass REV.

The results of the sensitivity study shown in Figure 6-13 suggest that the Voronoi-shaped lattice does not have a large influence on the normalized strength and deformation modulus of both the massive intact rock and the large-scale rock mass (dimension 40 m × 40 m × 80 m). The strength and the deformation modulus of the large-scale rock mass are normalized using the corresponding intact rock values for the lattice size range of 80–200 cm. However, the post-peak deformation modulus increases with the increase of lattice size, suggesting that the brittleness of the intact rock decreases with the decrease of lattice size.

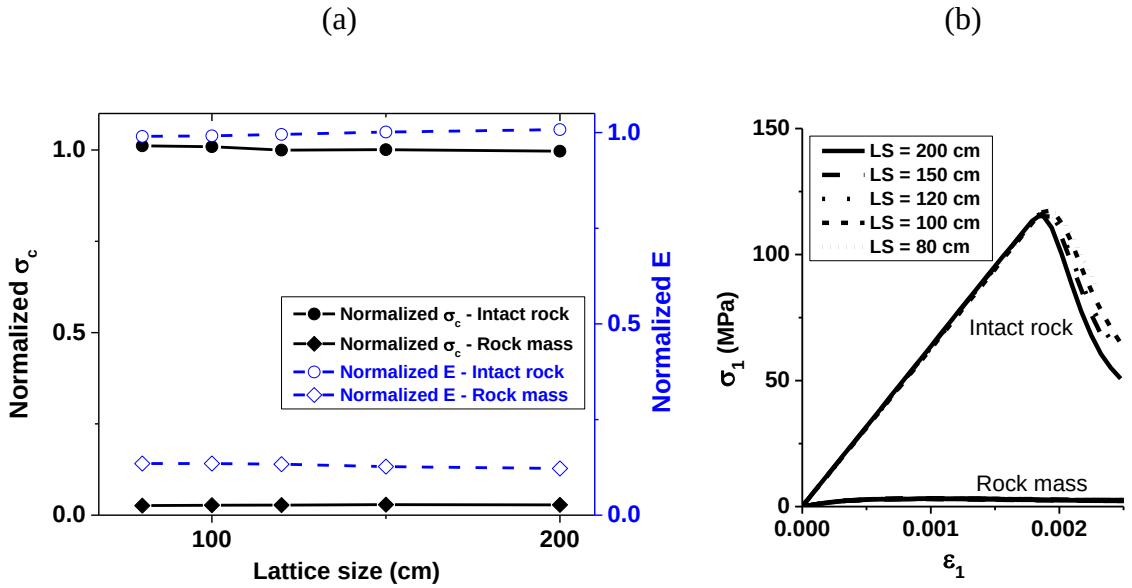

Figure 6-13 (a) Influence of lattice size (LS) on normalized σ_c and normalized E, (b) axial stress–axial strain plot for massive intact rock and rock mass of dimensions 40 m × 40 m × 80 m using Voronoi shaped lattice structure.

The base case SRM model, which includes a large-scale release structure, is used for the calibration and validation of the base case slope model. The release structure forms the basal sliding surface of the slope failure (Sainsbury et al., 2007). Lattice model parameters of the calibrated jointed rock mass model (Section 6.3.3) are used for the calibration of the base case slope model except that the lattice size is 150 cm.

Five direct shear test simulations are conducted under the normal stress of 0.5 MPa using the lattice size of 250, 200, 150, 100, and 50 cm on rock mass models of dimensions 150 m × 150 m × 15 m with non-planar discontinuity to determine the practical lattice resolution that is sufficient to correctly represent the mechanics of sliding and cracking on the walls of wavy rough fractures but is computationally possible for the large-scale slope model. Direct shear test simulation results (Figure 6-14) show that the lattice resolution corresponding to the lattice size of 150 cm is

sufficient to simulate the cracking mechanism on the wall of the rough discontinuity. With further increase of the lattice size beyond 150 cm, there is an increase of the peak shear strength even though the amount of increase is small with the increase of lattice size. Figure 6-15 shows the micro-crack development along the wavy section of the non-planar discontinuity.

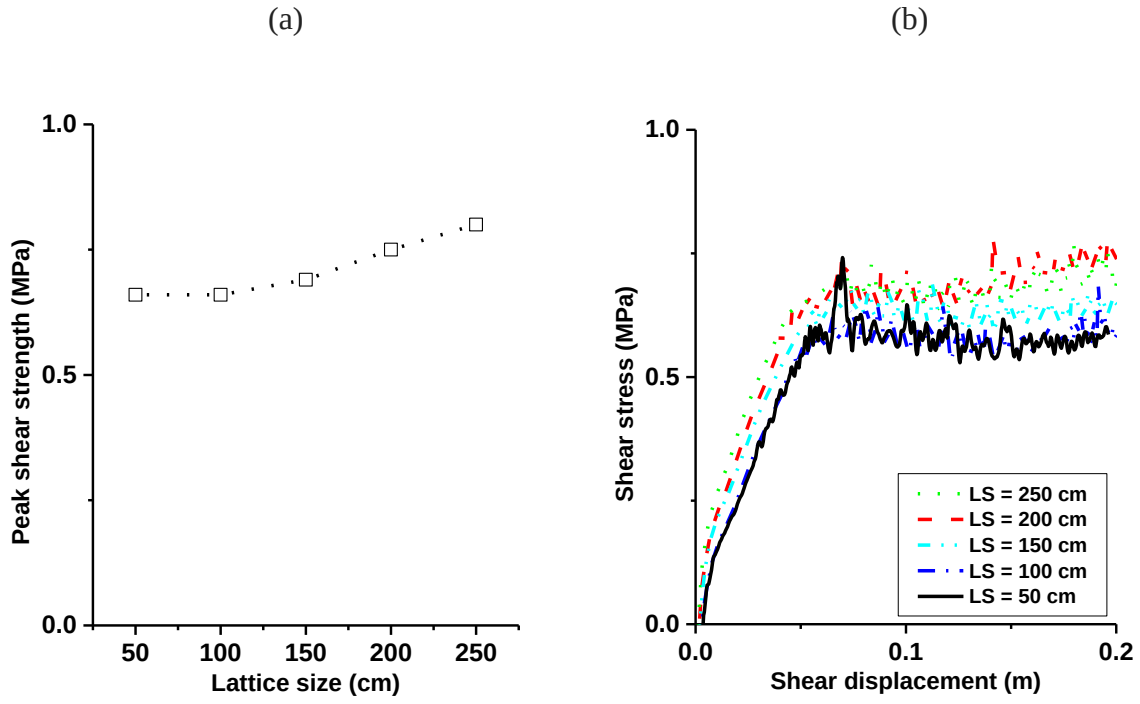

Figure 6-14 (a) Influence of lattice resolution on peak shear strength and (b) shear stress–shear displacement plots of a non-planar discontinuity under a constant normal stress of 0.5 MPa.

Based on the results of sensitivity analysis of compression (Figure 6-13) and direct shear test simulations (Figure 6-14 & Figure 6-15), Voronoi-shaped lattice structures with lattice size of 150 cm is used in slope model. Although direct stress measurements were not conducted at the Cadia Hill Open Pit site, *in-situ* stresses were adopted from the stress measurements at Ridgeway underground mine, which is situated within the same thrust fault system approximately 3 km away from the open pit (Li et al., 2003). The bottom of the open pit is under the influence of confining

stresses to the order of σ_z = 4.05 MPa, σ_x = 6.90 MPa, σ_y = 5.06 MPa such that the ratio of the maximum horizontal to the vertical *in-situ* stress ($k_0 = \sigma_x/\sigma_z$) is 1.7 and the top of the open pit is free of any confining pressure (Figure 6-16a).

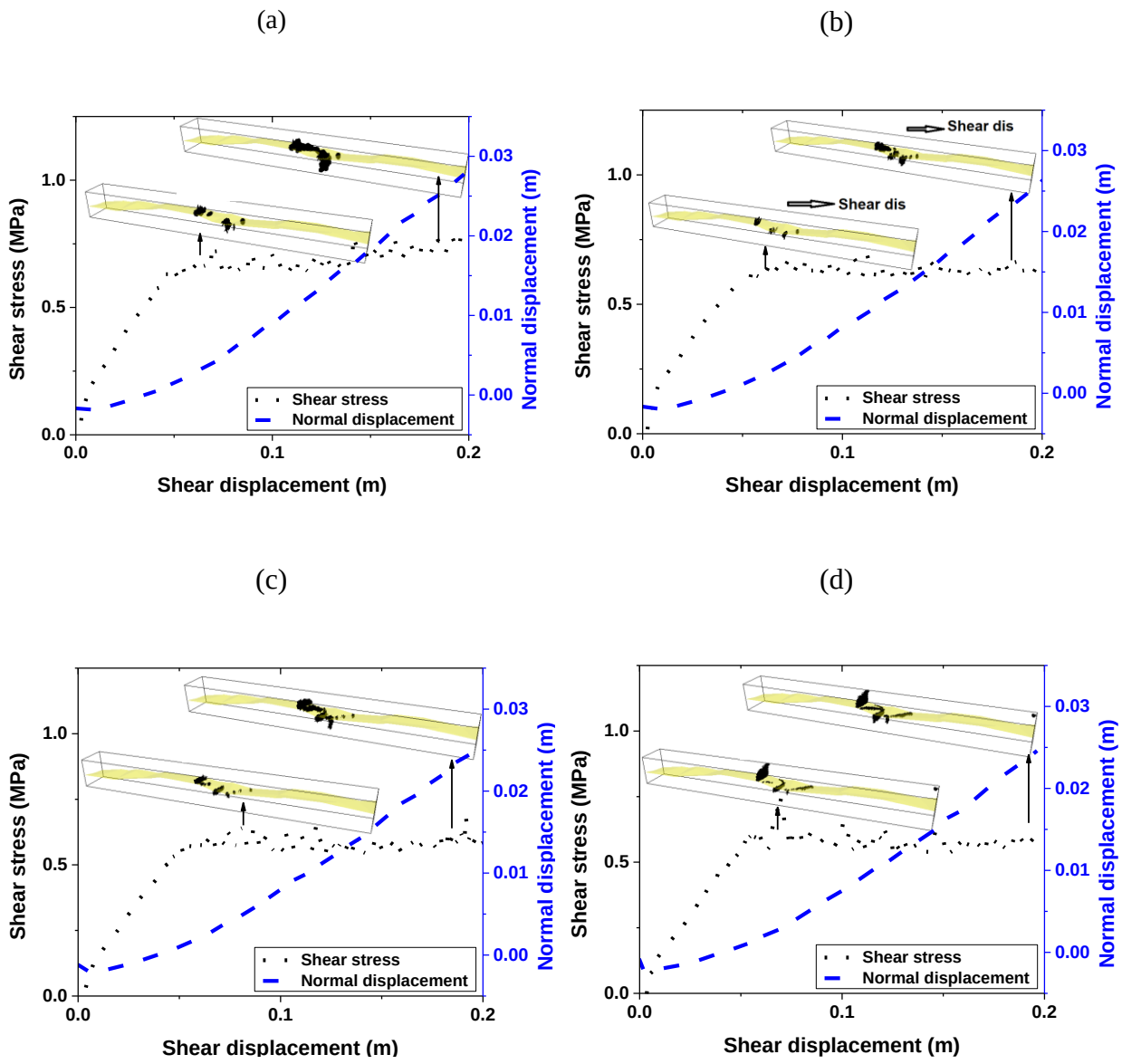

Figure 6-15 Shear stress–shear displacement and shear displacement–normal displacement curves illustrating the development of micro-cracks along the wavy section of the non-planar discontinuity during direct shear under the normal stress of 0.5 MPa and lattice size of (a) 200 cm; (b) 150 cm; (c) 100 cm; and (d) 50 cm.

The bottom boundary of the slope model is fixed, the top surface is free, and roller boundary conditions are applied to the surfaces perpendicular to the x and y-axes. Failure occurs purely under the influence of gravity and the *in-situ* stress as a result of excavation.

The slope models are simulated in 25 steps. In the first step, initial equilibrium is established under the influence of *in-situ* stress and gravitational force without any excavation. Displacements incurred during the first step are reset to zero and induced microcracks are healed. Then, excavations are made by removing the blocks of 5 m height in sequence to simulate the mining activity in 24 stages as shown in Figure 6-16. After excavating 5 m height of rock mass in each mining stage, the model is saved and excavated for another 5 m until the final depth is reached.

(a) (b)

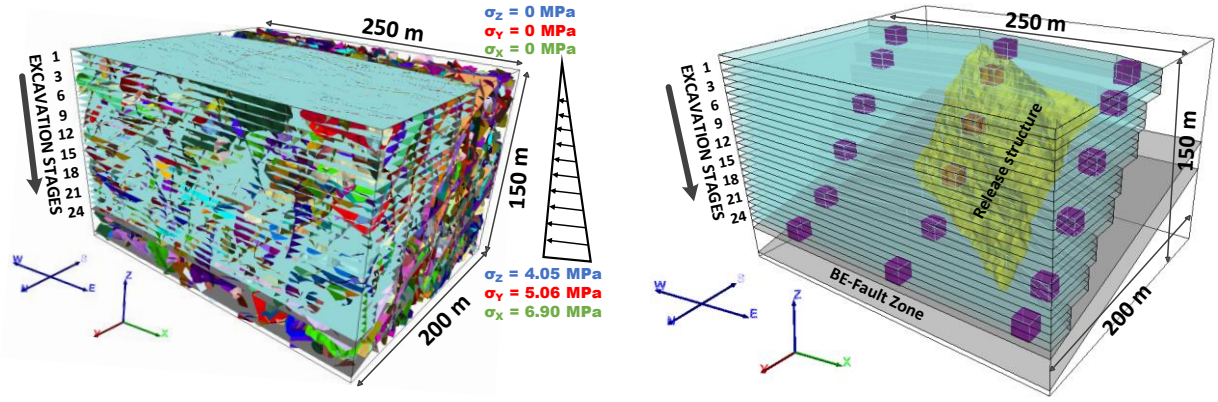

Figure 6-16 Slope model for Cadia Hill open pit illustrating 24 excavation stages (a) with non-planar discontinuities (b) without discontinuities. The BE-Fault zone and displacement monitoring points are shown as sub-horizontal planes and cubes, respectively.

Both vertical and horizontal displacements are recorded using 18 monitoring points shown as cubes in Figure 6-16b. The numbers of microcracks formed during each stage are also recorded. The bands of the weaker rocks within the BE-Fault zone are shown as sub-horizontal planes with

a dip of 20° and are located at the lower section of the pit (Figure 6-16). The large-scale release structure with a dip of 56° and a joint friction angle of 20° is also defined which forms the basal sliding surface of the slope failure (Figure 6-16b). The extent of the release structure is about 90 m along the vertical direction of the slope which is the approximate vertical extent of slope failure.

The slope model with the base case DFN, the release structure, and non-planar discontinuities is used for model validation. The model is calibrated using the displacements recorded along x, y, and z directions at the south wall of the open pit. Displacements recorded in the field on the monitoring prism are compared with the displacements recorded in the slope model during excavation at the same location. Excavation stages 20 to 24 are located in the region of weaker rock mass pertaining to the BE Fault zone. The increase in slope movement has also been reported to be coincident to rainfall and blasting events (Sainsbury et al., 2007). Therefore, the blasting and rainfall during the excavation of the weak rock mass could have had a combined influence on the sudden changes in X and Z displacements at the later excavation stages. It is seen from Figure 6-17 that the slope model displacements agree reasonably well with field monitoring data and the displacement contours of the simulated slope model are concentrated at or near the location of the release structure (Figure 6-18). Compared with Z-displacement, the higher magnitude of X-displacement is attributed to the higher horizontal *in-situ* stress in the X direction which corresponds to the respective displacement contours. In addition, the displacement contours of the slope model show a very good correlation with the vertical extent of failure of 90 m as observed in the field. This leads to a calibrated slope model. The SRM model for rock slope simulation can represent slope failure more realistically because the failure is the result of crack propagation and coalescence associated with the pre-existing discontinuities (Figure 6-19) along the release structure as investigated by Sainsbury et al. (2007). Cracking is predominant on the edges of the

excavations (benches) and at the location of the weaker band of rock mass within the BE-Fault zone. The lattice parameters of the calibrated slope model are used in models in Sections 6.4.1–6.4.4.

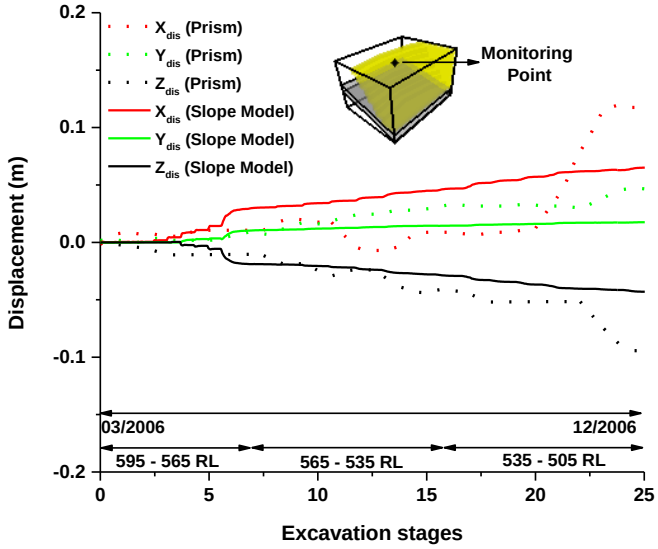

Figure 6-17 Comparison of displacements recorded on the monitoring prisms (dotted line) in the field and in the slope model with non-planar discontinuities (solid line) during excavation. The time of excavation corresponding to the pit depth (RL) are also shown.

(a) (b)

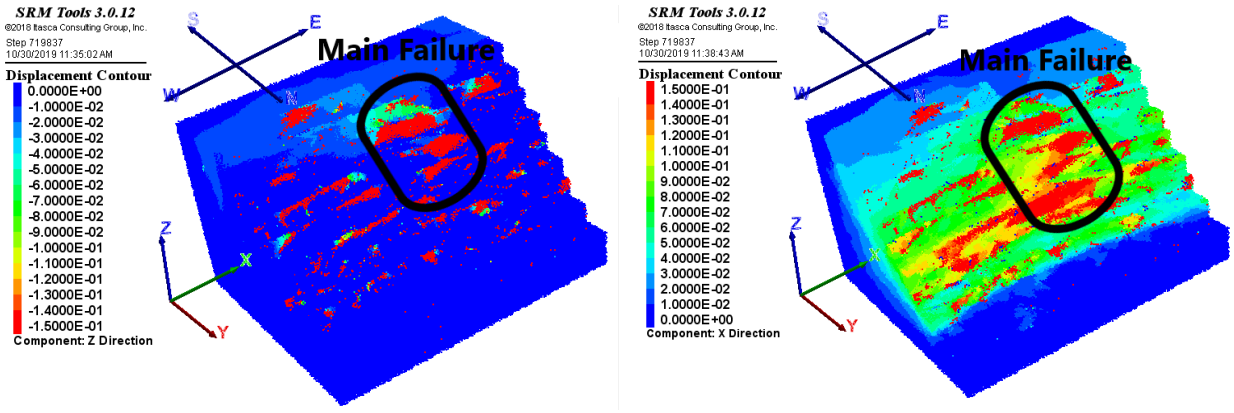

Figure 6-18 Displacements contours along (a) vertical Z direction and (b) horizontal X direction in the base case slope model. Displacement unit is in m.

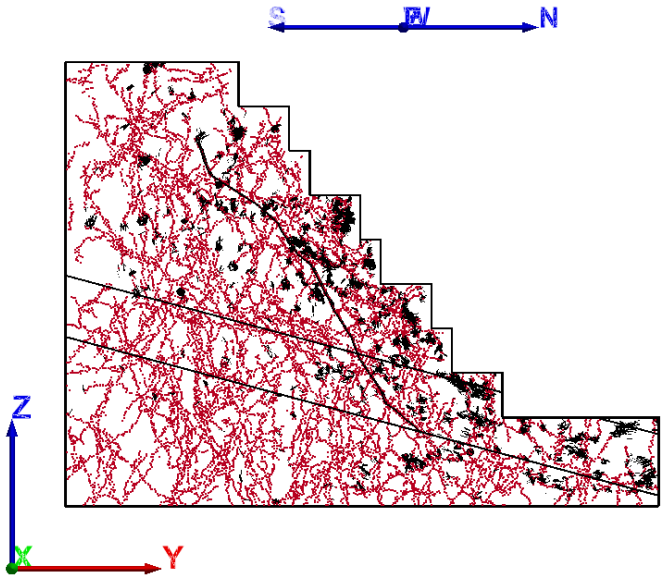

Figure 6-19 Cross-section along NS plane at the center of the slope model illustrating rock failure (cluster of black discs) induced by the propagation and coalescence of cracks (discs) along pre-existing non-planar discontinuities.

6.4 Influence of different parameters on slope stability

Slope deformation and failure depend on many factors such as lithology, slope and discontinuity geometry, geomechanical properties of intact rock and discontinuities, hydrogeology, *in-situ* stress and dynamic loadings (Kulatilake & Shu, 2015b). In this section, using the lattice model parameters of the validated slope model, the influence of discontinuity waviness (Section 6.4.1), discontinuity intensity (Section 6.4.2), discontinuity size (Section 6.4.3), and *in-situ* stress state (Section 6.4.4) on slope displacements and factor of safety are investigated. The factor of safety is computed using the strength reduction method. The release structure is not included in the models in Sections 6.4.2 & 6.4.3 because the relative size of the release structure is too small in comparison with the size of the discontinuities in DFN with a higher P_{32} of 0.72 m^{-1} while the relative size of the release structure is significantly larger than the size of the discontinuities in DFN with a lower P_{32} of 0.1 m^{-1}.

6.4.1 Influence of discontinuity waviness

It has been demonstrated that non-planar crack surface has a large influence on the mechanical properties and crack evolution of the laboratory-scale cracked marble under compression (Bastola & Cai, 2019). In this section, parameters of the calibrated large-scale slope model with the release structure are used in conjunction with the jointed rock mass models generated in Section 6.3.3 to investigate the influence of discontinuity waviness on slope stability, except that the slope model with planar discontinuities is assigned a higher friction angle of 45° (= 30° + 15°). This 15° increment in the basic friction angle would account for the additional frictional component contributed by the large-scale discontinuity waviness and small-scale roughness (Cai et al., 2004).

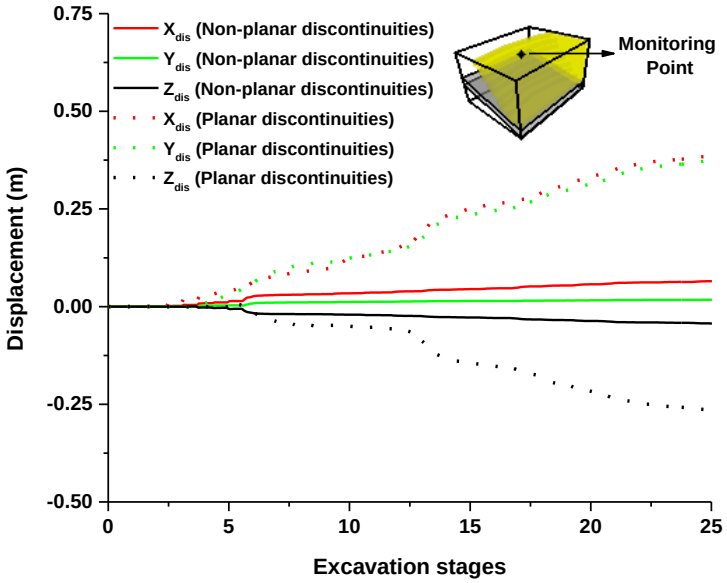

Figure 6-20 Comparison of displacements recorded in the slope models with planar discontinuities (dotted lines) and non-planar (solid lines) discontinuities.

Displacements and contours of factor of safety after each excavation stage are compared between the jointed slope models with planar and non-planar discontinuities. The modeling results shown in Figure 6-20 suggest that the magnitude of displacements along the x, y, z directions in the slope

model with planar discontinuities (dotted lines) are higher than the slope model with non-planar discontinuities (solid lines). In addition, the contours of factor of safety suggest that the slope model with planar discontinuities comprises of bigger unstable zones than the slope model with non-planar discontinuities (Figure 6-21). Cross-sectional analysis along the NS plane at the center of the slope suggest that the slope model with planar discontinuities constitutes unstable zones deep into the slope than the slope with non-planar discontinuities (Figure 6-22). This is because the slope excavated in the SRM model with non-planar discontinuities is relatively stiffer than the one with planar discontinuities because of block interlockings along the wavy surfaces. As a result, fewer cracks are observed on the slope with non-planar discontinuities (Figure 6-19) than the one with planar discontinuities (Figure 6-23).

(a) (b)

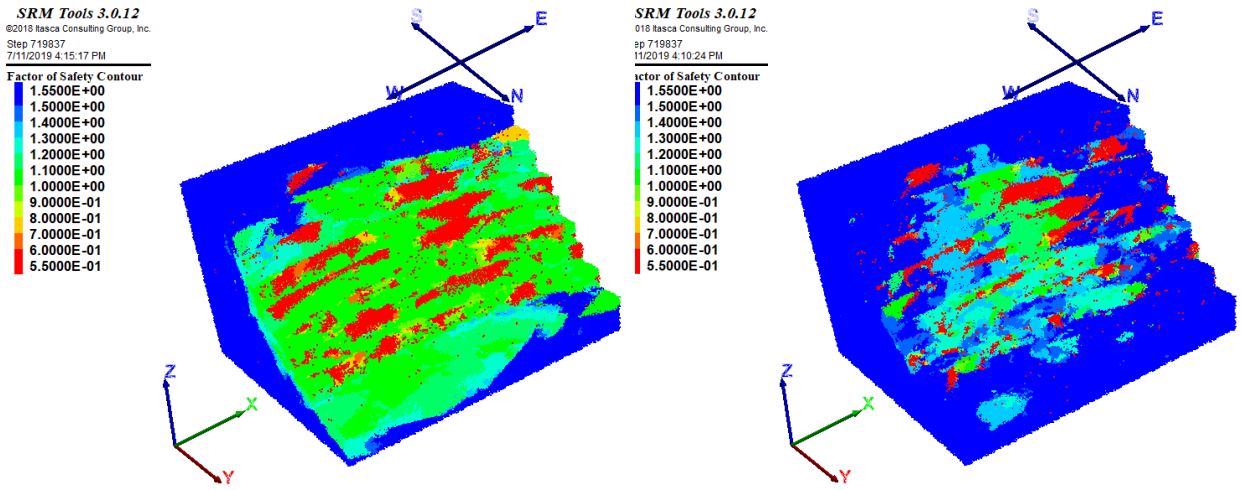

Figure 6-21 Contours of safety factor for the slope excavated in base case SRM model with (a) planar discontinuities and (b) non-planar discontinuities.

(a) (b)

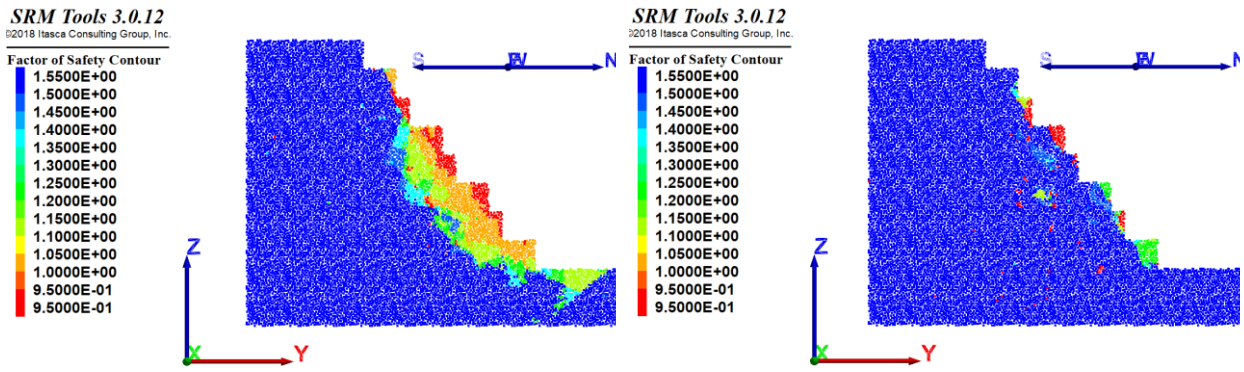

Figure 6-22 Cross-sections along NS plane at the center of the slope model illustrating contours of factor of safety for the slope excavated in base case SRM model with (a) planar discontinuities and (b) non-planar discontinuities.

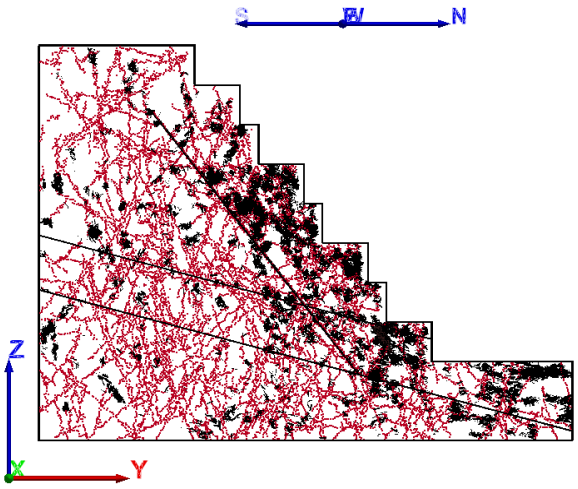

Figure 6-23 Cross-section along NS plane at the center of the slope model illustrating rock failure (cluster of black discs) induced by the propagation and coalescence of cracks (discs) along the pre-existing planar discontinuities.

The results show that the displacements recorded in the slope model with the non-planar discontinuities are closer to the field measured displacements than the ones recorded in the slope model with planar discontinuities. This suggests that the adjusted discontinuity friction angle value to account for the roughness component is not enough to simulate the physics of the slope with non-planar discontinuities using the slope model with planar discontinuities. Therefore, it is

recommended to employ the realistic geometry of the discontinuities to solve the geomechanical problems in rock masses with wavy discontinuities.

6.4.2 Influence of discontinuity intensity

Strength and deformation modulus of rock mass decrease with the increase of the number of discontinuities. Hence, there is a very high likelihood that a slope excavated in a rock mass with a higher discontinuity intensity (P_{32}) would exhibit larger slope deformation. To investigate the influence of P_{32} on slope displacements and the factor of safety, the DFN in the base case slope model with a P_{32} value of 0.4 m^{-1} is replaced with a DFN model that has a P_{32} value of 0.72 m^{-1}.

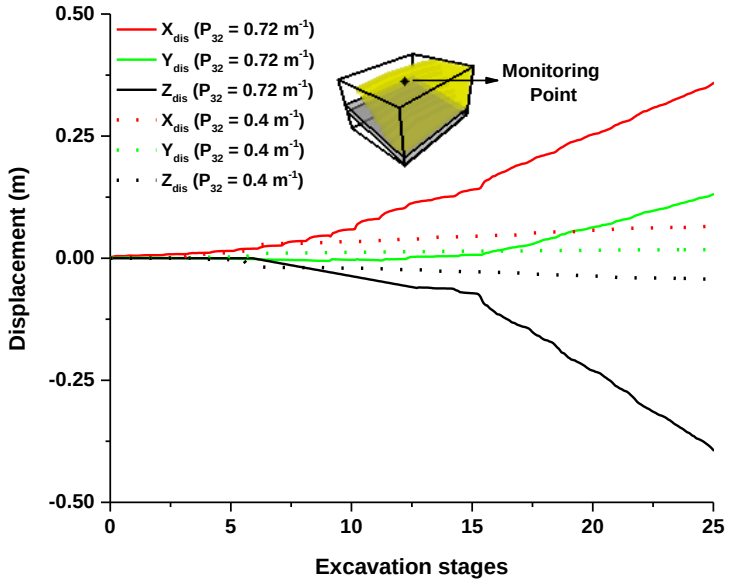

Figure 6-24 Comparison of displacements recorded on slope models with non-planar discontinuities and different P_{32} values.

The modeling results presented in Figure 6-24 show that the displacements along the x, y, z directions in the slope model excavated in the SRM model with P_{32} = 0.72 m^{-1} (solid lines) are higher than the ones with P_{32} = 0.4 m^{-1} (dotted lines). The slopes excavated in the jointed rock mass with both planar and non-planar discontinuities and a higher P_{32} are highly unstable. The

contours of factor of safety suggest that the slope models excavated in the SRM models with P_{32} = 0.72 m^{-1} (Figure 6-25) comprises of larger unstable zones than the models with P_{32} = 0.4 m^{-1} (Figure 6-21), for both planar and non-planar discontinuities. This is because that the slopes excavated in the SRM models with P_{32} = 0.72 m^{-1} are heavily jointed with large discontinuities, which decrease the strength and stiffness of the rock mass.

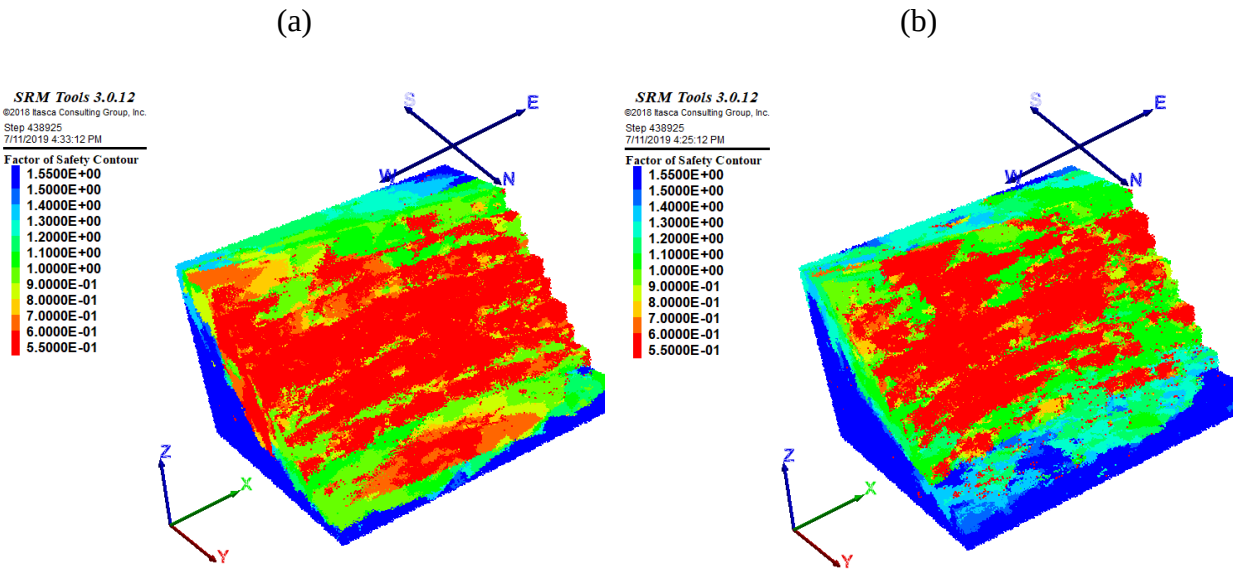

Figure 6-25 Contours of factor of safety for slopes excavated in SRM models with P_{32} = 0.72 m^{-1}: (a) planar discontinuities, (b) non-planar discontinuities.

6.4.3 Influence of discontinuity size

The strength and deformation modulus of rock mass decreases with the increase of the discontinuity size relative to the scale of the slope. To investigate the influence of maximum discontinuity area (A_{max}) on the slope displacements and the factor of safety, the DFN in the base case slope model (with A_{max} = 10,000 m^2) is replaced with a DFN that has A_{max} = 100 m^2.

The modeling results presented in Figure 6-26 suggest that the displacements along the x, y, z directions in the slope excavated in the SRM model with A_{max} = 100 m^2 (solid lines) are smaller

than the ones for the slope excavated in the base case SRM model with A_{max} = 10,000 m^2 (dotted lines). The slope excavated in the SRM model with A_{max} = 100 m^2 is very stable. The contours of factor of safety suggest that slope excavated in the base case SRM model comprises of larger unstable zones (Figure 6-21) but the slope excavated in the SRM model with A_{max} = 100 m^2 (Figure 6-27) has no unstable zone. This is because that the SRM model with A_{max} = 100 m^2 comprises of massive rock blocks formed by non-persistent discontinuities which increase the strength and stiffness of the rock mass. The slopes excavated in the jointed rock mass with both planar and non-planar discontinuities for A_{max} = 100 m^2 are stable (Figure 6-27).

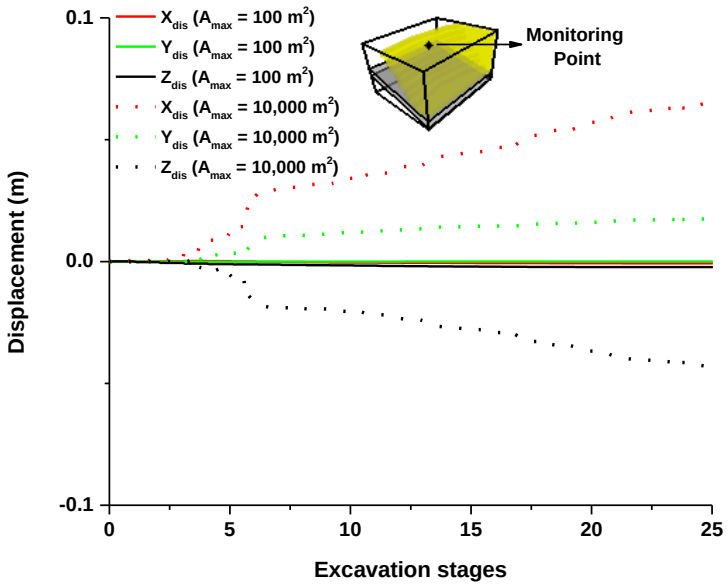

Figure 6-26 Comparison of displacements recorded in slope models excavated in SRM models with non-planar discontinuities and different discontinuity sizes.

(a) (b)

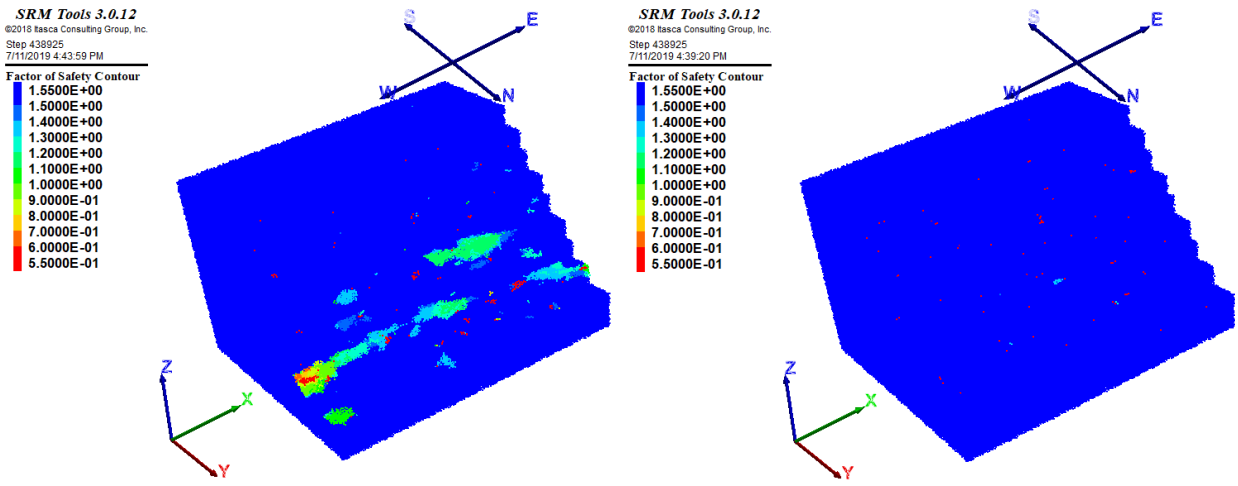

Figure 6-27 Contours of factor of safety for the slope models excavated in the base case SRM model with A_{max} = 100 m^2: (a) planar discontinuities, (b) non-planar discontinuities.

6.4.4 Influence of *in-situ* stress

With the increase of the pit depth, the local *in-situ* stress state changes due to the change in regional geology and tectonics. High horizontal stresses tend to promote the extension of pre-existing discontinuities and coalescence of these, resulting in macroscopic failure plane. To investigate the influence of the *in-situ* stress on slope displacements and factor of safety for models with planar and non-planar discontinuities, the magnitude of *in-situ* stress state in the slope models with both planar and non-planar discontinuities in Section 6.4.1 are altered such that slope models with maximum horizontal to vertical stress ratio (k_0) of 0.85 and 2.55 are simulated, in addition to the base case slope model with k_0 of 1.7.

The modeling results suggest that the magnitude of displacements along x, y, z directions in slope model excavated in the SRM models with both planar discontinuities (Figure 6-28a) and non-planar discontinuities (Figure 6-28b) increase with the increase of k_0 as shown in Figure 6-28. As

witnessed in Section 6.4.1, the displacements on the slope models with planar discontinuities are higher than on the slope models with non-planar discontinuities. This is because of the higher rate of extension of the pre-existing discontinuities due to the increase of induced microcracks leading to the localized instability of the pit benches (Figure 6-19, Figure 6-23, Figure 6-29 & Figure 6-30). The rate of increase of extensile cracks with the increase of 'k_0' is larger for the slope model with planar discontinuities.

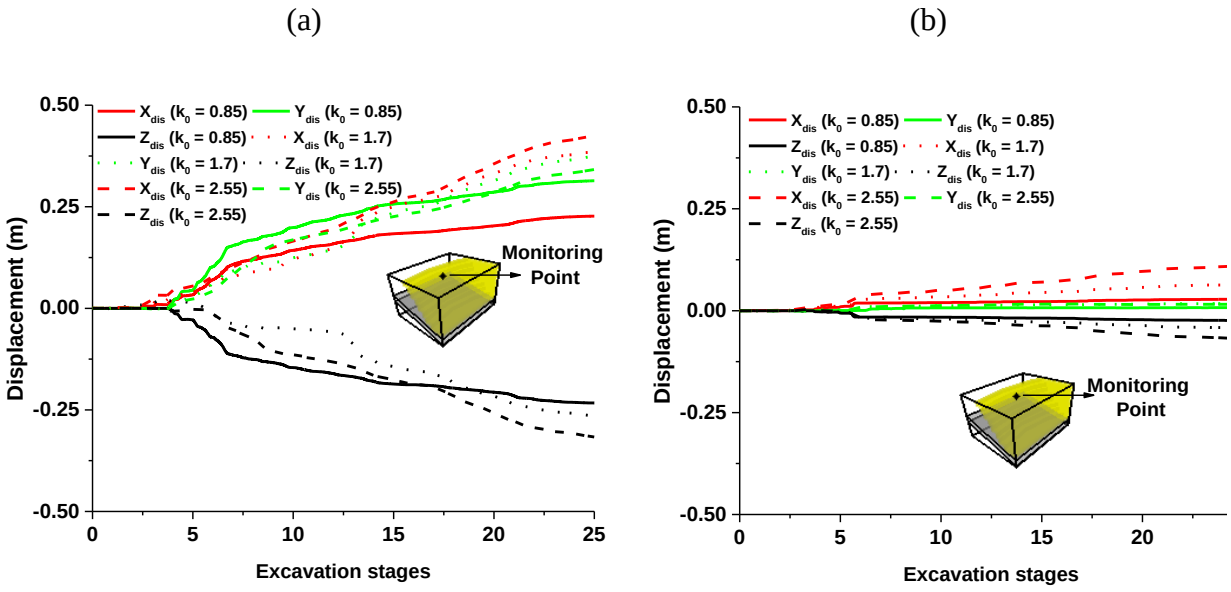

Figure 6-28 Comparison of displacements recorded on the slope models with (a) planar discontinuities and (b) non-planar discontinuities under the influence of different horizontal stresses, where k_0 is the ratio of maximum horizontal to vertical *in-situ* stress.

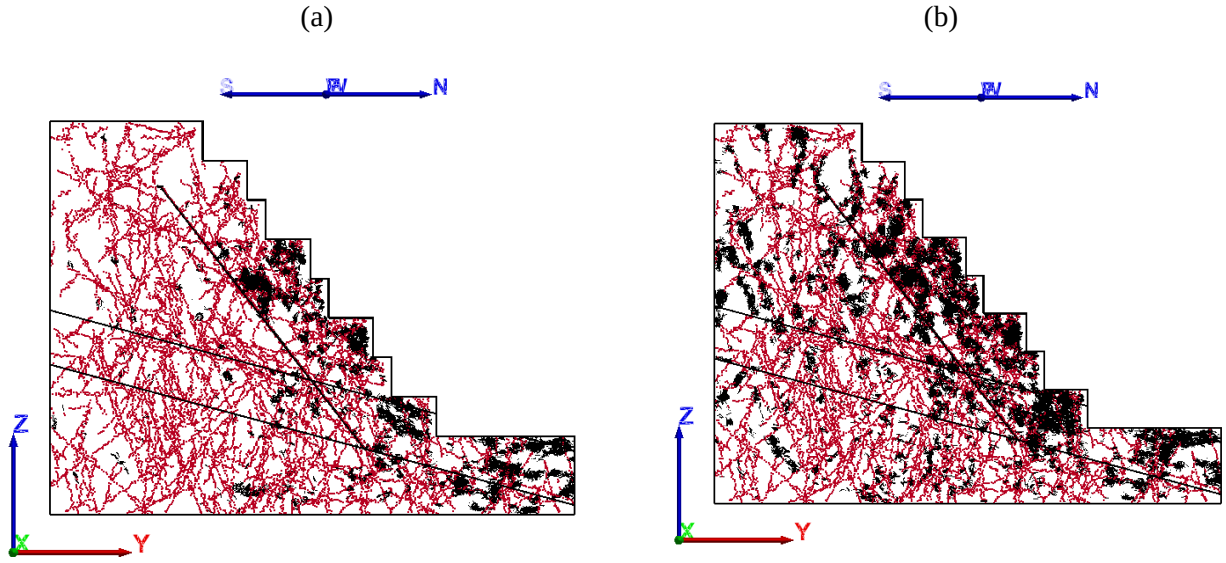

Figure 6-29 Crack development in the slope models with planar discontinuities under the influence of (a) k_0 = 0.85, (b) k_0 = 2.55.

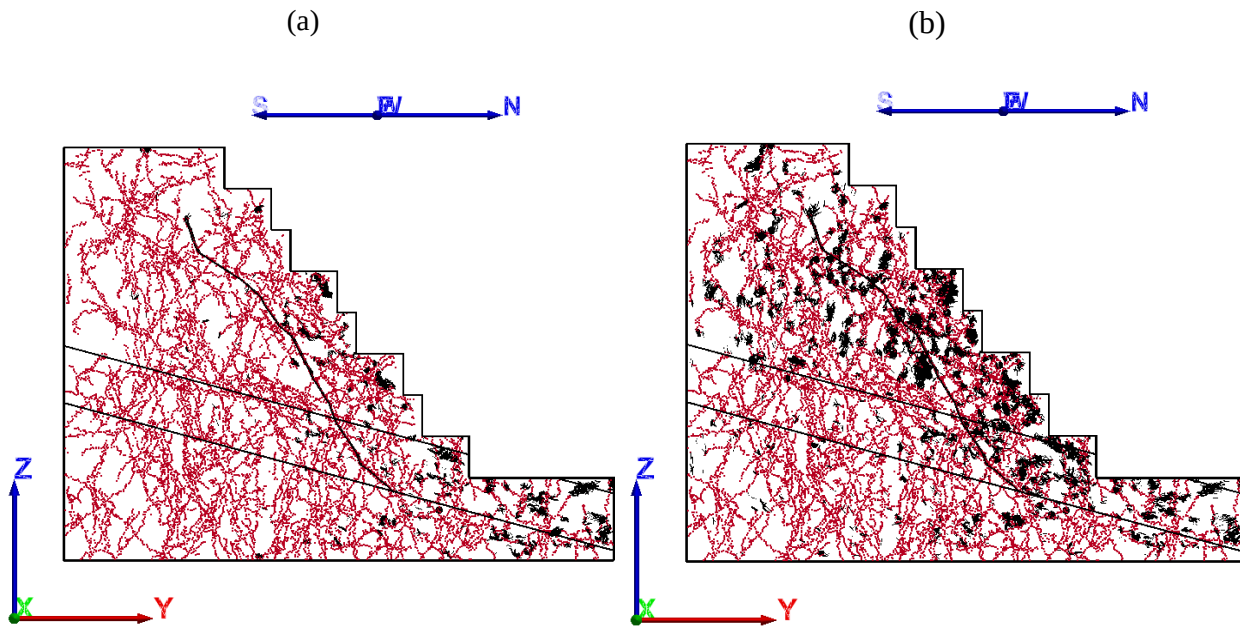

Figure 6-30 Crack development in the slope models with non-planar discontinuities under the influence of (a) k_0 = 0.85, (b) k_0 = 2.55.

The instability is also illustrated by the contours of safety factor and cross-sections. The slope models with both planar discontinuities (Figure 6-31 & Figure 6-21a) and non-planar discontinuities (Figure 6-33 & Figure 6-21b) with higher horizontal stresses comprises of larger unstable zones. The cross-sectional plots along the NS plane at the center of the slope suggest that the slope model with higher horizontal stresses constitutes unstable zones deep into the slope (Figure 6-22, Figure 6-32 & Figure 6-34). The observations are in line with the ones made by Herrero (2015) in the slope model excavated in a hypothetical rock mass with planar discontinuities under the influence of different magnitude of horizontal stresses. As expected, the extent of unstable zone is larger and deeper for the slope model with planar discontinuities.

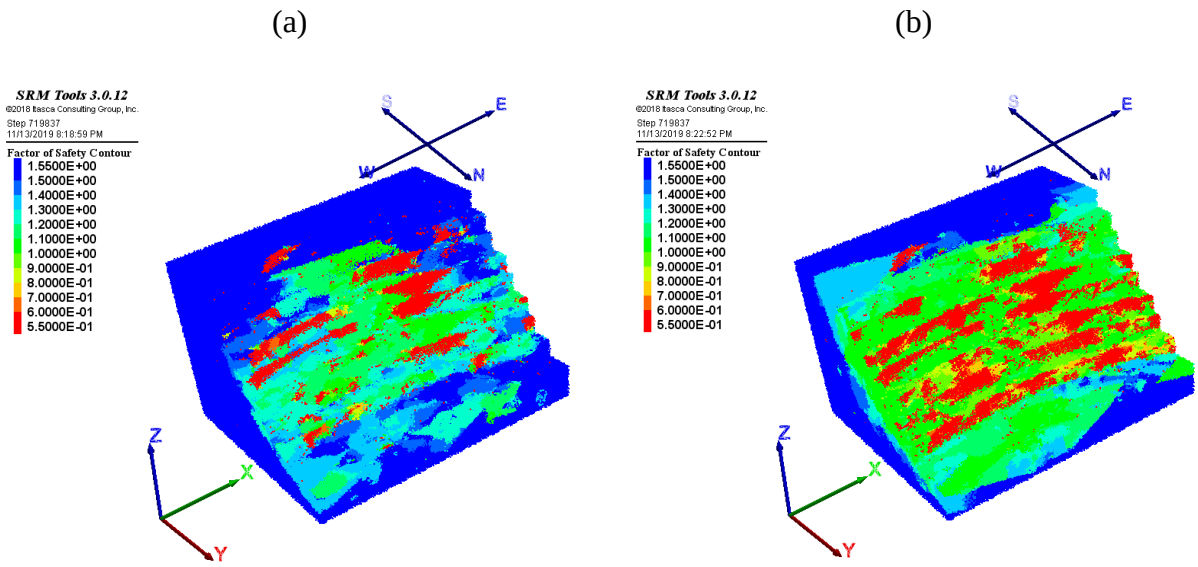

Figure 6-31 Contours of safety factor for the slope models with planar discontinuities under the influence of (a) k_0 = 0.85, (b) k_0 = 2.55.

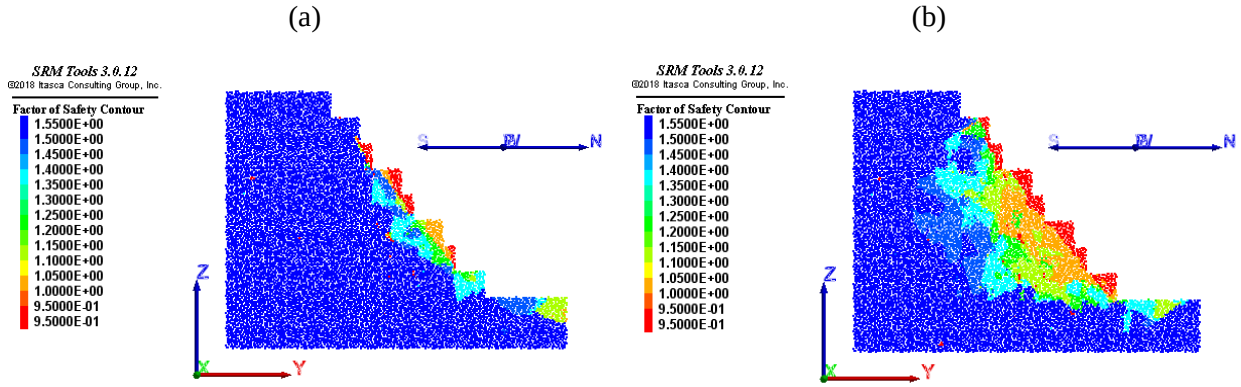

Figure 6-32 Cross-sections along NS plane at the center of the slope models with planar discontinuities under the influence of (a) k_0 = 0.85, (b) k_0 = 2.55.

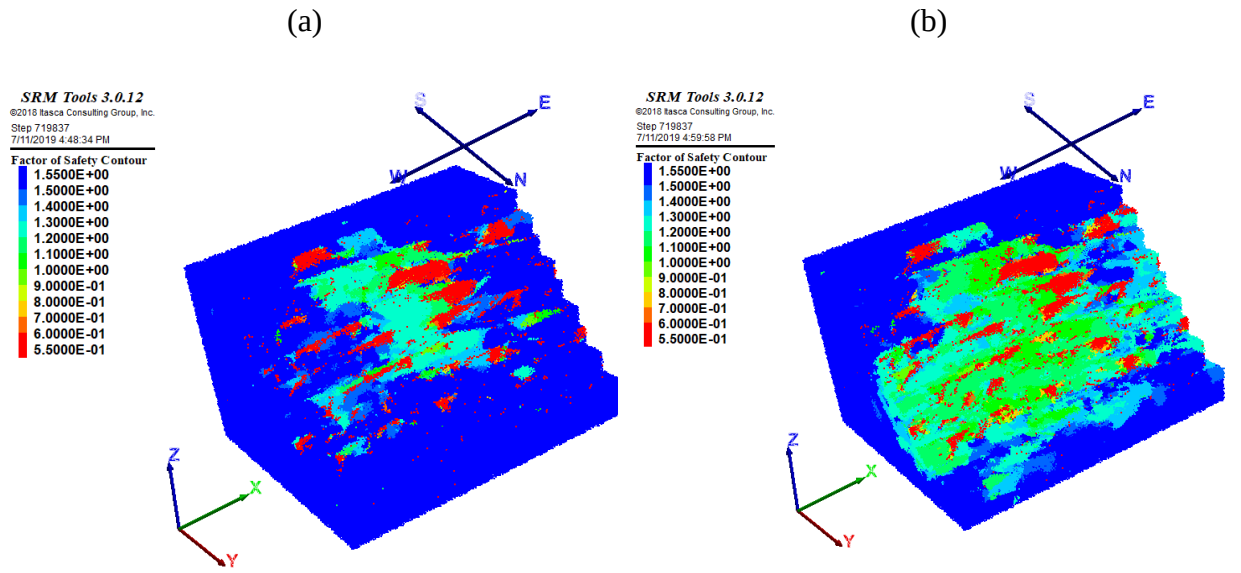

Figure 6-33 Contours of safety factor for the slope models with non-planar discontinuities under the influence of (a) K_0 = 0.85, (b) K_0 = 2.55.

(a) (b)

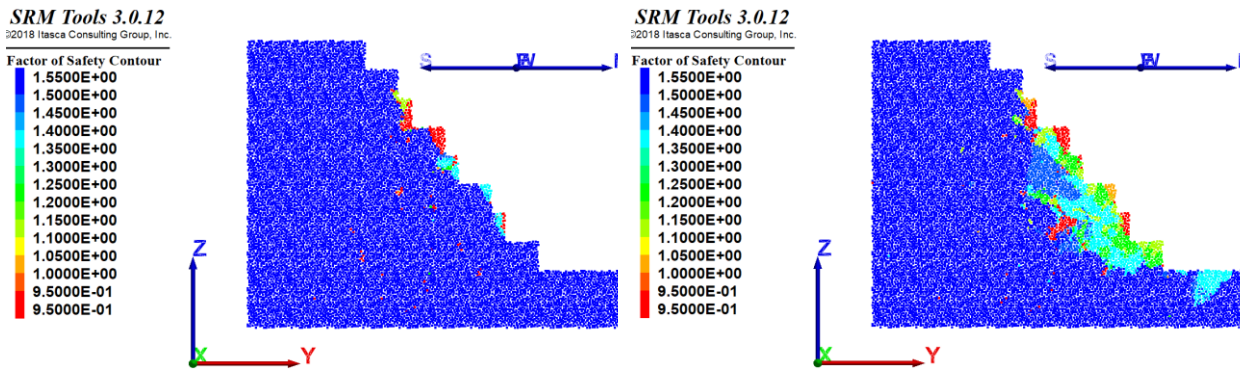

Figure 6-34 Cross-section along NS plane at the center of the base case slope model under the influence of (a) K_0 = 0.85, (b) K_0 = 2.55, where K_0 is the ratio of maximum horizontal to vertical *in-situ* stress.

6.5 Remarks

In this Chapter, slope deformation and failure on the south wall of Cadia Hill open pit mine are successfully simulated using the LS-SRM modeling approach in Slope Model. First, the capability of Slope Model to assess the stability of a slope with both planar and non-planar discontinuity surfaces is validated. A planar sliding problem is simulated in the Slope Model software to validate the capability of the tool to analyze the stability of slope with both planar and non-planar cohesionless and persistent discontinuities. The results from the validation exercise suggest that the factor of safety computed from the analytical solution of the cohesionless and persistent planar discontinuity is the same as the one from the Slope Model software. In addition, the factor of safety is found to be higher for the slope with the non-planar discontinuity than the slope with the planar one. This verification exercise invigorates the confidence of the numerical modeling performed using the Slope Model code.

Slope failure and larger displacements are localized around the release structure. The failure behavior and the displacements of the South Wall of the Cadia Hill open pit are captured by representing the realistic geometrical and mechanical properties of rock mass and discontinuities. Slope stability and displacements are highly dependent on the discontinuity characteristics such as waviness, intensity, size, and the magnitude of *in-situ* stress.

The slope model excavated in the rock mass with planar discontinuities is more deformable and less stable than the slope model excavated in the rock mass with non-planar discontinuities. In addition, the deformability and instability increase for the slopes excavated in the rock mass with higher discontinuity intensity and larger discontinuity sizes. At greater pit depth with higher *in-situ* stress, both the slope models with planar and non-planar discontinuities experience localized failures due to very high stress concentrations and the slope model with planar discontinuities is more deformable and less stable than the slope model with non-planar discontinuities.

LS-SRM models used in this study have opened new avenues for slope stability assessment using realistic non-planar discontinuities. Moreover, these models are computationally more efficient than other DEM tools; they can also consider interesting and non-planar discontinuities in slope stability analysis. Due to limited computer resource, the dimensions of the analyzed slope models in this study are intermediate. The model dimensions can be extended to full pit scale using more powerful computing services such as a supercomputer and cloud computing.

Chapter 7

7 Mechanical behavior of a large-scale rock mass[6]

In this Chapter, the mechanical behaviors of jointed rock masses are investigated using the rock mass samples derived from the calibrated base case SRM model in Section 6.3.3. It is not feasible to perform the compression tests on very large-scale rock mass. Therefore, a scale-effect study is conducted to determine the REV of the large-scale jointed rock mass in Section 7.1. Using the REV sized rock mass samples, the influence of volumetric discontinuity intensity, P_{32} (Section 7.2) and confining pressure (Section 7.3) on the mechanical properties of jointed rock masses are investigated.

7.1 Scale effect on the mechanical properties of rock mass

It is widely accepted that the mechanical properties of rock mass changes with the change in scale. Lajtai (1974) indicated that small rock blocks should have strengths higher than the larger ones because the maximum allowable discontinuity size is limited by the dimensions of the rock specimen. Other investigators (Ivars et al., 2008; Esmaieli et al., 2010; Ivars et al., 2011) found that the strength and deformation modulus of the rock mass decrease with the increase of scale to some threshold volume beyond which these properties are assumed to be constant. This threshold volume beyond which the geometrical and mechanical properties of the jointed rock mass does not change significantly is termed as the mechanical REV of the rock mass.

[6] Manuscript under preparation for submission to the Journal of Rock Mechanics and Rock Engineering

In this sub-section, a study is conducted to investigate the influence of rock mass size on the mechanical properties of the jointed rock mass located in Cadia Open pit slope (Section 6.3.3) and to determine the mechanical REV. In the first step, it is important to determine largest scale up to which the investigations are performed. Due to the limitation of computational capability, the dimension of the largest model that can be practically simulated is 15 m × 15 m × 30 m, which corresponds to 1.2 million nodes and 9.0 million springs with the lattice size of 18.75 cm. Therefore, the study of scale-effect is performed for models with dimensions 5 m × 5 m × 10 m, 10 m ×10 m × 20 m, and 15 m × 15 m × 30 m. To generate the DFN model of these dimensions, DFN models with these dimensions are sampled from the base case DFN model generated in Section 6.3.2. To ensure that all the models have similar joint intensity, only DFNs with P_{32} value of 0.39 are chosen for all SRM models. SRM models (Figure 7-1) are generated by importing these DFNs into the intact rock models that were calibrated in Section 6.3.1 and are subjected to unconfined compression.

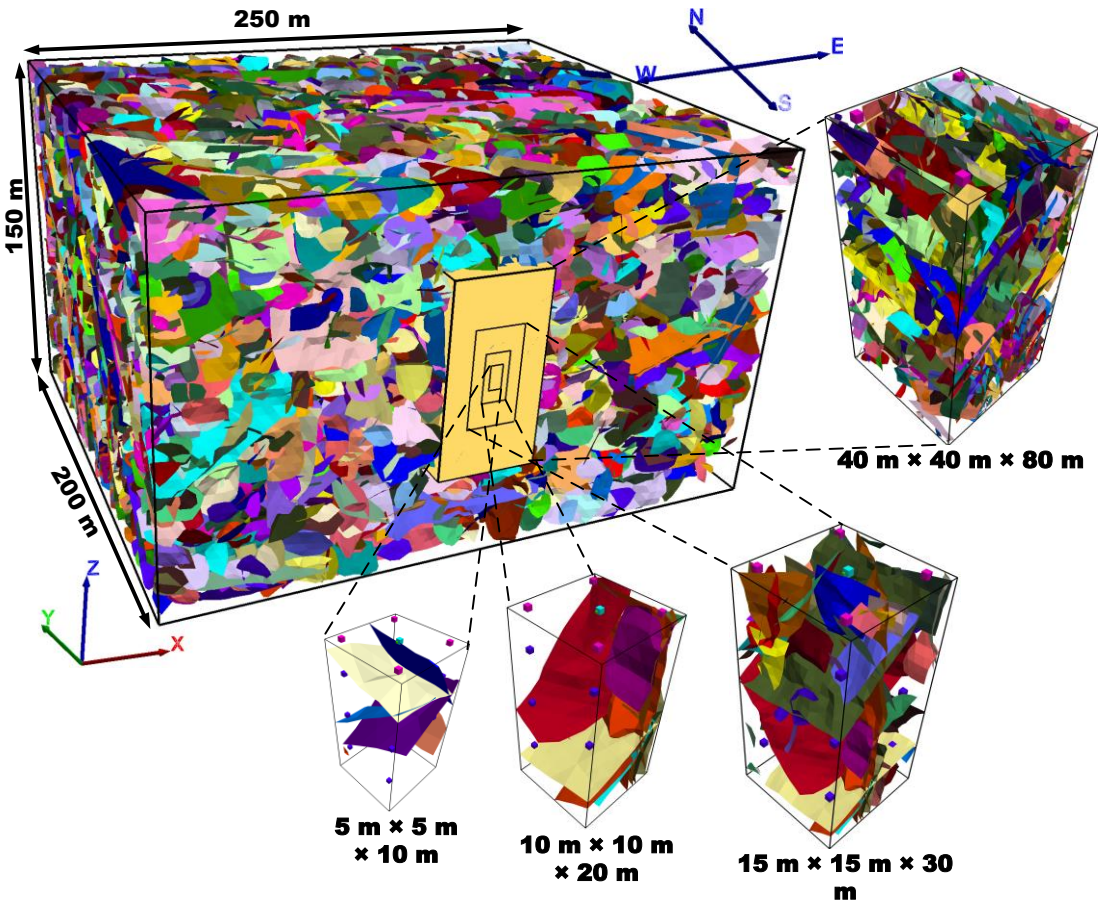

Figure 7-1 LS-SRM samples of different scales with non-planar discontinuities.

The number of DFN samples that can be extracted from the parent DFN model depends on the size of the parent DFN sample. P_{32} is calculated for each sample and are plotted against the sample volume. P_{32} analysis indicates that the variance (σ^2_{P32}) of P_{32} decreases with the increase of sample volume and vice-versa. The volume beyond which there is no significant change in P_{32} is selected as the geometrical REV for this large-scale DFN. Based on the P_{32} analysis, the representative DFN model for the rock mass is the one with the dimension of 10 m × 10 m × 20 m (Figure 7-2) because most of the P_{32} data falls within 95% confidence interval ($\mu_{P32} \pm 2\sigma_{P32}$), where μ_{P32} and σ_{P32} are mean and standard deviation of P_{32}, respectively.

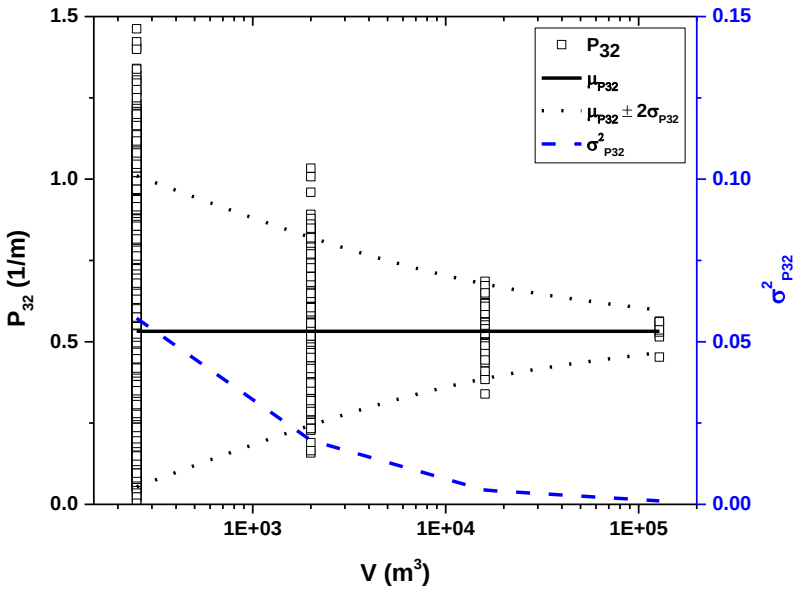

Figure 7-2 Log–log plot of the variance of P_{32} with the volume of DFN samples.

Five monitoring points are installed on the top of the model to record the vertical displacement (see Figure 7-1). Similarly, six monitoring points are installed on each lateral faces of the model (i.e. a total of 24 history points) to record the horizontal displacements in the x and y directions (Figure 7-1). The applied force is recorded on the top of the model and the number of cracks is also recorded. All the model parameters such as lattice size, loading rate, and material properties for both intact rock and DFN are kept the same for all models as in Section 6.3.3.

The modeling results presented in Figure 7-3 suggest that the normalized values of peak strength (σ_1/σ_c), pre-peak deformation modulus (E_m/E_i), and post-peak deformation modulus (E_{mpp}/E_i) of the jointed rock mass decrease with the increase of rock mass volume for both the models with planar and non-planar discontinuities under unconfined compression (Figure 7-3a,b&c). The axial stress–axial strain plots suggest that the post-peak deformation behavior of jointed rock masses transforms from brittle to strain softening and ductile-plastic (Figure 7-3d,e&f) with the increase

of rock mass scale for both models with planar and non-planar discontinuities under unconfined compression.

In general, the jointed rock mass models with non-planar discontinuities have higher values of σ_1/σ_c, E_m/E_i, and E_{mpp}/E_i (Figure 7-3) than the ones with planar discontinuities; however, the relative difference between them is reduced with the increase of rock mass volume. This behavior is also illustrated using axial stress–axial strain plots (Figure 7-3d,e&f).

(a)

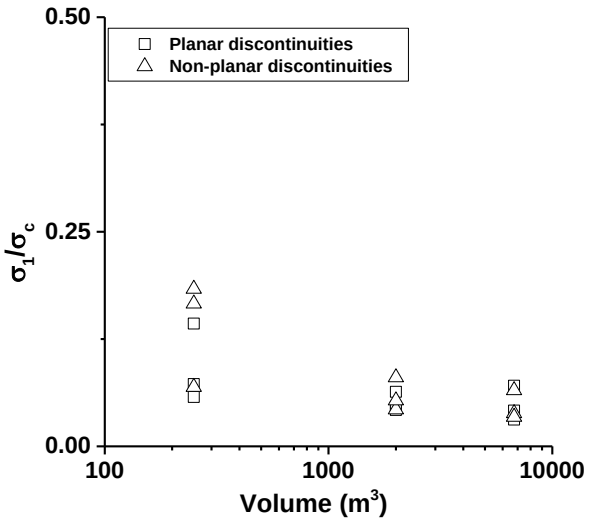

(b)

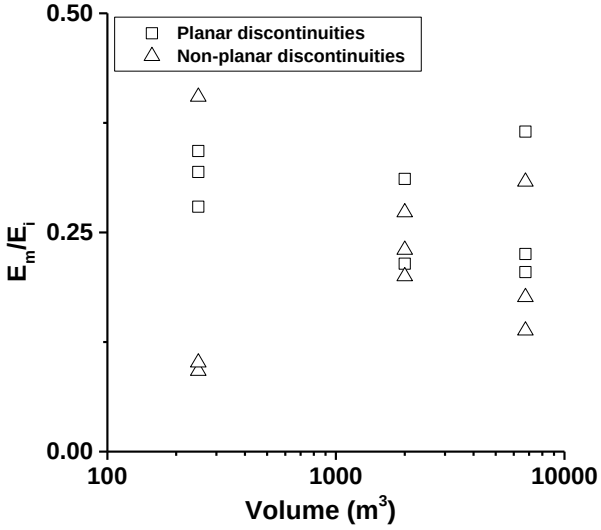

(c)

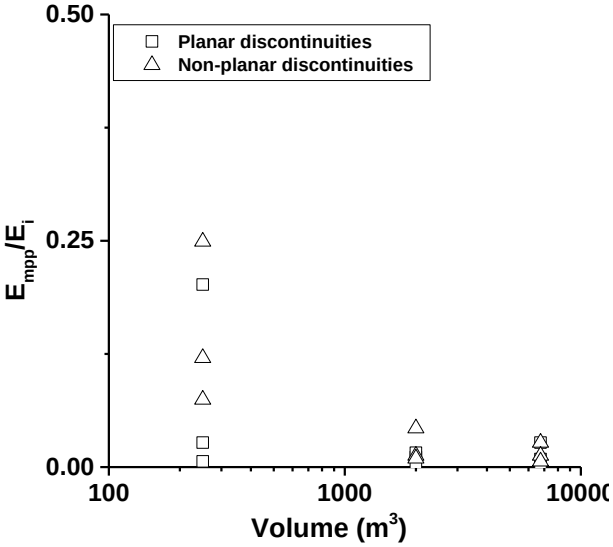

(d)

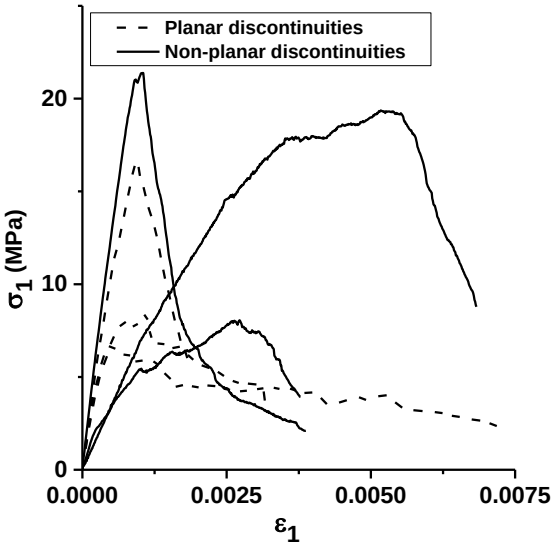

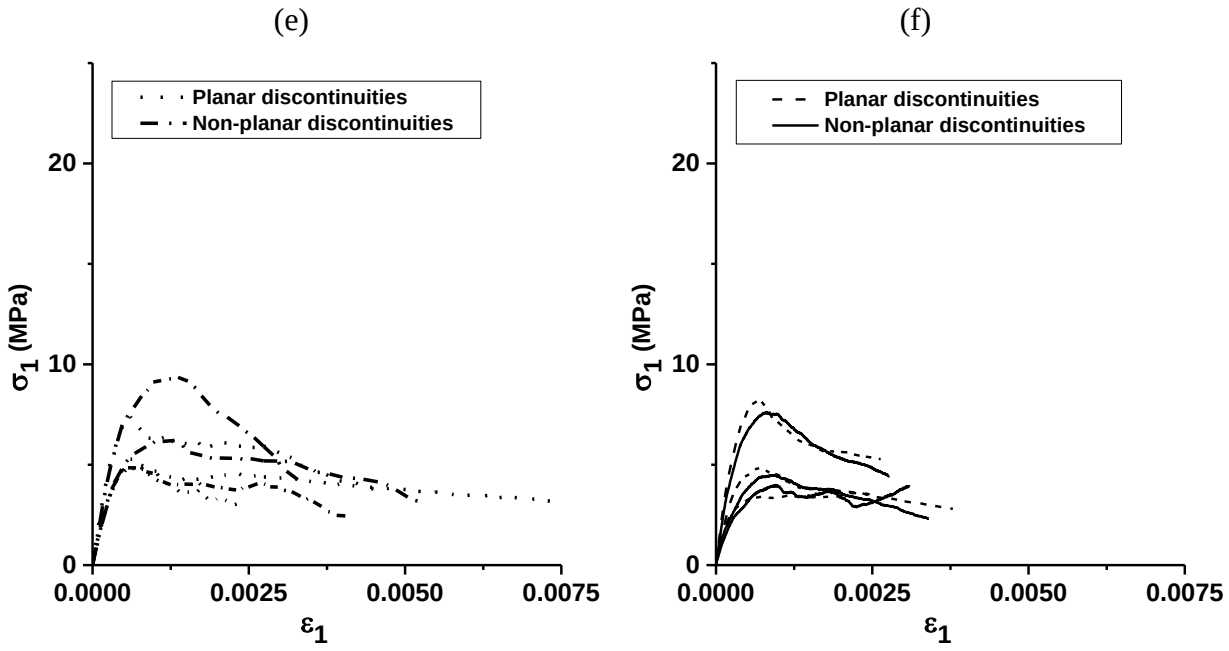

Figure 7-3 Influences of rock mass scale on (a) σ_1/σ_c, (b) E_m/E_i, (c) E_{mpp}/E_i for rock mass models with planar (unfilled square) and non-planar (unfilled triangle) discontinuities (shown on a log–log plot) under unconfined compression. (d) Axial stress–axial strain plots for three rock mass models with planar discontinuities (dashed line) and three rock mass models with non-planar discontinuities (solid line) of 5 m × 5 m × 10 m dimensions (e) Axial stress–axial strain plots for three rock mass models with planar discontinuities (dotted line) and three rock mass models with non-planar discontinuities (dash dot line) of 10 m × 10 m × 20 m dimensions (e) Axial stress–axial strain plots for three rock mass models with planar discontinuities (dashed line) and three rock mass models with non-planar discontinuities (solid line) of 15 m × 15 m × 30 m dimensions, under unconfined compression.

The anisotropy is more pronounced in the smaller rock mass samples and it decreases with the increase of the rock mass scale. The σ_1/σ_c, E_m/E_i, and E_{mpp}/E_i begin to converge for the model with dimensions 10 m × 10 m × 20 m. Thus, the rock mass sample with dimensions 10 m × 10 m × 20 m is the mechanical REV for the rock mass and this sample size is used to investigate the influence of discontinuity intensity (Section 7.2) and confining pressure (Section 7.3) on the mechanical responses under compression.

7.2 Influence of P_{32} on the mechanical properties of rock mass

It is demonstrated in Section 5.3.1 that the strength and deformation modulus of the laboratory-scale jointed granite decrease with the increase of P_{32}. In this section, the influence of P_{32} on the strength and deformation modulus of a large-scale rock mass is investigated. LS-SRM models with a of dimension 10 m × 10 m × 20 m with both planar and non-planar discontinuities are constructed using the DFN samples, extracted in Section 7.1, of varying P_{32} = 0.23 m^{-1}, 0.39 m^{-1}, and 0.53 m^{-1}. These SRM models are loaded under unconfined compression. The same lattice input parameters as the ones used in Section 7.1 are used.

The modeling results suggest that the σ_1/σ_c (Figure 7-4a), E_m/E_i (Figure 7-4b), and E_{mpp}/E_i (Figure 7-4c) ratios of the jointed rock mass decrease with the increase of P_{32} for both the models with planar and non-planar discontinuities. This is because that the volume of the intact rock is reduced progressively with the increase of P_{32} and the rock mass strength and deformation modulus also decrease. The jointed rock mass models with non-planar discontinuities have higher values of σ_1/σ_c, E_m/E_i, and E_{mpp}/E_i than the ones with planar discontinuities; however, the relative difference between models with planar and non-planar discontinuities reduces with the increase of P_{32}. This behavior is also illustrated using the axial stress–axial strain plots (Figure 7-4d,e&f).

(a)

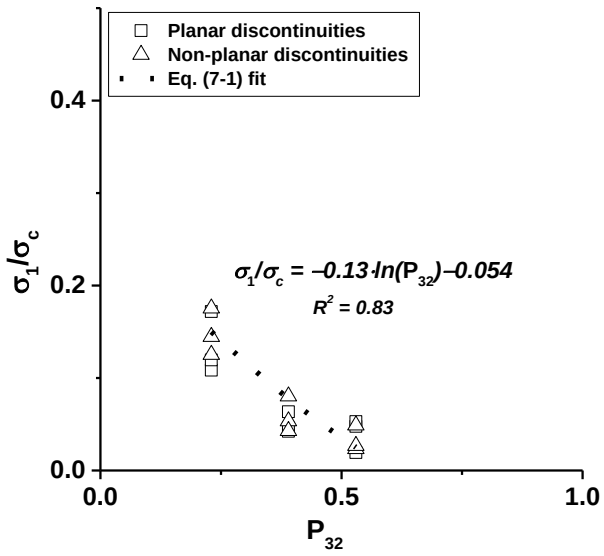
Planar discontinuities
Non-planar discontinuities
Eq. (7-1) fit
σ1/σc = –0.13·ln(P32)–0.054
R2 = 0.83
σ1/σc
P32
0.0
0.2
0.4
0.0
0.5
1.0

(b)

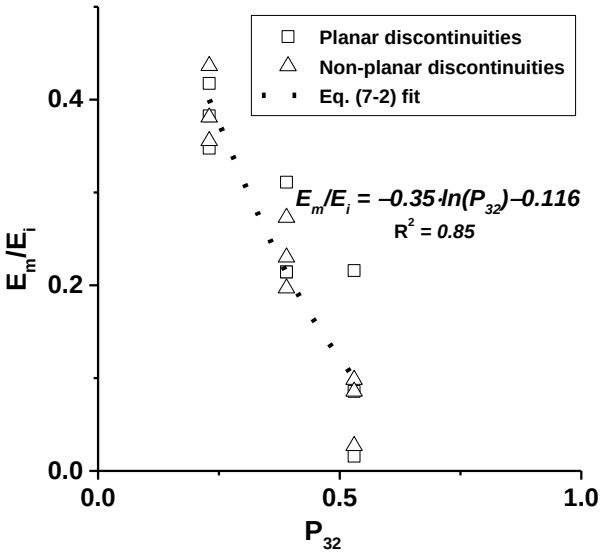
Planar discontinuities
Non-planar discontinuities
Eq. (7-2) fit
Em/Ei = –0.35·ln(P32)–0.116
R2 = 0.85
Em/Ei
P32
0.0
0.2
0.4
0.0
0.5
1.0

(c)

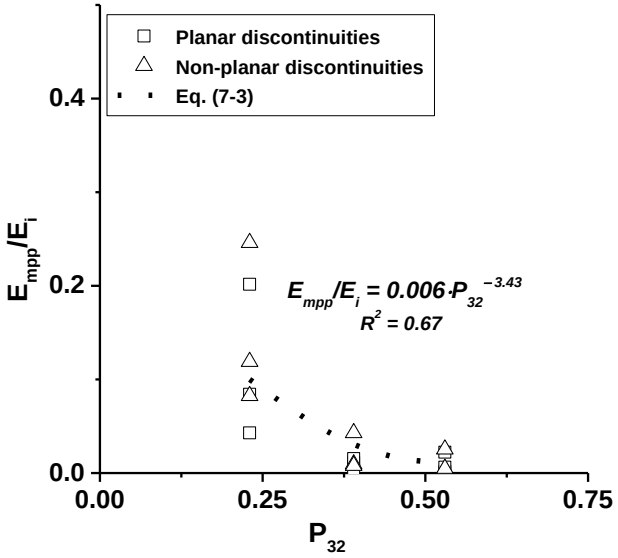
Planar discontinuities
Non-planar discontinuities
Eq. (7-3)
Empp/Ei = 0.006·P32 −3.43
R2 = 0.67
Empp/Ei
P32
0.0
0.2
0.4
0.00
0.25
0.50
0.75

(d)

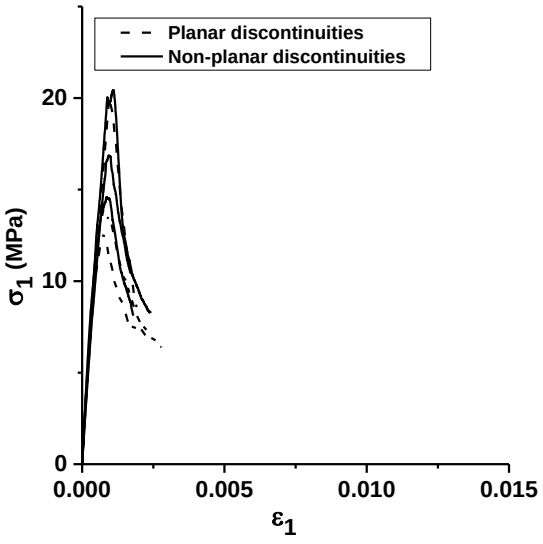
Planar discontinuities
Non-planar discontinuities
σ1 (MPa)
ε1
0
10
20
0.000
0.005
0.010
0.015

(e) (f)

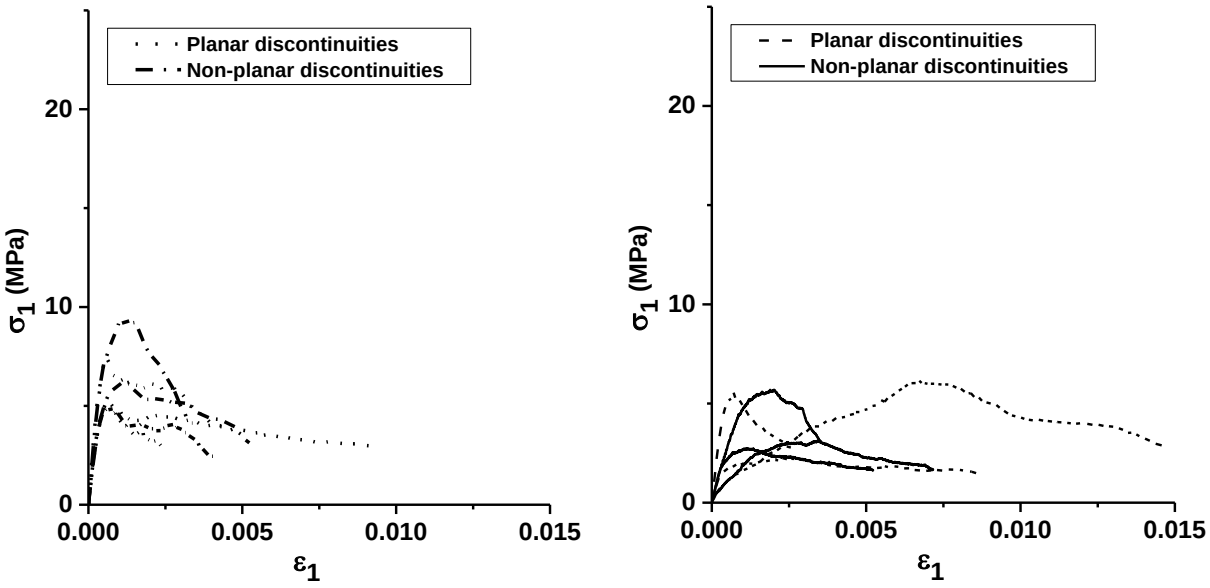

Figure 7-4 Influences of P_{32} on (a) σ_1/σ_c, (b) E_m/E_i, and (c) E_{mpp}/E_i of rock mass with a dimension of 10 m × 10 m × 20 m with planar (unfilled square) and non-planar (unfilled triangle) discontinuities under unconfined compression. (d) Axial stress–axial strain plots for three rock mass models with planar discontinuities (dashed line) and three rock mass models with non-planar discontinuities (solid line) of P_{32} = 0.23 m^{-1} (e) Axial stress–axial strain plots for three rock mass models with planar discontinuities (dotted line) and three rock mass models with non-planar discontinuities (dashed dot line) of P_{32} = 0.39 m^{-1} (e) Axial stress–axial strain plots for three rock mass models with planar discontinuities (dashed line) and three rock mass models with non-planar discontinuities (solid line) of P_{32} = 0.53 m^{-1}, under unconfined compression.

The influences of P_{32} on σ_1/σ_c, E_m/E_i, and E_{mpp}/E_i are quantified by performing regression analysis and the following relations are derived,

$$\sigma_1/\sigma_c = -0.13 \cdot \ln(P_{32}) - 0.054 \quad \text{(MPa)} \quad R^2 = 0.83 \text{ for } P_{32} \leq 0.53 \text{ m}^{-1} \tag{7-1}$$

$$E_m/E_i = -0.35 \cdot \ln(P_{32}) - 0.116 \cdot \quad \text{(GPa)} \quad R^2 = 0.85 \text{ for } P_{32} \leq 0.53 \text{ m}^{-1} \tag{7-2}$$

$$E_{mpp}/E_i = 0.006 \cdot P_{32}^{-3.43} \cdot \quad \text{(GPa)} \quad R^2 = 0.67 \text{ for } P_{32} \leq 0.53 \text{ m}^{-1} \tag{7-3}$$

These relations can be used to estimate the rock mass strength and deformation modulus. It is not practical to measure the P_{32} parameter directly from the field and it needs to be inferred from the P_{21} and P_{10} parameters as these can be measured directly on the field. To this end, 177 P_{21} values are extracted from 59 planar slices (Figure 7-5a) on three DFNs generated in Section 6.3.2 and these are used to derive a power law relation between P_{21} and P_{32} (Figure 7-5b) as,

$$P_{32} = 0.9579 \cdot P_{21}^{0.9789} \qquad R^2 = 0.96 \tag{7-4}$$

Similarly, 180 P_{10} values are extracted from sixty scanlines along all six planes on the three DFNs generated in Section 6.3.2 and these are used to derive a power law relation between P_{10} and P_{32} (Figure 7-5c) as,

$$P_{32} = 1.3823 \cdot P_{10}^{0.8821} \qquad R^2 = 0.83 \tag{7-5}$$

The Eqs. (7-4) & (7-5) can be used to convert the field measured P_{21} and P_{10} values into P_{32}. The P_{32} values can then be used to estimate the values of σ_1/σ_c, E_m/E_i, and E_{mpp}/E_i using Eqs. (7-1), (7-2), and (7-3), respectively.

(a)

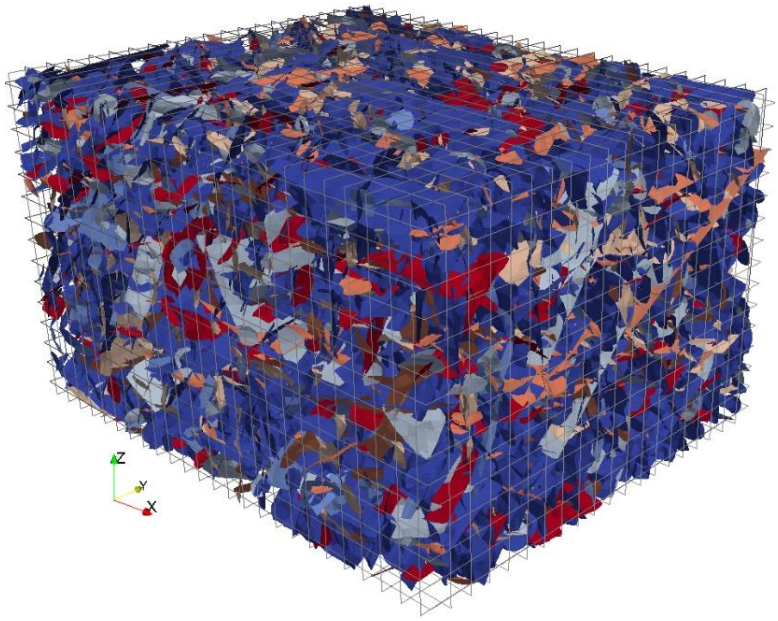

(b)

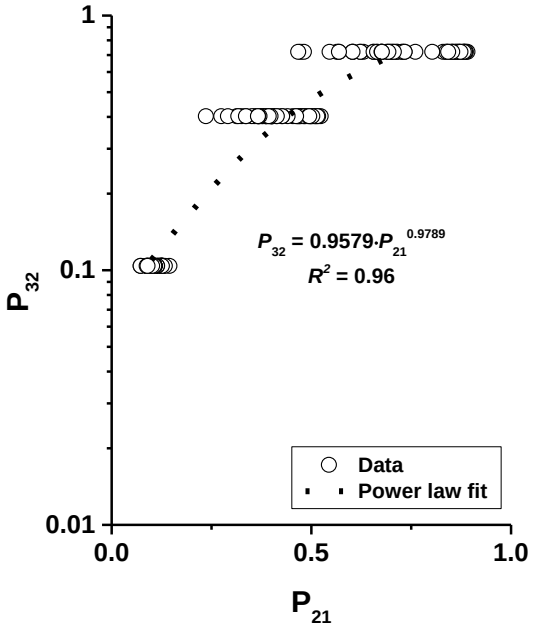

(c)

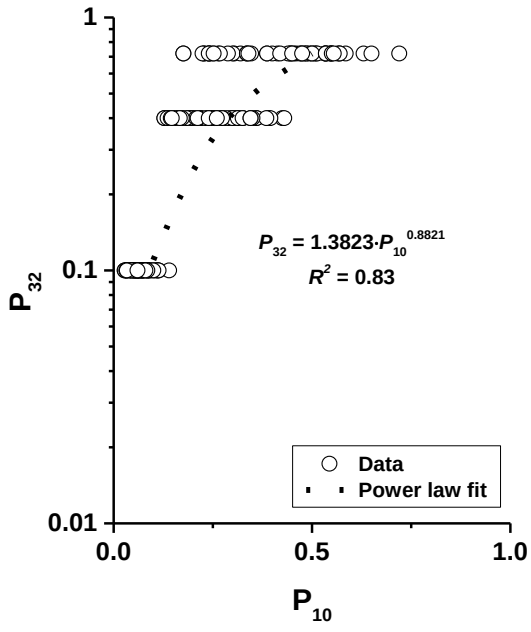

Figure 7-5 (a) Multiple planes through which the DFN is sliced; (b) regression analysis of P_{32} and P_{21} with a power law fit; (c) regression analysis of P_{32}–P_{10} with a power law fit.

7.3 Effect of confinement on the peak strength of rock mass

In a moderately jointed rock mass with non-persistent discontinuities, failure normally occurs due to the coalescence of cracks propagating from pre-existing discontinuities and the failure of intact rock bridges. The crack initiation and propagation are hindered by the confining pressure attributing to the increase of the strength of the jointed rock as shown in Section 4. Large-scale rock masses could also show similar behavior under confined compression. Results from various laboratory and numerical studies on the laboratory-scale jointed rock (Alejano et al., 2017), rock mass analogs (Bahrani, 2015), and synthetic rock mass models (Farahmand, 2018) have demonstrated that there is a clear influence of confining pressure on the peak strength. However, these investigations were either limited to 2D models (Bahrani, 2015; Farahmand, 2018) or did not incorporate realistic non-planar discontinuities in the synthetic rock mass models (Poulsen et al., 2015; Zhang, 2014).

In this section, the influence of confining pressure on the peak strength of rock mass is investigated using three rock mass models with a dimension of 10 m × 10 m × 20 m and containing non-planar discontinuities with P_{32} values of 0.23, 0.39, and 0.53 m^{-1}. The rock mass models are subjected to triaxial loading under confining pressures of 0, 1, 2, 4, and 6 MPa. Same lattice input parameters as the ones used in Section 7.1 are used.

As expected, the normalized strength (σ_1/σ_c) of the jointed rock mass increases (Figure 7-6a) with the increase of σ_3 but decreases with the increase of P_{32}. With the increase of σ_3, the growth of the tensile cracks is suppressed because by increasing σ_3, a higher ratio of applied principal stresses (σ_1/σ_3) is required for the initiation and propagation of cracks through the intact rock bridges. This behavior is also illustrated using differential stress–axial strain plots in Figure 7-6b,c&d. The

stress–strain curves of these highly jointed rock masses exhibit a non-linear pre-peak deformation behavior and a ductile–plastic post-peak deformation behavior under confinement σ_3 = 6, 4, 2, and 1 MPa for P_{32} values of 0.23, 0.39, and 0.53 m^{-1}, respectively.

The influence of P_{32} and σ_3 on σ_1/σ_c is quantified by performing a bi-variate regression analysis and the following relation is derived,

$$\sigma_1/\sigma_c = (0.064\sigma_3 + 0.97exp^{-7.38P_{32}} + 0.002) \quad \text{(MPa)} \qquad \text{(7-6)}$$
$$\text{for } 0 \leq P_{32} \leq 0.53, \sigma_3 \leq 6 \text{ MPa, and } R^2 = 0.99$$

(a)

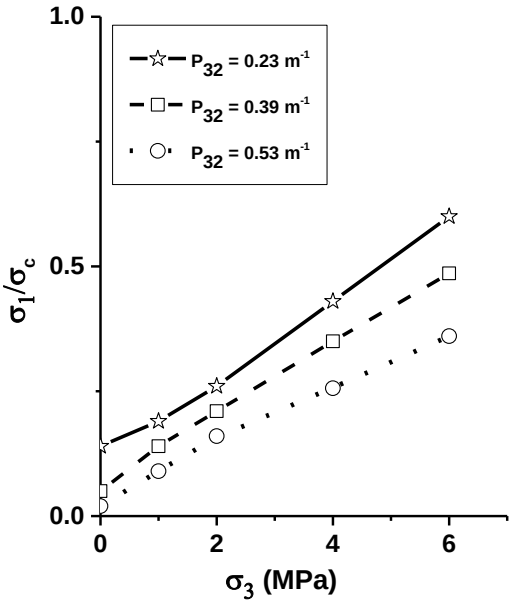

(b)

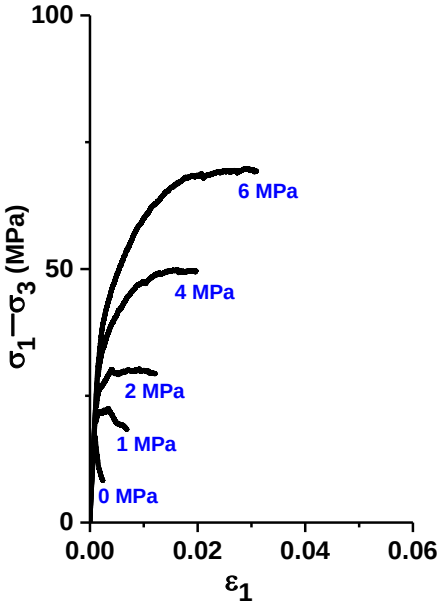

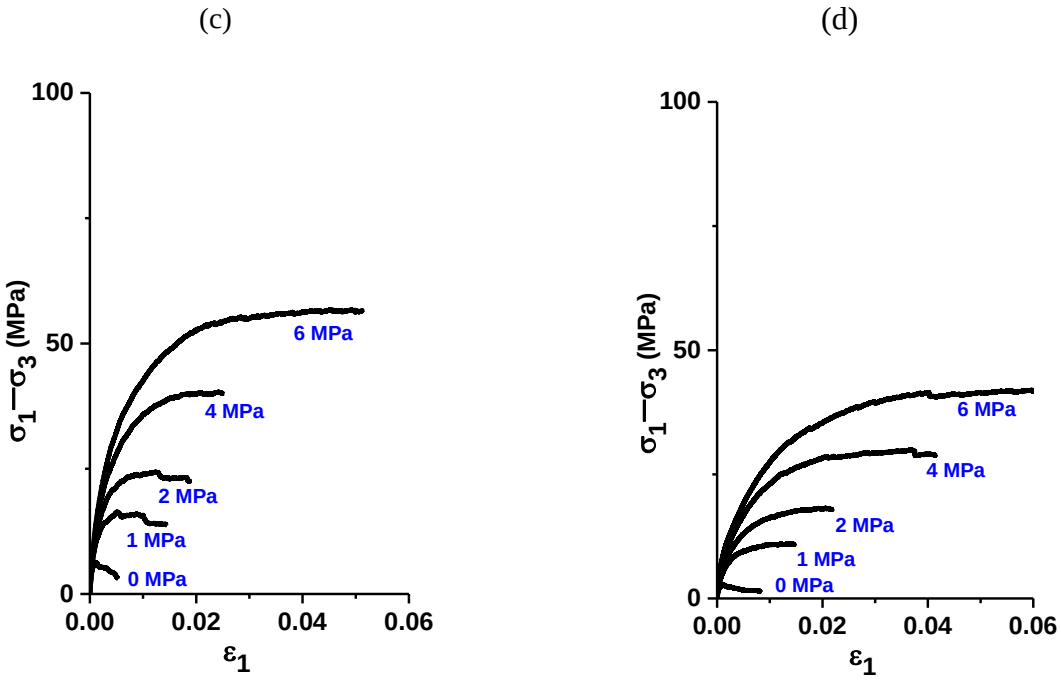

Figure 7-6 (a) Comparison of σ_1/σ_c–σ_3 plot for jointed rock masses with different P_{32} under triaxial compression; differential stress–axial strain plots for rock mass models with (b) P_{32} = 0.23 m^{-1}, (c) P_{32} = 0.39 m^{-1}, and (d) P_{32} = 0.53 m^{-1} under triaxial compression.

Due to the unavailability of the triaxial test data, it is not possible to directly validate Eq. (7-6) for the estimation of peak strength of large-scale rock mass. The reliability of the equation can be enhanced by verifying its utility using the additional experimental test data in the future as they become available.

7.4 Remarks

In this Chapter, the mechanical response of a large-scale rock mass is investigated under unconfined and confined compressions. The mechanical response of the jointed rock mass is influenced by the scale, discontinuity intensity, and confining pressure. It is not feasible to perform the compression tests on very large-scale rock mass. Therefore, a scale-effect study is conducted to determine the rock mass REV which has a dimension of 10 m × 10 m × 20 m. Peak strength,

pre-peak and post-peak deformation moduli of the rock mass decrease with the increase of the rock mass scale under unconfined compression. The results from the unconfined compression simulations on the REV sized rock mass samples indicate that peak strength and deformation modulus of the rock mass decrease with the increase of P_{32}. In addition, both the strength and deformation modulus of the rock mass with non-planar discontinuities are higher than of the ones with planar discontinuities; however, the relative difference diminishes with the increase of discontinuity intensity. The peak strength of the REV sized jointed rock mass increases with the increase of the confining pressure. The stress–strain curves of these highly jointed rock masses exhibit a very high degree of nonlinearity in pre-peak deformation stage and a ductile–plastic post-peak deformation behavior even under a low confinement. The empirical relation is derived for the estimation of rock mass strength under confined compression. The modeling approach has the potential to simulate deformation responses of underground excavations.

Chapter 8

8 Conclusions and future research

The main objective of this PhD research is to study the mechanical behaviors of both laboratory-scale and large-scale jointed rock masses with planar and non-planar discontinuities under compression using the LS-SRM modeling approach. An emphasis is placed on understanding the influence of realistic non-planar discontinuities on the mechanical response of laboratory-scale jointed rock, large-scale rock mass, and slope stability. State-of-the-art of the existing literatures are fully reviewed in Chapter 2 and Itasca's SRMTools software is used for model simulations. The results of the investigative study in Chapters (3, 4, 5, and 7) strengthen the understanding of the mechanical response of jointed rock mass. Stability and deformability of slopes excavated in rock mass with different degree of jointing are investigated in Chapter 6. The main conclusions from the thesis work are presented in Section 8.1 and potential future research works are recommended in Section 8.2.

8.1 Conclusions

Because SRMTools is a relatively new software tool, an extensive sensitivity study of the lattice model parameters are performed in Chapters 3 and the following conclusions are made:

a) The strength of intact rock depends on the lattice size when the spherical-shaped lattice structure is used and the dependence on lattice size is low for the Voronoi-shaped lattice structure.

b) The compressive and tensile strengths and angle of the internal friction of intact rock increase non-linearly with the increase of the radius multiplier.

c) The intact rock's deformation modulus increases linearly with the increase of the lattice deformation modulus. Similarly, the intact rock's compressive to tensile strength ratio increases linearly with the increase of the lattice's compressive to tensile strength ratio.

d) The angle of internal friction of intact rock increases linearly with the increase of the peak friction angle of the flat joint and the post-peak deformation behavior is controlled by the residual friction angle of the flat joint.

Using the results of the sensitivity analysis and the laboratory test results of Zhenping marble, a methodology is developed for the calibration of LS-SRM model parameters of intact rock.

In Chapter 4, the influence of discontinuity surface geometry on the cracking mechanism and mechanical properties of pre-cracked rocks has been investigated using the LS-SRM modeling approach under unconfined and confined compressions, using eight different models with planar and non-planar crack configurations. Using the results of the sensitivity analysis of the joint stiffness on the strength and deformability of the pre-cracked marble, a methodology is developed for the calibration of jointed rock. The following conclusions are made based on the numerical modeling results:

a) The mechanical response and the cracking patterns of pre-cracked rocks are highly dependent on the spatial location, persistence, waviness, and the number of cracks.

b) In the cracked rock models with planar cracks, initiation of tensile wing cracks from the internal crack tips is accompanied with the breakage of intact rock bridges between the cracks; in the cracked rock models with wavy or non-planar cracks, slipping along the

cracks is hindered by the asperities with the initiation of secondary cracks from the wavy section of the cracks along with the tensile wing-cracks from the internal crack tips.

c) Five types of failure are identified, and the failure mode is mixed tensile splitting and shearing failures under unconfined compression. Under the confined compression condition, shear failure dominates because tensile damage is largely suppressed.

d) As expected, compared with the intact marble, the cracked marbles have lower strength and deformation modulus. Both the peak strength and the deformation modulus decrease with the increase of the crack angle, crack length, ligament angle, and the number of cracks. The strength and the stiffness of the cracked marble with non-planar cracks are higher than the ones with planar cracks when the crack persistence is high, indicating that the influence of crack waviness on rock properties is high only when the crack persistency is large.

e) The model results are reasonably consistent with the results of previous experimental studies (Yang et al., 2009, 2008) and numerical modelings (Wang et al., 2014).

The mechanical behaviors of laboratory-scale jointed granite with different joint configurations (orientation, intensity, waviness, and persistence) are investigated under triaxial compression using the LS-SRM modeling approach in Chapter 5 and the following conclusions are made:

a) The strength and deformability of the jointed granites are lower than those of the intact granite and are highly depended on the orientation, intensity, waviness, and persistence of the joints.

b) The jointed granites exhibit a U-shaped strength curve with the increase of joint dip from 35° to 67° and the deformation modulus increases non-linearly with the increase of joint dip.

c) Both the strength and deformation modulus decrease with the increase of joint intensity and joint persistence.

d) The strength and deformation modulus of the jointed rocks with non-planar joints are higher than the ones with planar joints because of the additional resistance provided by the asperities along the rough joints.

e) For both the intact and the jointed rock under true triaxial compression, the strength and deformation modulus increase with the increase of the intermediate principal stress. Furthermore, the degree of strength enhancement due to the intermediate principal stress depends on the relative orientation of the intermediate principal stress to the orientation of the dominant joint set, which influences the stiffening effect of the jointed rock due to joint clamping.

f) The results of the numerical investigation of intact and jointed granite are reasonably consistent with the laboratory test results (Arzua et al., 2014; Alejano et al., 2017).

In Chapter 6, a planar sliding problem is simulated first in Slope Model to validate the capability of the tool to analyze the stability of slopes with both planar and non-planar cohesionless and persistent discontinuities. The results from the validation exercise suggest that the factor of safety computed from the analytical solution of the cohesionless and persistent planar discontinuities is the same as the one form the Slope Model software. In addition, the factor of safety is found to be

higher for slopes with non-planar discontinuities than for slopes with planar ones. Next, the slope stability of the Cadia Hill Open Pit mine is assessed using the LS-SRM modeling approach in Slope Model and the model is calibrated using failure information of the South wall and the field measured displacements. A parametric study is conducted using the calibrated model to investigate the influence of different discontinuity configurations (waviness, intensity, size) and *in-situ* stress on the displacement and stability of the slope and the following conclusions are made:

a) The displacements decrease and the slope is relatively stable when the surface of the discontinuities is changed from planar to non-planar ones for moderately jointed rock masses.

b) The displacements increase and the slope is increasingly unstable with the increase of discontinuity size and intensity.

c) At greater pit depth with higher *in-situ* stress, both the slope models with planar and non-planar discontinuities experience localized failures due to very high stress concentrations and the slope model with planar discontinuities is more deformable and less stable than the slope model with non-planar discontinuities.

The mechanical responses of jointed rock masses are influenced by the scale, discontinuity intensity, and confining pressure as investigated in Chapter 7 and the following conclusions are made:

a) The results of the scale-effect study suggest that the rock mass with the dimension of 10 m ×10 m × 20 m is the REV of the rock mass and both the strength and deformation modulus of the rock mass decreases with the increase of the rock mass scale under compression.

b) The strength and deformation modulus of the rock mass decrease with the increase of P_{32}.

c) The strength and deformation modulus of the rock mass with non-planar discontinuities are higher than of the ones with planar discontinuities; however, the relative difference diminishes with the increase of the discontinuity intensity.

d) The strength of the rock mass increases with the increase of confining pressure. An empirical relation is derived for the estimation of rock mass strength under confined compression.

The results from this thesis have provided new avenues in the characterization of the mechanical properties of jointed rock masses and the stability assessment of jointed slopes with realistic non-planar discontinuities.

8.2 Recommendations for future research

The LS-SRM modeling approach used in this research is a relatively new method. Although very interesting conclusions are drawn, the developed models are not flawless, and improvements can be made. Some recommendations for future research and development are:

a) Some of the limitations of the software (SRMTools) can be improved in future versions. For example, (i) Poisson's ratio of the intact rock is very low for the LS-SRM models with flat joint contacts; (ii) confining pressures along with the axial load are applied simultaneously, unlike the laboratory test procedure during triaxial and direct shear test simulations; (iii) cross-section of the synthetic rock sample is square in SRMLab, and (iv) the flexibility of modeling using powerful cloud computing would allow to solve large-scale geotechnical problems.

b) More robust characterization of the degree of waviness during the generation of DFNs with non-planar discontinuities in MoFrac could provide a more reliable estimate of geomechanical parameters for rock mass with realistic discontinuity structures.

c) The current research approach should be extended to achieve a reliable estimate of support system requirements for engineering structures built in and on jointed rock mass with realistic discontinuities.

d) The LS-SRM modeling approach should be applied to solving geotechnical problems relating to underground mine pillars, caverns for fuel storage and nuclear waste disposal, tunnel design, dam foundation design, etc.

References

Alejano, L. R., Arzua, J., Bozorgzadeh, N., & Harrison, J. P. (2017). Triaxial strength and deformability of intact and increasingly jointed granite samples. *International Journal of Rock Mechanics and Mining Sciences*, *95*, 87–103.

Alghalandis, Y. F. (2017). ADFNE: Open source software for discrete fracture network engineering, two and three dimensional applications. *Computers & Geosciences*, *102*, 1–11.

Arzua, J., Alejano, L. R., & Walton, G. (2014). Strength and dilation of jointed granite specimens in servo-controlled triaxial tests. *International Journal of Rock Mechanics and Mining Sciences*, *69*, 93–104.

Aydan, O., & Dalgic, S. (1998). Prediction of deformation behaviour of 3-lanes Bolu tunnels through squeezing rocks of North Anatolian fault zone (NAFZ). *Proceedings of the Regional Symposium on Sedimentary Rock Engineering*, 228–233. Taipei.

Bahrani, N. (2015). *Estimation of confined peak strength for highly interlocked jointed rockmasses. PhD Thesis. Laurentian University, Sudbury, Ontario;*

Bandis, S., Lumsden, A. C., & Barton, N. (1981). Experimental studies of scale effects on the shear behaviour of rock joints. *International Journal of Rock Mechanics and Mining Sciences & Geomechanics Abstracts*, *18*, 1–21.

Barton, N. (1973). Review of a new shear-strength criterion for rock joints. *Engineering Geology*, *7*(4), 287–332.

Barton, N. (2002). Some new Q-value correlations to assist in site characterisation and tunnel design. *International Journal of Rock Mechanics and Mining Sciences*, *39*(2), 185–216.

Barton, N., & Choubey, V. (1977). The shear strength of rock joints in theory and practice. *Rock Mechanics*, *10*(1–2), 1–54.

Barton, N., Lien, R., & Lunde, J. (1974). Engineering classification of rock masses for the design of tunnel support. *Rock Mechanics*, *6*(4), 189–236.

Bastola, S., & Cai, M. (2018a). Investigation of strength and deformation behaviors of intact and jointed Granite using lattice-spring-based synthetic rock mass models. *2nd International Discrete Fracture Network Engineering Conference*. Seattle.

Bastola, S., & Cai, M. (2018b). Simulation of stress–strain relations of Zhenping marble using lattice-spring-based synthetic rock mass models. *52nd U.S. Rock Mechanics/Geomechanics Symposium*. Seattle; 17-20 June.

Bastola, S., & Cai, M. (2019). Investigation of mechanical properties and crack propagation in pre-cracked marbles using lattice-spring-based synthetic rock mass (LS-SRM) modeling approach. *Computers and Geotechnics*, *110*, 28–43.

Beiki, M., Bashari, A., & Majdi, A. (2010). Genetic programming approach for estimating the deformation modulus of rock mass using sensitivity analysis by neural network. *International Journal of Rock Mechanics and Mining Sciences*, *47*(7), 1091–1103.

Bhasin, R., & Grimstad, E. (1996). The use of stress-strength relationships in the assessment of tunnel stability. *Tunnelling and Underground Space Technology*, *11*(1), 93–98.

Bieniawski, Z. T. (1973). Engineering classification of jointed rock masses. *South African Institute of Civil Engineers*, *15*(12), 335–343.

Bieniawski, Z. T. (1978). Determining rock mass deformability: Experience from case histories. *International Journal of Rock Mechanics and Mining Sciences & Geomechanics Abstracts*, *15*(5), 237–247.

Billaux, D. B., Luvison, D., & B.P. Darcel. (2006). *3FLO, calculs d'écoulements tridimensionnels, bases théoretiques*. Lyon: Itasca Consultants SAS.

Bobet, A., & Einstein, H. H. (1998). Fracture coalescence in rock-type materials under uniaxial and biaxial compression. *International Journal of Rock Mechanics and Mining Sciences*, *35*(7), 863–888.

Bonilla-Sierra, V., Scholtès, L., Donzé, F. V., & Elmouttie, M. K. (2015a). DEM analysis of rock bridges and the contribution to rock slope stability in the case of translational sliding failures. *International Journal of Rock Mechanics and Mining Sciences*, *80*, 67–78.

Bonilla-Sierra, V., Scholtès, L., Donzé, F. V., & Elmouttie, M. K. (2015b). Rock slope stability analysis using photogrammetric data and DFN-DEM modelling. *Acta Geotechnica*, *10*(4), 497–511.

Brady, B., & Brown, E. (2006). Rock Mechanics for underground mining: Third edition. In *Rock Mechanics for underground mining: Third edition*.

Brideau, M.-A., Pedrazzini, A., Stead, D., Froese, C., Jaboyedoff, M., & van Zeyl, D. (2011). Three-dimensional slope stability analysis of South Peak, Crowsnest Pass, Alberta, Canada. *Landslides*, *8*(2), 139–158.

Brown, E. T. (2008). Estimating the mechanical properties of rock masses. *Proceedings of the 1st Southern Hemisphere International Rock Mechanics Symposium: SHIRMS*, *1*, 3–21.

Brown, E. T., & Trollope, D. H. (1970). Strength of a model of jointed rock. *Journal of the Soil Mechanics and Foundations Division*, *96*(2), 685–704.

Cai, M. (2008). Influence of intermediate principal stress on rock fracturing and strength near excavation boundaries—insight from numerical modeling. *International Journal of Rock Mechanics and Mining Sciences*, *45*(5), 763–772.

Cai, M. (2010). Practical Estimates of Tensile Strength and Hoek--Brown Strength Parameter mi of Brittle Rocks. *Rock Mechanics and Rock Engineering*, *43*(2), 167–184.

Cai, M. (2013). Fracture initiation and propagation in a brazilian disc with a plane interface: a numerical study. *Rock Mechanics and Rock Engineering*, *46*(2), 289–302.

Cai, M., & Kaiser, P. . (2004). Numerical simulation of the brazilian test and the tensile strength of anisotropic rocks and rocks with pre-existing cracks. *International Journal of Rock Mechanics and Mining Sciences*, *41*, 478–483.

Cai, M., Kaiser, P. ., Tasaka, Y., Maejima, T., Morioka, H., & Minami, M. (2004). Generalized crack initiation and crack damage stress thresholds of brittle rock masses near underground excavations. *International Journal of Rock Mechanics and Mining Sciences*, *41*(5), 833–847.

Cai, M., & Kaiser, P. K. (2014). In-situ rock spalling strength near excavation boundaries. *Rock Mechanics and Rock Engineering*, *47*(2), 659–675.

Cai, M., Kaiser, P. K., Tasaka, Y., & Minami, M. (2007). Determination of residual strength parameters of jointed rock masses using the GSI system. *International Journal of Rock Mechanics and Mining Sciences*, *44*(2), 247–265.

Cai, M., Kaiser, P. K., Uno, H., Tasaka, Y., & Minami, M. (2004). Estimation of rock mass deformation modulus and strength of jointed hard rock masses using the GSI system. *International Journal of Rock Mechanics and Mining Sciences*, *41*(1), 3–19.

Camones, L. A. M., Vargas, E. do A., de Figueiredo, R. P., & Velloso, R. Q. (2013). Application of the discrete element method for modeling of rock crack propagation and coalescence in the step-path failure mechanism. *Engineering Geology*, *153*, 80–94.

Cao, P., Liu, T., Pu, C., & Lin, H. (2015). Crack propagation and coalescence of brittle rock-like specimens with pre-existing cracks in compression. *Engineering Geology*, *187*, 113–121.

Castro-Filgueira, U. (2019). *Simulación numérica del comportamiento tenso-deformacional de muestras de granito naturales y artificialmente fisuradas mediante el código de partículas PFC3D. PhD Thesis. Universidad de Vigo, Spain; 2019*. PhD Thesis, Universidad de Vigo.

Castro-Filgueira, U., Alejano, L. R., Arzúa, J., & Mas Ivars, D. (2016). Numerical simulation of the stress-strain behavior of intact granite specimens with particle flow code. *ISRM International Symposium - EUROCK*. Ürgüp, Turkey; 29-31 August. pp. 421-426.

Chen, G., JM, K., & Harpalani, S. (1995). Fracture propagation and coalescence in Marble plates with pre-cut notches under compression. *Proceedings of Fractured and Jointed Rock Mass*, 443–448.

Cundall, P. (2011). Lattice method for modeling brittle, jointed rock. *Proceedings of the 2nd Int'l FLAC/DEM Symposium on Continuum and Distinct Element Numerical Modeling in Geomechanics*. Melbourne.

Cundall, P. A. (1971). A Computer Model for Simulating Progressive Large Scale Movements in Blocky Rock System. *International Proceedings Symposium, ISRM*, 128–132. Nancy: ISRM.

Cundall, P., Damjanac, B., & Varun, V. (2016). Considerations on slope stability in a jointed rock mass. *50th U.S. Rock Mechanics/Geomechanics Symposium*. Houston.

Damjanac, B., Detournay, C., & Cundall, P. (2016). Application of particle and lattice codes to simulation of hydraulic fracturing. *Computational Particle Mechanics*, *3*(2), 249–261.

Deere, D. U., Hendron, A. J., Patton, F. D., & Cording, E. J. (1966). Design of surface and near-surface construction in rock. *The 8th U.S. Symposium on Rock Mechanics (USRMS)*. Minneapolis; 15-17 September. pp. 237-302.

Dershowitz, W. (1984). *Rock joint systems*. PhD Thesis. Massachusetts Institute of Technology.

Dershowitz, W., & Herda, H. (1992). Interpretation of fracture spacing and intensity. *The 33rd US Symposium on Rock Mechanics*. New Mexico.

Diederichs, M., Espley, S., Langille, C., & Hutchinson, D. J. (2000). A semi-empirical hazard assessment approach to wedge instability in underground mine openings. *ISRM International Symposium*. Melbourne: International Society for Rock Mechanics and Rock Engineering.

Einstein, H. H., & Hirschfeld, R. C. (1973). Model studies on mechanics of jointed rocks. *Journal of Soil Mechanics & Foundations Divisions.*, *99*(3), 229–248.

Einstein, H. H., Hirschfeld, R. C., Nelson, R. A., & Bruhn, R. W. (1969). Model studies of jointed-rock behavior. *The 11th U.S. Symposium on Rock Mechanics (USRMS)*. Berkeley; 16-19 June. pp. 83-103.

Einstein, H. H., Veneziano, D., Baecher, G. B., & O'Reilly, K. J. (1983). The effect of discontinuity persistence on rock slope stability. *International Journal of Rock Mechanics and Mining Sciences & Geomechanics Abstracts*, *20*(5), 227–236.

Elmo, D. (2006). *Evaluation of a hybrid FEM/DEM approach for determination of rock mass strength using a combination of discontinuity mapping and fracture mechanics*. PhD Thesis, University of Exeter.

Elmo, D., Donati, D., & Stead, D. (2018). Challenges in the characterisation of intact rock bridges in rock slopes. *Engineering Geology*, *245*, 81–96.

Elmo, D., & Stead, D. (2010). An integrated numerical modeling-Discrete fracture network approach applied to the characterisation of rock mass strength of naturally fractured pillars. *Rock Mechanics and Rock Engineering*, *43*(1), 3–19.

Erhel, J., Dreuzy, J. De, & Poirriez, B. (2009). Flow simulation in three-dimensional discrete fracture networks. *SIAM Journal on Scientific Computing*, *31*(4), 2688–2705.

Esmaieli, K., Hadjigeorgiou, J., & Grenon, M. (2010). Estimating geometrical and mechanical REV based on synthetic rock mass models at Brunswick Mine. *International Journal of Rock Mechanics and Mining Sciences*, *47*(6), 915–926.

Esterhuizen, G. S., Dolinar, D. R., & Ellenberger, J. L. (2011). Pillar strength in underground stone mines in the United States. *International Journal of Rock Mechanics and Mining Sciences*, *48*(1), 42–50.

Fan, X., Kulatilake, P. H. S. W., & Chen, X. (2015). Mechanical behavior of rock-like jointed blocks with multi-non-persistent joints under uniaxial loading: A particle mechanics approach. *Engineering Geology*, *190*, 17–32.

Farahmand, K. (2018). *Characterization of rockmass properties and excavation damage zone (EDZ) using a synthetic rock mass (SRM) approach*. PhD Thesis, Queen's University.

Fisher, R. (1953). Dispersion on a sphere. *Proceedings of the Royal Society of London. Series A. Mathematical, Physical, and Engineering Sciences*, *217*(1130), 295–305.

Franz, J. (2009). *An investigation of combined failure mechanisms in large scale open pit slopes*. PhD Thesis, University of New South Wales.

Gao, F. (2013). *Simulation of failure mechanisms around underground coal mine openings using discrete element modeling*. PhD Thesis, Simon Fraser University.

Gao, F., & Stead, D. (2013). Discrete Element Modeling of cutter roof failure in coal mine roadways. *International Journal of Coal Geology*, *116*, 158–171.

Gao, F., & Stead, D. (2014). The application of a modified Voronoi logic to brittle fracture modeling at the laboratory and field scale. *International Journal of Rock Mechanics and Mining*, *68*, 1–14.

Garza-Cruz, T., Pierce, M., & Kaiser, P. K. (2014). Use of 3DEC to study spalling and deformation associated with tunnelling at depth. *Deep Mining*. Sudbury: Australian Center for Geomechanics.

Germanovich, L. N., Salganik, R. L., Dyskin, A. V, & Lee, K. K. (1994). Mechanisms of brittle fracture of rock with pre-existing cracks in compression. *Pure and Applied Geophysics*, *143*(1), 117–149.

Ghazvinian, E., Diederichs, M. S., & Quey, R. (2014). 3D random Voronoi grain-based models for simulation of brittle rock damage and fabric-guided micro-fracturing. *Journal of Rock Mechanics and Geotechnical Engineering*, *6*(6), 506–521.

Gokceoglu, C., Sonmez, H., & Kayabasi, A. (2003). Predicting the deformation moduli of rock masses. *International Journal of Rock Mechanics and Mining Sciences*, *40*(5), 701–710.

Golder. (2018). *FracMan, Ver. 7.5*. Redmond: Golder Associates.

González-Nicieza, C., Álvarez-Fernández, M. I., Menéndez-Díaz, A., & Álvarez-Vigil, A. E. (2006). A comparative analysis of pillar design methods and its application to Marble mines. *Rock Mechanics and Rock Engineering*, *39*(5), 421–444.

González-Palacio, C., Menéndez-Díaz, A., Álvarez-Vigil, A. E., & González-Nicieza, C. (2005). Identification of non-pyramidal key blocks in jointed rock masses for tunnel excavation. *Computers and Geotechnics*, *32*(3), 179–200.

Guo, S., & Qi, S. (2015). Numerical study on progressive failure of hard rock samples with an unfilled undulate joint. *Engineering Geology*, *193*, 173–182.

Haeri, H., Shahriar, K., Marji, M. F., & Moarefvand, P. (2014). On the strength and crack propagation process of the pre-cracked rock-like specimens under uniaxial compression. *Strength of Materials*, *46*(1), 140–152.

Haimson, B. (2006). True triaxial stresses and the brittle fracture of rock. *Pure and Applied Geophysics*, *163*(5), 1101–1130.

Hamdi, E., & du Mouza, J. (2005). A methodology for rock mass characterisation and classification to improve blast results. *International Journal of Rock Mechanics and Mining Sciences*, *42*(2), 177–194.

Hardy, P., & Agapito, J. F. T. (1982). Induced horizontal stress method of pillar design in oil shale. *Proc. 15th Oil Shale Symposium*, 191–197. Golden: Colorado School of Mines.

Harthong, B., Scholtès, L., & Donzé, F.-V. (2012). Strength characterization of rock masses, using a coupled DEM–DFN model. *Geophysical Journal International*, *191*(2), 467–480.

Havaej, M., Coggan, J., Stead, D., & Elmo, D. (2016). A combined remote sensing-Numerical modelling approach to the stability analysis of Delabole Slate Quarry, Cornwall, UK. *Rock Mechanics and Rock Engineering*, *49*(4), 1227–1245.

Havaej, M., & Stead, D. (2016). Investigating the role of kinematics and damage in the failure of rock slopes. *Computers and Geotechnics*, *78*, 181–193.

Hedley, D., & Grant, F. (1972). Stope-and-pillar design for Elliot lake uranium mines. *Canadian Mining and Metalurgical Bulletin*, *65*(723), 37.

Herrero, C. (2015). *Quantifying the effect of in-situ stresses and pit depth on slope stability by incorporating brittle fracturing in numerical model analyses*. PhD Thesis, Colorado School of Mines.

Hoek, E. (1994). Strength of rock and rock masses. *ISRM News Journal*, *2*(2), 4–16.

Hoek, E., & Bieniawski, Z. T. (1965). Brittle fracture propagation in rock under compression. *International Journal of Fracture Mechanics*, *1*(3), 137–155.

Hoek, E., & Brown, E. T. (1997). Practical estimates of rock mass strength. *International Journal of Rock Mechanics and Mining Sciences*, *34*(8), 1165–1186.

Hoek, E., & Brown, E. T. (2018). The Hoek–Brown failure criterion and GSI – 2018 edition. *Journal of Rock Mechanics and Geotechnical Engineering*.

Hoek, E., Carranza-Torres, C., & Corkum, B. (2002). Hoek-Brown failure criterion-2002 edition. *Proceedings of NARMS-Tac*, *1*, 267–273.

Hoek, E., & Diederichs, M. S. (2006). Empirical estimation of rock mass modulus. *International Journal of Rock Mechanics and Mining Sciences*, *43*(2), 203–215.

Hoek, E., Kaiser, P. K., & Bawden, W. F. (1995). *Support of Underground Excavations in Hard Rock*. Rotterdam: AA Balkema.

Hoek, E., & Marinos, P. (2007). A brief history of the development of the Hoek-Brown failure criterion. *Soils and Rocks*, *2*, 13.

Hyman, J. D., Karra, S., Makedonska, N., Gable, C. W., Painter, S. L., & Viswanathan, H. S. (2015). dfnWorks: A discrete fracture network framework for modeling subsurface flow and transport. *Computers & Geosciences*, *84*, 10–19.

Itasca. (2016a). *3DEC, Ver. 5.0*. Minneapolis: Itasca Consulting Group, Inc.

Itasca. (2016b). *SRMTools - User's guide and tutorial*. Minneapolis.

Itasca. (2017). *Email correspondence*. Minneapolis.

Ivanova, V. M., Sousa, R., Murrihy, B., & Einstein, H. H. (2014). Mathematical algorithm development and parametric studies with the GEOFRAC three-dimensional stochastic model of natural rock fracture systems. *Computers and Geosciences*, *67*, 100–109.

Ivars, D., Deisman, N., Pierce, M., & Fairhurst, C. (2007). The synthetic rock mass approach-a step forward in the characterization of jointed rock masses. *11th ISRM Congress*. Lisbon: International Society for Rock Mechanics and Rock Engineering.

Ivars, D., Pierce, M., Darcel, C., Reyes-Montes, J., Potyondy, D., & Young RP, Cundall, P. (2011). The synthetic rock mass approach for jointed rock mass modeling. *International Journal of Rock Mechanics and Mining Sciences*, *48*(2), 219–244.

Ivars, D., Pierce, M., & DeGagné, D. (2008). Anisotropy and scale dependency in jointed rock-mass strength—A synthetic rock mass study. In R. Hart, C. Detrouney, & P. Cundal (Eds.), *1st Int. FLAC/DEM Symp. on Numerical Modeling* (pp. 231–239). Minneapolis: Itasca Consulting Group, Inc.

Jade, S., & Sitharam, T. G. (2003). Characterization of strength and deformation of jointed rock mass based on statistical analysis. *International Journal of Geomechanics*, *3*(1), 43–54.

Janeczek, D. (2015). *MoFrac 2.0: Fracture network software for site characterization* (p. 127). p. 127. Sudbury.

Jennings, J. E. (1970). A mathematical theory for the calculation of the stability of open cast mines. In P. W. J. van Rensberg (Ed.), *Symposium on Planning of Open Pit Mines*. Netherlands: CRC Press.

Jiefan, H., Ganglin, C., Yonghong, Z., & Ren, W. (1990). An experimental study of the strain field development prior to failure of a marble plate under compression. *Tectonophysics*, *175*(1–3), 269–284.

Jin, G., & Pashin, J. (2007). DFNModeler: An efficient discrete fracture network modeler. *International Coalbed Methane Symposium*, 143–158. Tuscaloosa, Alabama: University of Alabama.

Jing, L. (2003). A review of techniques, advances and outstanding issues in numerical modeling for rock mechanics and rock engineering. *International Journal of Rock Mechanics and Mining Sciences*, *40*(3), 283–353.

Jing, L. (2007). Fundamentals of discrete element methods for rock engineering - Theory and applications. *Developments in Geotechnical Engineering*, *85*, 47–109.

Jing, L., & Stephansson, O. (2007). Discrete fracture network (DFN) method. In *Developments in Geotechnical Engineering* (Vol. 85, pp. 365–398).

JKMRC. (2000). *Jointstats*.

Junkin, W., Janeczek, D., Bastola, S., Wang, X., Cai, M., Fava, L., Sykes, E., Munier, R., & Srivastava, R. M. (2017). Discrete Fracture Network Generation for the Äspö TAS08 Tunnel Using MoFrac. *51st U.S. Rock Mechanics/Geomechanics Symposium*. San Francisco, California, USA.

Kaiser, P. K., Diederichs, M. S., Martin, C. D., Sharp, J., & Steiner, W. (2000). Underground Works In Hard Rock Tunnelling And Mining. *ISRM International Symposium*, 87. Melbourne, Australia: International Society for Rock Mechanics and Rock Engineering.

Kaiser, P. K., Kim, B., Bewick, R. P., & Valley, B. (2011). Rock mass strength at depth and implications for pillar design. *Mining Technology*, *120*(3), 170–179.

Kalamaras, G. S., & Bieniawski, Z. T. (1993). A rock mass strength concept for coal seams. *Proceedings of the 12th International Conference on Ground Control in Mining*, 3–5. Morgantown: Society of Mining Metallurgy and Exploration.

Kayabasi, A., Gokceoglu, C., & Ercanoglu, M. (2003). Estimating the deformation modulus of rock masses: A comparative study. *International Journal of Rock Mechanics and Mining Sciences*, *40*(1), 55–63.

Kim, B. H., Cai, M., Kaiser, P. K., & Yang, H. S. (2006). Estimation of block sizes for rock masses with non-persistent joints. *Rock Mechanics and Rock Engineering*, *40*(2), 169.

Kozicki, J., & Donzé, F. V. (2008). A new open-source software developed for numerical simulations using discrete modeling methods. *Computer Methods in Applied Mechanics and Engineering*, *197*(49–50), 4429–4443.

Kozicki, J., & Donzé, F. V. (2009). YADE-OPEN DEM: an open-source software using a discrete element method to simulate granular material. *Engineering Computations*, *26*(7), 786–805.

Krauland, N., & Soder, P. E. (1987). Determining pillar strength-from pillar failure observation. *Engineering and Mining Journal*, *188*(8), 34–40.

Kulatilake, P. H. S. W., He, W., Um, J., & Wang, H. (1997). A physical model study of jointed rock mass strength under uniaxial compressive loading. *International Journal of Rock Mechanics and Mining Sciences*, *34*(3–4), 165(1-15).

Kulatilake, P. H. S. W., Liang, J., & Gao, H. (2001). Experimental and numerical simulations of jointed rock block strength under uniaxial loading. *Journal of Engineering Mechanics*, *127*(12), 1240–1247.

Kulatilake, P. H. S. W., Mehranpour, M. H., Xingen, M., & He, M. (2018). A new three-dimensional rock mass strength criterion. *Recent Advances in Geo-Environmental Engineering, Geomechanics and Geotechnics, and Geohazards*. Cham. pp.3-6.

Kulatilake, P. H. S. W., & Shu, B. (2015). Prediction of rock mass deformations in three dimensions for a part of an open pit mine and comparison with field deformation monitoring data. *Geotechnical and Geological Engineering*, *33*(6), 1551–1568.

Kulatilake, P., & Wu, T. (1984). Estimation of mean trace length of discontinuities. *Rock Mechanics and Rock Engineering*, *17*(4), 215–232.

Lajtai, E. Z. (1974). Brittle fracture in compression. *International Journal of Fracture*, *10*(4), 525–536.

Laubscher, D. H., & Jakubec, J. (2001). The MRMR rock mass classification for jointed rock masses. In W. Hustrulid & R. Bullock (Eds.), *Underground Mining Methods: Engineering Fundamentals and International Case Studies* (pp. 475–481). Society of Mining Metallurgy and Exploration.

Le Goc, R., Darcel, C., Davy, P., Pierce, M., & Brossault, M. A. (2014). Effective elastic properties of 3D fractured systems. *1st International Discrete Fracture Network Engineering Conference*, 8. Vancouver.

Lee, H., & Jeon, S. (2011). An experimental and numerical study of fracture coalescence in pre-cracked specimens under uniaxial compression. *International Journal of Solids and Structures*, *48*(6), 979–

999.

Lee, J., Hong, J.-W., & Jung, J.-W. (2017). The mechanism of fracture coalescence in pre-cracked rock-type material with three flaws. *Engineering Geology*, *223*, 31–47.

Lei, Q., Latham, J.-P., & Tsang, C.-F. (2017). The use of discrete fracture networks for modeling coupled geomechanical and hydrological behaviour of fractured rocks. *Computers and Geotechnics*, *85*, 151–176.

Li, T., Hewson, S., & Pothitos, F. (2003). Design and optimisation of Cadia Hill Open Pit, Cadia Valley Operations, Newcrest Mining Limited. *Proc. 5th Large Open Pit Conference*, 123–126. Kalgoorie, WA: AusIMM.

Li, X. F., Li, H. B., Li, J. C., & Xia, X. (2016). Crack initiation and propagation simulation for polycrystalline-based brittle rock utilizing three dimensional distinct element method. In *Rock Dynamics: From Research to Engineering* (pp. 341–348). CRC Press.

Li, Y.-P., Chen, L.-Z., & Wang, Y.-H. (2005). Experimental research on pre-cracked marble under compression. *International Journal of Solids and Structures*, *42*(9–10), 2505–2516.

Li, Y., & Huang, R. (2015). Relationship between joint roughness coefficient and fractal dimension of rock fracture surfaces. *International Journal of Rock Mechanics and Mining Sciences*, *75*, 15–22.

Lorig, L., Darcel, C., & Damjanac, B. (2015). Application of discrete fracture networks in mining and civil geomechanics. *Mining Technology*, *124*(4), 239–254.

Lunder, P. J., & Pakalnis, R. C. (1997). Determination of the strength of hard-rock mine pillars. *CIM Bulletin*, *90*(1013), 51–55.

Mahabadi, O. K., Grasselli, G., & Munjiza, A. (2010). Y-GUI: A graphical user interface and pre-processor for the combined finite-discrete element code, Y2D, incorporating material heterogeneity. *Computers & Geosciences*, *36*(2), 241–252.

Manouchehrian, A., & Marji, M. F. (2012). Numerical analysis of confinement effect on crack propagation mechanism from a flaw in a pre-cracked rock under compression. *Acta Mechanica Sinica*, *28*(5), 1389–1397.

Manouchehrian, A., Sharifzadeh, M., Marji, M. F., & Gholamnejad, J. (2014). A bonded particle model for analysis of the flaw orientation effect on crack propagation mechanism in brittle materials under compression. *Archives of Civil and Mechanical Engineering*, *14*(1), 40–52.

Mark, C. (2016). Science of empirical design in mining ground control. *International Journal of Mining Science and Technology*, *26*(3), 461–470.

Martin, C. D. (1993). *The strength of massive Lac du Bonnet granite around underground openings*. University of Manitoba.

Martin, C. D., Kaiser, P. K., & McCreath, D. R. (1999). Hoek-Brown parameters for predicting the depth of brittle failure around tunnels. *Canadian Geotechnical Journal*, *36*(1), 136–151.

Martin, C. D., & Stimpson, B. (1994). The effect of sample disturbance on laboratory properties of Lac du

Bonnet granite. *Canadian Geotechnical Journal*, *31*(5), 692–702.

Martinez, A. (1999). *Fracture coalescence in natural rocks*. Massachutes Institute of Technology.

Mauldon, M., Dunne, W. M., & Rohrbaugh, M. B. (2001). Circular scanlines and circular windows: new tools for characterizing the geometry of fracture traces. *Journal of Structural Geology*, *23*(2–3), 247–258.

Mehrotra, V. K. (1992). *Estimation of engineering parameters of rock mass*. University of Roorkee.

Merrien-Soukatchoff, V., Korini, T., & Thoraval, A. (2012). Use of an integrated discrete fracture network code for stochastic stability analyses of fractured rock masses. *Rock Mechanics and Rock Engineering*, *45*(2), 159–181.

Miller, J. T., & Einstein, H. H. (2008). Crack coalescence tests on granite. *The 42nd U.S. Symposium on Rock Mechanics*. San Francisco, California: American Rock Mechanics Association.

Mogi, K. (1967). Effect of the intermediate principal stress on rock failure. *Journal of Geophysical Research*, *72*(20), 5117–5131.

Mogi, K. (1971). Fracture and flow of rocks under high triaxial compression. *Journal of Geophysical Research*, *76*(5), 1255–1269.

Noorian Bidgoli, M., & Jing, L. (2014). Anisotropy of strength and deformability of fractured rocks. *Journal of Rock Mechanics and Geotechnical Engineering*, *6*(2), 156–164.

Palmstrøm, A. (1996). Characterizing rock masses by the RMi for use in practical rock engineering: Part 1: The development of the Rock Mass index (RMi). *Tunnelling and Underground Space Technology*, *11*(2), 175–188.

Palmström, A., & Singh, R. (2001). The deformation modulus of rock masses — Comparisons between in situ tests and indirect estimates. *Tunnelling and Underground Space Technology*, *16*(2), 115–131.

Park, C. H. (2008). *Coalescence of frictional fractures in rock materials*. PhD Thesis, Purdue University.

Patton, F. D. (1966). Multiple modes of shear failure in rock. *1st ISRM Congress*, 509–513. Lisbon: International Society for Rock Mechanics and Rock Engineering.

Peng, J., Cai, M., Rong, G., Yao, M.-D., Jiang, Q.-H., & Zhou, C.-B. (2017). Determination of confinement and plastic strain dependent post-peak strength of intact rocks. *Engineering Geology*, *218*, 187–196.

Pierce, M., Cundall, P., Potyondy, D., & Ivars, D. M. (n.d.). A synthetic rock mass model for jointed rock. *1st Canada-US Rock Mechanics Symposium*. Vancouver; 27-31 May 2007. pp. 341-349.

Pine, R. J., Coggan, J. S., Flynn, Z. N., & Elmo, D. (2006). The development of a new numerical modeling approach for naturally fractured rock masses. *Rock Mechanics and Rock Engineering*, *39*(5), 395–419.

Porter, J. D., Herbert, A. W., Clarke, D. S., Roe, P., Vassilic Melling, D., Einfeldt, B., Mackay, R., & Glendinning, R. (1992). *Verification and validation of models: far-field modeling of radionuclide*

migration.

Potvin, Y., Hudyma, M. R., & Miller, H. D. S. (1989). Design guidelines for open stope support. *CIM Bulletin*, *82*(926), 53–62.

Potyondy, D. (2015). The bonded-particle model as a tool for rock mechanics research and application: current trends and future directions. *Geosystem Engineering*, *18*(1), 1–28.

Potyondy, D. O. (2017). *Material-modeling support in PFC [fistPkg25]*. Minneapolis.

Potyondy, D. O., & Cundall, P. (2004). A bonded-particle model for rock. *International Journal of Rock Mechanics and Mining Sciences*, *41*(8), 1329–1364.

Poulsen, B. A., Adhikary, D. P., Elmouttie, M. K., & Wilkins, A. (2015). Convergence of synthetic rock mass modeling and the Hoek–Brown strength criterion. *International Journal of Rock Mechanics and Mining Sciences*, *80*, 171–180.

Priest, S. D. (1993). Discontinuities and rock deformability. In *Discontinuity Analysis for Rock Engineering*. Dordrecht: Springer. pp. 300-339.

Priest, S. D., & Hudson, J. A. (1976). Discontinuity spacings in rock. *International Journal of Rock Mechanics and Mining Sciences & Geomechanics Abstracts*, *13*(5), 135–148.

Priest, S. D., & Hudson, J. A. (1981). Estimation of discontinuity spacing and trace length using scanline surveys. *International Journal of Rock Mechanics and Mining Sciences & Geomechanics Abstracts*, *18*(3), 183–197.

Prudencio, M., & Van Sint Jan, M. (2007). Strength and failure modes of rock mass models with non-persistent joints. *International Journal of Rock Mechanics and Mining Sciences*, *44*(6), 890–902.

Ramamurthy, T. (2001). Shear strength response of some geological materials in triaxial compression. *International Journal of Rock Mechanics and Mining Sciences*, *38*(5), 683–697.

Ramamurthy, T. (2004). A geo-engineering classification for rocks and rock masses. *International Journal of Rock Mechanics and Mining Sciences*, *41*(1), 89–101.

Ramamurthy, T., & Arora, V. K. (1994). Strength predictions for jointed rocks in confined and unconfined states. *International Journal of Rock Mechanics and Mining Sciences & Geomechanics Abstracts*, *31*(1), 9–22.

Read, S. A. L., Perrin, N. D., & Richards, L. R. (1999). Applicability of the Hoek-Brown failure criterion to New Zealand Greywacke rocks. *9th ISRM Congress*. Paris, France: International Society for Rock Mechanics and Rock Engineering.

Reyes, O., & Einstein, H. H. (1991). Failure mechanisms of fractured rock - A fracture coalescence model. *7th ISRM Congress*. Aachen, Germany: International Society for Rock Mechanics and Rock Engineering.

Rockfield. (2016). *ELFEN*. Swansea.

Rocscience. (2016). *DIPS, Ver. 6.0.17*. Toronto: Rocscience.

Rogers, S. (2015). Volumetric fracture intensity measurement for improved rock mass characterisation and fragmentation assessment in block caving operations. *Rock Mechanics and Rock Engineering*, *48*(2), 633–649.

Rosengren, K. J., & Jaeger, J. C. (1968). The mechanical properties of an interlocked low-porosity aggregate. *Géotechnique*, *18*(3), 317–326.

Sagong, M., & Bobet, A. (2002). Coalescence of multiple flaws in a rock-model material in uniaxial compression. *International Journal of Rock Mechanics and Mining Sciences*, *39*(2), 229–241.

Sainsbury, D. P., Vakili, A., Lucas, D. S., & Hutchison, B. J. (2016). Three-dimensional numerical modelling of potential structurally controlled failure mechanisms at the Kanmantoo open pit. In P. M. Dight (Ed.), *1st Asia Pacific Slope Stability in Mining Conference* (pp. 143–156). Perth: Australian Centre for Geomechanics.

Sainsbury, D., Pothitos, F., Finn, D., & Silva, R. (2007). Three-dimensional discontinuum analysis of structurally controlled failure mechanisms at the Cadia Hill Open Pit. In Y. Potvin (Ed.), *Int. Sym. on Rock Slope Stability in Open Pit Mining & Civil Engineering* (pp. 307–320). Perth.

Scavia, C. (1995). A method for the study of crack propagation in rock structures. *Géotechnique*, *45*(3), 447–463.

Scholtès, L., & Donzé, F.-V. (2012). Modelling progressive failure in fractured rock masses using a 3D discrete element method. *International Journal of Rock Mechanics and Mining Sciences*, *52*, 18–30.

Sharafisafa, M., & Nazem, M. (2014). Application of the distinct element method and the extended finite element method in modelling cracks and coalescence in brittle materials. *Computational Materials Science*, *91*, 102–121.

Sheorey, P. R. (1997). *Empirical rock failure criteria*. AA Balkema.

Sheorey, P. R., Loui, J. P., Singh, K. B., & Singh, S. K. (2000). Ground subsidence observations and a modified influence function method for complete subsidence prediction. *International Journal of Rock Mechanics and Mining Sciences*, *37*(5), 801–818.

Shi, G. H. (1988). *Discontinuous deformation analysis: A new numerical model for the statics and dynamics of block systems*. PhD Thesis, University of California Berkeley.

Singh, B., Villadkar, M. N., Samadhiya, N. K., & Mehrotra, V. K. (1997). Rock mass strength parameters mobilised in tunnels. *Tunnelling and Underground Space Technology*, *12*(1), 47–54.

Singh, M., Rao, K. S., & Ramamurthy, T. (2002). Strength and deformational behaviour of a jointed rock mass. *Rock Mechanics and Rock Engineering*, *35*(1), 45–64.

Singhal, B. B. S., & Gupta, R. P. (2010a). Applied hydrogeology of fractured rocks: Second edition. In *Applied Hydrogeology of Fractured Rocks: Second Edition*. Springer Netherlands.

Singhal, B. B. S., & Gupta, R. P. (2010b). Fracture and discontinuities. In *Applied Hydrogeology of Fractured Rocks: Second Edition* (2nd ed., p. 415). Springer.

Sjoberg, J. (1996). *Large scale slope stability in open pit mining - A review*. Lulea.

Sjoberg, J. S. (1992). Failure modes and pillar behaviour in the Zinkgruvan mine. *The 33th US Symposium on Rock Mechanics*. New Mexico.

Srivastava, R. M. (2002). *The discrete fracture network model in the local scale flow system for The Case Study*. Toronto.

SYSTAT. (2016). *TableCurve 3D*. Systat Software Inc.

Tang, C. A., Lin, P., Wong, R. H. C., & Chau, K. T. (2001). Analysis of crack coalescence in rock-like materials containing three flaws—Part II: numerical approach. *International Journal of Rock Mechanics and Mining Sciences*, *38*(7), 925–939.

Tang, C., & Tang, S. (2011). Applications of rock failure process analysis (RFPA) method. *Journal of Rock Mechanics and Geotechnical Engineering*, *3*(4), 352–372.

Tatone, B. S. A., & Grasselli, G. (2013). An investigation of discontinuity roughness scale dependency using high-resolution surface measurements. *Rock Mechanics and Rock Engineering*, *46*(4), 657–681.

Tiwari, R. P., & Rao, K. S. (2004). Physical modeling of a rock mass under a true triaxial stress state. *International Journal of Rock Mechanics and Mining Sciences*, *41*(Supplement 1), 396–401.

Tiwari, R. P., & Rao, K. S. (2006). Post failure behaviour of a rock mass under the influence of triaxial and true triaxial confinement. *Engineering Geology*, *84*(3), 112–129.

Trueman, R. (1988). *An evaluation of strata support techniques in dual life gateroads*. PhD, University of Wales.

Turichshev, A., & Hadjigeorgiou, J. (2017). Development of synthetic rock mass bonded block models to simulate the behaviour of intact veined rock. *Geotechnical and Geological Engineering*, *35*(1), 313–335.

Vallejos, J. A., Suzuki, K., Brzovic, A., & Ivars, D. M. (2016). Application of synthetic rock mass modeling to veined core-size samples. *International Journal of Rock Mechanics and Mining Sciences*, *81*, 47–61.

Varun, V., & Damjanac, B. (2012). *Slope Model - Validation report*. Minneapolis.

Vásárhelyi, B., & Bobet, A. (2000). Modeling of crack initiation, propagation and coalescence in uniaxial compression. *Rock Mechanics and Rock Engineering*, *33*(2), 119–139.

Von Kimmelmann, M. R., Hyde, B., & Madgwick, R. J. (1984). 7 The use of computer applications at BCL Limited in planning pillar extraction and the design of mining layouts. *Design and Performance of Underground Excavations: ISRM Symposium*, 53–63. Cambridge.

Wang, R., Zhao, Y., Chen, Y., Van, H., Yin, Y.-Q., Yao, C.-Y., & Zhang, H. (1987). Experiment and finite element simulation of X-type shear fractures from a crack in marble. *Tectonophysics*, *144*(1–3), 141–150.

Wang, S. Y., Sloan, S. W., Sheng, D. C., Yang, S. Q., & Tang, C. A. (2014). Numerical study of failure behaviour of pre-cracked rock specimens under conventional triaxial compression. *International*

Journal of Solids and Structures, *51*(5), 1132–1148.

Wang, X. (2005). *Stereological interpretation of rock fracture traces on borehole walls and other cylindrical surfaces*. PhD Thesis. Virginia Polytechnic Institute and State University.

Wang, X., & Cai, M. (2018a). A DFN-DEM multi-scale modeling approach for jointed rock mass. *2nd International Discrete Fracture Network Engineering Conference*, 11. Seattle, USA.

Wang, X., & Cai, M. (2018b). Modeling of brittle rock failure considering inter- and intra-grain contact failures. *Computers and Geotechnics*, *101*, 224–244.

Wang, Y., Zhou, X., & Shou, Y. (2017). The modeling of crack propagation and coalescence in rocks under uniaxial compression using the novel conjugated bond-based peridynamics. *International Journal of Mechanical Sciences*, *128–129*, 614–643.

Wilson, A. J. (2003). *The geology, genesis and exploration context of the Cadia gold-copper porphyry deposits, New South Wales, Australia*. PhD Thesis, University of Tasmania.

Wong, L. N. Y., & Einstein, H. H. (2009a). Crack coalescence in molded Gypsum and Carrara Marble: Part 1. macroscopic observations and interpretation. *Rock Mechanics and Rock Engineering*, *42*(3), 475–511.

Wong, L. N. Y., & Einstein, H. H. (2009b). Crack coalescence in molded Gypsum and Carrara Marble: Part 2-microscopic observations and interpretation. *Rock Mechanics and Rock Engineering*, *42*(3), 513–545.

Wong, L. N. Y., & Einstein, H. H. (2009c). Systematic evaluation of cracking behavior in specimens containing single flaws under uniaxial compression. *International Journal of Rock Mechanics and Mining Sciences*, *46*(2), 239–249.

Wong, R. H. C., & Chau, K. T. (1998). Crack coalescence in a rock-like material containing two cracks. *International Journal of Rock Mechanics and Mining Sciences*, *35*(2), 147–164.

Wong, R. H. C., Chau, K. T., Tang, C. A., & Lin, P. (2001). Analysis of crack coalescence in rock-like materials containing three flaws—Part I: experimental approach. *International Journal of Rock Mechanics and Mining Sciences*, *38*(7), 909–924.

Wyllie, D. C. (2017a). Numerical analysis. In C. Press (Ed.), *Rock Slope Engineering* (pp. 319–348).

Wyllie, D. C. (2017b). Rock strength properties and their measurements. In C. Press (Ed.), *Rock Slope Engineering* (pp. 117–162). Taylor & Francis.

Wyllie, D. C. (2017c). Site investigation and geologic data collection. In *Rock Slope Engineering* (5th ed., p. 621). CRC Press.

Wyllie, D. C. (2017d). Structural geology and data interpretation. In *Rock Slope Engineering* (p. 621). CRC Press.

Xu, C., & Dowd, P. (2010). A new computer code for discrete fracture network modeling. *Computers and Geosciences*, *36*(3), 292–301.

Xu, J., Zheng, Z., Xiao, X., & Li, Z. (2018). Crack propagation and coalescence due to dual non-penetrating surface flaws and their effect on the strength of rock-like material. *Journal of Geophysics and Engineering*, *15*(3), 938.

Yang, S. Q., Dai, Y. H., Han, L. J., & Jin, Z. Q. (2009). Experimental study on mechanical behavior of brittle marble samples containing different flaws under uniaxial compression. *Engineering Fracture Mechanics*, *76*(12), 1833–1845.

Yang, S. Q., Jiang, Y. Z., Xu, W. Y., & Chen, X. Q. (2008). Experimental investigation on strength and failure behavior of pre-cracked marble under conventional triaxial compression. *International Journal of Solids and Structures*, *45*(17), 4796–4819.

Yin, P., Wong, R. H. C., & Chau, K. T. (2014). Coalescence of two parallel pre-existing surface cracks in granite. *International Journal of Rock Mechanics and Mining Sciences*, *68*, 66–84.

Yudhbir, Y., Lemanza, W., & Prinzl, F. (1983). An empirical failure criterion for rock masses. *5th ISRM Congress*. Melbourne, Australia.

Zhang, L. (2010). Estimating the strength of jointed rock masses. *Rock Mechanics and Rock Engineering*, *43*(4), 391–402.

Zhang, L. (2017). Evaluation of rock mass deformability using empirical methods – A review. *Underground Space*, *2*(1), 1–15.

Zhang, L., & Einstein, H. (1998). Estimating the mean trace length of rock discontinuities. *Rock Mechanics and Rock Engineering*, *31*(4), 217–235.

Zhang, L., & Einstein, H. . (2000). Estimating the intensity of rock discontinuities. *International Journal of Rock Mechanics and Mining Sciences*, *37*(5), 819–837.

Zhang, L., & Einstein, H. H. (2004). Using RQD to estimate the deformation modulus of rock masses. *International Journal of Rock Mechanics and Mining Sciences*, *41*(2), 337–341.

Zhang, X.-P., & Wong, L. N. Y. (2012). Cracking processes in rock-like material containing a single flaw under uniaxial compression: A numerical study based on parallel bonded-particle model approach. *Rock Mechanics and Rock Engineering*, *45*(5), 711–737.

Zhang, X.-P., & Wong, L. N. Y. (2013). Crack initiation, propagation and coalescence in rock-like material containing two flaws: A numerical study based on bonded-particle model approach. *Rock Mechanics and Rock Engineering*, *46*(5), 1001–1021.

Zhang, Y. (2014). *Modeling hard rock pillars using a synthetic rock mass approach*. PhD Thesis, Simon Fraser University.

Zhou, X.-P., Zhang, J.-Z., & Wong, L. N. Y. (2018). Experimental study on the growth, coalescence and wrapping behaviors of 3D cross-embedded flaws under uniaxial compression. *Rock Mechanics and Rock Engineering*, *51*(5), 1379–1400.

Curriculum Vitae

Name: Subash Bastola

Education:

- BS in Mining Engineering (2010), Instituto Superior Minero Metalúrgico de Moa, Cuba
- MS in Mining Engineering (2015), Southern Illinois University Carbondale, USA

Work experience: Researcher at MIRARCO Mining Innovation, Laurentian University, Sudbury, Canada (2015-2019)

PhD Thesis related publications:

Journals:

[1] **Bastola, S.** and Cai, M. (2019) 'Investigation of mechanical properties and crack propagation in pre-cracked marbles using lattice-spring-based synthetic rock mass (LS-SRM) modeling approach', *Computers and Geotechnics*, 110, 28–43.

[2] **Bastola, S.,** Cai, M., and Damjanac, B. (2019) 'Investigation of the slope stability of an open pit using lattice-spring-based synthetic rock mass (LS-SRM) modeling approach', (Resubmitted to *Journal of Rock Mechanics and Geotechnical Engineering* with minor revisions)

[3] **Bastola, S.** and Cai, M. (2019) 'Investigation of mechanical properties of jointed granite under compression using lattice-spring-based synthetic rock mass (LS-SRM) modeling approach' (Accepted for publication in the *International Journal of Rock Mechanics and Mining Sciences*)

Conference proceedings:

[1] **Bastola, S**. and Cai, M. (2018) 'Investigation of Strength and Deformation Behaviors of Intact and Jointed Granite using Lattice-Spring-Based Synthetic Rock Mass Models', in *2nd International Discrete Fracture Network Engineering Conference*. Seattle, Washington, USA: American Rock Mechanics Association.

[2] **Bastola, S.** and Cai, M. (2018) 'Simulation of Stress–Strain Relations of Zhenping Marble using Lattice-Spring-Based Synthetic Rock Mass Models', in *52nd U.S. Rock Mechanics/Geomechanics Symposium*. Seattle, Washington, USA: American Rock Mechanics Association.

[3] Junkin, W., Janeczek, D., **Bastola, S.**, Wang, X., Cai, M., Fava, L., Sykes, E., Munier, R. and Srivastava, R. M. (2017) 'Discrete Fracture Network Generation for the Äspö TAS08 Tunnel Using MoFrac', in *51st U.S. Rock Mechanics/Geomechanics Symposium*. San Francisco, California, USA: American Rock Mechanics Association.

Reports:

[1] **Bastola, S.**, Cai, M., Fava, L. Validation of MoFrac using The Third Case Study datasets. Report prepared for *Nuclear Waste Management Organization* Feb. 2016.
[2] **Bastola, S.**, Cai, M., Fava, L. Validation of MoFrac using Aspo datasets. Report prepared for *Nuclear Waste Management Organization* Dec. 2015.

Other publications:

[1] Aguilera-Fernández, I., Batista-Legrá, Y., **Bastola, S.**, Rojas-Purón, L. (2016) 'Impacto visual generado por la explotación minera en el yacimiento Punta Gorda', *Minería y Geología*, 32(4), 141–159
[2] **Bastola, S.,** Chugh, Y. P. (2015) Shear strength and stiffness of bedding planes and discontinuities in the immediate roof rocks overlying the No. 6 coal seam in Illinois. *Proc. of ISRM conference,* Montreal, Canada.
[3] **Bastola**, **S.,** Carlton, C., Abbasi, B., Chugh, Y. P. (2013) Stress distribution around typical field intersection geometries in coal mines. *Proc. of SME conf.*, Denver, USA.
[4] Chugh, Y. P., Gurley, H., Abbasi, B., **Bastola, S.,** Carlton, C. (2012) Analysis and measurement of ground control stability in setup rooms and gate roads in an Illinois longwall operation. *Illinois Mining Institute Annual Meeting*, Illinois, USA.